ASME
SETTING THE STANDARD

Journal of Fluids Engineering

Published Monthly by ASME

VOLUME 131 • NUMBER 11 • NOVEMBER 2009

Transactions of the ASME, Journal of Fluids Engineering (ISSN 0098-2202) is published monthly by The American Society of Mechanical Engineers, Three Park Avenue, New York, NY 10016. Periodicals postage paid at New York, NY and additional mailing offices.
POSTMASTER: Send address changes to Transactions of the ASME, Journal of Fluids Engineering, c/o THE AMERICAN SOCIETY OF MECHANICAL ENGINEERS, 22 Law Drive, Box 2300, Fairfield, NJ 07007-2300.
CHANGES OF ADDRESS must be received at Society headquarters seven weeks before they are to be effective. Please send old label and new address.

RESEARCH PAPERS

Flows in Complex Systems

111101 Flow Patterns and Aerodynamic Performance of Unswept and Swept-Back Wings
Shun C. Yen and Lung-C. Huang

111102 Theoretical Study of the Laminar Flow in a Channel With Moving Bars
Hai-Ping Hu and Rong-Hua Yeh

111103 2D Numerical Simulations of Blade-Vortex Interaction in a Darrieus Turbine
E. Amet, T. Maître, C. Pellone, and J.-L. Achard

111104 Modification of Axial Fan Flow by Trailing Edge Self-Induced Blowing
Matjaž Eberlinc, Brane Širok, Matevž Dular, and Marko Hočevar

111105 Pressure Drop in Laminar Developing Flow in Noncircular Ducts: A Scaling and Modeling Approach
Y. S. Muzychka and M. M. Yovanovich

Fundamental Issues and Canonical Flows

111201 Direct Simulation Based Model-Predictive Control of Flow Maldistribution in Parallel Microchannels
Mathieu Martin, Chris Patton, John Schmitt, and Sourabh V. Apte

111202 Control of Vortex Shedding From a Plate at Incidence Angles in the Range of 0–90 Deg
Chuan Ping Shao and Jian Zhong Lin

111203 Assessment of DES Models for Separated Flow From a Hump in a Turbulent Boundary Layer
Daniel C. Lyons, Leonard J. Peltier, Frank J. Zajaczkowski, and Eric G. Paterson

Multiphase Flows

111301 Creation and Maintenance of Cavities Under Horizontal Surfaces in Steady and Gust Flows
R. E. A. Arndt, W. T. Hambleton, E. Kawakami, and E. L. Amromin

111302 Cavitation Inception in the Wake of a Jet-Driven Body
Roger E. A. Arndt, Eduard L. Amromin, and William Hambleton

111303 CFD Modeling and X-Ray Imaging of Biomass in a Fluidized Bed
Mirka Deza, Nathan P. Franka, Theodore J. Heindel, and Francine Battaglia

(Contents continued on inside back cover)

This journal is printed on acid-free paper, which exceeds the ANSI Z39.48-1992 specification for permanence of paper and library materials. ♾™
♻ 85% recycled content, including 10% post-consumer fibers.

(**Contents continued**)

Techniques and Procedures

111401 Application of MI Simulation Using a Turbulent Model for Unsteady Orifice Flow
Mitsuhiro Nakao, Kenji Kawashima, and Toshiharu Kagawa

The ASME Journal of Fluids Engineering is abstracted and indexed in the following:

Applied Science & Technology Index, Chemical Abstracts, Chemical Engineering and Biotechnology Abstracts (Electronic equivalent of Process and Chemical Engineering), Civil Engineering Abstracts, Computer & Information Systems Abstracts, Corrosion Abstracts, Current Contents, Ei EncompassLit, Electronics & Communications Abstracts, Engineered Materials Abstracts, Engineering Index, Environmental Engineering Abstracts, Environmental Science and Pollution Management, Excerpta Medica, Fluidex, Index to Scientific Reviews, INSPEC, International Building Services Abstracts, Mechanical & Transportation Engineering Abstracts, Mechanical Engineering Abstracts, METADEX (The electronic equivalent of Metals Abstracts and Alloys Index), Petroleum Abstracts, Process and Chemical Engineering, Referativnyi Zhurnal, Science Citation Index, SciSearch (The electronic equivalent of Science Citation Index), Shock and Vibration Digest, Solid State and Superconductivity Abstracts, Theoretical Chemical Engineering

Flow Patterns and Aerodynamic Performance of Unswept and Swept-Back Wings

Shun C. Yen[1]
Associate Professor
Department of Mechanical and Mechatronic Engineering,
National Taiwan Ocean University,
Keelung, Taiwan 202, R.O.C.
e-mail: scyen@mail.ntou.edu.tw

Lung –C. Huang
Department of Mechanical Engineering,
National Taiwan University of Science and Technology,
Taipei, Taiwan 106, R.O.C.

The effects of sweep-back angle (Λ), Reynolds number (Re), and angle of attack (α) on the boundary-layer flow structures and aerodynamic performance of a finite swept-back wing were experimentally investigated. The Reynolds number and sweep-back angle used in this test is $30,000 < Re < 130,000$ and $0 \text{ deg} \leq \Lambda \leq 45$ deg. The wing model was made of stainless steel, and the wing airfoil is NACA 0012. The chord length is 6 cm, and the semiwing span is 30 cm; and therefore, the semiwing aspect ratio is 5. The boundary-layer flow structures were visualized using the surface oil-flow technique. Seven boundary-layer flow modes were categorized by changing Re and α. A six-component balance is used to determine aerodynamic loadings. The aerodynamic performance is closely related to the boundary-layer flow modes. The stall angle of attack (α_{stall}) is deferred from 9 deg to 10 deg (for an unswept wing), to 30 deg to 35 deg (for a swept-back wings of $\Lambda > 30$ deg). The deferment of α_{stall} is induced from the increased rotation energy and turbulent intensity generated from the secondary flow. Furthermore, the increased rotation energy and turbulent intensity resisted the reverse pressure generated at high α. [DOI: 10.1115/1.4000260]

Keywords: swept-back wings, surface oil-flow, aerodynamic performance

1 Introduction

Swept wings are extensively adopted in industrial applications. This study attempts to enhance the performance of a flow-guiding vane in a swirl-flow generator at low Reynolds number (Re). The experimental results can be applied in designing, for example, rotary fan blades, wind-power generators, fluid mixers, and micro unmanned aerial vehicles (UAVs). The pitch up is induced from tip stall [1], however, the properties of swept-back wings remain worthy of study because they associate with many steady/unsteady aerodynamic phenomena. For example, the surface-flow patterns affect laminar separation, transition, turbulent reattachment, and bubble burst [2–6] due to its significant effect on the aerodynamic performance [7–9].

Purser and Spearman [10] studied the general behaviors and stall patterns of the surface flow on swept-back wings at low Reynolds numbers using the tuft-sketch scheme. At a moderate lift coefficient (C_L), the flow is disturbed near the leading edge, and the tip stall moves toward the central section of the wings. In addition, the shape and size of a taper wing did not appreciably affect the stall pattern. Black [11] elucidated the general behavior of the surface flow by examining the formation of short and long laminar separation bubbles on thin swept-back wings. Black [11] demonstrated that the flow separates on the leading edge and then reattaches behind a short separation bubble over the inboard sections. However, in the outboard section, the flow only reattaches near the trailing edge, thereby generating a long separation bubble that does not attach. The separated flow in tip stall is a tip vortex, and the origin of which is at the junction of the two bubbles on the leading edge. Research investigating the thin oil flow can be traced back to Squire's theoretical work [12]. Squire deduced that oil flow moves along the direction of surface-flow skin friction, except at the separation region. In addition, Squire's experimental results are independent of the oil viscosity, and the effect of oil flow on surface-flow behavior is very small. Poll [13] adopted the surface oil-flow visualization scheme to analyze the surface-flow structure on a RAE 101 airfoil at $\text{Re} = 1.1 \times 10^6 - 2.7 \times 10^6$. Poll identified that no spiral vortex flow occurs at sweep-back angles (Λ) of 0 deg and 15 deg. When the sweep-back angle exceeded 15 deg, the oil flow indicated that spiral vortices occur due to one of the following three mechanisms. First, a full-span vortex can be formed by rolling up the shear layer, leaving the airfoil surface at the primary separation line. Second, a part-span vortex can be formed when the shear layer from the primary separation reattaches and forms a short bubble on the inboard wing portion. Third, a part-span vortex can be formed when the boundary-layer flow downstream of a short separation bubble leaves the surface close to the bubble along the secondary separation line.

The bubble generally extends a large portion of the boundary layer, and significantly changes the pressure distribution. The aerodynamic performance is thus altered markedly. Mueller et al. [14,15] experimentally examined the hysteresis loop in aerodynamic performance with Lissaman 7769, Miley M06-13-128, and NACA 63_3-018 airfoils at low Reynolds numbers. Liu et al. [16] investigated a swept-back wing with $\Lambda = 30$ deg. They found that the lift increase is caused from the impact of strake vortex on the inner and outer panels. Additionally, the impact on the wing at low speeds leads to a nonlinear change of pitching moment by changing the angle of attack (α). The increase rate of lift declines as the Mach number increases at transonic speeds. The increase in the lift/drag ratio is caused by the lift increase at low speeds and drag decline at supersonic speeds, respectively. Huang et al. [17] analyzed the aerodynamic performance of a NACA 0012 airfoil by changing the surface-flow modes at various Reynolds numbers. The surface-flow configurations and free-stream turbulence inevitably change the aerodynamic performance. Furthermore, the highest change rate of lift coefficient ($dC_L/d\alpha$) occurs in the laminar separation mode, and $dC_L/d\alpha$ declines when a separation bubble and stalling occur in the turbulent separation mode. The

[1]Corresponding author.

Contributed by the Fluids Engineering Division of ASME for publication in the JOURNAL OF FLUIDS ENGINEERING. Manuscript received March 7, 2009; final manuscript received July 30, 2009; published online October 19, 2009. Editor: Joseph Katz.

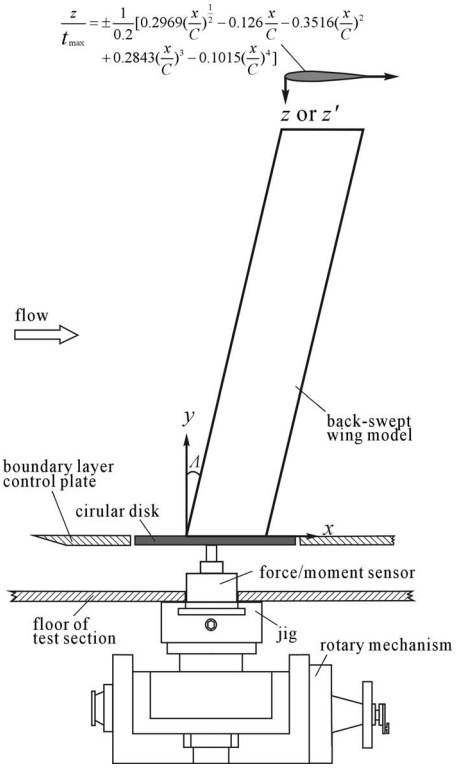

Fig. 1 Experimental setup

drag coefficient (C_D), which decreases slightly in the laminar separation mode, remains almost constant in the separation bubble mode, and increases in the transition mode.

Bubble behaviors in the boundary layer significantly affect the lift, drag, and moment coefficients. The oil-flow scheme was used to visualize the bubble behaviors and surface-flow structures. Yen and Hsu [18] utilized the oil-flow scheme to determine the aerodynamic performance of a finite swept-back wing using various Reynolds numbers and angles of attack. Yen and Hsu also utilized an NACA 0012 airfoil with $\Lambda=15$ deg to visualize surface-flow structures in the range of $30,000<\mathrm{Re}<130,000$. Their experimental results demonstrate that the bubble length was reduced significantly in the separation bubble and leading-edge bubble modes as α increases, and no hysteresis was observed in the aerodynamic performance. This study examines the effects of the sweep-back angle on the boundary-layer flow structures and aerodynamic performance. Therefore, the objectives of this study are listed as follows: (1) to investigate the boundary-layer flow structures; (2) to measure the aerodynamic loadings with a six-component balance; (3) to identify the effect of boundary-layer flow modes on the aerodynamic coefficients; and (4) to correlate the aerodynamic coefficients with the Re, α, and Λ.

2 Experimental Arrangements

The experiments were performed in a closed-return wind tunnel, as depicted in Fig. 1. This wind tunnel consisted of a test section of $60\times60\times120$ cm^3. A polished aluminum alloy plate was used as the test-section floor, and three highly transparent acrylic panels were utilized as the ceiling and side walls of the test-section for photography and visualization. The free-stream velocity (u_∞) was adjusted in the range of 0.56–60 m/s. Therefore, the turbulent intensity was $<0.2\%$, and the nonuniformity of the average velocity profile across the cross section was $<0.5\%$. The free-stream velocity was monitored by a Pitot-static tube. The boundary-layer thicknesses [19] were $\approx$4.0 mm and $\approx$1.7 mm at $u_\infty=5$ m/s and 30 m/s, respectively. In addition, an aluminum plate with sharp leading and trailing edges was placed 50 mm over the test-section floor to control the boundary-layer thickness.

The wing model was made of stainless steel, and the wing airfoil was NACA 0012 [20]. The sweep-back angle Λ was set at 0 deg, 15 deg, 30 deg, 38 deg, and 45 deg. The chord length (C) was 6 cm, and the wing span was 30 cm; and therefore, the half-span wing aspect ratio is equal to 5. Moreover, the wing model was mounted on a supporter and then inset perpendicularly through both the test-section floor and the boundary-layer thickness control plates.

The surface oil-flow technique, as described theoretically by Squire [12], was adopted to detect the surface-flow modes. Mineral oil mixed with blue dye powder was brush coated on the suction surface. The dark traces on the wing surface indicated the position of the accumulated dyed oil. The flow direction on the wing surface was observed using the skin-friction lines visualized by the oil flow. The flow separation and reattachment positions of the boundary layer were obtained from the recorded video images visualized by the surface oil-flow patterns.

The aerodynamic performances were measured by a JR^3 universal force-moment system. The wing assembly and JR^3 force-moment system were mounted on a rotary supporter. The resolution of the rotary supporter is 0.012 deg/div. A six degree-of-freedom force sensor was included in the JR^3 balance. The output electronic signals of the force sensor were sampled by a PC-based high-speed data acquisition system.

The accuracy of u_∞ was affected primarily by the alignment of the Pitot tube and the calibration of the pressure transducer. The uncertainty of u_∞ was estimated $\sim$3% by using a synchronized micropressure calibration system with a careful alignment of Pitot tube. The accuracy of the α was controlled within 0.5%. The uncertainty of separation position was estimated $<4\%$. The uncertainty of the reattachment position was $<6\%$. The accuracy of the force-moment system was determined depending on the mounting and calibration method. The accuracies of lift, drag, and quarter-chord moment were estimated about $\pm1.5\%$, $\pm2\%$, and $\pm2.5\%$, respectively, by using the calibration matrix. Consequently, the accuracies of lift coefficient (C_L), drag coefficient (C_D), and quarter-chord moment coefficient (C_M) were about $\pm2.5\%$, $\pm3\%$ and $\pm3.5\%$, respectively.

3 Results and Discussion

Boundary-layer flow is transited from laminar to turbulent flow at some specific points as the flow moves over an airfoil. This transition typically associates with a separation bubble that thickens the wing profile. The thickened wing profile increases the drag and skin frictions. The image flow structures of separation bubbles are shown in the following sections.

3.1 Flow Over the Wing Surface. The surface oil-flow patterns or skin-friction patterns were employed to visualize the surface-flow structures for $\mathrm{Re}>30,000$ [21]. Figure 2 presents the surface oil-flow patterns on the suction surface of a NACA 0012 swept-back wing using $\Lambda=0$ deg, 15 deg, 30 deg, and 45 deg at $\mathrm{Re}=4.6\times10^4$. Moreover, Fig. 2 shows the effects of α on the surface-flow patterns. Figure 3 delineates the schematic sketches of surface-flow structures by referencing the oil-flow patterns shown in Fig. 2. The dark lines shown in Fig. 2 or the bold lines shown in Fig. 3 indicate the positions of flow separation or reattachment. In addition, the arrowed lines reveal the oil-flow directions. Furthermore, the schematic sketches shown in the bottom panel of Fig. 3 present the profile of boundary-layer flow structures in two-dimensional (2D) configurations.

3.1.1 Type of Surface Oil-Flow Patterns. Figures 2-I and 3-I show the surface oil-flow structures and schematic sketches of an unswept wing (or a straight wing, i.e., $\Lambda=0$ deg) at $\alpha=2$ deg, 6 deg, 9 deg, 11 deg, 15 deg, and 42 deg. Figure 2-I(a) shows that the boundary-layer flow was separated at $x/C\approx0.7$ as $\alpha=2$ deg.

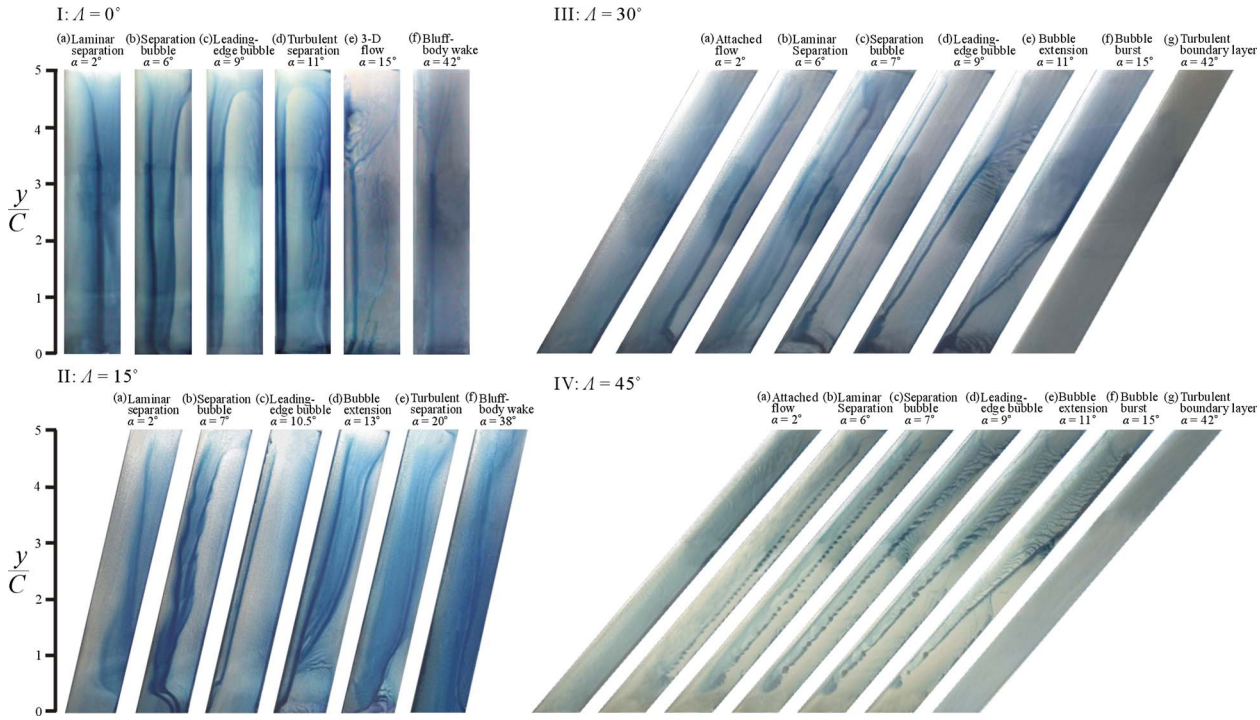

Fig. 2 Surface oil-flow patterns at Re=4.6×10⁴

The dark line indicates the flow separation due to the accumulation of pigmented oil. Furthermore, the boundary-layer flow is 2D, except the at the region near the wing junction and wingtip. The oil-flow direction was reversed in the separation region, and the separation line moves toward the leading-edge while α increases. In addition, no flow reattachment occurs in this flow pattern. This boundary-layer flow pattern at low α is named as the *laminar separation mode*. Figures 2-I(*b*) and 3-I(*b*) show three dark/bold

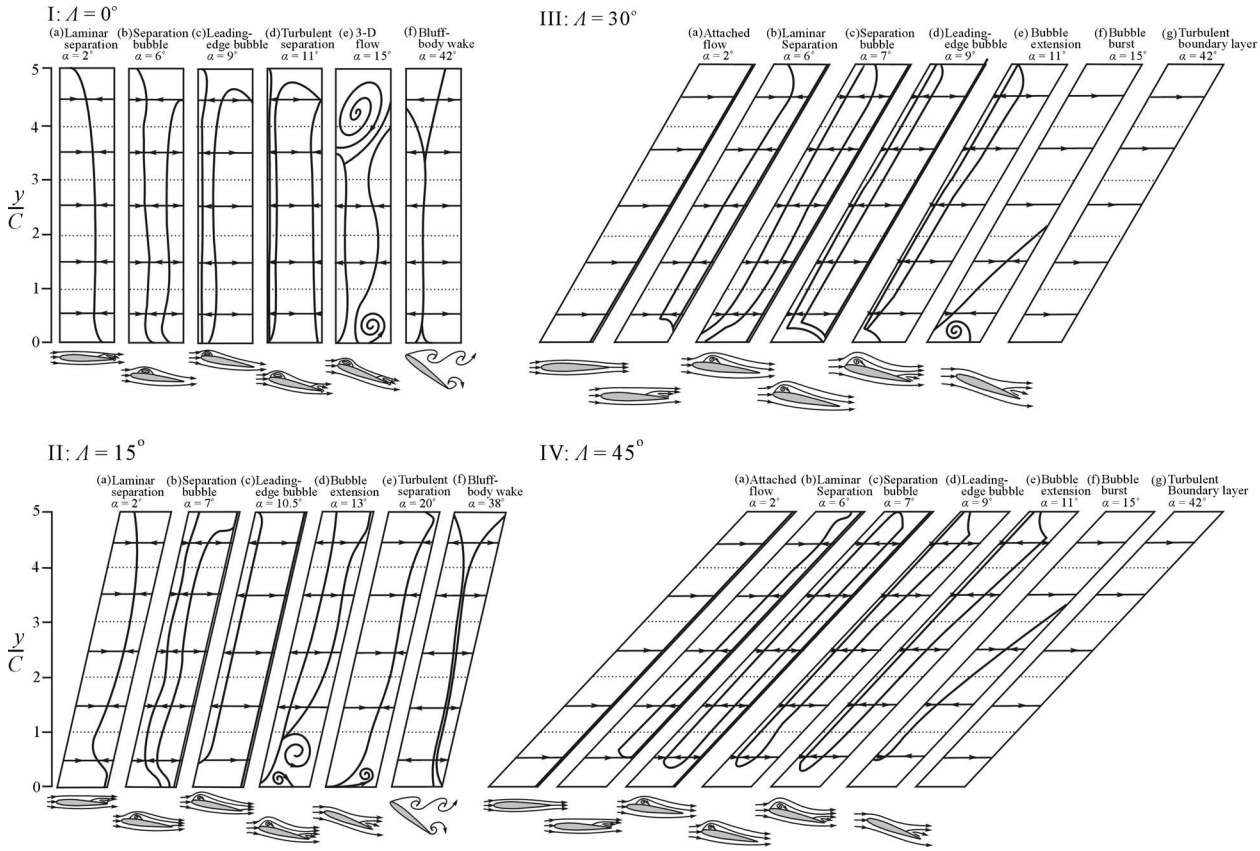

Fig. 3 Schematic sketches of surface oil-flow patterns

lines at $\alpha=6$ deg. The left dark/bold lines indicate the position of the boundary-layer separation. The center dark/bold lines reveal the position of the boundary-flow reattachment. Moreover, the right dark/bold lines delineate the position of the turbulent boundary-layer separation near the trailing edge. In addition, Fig. 3-I(*b*) displays the oil-flow direction, and a separation bubble exists between the left and center bold lines. This separation bubble moves toward the leading edge and then shrinks as α increases. Consequently, this boundary-layer pattern is called the *separation bubble mode*.

At $\alpha=9$ deg, the separation and reattachment lines move simultaneously toward the leading edge, and the distance between the separation and reattachment lines is shortened, as shown Figs. 2-I(*c*) and 3-I(*c*). This boundary-layer pattern is named the *leading-edge bubble mode*. At $\alpha=11$ deg, the separation bubble moves close to the leading edge, and a turbulent boundary separation occurs near the trailing edge, as displayed in Figs. 2-I(*d*) and 3-I(*d*). The dark/bold lines near the trailing edge demarcate the location of the turbulent separation. This boundary-layer flow pattern is called the *turbulent separation mode*. Figures 2-I(*e*) and 3-I(*e*) show that a separation bubble occurs near the leading edge at $\alpha=15$ deg. Furthermore, two surface vortices occurred near the wing junction and wingtip. The region occupied by the surface vortex near the wingtip is larger than that near the wing junction [17]. The dark/bold lines in these figures revealed that the flow structures are three-dimensional (3D). Consequently, this boundary-layer flow pattern is called the *three-dimensional flow mode*. Figure 2-I(*f*) and 3-I(*f*) show that the oil flow moves slowly at $\alpha=42$ deg. The 2D schematic sketches demonstrate that the airflow moves upstream and then impacts on the wing surface. The surface oil flow was therefore divided into two main streams: one moves toward the leading edge, and the other moves toward the trailing edges. This flow pattern is called the *bluff-body wake mode*.

Figures 2-II and 3-II show the surface oil-flow patterns at $\Lambda=15$ deg by changing the angle of attack. The surface-flow patterns were classified into six flow modes—laminar separation, separation bubble, leading-edge bubble, bubble extension, turbulent separation, and bluff-body wake. Yen and Hsu [18] characterized and analyzed these flow modes.

Figures 2-III and 3-III show the oil-flow patterns and schematic sketches on a swept-back wing at $\Lambda=30$ deg. Seven characteristic flow modes are categorized by altering the angle of attack. Figures 2-III(*a*) and 3-III(*a*) show the surface-flow patterns at $\alpha=2$ deg. The laminar boundary layer is attached on the wing surface, and no separation or vortical structure exist due to the high sweep-back angle. The airflow moves smoothly past the wing surface, and the Kutta condition is met. This flow pattern is identified as the *attached flow mode*. Figures 2-III(*b*) and 3-III(*b*) show the surface-flow structures at $\alpha=6$ deg. The dark/bold lines show that a laminar separation occurred near the trailing edge. The dark/bold lines were distorted near the wing junction and wingtip due to the end effects [22]. A substantial portion of the boundary layer is 2D, except for the one near the wall and tip. The oil flow moves in the main-stream direction within the attached flow region. However, the oil-flow direction was reversed in the separation region, and the separation line moved toward the leading edge with increasing α. Furthermore, no reattachment was observed in this flow pattern. This boundary-layer pattern is named as the *laminar separation mode*. Figures 2-III(*c*) and 3-III(*c*) display three dark/bold lines at $\alpha=7$ deg. The left dark/bold lines indicate where the boundary layer separates. The center dark/bold lines reveals where the separated flow reattaches on the wing surface. Moreover, the right dark/bold lines delineate where the turbulent boundary layer is separated. The oil-flow direction shows that a separation bubble occurred between the left and center dark/bold lines. Additionally, this separation bubble moves toward the leading edge and then shrinks as α increases. This boundary-layer pattern is called the *separation bubble mode*.

Figures 2-III(*d*) and 3-III(*d*) present the surface-flow structures at $\alpha=9$ deg. The separation bubble becomes smaller than those in Figs. 2-III(*c*) and 3-III(*c*), and furthermore, the separation and reattachment lines move closely near the leading edge. Consequently, a narrow separation bubble was generated near the leading edge. In addition, a turbulent separation delineated by the accumulated pigmented oil occurs near the trailing edge. This boundary-layer pattern is named as the *leading-edge bubble mode*. Figures 2-III(*e*) and 3-III(*e*) show the surface-flow structure at $\alpha=11$ deg. The separation bubble extends and then moves toward the trailing edge. Furthermore, a turbulent boundary layer separates near the trailing edge. This boundary layer pattern is called the *bubble extension mode*. Figures 2-III(*f*) and 3-III(*f*) show the boundary-layer flow structure at $\alpha=15$ deg. The separation bubble bursts, and the turbulent boundary-layer flow separates near the trailing edge. The dark/bold lines delineate where the flow separates. Additionally, a surface vortex occurred near the wing junction, causing from the wall effect. This surface vortex delays the occurrence of turbulent separation near the wing junction. The boundary-flow pattern is therefore named as the *bubble burst mode*. Figures 2-III(g) and 3-III(g) show that the oil flow on the wing surface moves slowly at $\alpha=42$ deg. The surface-flow pattern is called the *turbulent boundary layer mode*.

Figures 2-IV and 3-IV show the boundary-layer flow patterns at $\Lambda=45$ deg at various angles of attack. These flow patterns are similar to the flow patterns shown in Figs. 2-III and 3-III. Therefore, the characteristic flow modes are—attached flow, laminar separation, separation bubble, leading-edge bubble, bubble extension, bubble burst, and turbulent boundary layer.

3.1.2 Characteristic Boundary-Layer Flow Modes. Figure 4 presents the distributions of boundary-layer flow modes classified by changing Re and α for $\Lambda=0$ deg, 15 deg, 30 deg, and 45 deg. Figure 4(*a*) shows that α is the primary factor to control the boundary-layer flow modes for $0 \text{ deg} < \alpha < 24$ deg. The laminar separation mode is located in the range of $0 \text{ deg} < \alpha < 4$ deg, the separation bubble mode occurs at $4 \text{ deg} < \alpha < 7$ deg, the leading-edge bubble mode occurs at $7 \text{ deg} < \alpha < 10$ deg, and the turbulent separation mode occurs at $10 \text{ deg} < \alpha < 13$ deg. For $\alpha > 24$ deg, the bluff-wake mode occurs at smaller α at high Re than that at low Re. Figure 4(*b*) shows the distributions of boundary-layer flow mode for a swept-back wing of $\Lambda=15$ deg. This mode distribution is similar to the ones shown in Fig. 4(*a*), except that the laminar separation mode does not exist at high Reynolds numbers, and the bubble burst mode occurs between the leading-edge bubble and turbulent separation modes. Additionally, the 3D flow mode is not observed in Fig. 4(*b*). The properties of these boundary-layer flow modes were described by Yen and Hsu [18]. The boundary-layer flow modes were significantly influenced by Re and α at $\Lambda=30$ deg and 45 deg, as shown in Figs. 4(*c*) and 4(*d*). Seven boundary-layer flow modes are defined—attached flow, laminar separation, separation bubble, leading-edge bubble, bubble extension, bubble burst, and turbulent boundary layer. However, the attached flow mode does not exist at high Reynolds numbers at $\Lambda=45$ deg.

3.1.3 Separation, Reattachment, and Bubble Length. Figure 5(*a*) shows the normalized separation position x_s'/C and the normalized reattachment position x_r'/C as the functions of α at Re $=4.6\times10^4$, where x_s' is the position of separation, x_r' is the position of reattachment, and C is the chord length. The x'-axis is located along the midwing section $(y/C=2.5)$ to eliminate the effects of wingtip and wing junction. The profiles of x_s'/C show that the separation lines move toward the leading edge at high α. However, the distributions of x_r'/C indicate that the reattachment line moves toward the trailing edge in the bubble extension mode for a swept-back wing or in the 3D flow mode for a unswept wing.

The flow separation and reattachment generate a separation bubble. Figure 5(*b*) shows the distribution of normalized bubble

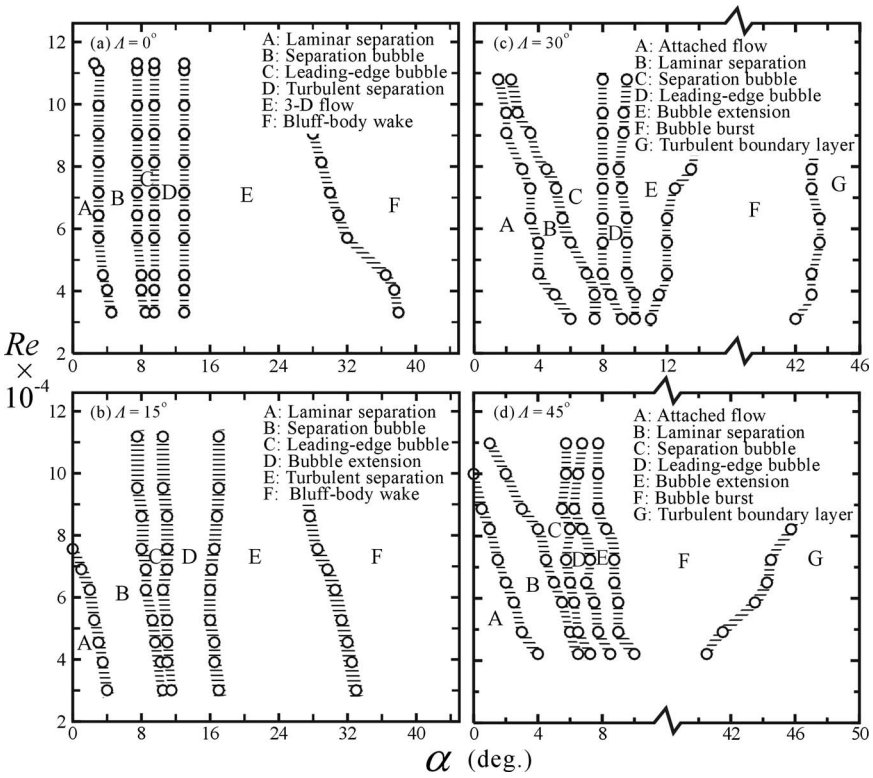

Fig. 4 Distributions of boundary-layer flow modes

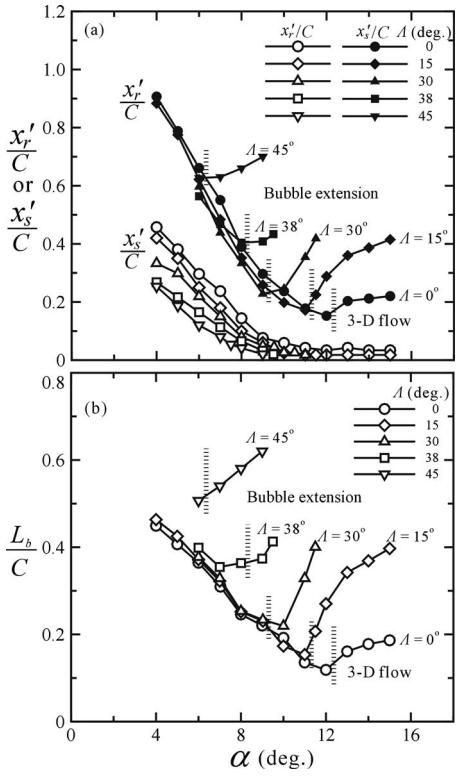

Fig. 5 (*a*) Distributions of normalized reattachment position (x_r'/C) and normalized separation position (x_s'/C) as the functions of angle of attack (α), and (*b*) distribution of normalized bubble length (L_b/C) versus α; Re=4.6×10^4

length (L_b/C) against α at Re=4.6×10^4. In addition, Fig. 5(*b*) indicates that a high sweep-back angle introduces a longer bubble length than that at low sweep-back angle. For instance, at α =6 deg and Re=4.6×10^4, L_b/C is about 0.36 at Λ=0 deg, and is about 0.5 at Λ=45 deg. Therefore, the bubble length is increased approximately by 39%, comparing the values of Λ =0 deg and 45 deg.

3.2 Aerodynamic Performance. The aerodynamic performance of a wing is markedly affected by the behaviors of the boundary-layer flow and the 3D flow structures caused from the end effects.

3.2.1 Aerodynamic Coefficients. Figure 6 shows the profiles of the lift coefficient (C_L), drag coefficient (C_D), and quarter-chord moment coefficient (C_M) by changing the angles of attack at Re =4.6×10^4 for two finite swept-back wings of Λ=0 deg and 30 deg.

Figure 6(*a*), at Λ=0 deg, shows that C_L increases with α in the laminar separation, separation bubble and leading-edge bubble modes. In the separation bubble mode, the increase rate of C_L with respect to α ($\Delta C_L/\Delta\alpha$) is approximately 1.19 π/rad, and the maximum C_L of ≈0.69 occurs in the leading-edge bubble mode. However, C_L decreases with increasing α for $\alpha>9$ deg (turbulent separation mode). In the turbulent separation mode, the reattached turbulent boundary layer generates a secondary separation. The secondary separation line moves toward the leading edge as the angle of attack increases, as shown in Fig. 2-I(*d*). Finally, the wing stalls as a result of the forward movement of the secondary separation line [17]. The minimum C_L of ≈0.5 behind the stall point occurs at $\alpha\approx$13 deg. After the minimum C_L point, C_L increases again as α is further increased into the 3D flow mode. This lift-rise phenomenon is caused by the scavenging effect on the suction surface and impact pressure on the pressure surface [23]. Additionally, the C_L-curve resembles that obtained by Huang and Lee [24], in which Re=5.0×10^4. Figure 6(*d*) displays the

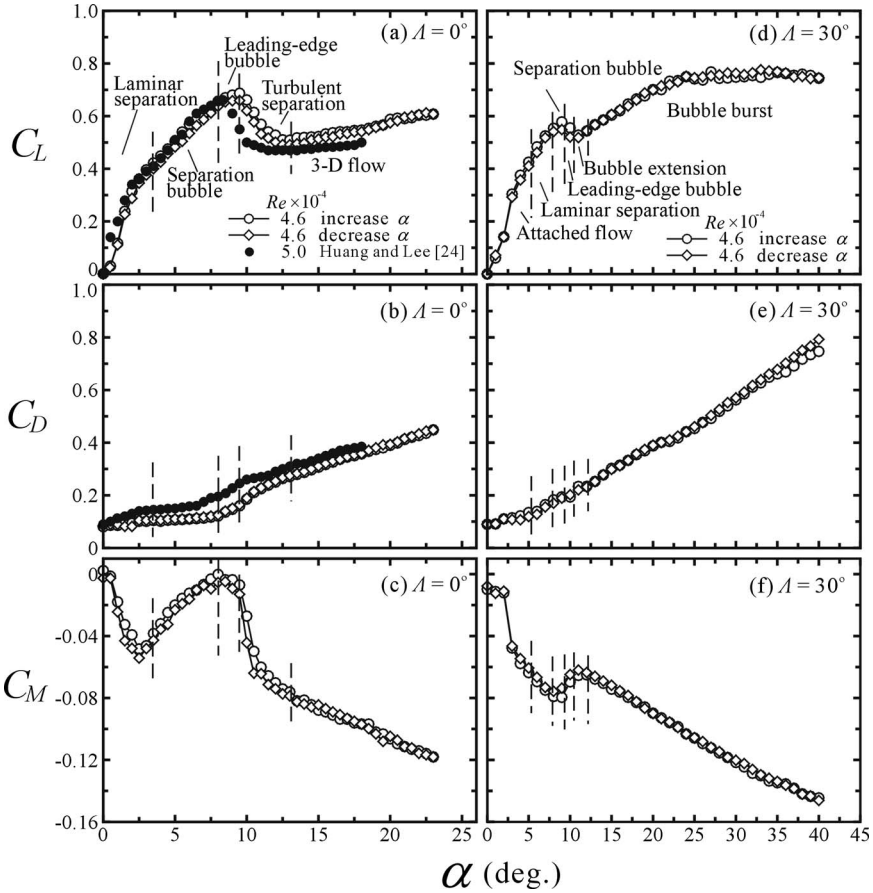

Fig. 6 Distributions of (*a*) lift coefficient (C_L), (*b*) drag coefficient (C_D), and (*c*) quarter-chord moment coefficient (C_M) versus angle of attack (α) at $\Lambda=0$ deg. Distributions of (*d*) C_L versus α, (*e*) C_D versus α, and (*f*) C_M versus α at $\Lambda=30$ deg; Re $=4.6\times10^4$.

profiles of C_L versus α at Re$=4.6\times10^4$ for a finite swept-back wing of $\Lambda=30$ deg. The lift coefficient increases with α in the attached flow, laminar separation, separation bubble, and leading-edge bubble modes. However, C_L decreases from 0.58 to 0.53 when the boundary-layer flow is transited from leading-edge bubble to bubble extension mode. This lift-fall phenomena is termed as the "pseudo-stall" in this study. When the boundary layer is transited from the bubble extension to bubble burst regimes, C_L increases with α in the range of 12 deg$<\alpha<$30 deg, and, however, C_L decreases with increasing α for $\alpha>30$ deg. Consequently, the stall angle of attack (α_{stall}) and the maximum lift coefficient ($C_{L\text{max}}$) are about 30 deg, and 0.83 for $\Lambda=30$ deg. Furthermore, the hysteresis phenomenon identified by Muller et al. [15] was not observed in Figs. 6(*a*) and 6(*d*) as the result of 3D flow effect and high free-stream turbulent intensity [25].

Figures 6(*b*) and 6(*e*) show the distribution of C_D versus α at Re$=4.6\times10^4$ for $\Lambda=0$ deg and 30 deg. Figure 6(*b*) shows C_D increases with α, and the skin drag is the dominant factor at low α. The reverse flow caused from the laminar separation is extended as α increases. In the separation bubble mode, the skin drag decreases, and the form drag increases with increasing α. However, the skin drag and form drag increase in the turbulent separation and 3D flow modes as the result of flow reattachment, flow separation, and the surface vortices near the wing junction and wing tip. Consequently, the slope of the C_D curve in the separation bubble mode is less than that behind the leading-edge bubble mode. Furthermore, the C_D-curve is similar to that obtained by Huang and Lee [24], in which Re$=5.0\times10^4$. Figure 6(*e*) shows that a linear correlated relationship exists between C_D and α. In addition, C_D increases with α, due to the forward movement of the separation line and the shrinkage of the separation bubble.

Figure 6(*c*) shows the distribution of C_M against α at Re$=4.6\times10^4$ for $\Lambda=0$ deg. In the laminar separation mode, C_M decreases as α increases. In the separation bubble mode, C_M increases with α as a result of the wing stall. In the lead-edge bubble mode, C_M reaches the local maximum due to the increase in form drag. In the turbulent separation mode, C_M decreases abruptly as α increases because of the large increase in the form drag. Figure 6(*f*) presents the distribution of C_M versus α at Re$=4.6\times10^4$ for $\Lambda=30$ deg. In the attached flow, laminar separation, separation bubble, and leading-edge bubble modes, C_M decreases as α increases because of the separation bubble moving toward the leading edge. Therefore, the pressure center moves toward the leading edge, and the resultant of lift and drag causes a counterclockwise moment relative to the aerodynamic center. In the bubble extension mode, C_M decreases due to the wing stall. In the bubble burst mode, the form drag increases with α, and therefore, C_M is decreased.

3.2.2 Lift-Drag Ratio. Figure 7(*a*) shows the distribution of C_L/C_D against α at Re$=4.6\times10^4$ for $\Lambda=0$ deg. In the laminar separation mode, C_L/C_D increases from 0 to 4 as α increases from

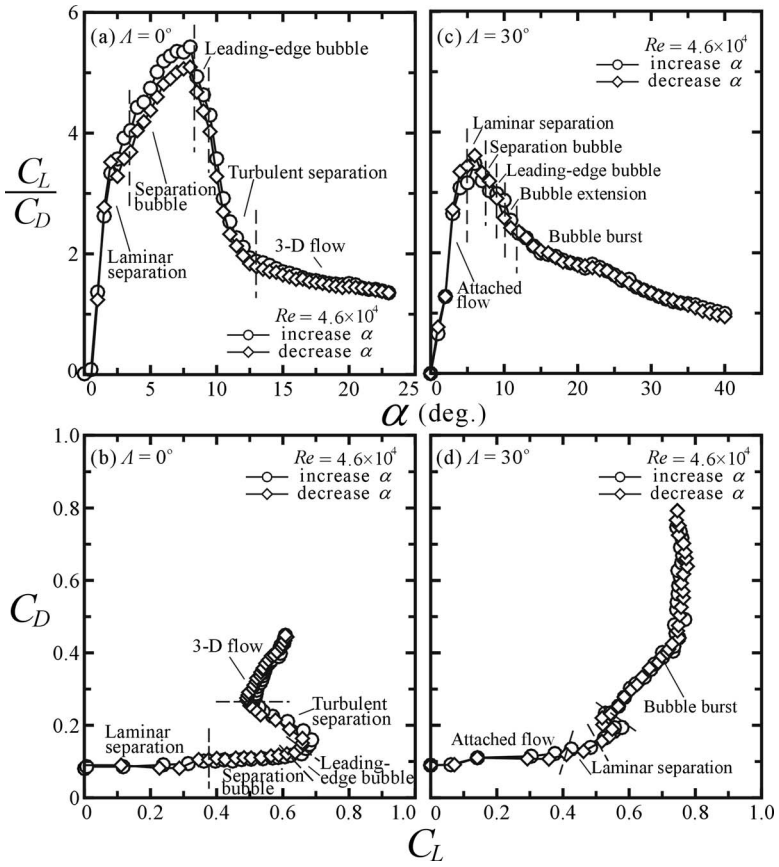

Fig. 7 Distributions of (*a*) lift-drag ratio (C_L/C_D) versus angle of attack (α), and (*b*) drag coefficient (C_D) versus lift coefficient (C_L) at $\Lambda=0$ deg. Distributions of (*c*) C_L/C_D versus α, and (*d*) C_D versus C_L at $\Lambda=30$ deg; Re=4.6 $\times 10^4$.

0deg to 4 deg, and therefore, the increase rate of C_L/C_D relative to α is 20.84 π/rad. The peak value of C_L/C_D is around 5.4, occurring in the separation bubble mode. The increase rate of C_L/C_D relative to α is 2.74 π/rad, that is, the separation bubble retards the increase rate of C_L/C_D. In the leading-edge bubble and turbulent separation modes, C_L/C_D drops from 4.9 to 1.9 with increasing α from 8 deg to 13 deg because of the abrupt loss of lift (or wing stall). In the 3D flow mode, C_L/C_D then decreases gradually with increasing α since C_L increases slightly, and C_D increases rapidly in this mode. Figure 7(*c*) presents the profile of C_L/C_D against α at Re=4.6$\times 10^4$ for $\Lambda=30$ deg. In the attached flow and laminar separation modes, C_L/C_D increases with α. When the flow mode is transited from the laminar separation mode to the separation bubble mode, the increase rate of C_L relative to α is less than that of C_D, and therefore, C_L/C_D decreases. In the bubble burst mode, C_L/C_D decreases as α increases since the high α induces the high form drag.

Figure 7(*b*) shows the curve of C_D against C_L for an unswept wing ($\Lambda=0$ deg) at Re=4.6$\times 10^4$. The drag coefficient does not change significantly with the lift coefficient in the laminar separation, separation bubble, and leading-edge bubble modes. In the turbulent separation mode, C_D increases as C_L decreases. At high angles of attack (i.e., in the 3D flow mode), C_D changes linearly with C_L due to the balance between the pressure drag and free-stream turbulent strength. Figure 7(*d*) displays the relationship between the C_D and C_L at Re=4.6$\times 10^4$ for $\Lambda=30$ deg. In the attached flow and laminar separation modes, C_D is not significantly influenced by the increase in C_L. However, in the separation bubble, leading-edge bubble, and bubble extension modes, the form drag plays a significant role, and therefore, the linear increase in C_D is not unexpected. Additionally, the curve of C_D versus C_L increases dramatically behind the bubble burst mode due to the large loss of C_L.

3.3 Effect of Swept-Back Angles. Figure 8 shows the distributions of C_L, C_D, and C_L/C_D against α at Re=4.6$\times 10^4$ for $\Lambda=0$ deg, 15 deg, 30 deg, 38 deg, and 45 deg. The pseudo-stall occurs when $\Lambda \geq 30$ deg. However, the pseudo-stall was not observed by Hoerner and Borst [23]. Hoerner and Borst identified a typical stall using an NACA 0012 airfoil by changing Λ from 0 deg to 75 deg. Figure 8(*a*) displays that $\alpha_{stall} \approx 7-9$ deg for $\Lambda \leq 15$ deg and $\alpha_{stall} \approx 30$ deg, 32 deg, and 35 deg for $\Lambda=30$ deg, 38 deg, and 45 deg, respectively. The pseudo-stall occurs in the bubble extension mode, and causes the C_L curve to decline. In the bubble burst mode, a turbulent separation line exists on the wing surface, as shown in Figs. 2-III and 2-IV. The boundary-layer flow transits into the turbulent boundary layer mode near the trailing edge, and the airflow moves along the wing surface. Consequently, C_L increases as α increases. Figure 8(*b*) shows that C_D is linearly correlated with α since the form drag is the dominant factor. Figure 8(*c*) shows that the maximum C_L/C_D occurs at $\alpha \approx 9$ deg for $\Lambda=0$ deg and 15 deg. However, the maximum C_L/C_D occurs at $\alpha \approx 7.5$ deg for $\Lambda=30$ deg, 38 deg, and 45 deg. Furthermore, C_L/C_D for an unswept wing is higher than those for swept-back wings at α_{stall}.

Hoerner and Borst [23] examined the theoretical relationships among C_L, α, and Λ for a swept-back wing model. They derived the following equation:

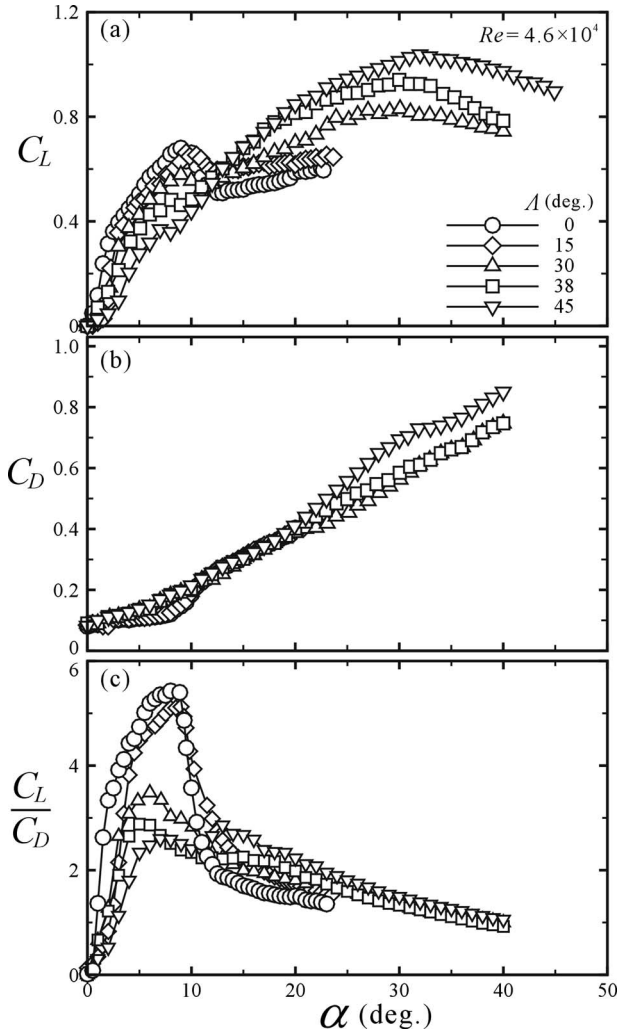

Fig. 8 Distributions of (*a*) lift coefficient (C_L), (*b*) drag coefficient (C_D), and (*c*) lift-drag ratio (C_L/C_D) as the functions of angle of attack (α) at Re=4.6×10^4

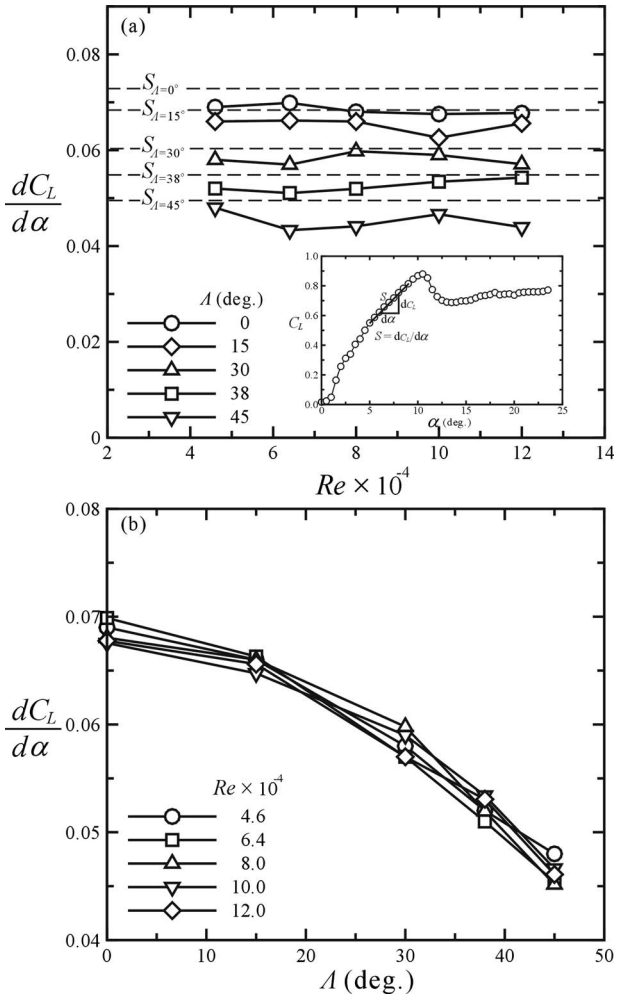

Fig. 9 Distributions of (*a*) change rate of lift coefficient relative to angle of attack ($dC_L/d\alpha$) against Reynolds number (Re), and (*b*) $dC_L/d\alpha$ as a function of sweep-back angle (Λ)

$$\frac{dC_L}{d\alpha} = \frac{\cos(\Lambda)}{\left[10 + \left(\frac{20}{A}\right)\right]} \tag{1}$$

where A is the wing aspect ratio. In this investigation, A is 5, based on the half-span wing models. Consequently, the theoretical change rates of $dC_L/d\alpha$ equal to 0.071/deg, 0.068/deg, 0.061/deg, 0.056/deg, and 0.050/deg for $\Lambda=0$ deg, 15 deg, 30 deg, 38 deg, and 45 deg, respectively. Figure 9(*a*) shows the experimental change rates of $dC_L/d\alpha$ against Re. The average change rates are 0.068/deg, 0.065/deg, 0.058/deg, 0.053/deg, and 0.048/deg for $\Lambda=0$ deg, 15 deg, 30 deg, 38 deg, and 45 deg, respectively. Consequently, the error of $dC_L/d\alpha$ between theoretical and experimental results is <5.3%. Notably, $dC_L/d\alpha$ is negatively correlated with Λ, that is, a high Λ induces a low $dC_L/d\alpha$, as shown in Fig. 9(*b*).

3.3.1 Maximum Lift-Drag Ratio. Figure 10(*a*) shows that the maximum lift-drag ratio $(C_L/C_D)_{max}$ decreases with increasing the sweep-back angle, and furthermore, $(C_L/C_D)_{max}$ increases with the Reynolds number for a specific Λ. The experimental results at $\Lambda=0$ deg agree with the work obtained by Lissaman [2]. Lissaman studied $(C_L/C_D)_{max}$ on the rough and smooth unswept wings by changing the Reynolds number in the range of $1.0\times10^3<\mathrm{Re}<1.0\times10^7$. Moreover, Fig. 10(*a*) determines that $(C_L/C_D)_{max}$ decreases ≈53% at $\mathrm{Re}=4.6\times10^4$, comparing the $(C_L/C_D)_{max}$ at $\Lambda=0$ deg and 45 deg. In addition, $(C_L/C_D)_{max}$ decreases ≈59% at $\mathrm{Re}=1.2\times10^5$ with comparing the $(C_L/C_D)_{max}$ at $\Lambda=0$ deg and 45 deg.

Figure 10(*b*) shows the distributions of C_L/C_D at the stall point $(C_L/C_D)_{stall}$ against Λ. Notably, $(C_L/C_D)_{stall}$ decreases as Λ increases, and $(C_L/C_D)_{stall}$ approaches a constant for $\Lambda\geq30$ deg. Furthermore, $(C_L/C_D)_{stall}$ increases with Re in the range of $\Lambda\leq30$ deg. For a specific Re, the highest $(C_L/C_D)_{stall}$ occurs at $\Lambda=0$ deg because the stall occurs at high α for a high swept-back angle wing, and the high α induces a high form drag. The $(C_L/C_D)_{stall}$ decreases by about 72–86%, comparing the values of $(C_L/C_D)_{stall}$ at $\Lambda=0$ deg and 45 deg in the range of $4.6\times10^4<\mathrm{Re}<1.2\times10^5$.

3.3.2 Angle of Attack at Stall. Figure 11 shows the distributions of α, C_L, and C_D at stall points (for $\Lambda<30$ deg) or pseudo-stall points (for $\Lambda>30°$) as the functions of Λ. The suffix "be" in Fig. 11 is the abbreviation for "bubble extension," and is used to delineate the stall or pseudo-stall occurring in the bubble extension mode. Notably, $(\alpha)_{be}$ increases with Λ for $\Lambda<15$ deg and then decreases as Λ increases, as shown in Fig. 11(*a*). The trend of $(\alpha)_{be}$ versus Λ agrees with the experimental results obtained by the oil-flow visualization shown in Fig. 4. Figure 11(*b*) shows that

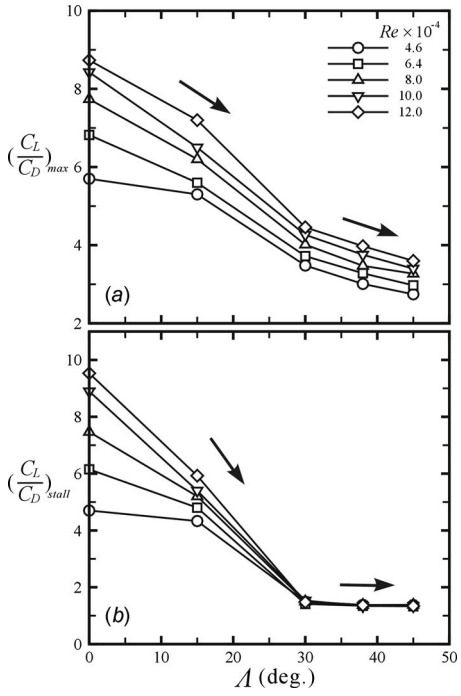

Fig. 10 Distributions of (*a*) maximum lift-drag ratio $(C_L/C_D)_{max}$ and (*b*) lift-drag ratio at stall point $(C_L/C_D)_{stall}$ as the functions of sweep-back angle (Λ) at Re=4.6×10⁴

$(C_L)_{be}$ decreases as Λ increases, and Fig. 11(*c*) shows that $(C_D)_{be}$ increases as Λ increases. Moreover, $(C_D)_{be}$ decreases as Re increases for a specific swept-back angle.

Figure 12 shows the distributions of α_{stall}, $(C_L)_{stall}$, and $(C_D)_{stall}$ against Λ at various Reynolds numbers. Figure 12(*a*) shows that $(\alpha)_{stall}$ increases with Λ. However, $(\alpha)_{stall}$ is not significantly affected by Re. Moreover, the stall occurs in the range of $8 < (\alpha)_{stall} < 10$ deg for 0 deg $< \Lambda <$ 15 deg, and stall occurs in the range of 29 deg $< (\alpha)_{stall} <$ 35 deg for $\Lambda \geq 30$ deg. Consequently, $(\alpha)_{stall}$ at $\Lambda=45$ deg is larger than that at $\Lambda=0$ deg by about 77%. This delay of $(\alpha)_{stall}$ is caused from the secondary flow, since the secondary flow increases the rotational energy and turbulent intensity. Therefore, the boundary-layer flow resists the effect of reverse pressure at high α. Figure 12(*b*) shows that $(C_L)_{stall}$ decreases with increasing the Λ from 0 deg to 15 deg, and increases as Λ increases from 15 deg to 45 deg. The $(C_L)_{stall}$ at $\Lambda=45$ deg increases by about 35%, comparing that at $\Lambda=0$ deg. Figure 12(*c*) demonstrates a positive correlated relationship between $(C_D)_{stall}$ and Λ. In addition, the $(C_D)_{stall}$ at $\Lambda=45$ deg increases by about 14.2%, comparing that at $\Lambda=0$ deg.

4 Concluding Remarks

The characteristic boundary-layer flow patterns and aerodynamic performance of numerous finite swept-back wings of $\Lambda=0$ deg, 15 deg, 30 deg, 38 deg, and 45 deg were investigated experimentally. The following conclusions are based on experimental results and discussions.

(1) The boundary-layer flow modes were characterized by considering the effects of Re, α, and Λ. These flow modes were photographed and named—attached flow, laminar separation, separation bubble, leading-edge bubble, bubble extension, bubble burst, turbulent separation, bluff-body wake, three-dimensional flow, and turbulent boundary layer modes.

(2) The separation point moves toward the leading edge and is fixed close to the leading edge at high angles of attack. However, the flow reattachment line moves backward to the trailing edge in the bubble extension mode (for swept-back wings) or in the 3D flow regime (for an unswept wing). Furthermore, a high sweep-back angle introduce a longer bubble length than that at the low sweep-back angle.

(3) Experimental results indicate that no hysteresis phenomenon existed on the swept-back wings. The $(\alpha)_{stall}$ was increased from 8 deg to 10 deg (for $\Lambda \leq 15$ deg), to 29 deg to 35 deg (for $\Lambda \geq 30$ deg). The highest C_L/C_D occurred at $\alpha \approx 9$ deg (for $\Lambda=0$ deg and 15 deg) and ≈7.5 deg (for $\Lambda \geq 30$ deg). Moreover, at stall points, the $(C_L/C_D)_{stall}$ of an unswept wing is higher than that for the swept-back wings.

(4) The $(C_L/C_D)_{max}$ decreased by about 53% as Λ increased from 0 deg to 45 deg at Re=4.6×10⁴. The $(C_L)_{stall}$ was increased by roughly 35%, compared with values for $\Lambda=0$ deg and 45 deg. The $(C_D)_{stall}$ increased by about 14.2% by comparing those values for $\Lambda=0$ deg and 45 deg.

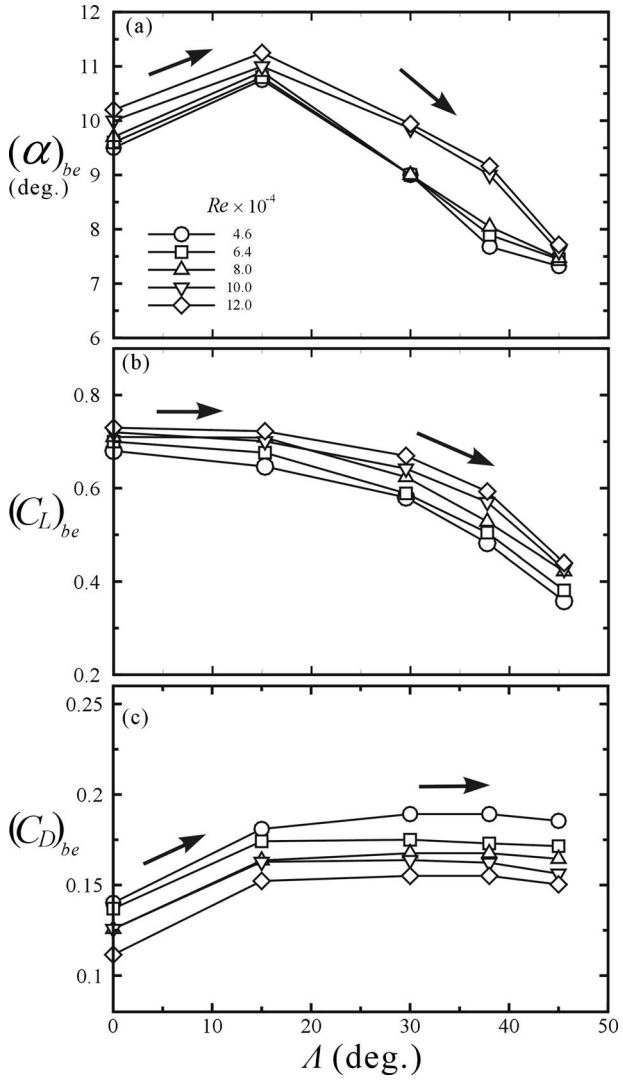

Fig. 11 Distributions of (*a*) angle of attack $(\alpha)_{be}$, (*b*) lift coefficient $(C_L)_{be}$, and (*c*) drag coefficient $(C_D)_{be}$ at stall point as the functions of sweep-back angle (Λ), where the suffix, be, means the bubble extension mode

Acknowledgment

This research was supported by the National Science Council of the Republic of China, under Grant No. NSC 94-2212-E-019-006.

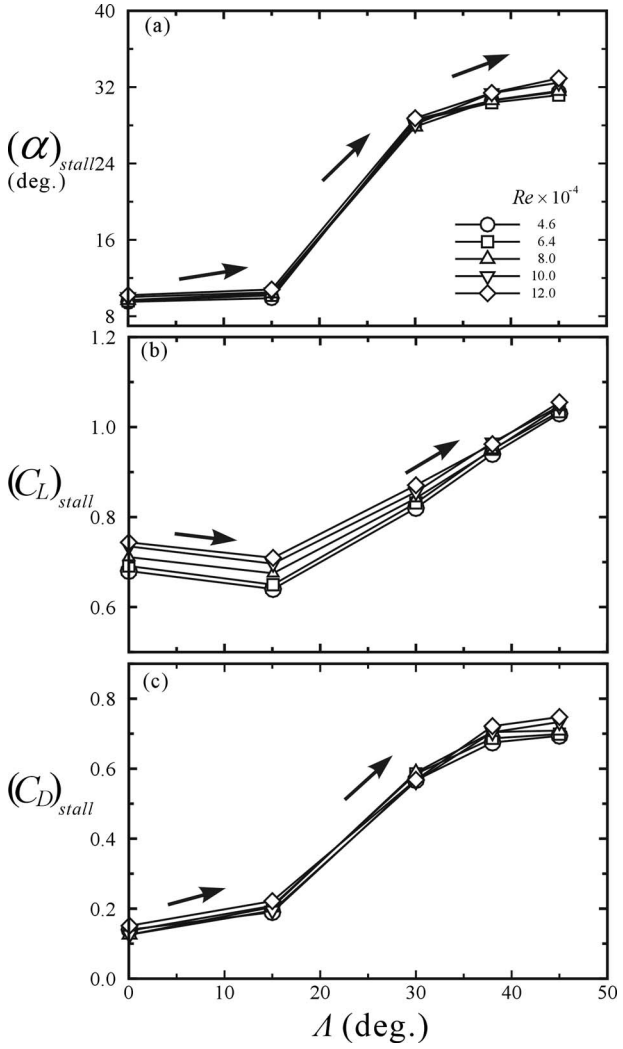

Fig. 12 Distributions of (*a*) angle of attack $(\alpha)_{stall}$, (*b*) lift coefficient $(C_L)_{stall}$, and (*c*) drag coefficient $(C_D)_{stall}$ at stall point as the functions of sweep-back angle (Λ)

The authors would like to thank Professor R. F. Huang of the National Taiwan University of Science and Technology for his help in this research.

Nomenclature

b = half-wing span (30 cm)
C = chord length (6 cm)
C_L = lift coefficient ($=L/qbC$)
C_D = drag coefficient ($=D/qbC$)
C_M = quarter-chord moment coefficient ($=M/qbC^2$)
D = drag
L = lift
L_b = bubble length
M = quarter-chord moment
q = dynamic pressure of free-stream ($=\rho u_\infty^2/2$)
Re = Reynolds number ($=u_\infty C/\nu$)
u_∞ = free-stream velocity
x = streamwise coordinate originated at leading edge
x' = streamwise coordinate originated at $x=0$ and $y/b=0.5$
x_r' = reattachment position of boundary-layer flow
x_s' = separation position of boundary-layer flow
y = spanwise coordinate originated at the wing root
y' = spanwise coordinate originated at $y/b=0.5$
α = angle of attack
Λ = sweep-back angle
ρ = density of airflow
ν = kinetic viscosity of airflow

References

[1] Clancy, L. J., 1975, *Aerodynamics*, Wiley, New York, pp. 72–73.
[2] Lissaman, P. B. S., 1983, "Low Reynolds Number Airfoils," Annu. Rev. Fluid Mech., **15**, pp. 223–239.
[3] Crabtree, L. F., 1957, "Effects of Leading-Edge Separation on Thin Wings in Two-Dimensional Incompressible Flow," J. Aeronaut. Sci., **24**(8), pp. 597–604.
[4] Ward, J. R., 1963, "The Behavior and Effects of Laminar Separation Bubbles on Airfoils in Incompressible Flow," J. R. Aeronaut. Soc., **67**(12), pp. 783–790.
[5] Arena, A. V., and Mueller, T. J., 1980, "Laminar Separation, Transition, and Turbulent Reattachment Near the Leading Edge of Airfoils," AIAA J., **18**(7), pp. 747–753.
[6] Katz, J., 1999, "Wing/Vortex Interactions and Wing Rock," Prog. Aerosp. Sci., **35**(7), pp. 727–750.
[7] Mueller, T. J., and Batill, S. M., 1982, "Experimental Studies of Separation on a Two-Dimensional Airfoil at Low Reynolds Numbers," AIAA J., **20**(4), pp. 457–463.
[8] Pohlen, L. J., and Mueller, T. J., 1984, "Boundary Layer Characteristics of the Miley Airfoil at Low Reynolds Numbers," J. Aircr., **21**(9), pp. 658–664.
[9] Hsiao, F.-B., Liu, C.-F., and Tang, Z., 1989, "Aerodynamic Performance and Flow Structure Studies of a Low Reynolds Number Airfoil," AIAA J., **27**(2), pp. 129–137.
[10] Purser, P. E., and Spearman, M. L., 1951, "Wind-Tunnel Tests at Low Speed of and Yawed Wings Having Various Plane Forms," NACA Technical Paper No. 2445.
[11] Black, J., 1956, "Flow Studies of the Leading Edge Stall on a Swept-Back Wing at High Incidence," J. R. Aeronaut. Soc., **60**, pp. 51–60.
[12] Squire, L. C., 1961, "The Motion of a Thin Oil Sheet Under the Steady Boundary Layer on a Body," J. Fluid Mech., **11**(2), pp. 161–179.
[13] Poll, D. I. A., 1986, "Spiral Vortex Flow Over a Swept-Back Wing," Aeronaut. J., **90**(895), pp. 185–199.
[14] Mueller, T. J., Pohlen, L. J., Conigliaro, P. E., and Jansen, B. J., 1983, "The Influence of Free-Stream Dimensional on Low Reynolds Number Airfoil Experiments," Exp. Fluids, **1**, pp. 3–14.
[15] Mueller, T. J., 1985, "The Influence of Laminar Separation and Transition on the Low Reynolds Number Airfoil Hysteresis," J. Aircr., **22**(9), pp. 763–770.
[16] Liu, M. J., Lü, Z. Y., Qiu, C. H., Su, W. H., Gao, X. K., Deng, X. Y., and Xiong, S. W., 1980, "Flow Patterns and Aerodynamics Characteristic of a Wing-Strake Configuration," J. Aircr., **17**(5), pp. 332–338.
[17] Huang, R. F., Shy, W. W., Lin, S. W., and Hsiao, F.-B., 1996, "Influence of Surface Flow on Aerodynamic Loads of a Cantilever Wing," AIAA J., **34**(3), pp. 527–532.
[18] Yen, S. C., and Hsu, C. M., 2007, "Influence of Boundary Layer Behavior on Aerodynamic Coefficients of a Swept-Back Wing," ASME J. Fluids Eng., **129**(6), pp. 674–681.
[19] Shames, I. H., 1992, *Mechanics of Fluid*, 3rd ed., McGraw-Hill, Singapore, p. 632.
[20] Abbott, I. H., and Von Doenhoff, A. E., 1959, *Theory of Wing Section*, Dover, New York, pp. 113–115.
[21] Merzkirch, W., 1974, *Flow Visualization*, Academic, New York, pp. 53–56.
[22] Bertin, J. J., and Smith, M. L., 1989, *Aerodynamics for Engineers*, 2nd ed., Prentice-Hall, Englewood Cliffs, NJ, pp. 204–213 and pp. 235–257.
[23] Hoerner, S. F., and Borst, H. V., 1975, *Fluid Dynamic Lift*, published by Mrs. Liselotte A. Hoerner, Brick Town, NJ, pp. 4.22–4.23 and 15.6–15.8.
[24] Huang, R. F., and Lee, H. W., 1999, "Effect of Freestream Turbulence on Wing-Surface Flow and Aerodynamics Performance," AIAA J., **36**(6), pp. 965–972.
[25] Schewe, G., 2001, "Reynolds-Number Effects in Flow Around More-or-Less Bluff Bodies," J. Wind. Eng. Ind. Aerodyn., **89**(14-15), pp. 1267–1289.

Theoretical Study of the Laminar Flow in a Channel With Moving Bars

Hai-Ping Hu[1]
Department of Marine Engineering,
National Taiwan Ocean University,
No. 2, Pei-Ning Road,
Keelung 20224, Taiwan
e-mail: hphu@mail.ntou.edu.tw

Rong-Hua Yeh
Department of Marine Engineering,
National Kaohsiung Marine University,
No. 142, Haijhuan Road,
Nanzih District, Kaohsiung City 81143, Taiwan
e-mail: rhyeh@mail.nkmu.edu.tw

This paper presents a study of the laminar flow in a channel with longitudinal moving bars arrayed along the channel width. The governing equations describing the fluid, which flows along the direction of the bar's length, are expressed with double Poisson equations and are solved by eigenfunction-expansion and point-match method. The result shows that when the solid bars move forward, the fluid flow will move in the same direction, and the f Re decreases as the positive velocity of bars increases. However, when the bars move backward, a reverse flow will occur in the channel, and the f Re is higher at larger negative velocity of bars. For a channel flow with moving bars, the f Re value is not a constant, such as a classical one without moving bars, in which the f Re value is a constant. Furthermore, when the area of the cross section of the bar is fixed, both the mean velocities and the f Re values of the fluid can be obtained under different velocities and aspect ratios of the bars. [DOI: 10.1115/1.4000261]

Keywords: channel flow, moving bars, point-match method

1 Introduction

In the research and analysis of fluid mechanics, the channel flow is a basic and important topic. Nowadays, more and more attention has been engrossed on flow in a channel with rectangular beams. Practical engineering applications can be found in galvanizing and coating processes on the moving bars, designing a lubrication system, and cooling elements in a mechanical device. The pressure drop in this process can be obtained from the calculation of flow velocity and friction factor in the channel.

Consequently, many significant efforts were directed toward researches with related fields. Sparrow and Loeffler [1] investigated the laminar flow between cylinders arranged in a regular array by using the eigenfunction-expansion and point-match method. Their analytical solution was obtained for the longitudinal fully developed laminar flow between cylinders arranged in a triangular or square array. Cheng [2] also presented an analog solution of laminar heat transfer in noncircular ducts by point-matching. The fully developed laminar flow characteristics in noncircular ducts and the steady temperature distribution in infinitely long prismatic bars can be obtained. Later, neglecting inertia effect, Trogdon and Joseph [3] solved the problem of plane flow of a second-order fluid over a rectangular slot by matching bi-orthogonal eigenfunction expansions in different regions of flow. In addition, some other efforts directed studies toward a channel with various cross sections such as a complex shaped duct or channel, in which the complicated regions might be decomposed into contiguous simpler subregions. In 1976, Zarling [4] proposed the semi-analytical method to solve the governing equation for fully developed laminar flow through bars of complex geometrical patterns. Employing the Schwarz–Neumann alternating method along with least-squares point-matching, the flow velocity in a duct with one pair of opposing walls being parallel plates, and the adjacent pair of walls semicircular arcs was obtained. In addition, the method was applied to a complex shaped duct and the resulting velocity was used to calculate the flow rate and pressure drop. In 1994, Wang [5] further studied the laminar viscous flow between parallel plates with evenly spaced longitudinal ribs. The flow in a channel with longitudinal ribs was solved by an eigenfunction-expansion and point-match method. It was found that both the wetted perimeter and the friction factor-Reynolds number product are unsuitable parameters for the flow through ducts of complex geometry. Besides, the earlier similar work for a flow between corrugated plates was also developed by Wang [6]. He analyzed the parallel flow between two fixed corrugated plates and discussed the dependence of flow rate on the effect of a wavy surface. Furthermore, some studies investigated a channel with a moving plate or moving block. Achiq and Naciri [7] investigated the laminar flow at high Reynolds numbers in the wake of a moving flat plate in a channel. It is found that the flow is with acceleration in a thin layer at the downstream edge of the plate. Fu et al. [8] presented a numerical investigation of the laminar forced convection in a channel with a block moving back and forth. They found that the moving velocity and the position of the block affect the heat transfer of the heated surface remarkably. Hydrodynamic properties of the flow such as the thickness of the liquid film that surrounds the bubbles, bubble velocity, bubble and slug lengths, mixing, flow circulation in the liquid slugs, and pressure drop were all considered. Recently, Fu et al. [9] investigated heat transfer phenomena caused by a moving block under a jet flow experimentally. They found that the enhancement of the heat transfer rate was generally accompanied with the increment of the jet Reynolds number and speed of the moving block. In addition, there are some recent studies toward the investigation on the field of the channel flow. For a collapsible channel, Luo and Pedley [10] presented a numerical investigation of the steady flow in a 2D channel with one plane rigid wall and with a segment of the other wall replaced by an elastic membrane. Bahrami et al. [11] investigated the fully developed laminar flow in smooth channels of arbitrary cross sections. For selected cross sections, they used existing analytical solutions for fluid flow to derive the f Re values.

Although many researches about channel flow under different conditions were discussed, the channel flow with arrayed moving bars of different aspect ratios and cross-sectional areas are also worth discussing particularly in the thermal and flow analysis of metallic bars under the coating and galvanizing processes. The present paper, thus, investigates the laminar channel flow passing a complex geometric configuration, i.e., a channel including rect-

[1]Corresponding author.

Contributed by the Fluids Engineering Division of ASME for publication in the JOURNAL OF FLUIDS ENGINEERING. Manuscript received April 10, 2009; final manuscript received July 26, 2009; published online October 19, 2009. Editor: Joseph Katz.

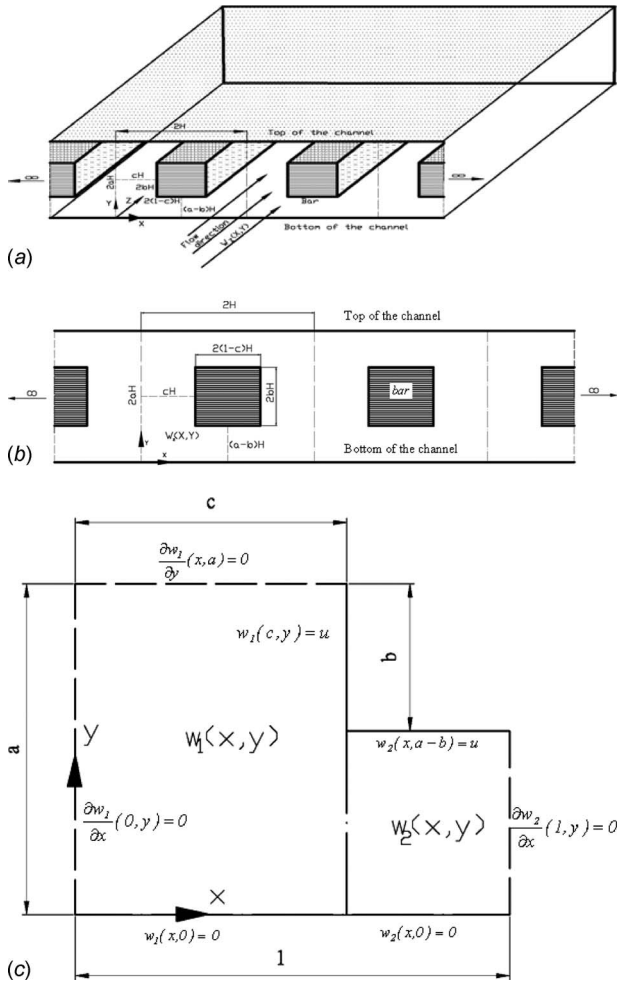

Fig. 1 (*a*) The overall view of the proposed model, (*b*) the cross section of the channel with moving bars, and (*c*) an enlarger view of the L-shape regions with dimensionless parameters

angular moving bars positioned along the X-direction with flow directing in the Z-direction. In addition, local dimensionless velocity, mean velocity, and friction factor-Reynolds number products are obtained for various sizes of moving bars in a channel.

2 Analysis

Figures 1(a) and 1(b) show the overall view of the physical model and cross section of the channel investigated. Assume that a steady-state, fully developed laminar channel flow between the upper and the lower plates. The height of the channel is $2aH$ and both the left and the right sides of the channel extend to infinity. Inside the channel, a series of bars were arrayed along the X-direction. The bars are moving slowly and parallel to the Z-direction for forward and reverse directions with different velocities. The height of bar is $2bH$ and the width of the bar is equal to $2(1-c)H$. Therefore, the cross-section area of each moving bar is $H^2b(1-c)$. Note that the flow direction is normal to the paper and is in the positive Z-direction. Since the flow velocity is very slow, the negligible inertia force is assumed.

The moving bars with the velocity U are arrayed along the X-direction in the channel. The governing equation can be expressed as follows:

$$\nabla^2 W_z(X,Y) = \frac{1}{\mu}\frac{dp}{dZ} = \text{const} \tag{1}$$

where W_z is the flow velocity in the z-direction, dp/dZ is the pressure gradient in the z-direction, and μ is the viscosity.

Introducing the dimensionless parameter

$$w = -W_z/\left(\frac{H^2 dp}{\mu dZ}\right)$$

$$x = \frac{X}{H}$$

and

$$y = \frac{Y}{H}$$

into Eq. (1), the constant dimensionless pressure gradient in the z-direction can be expressed as -1. The analysis considered the domain with a period $2H$ and focused on the range from $X=0$ to $X=H$ and $Y=0$ to $Y=aH$, where $2a$ is normalized distance between plates. The range is symmetric about the Y-axis in $X=0$ and symmetric about the X-axis in $Y=aH$. One part of the channel, an L-shaped region with two combined rectangles, as shown in Fig. 1(c), is selected to be investigated. The L-shaped region in Fig. 1(b) is re-expressed and magnified into Fig. 1(c) with length and width in a dimensionless form. The governing equation can be rewritten in the dimensionless form of Poisson equation

$$\nabla^2 w(x,y) = -1 \tag{2}$$

The dimensionless governing equation for the left rectangle of the L-shaped domain is

$$\nabla^2 w_1(x,y) = -1 \tag{3}$$

subject to the boundary conditions

$$w_1(x,0) = 0$$

$$\frac{\partial w_1}{\partial y}(x,a) = 0$$

$$\frac{\partial w_1}{\partial x}(0,y) = 0 \tag{4}$$

$$w_1(c,y) = u, \quad a-b \le y \le a$$

where u is the dimensionless velocity of the moving bars and given as

$$u = -U/\left(\frac{H^2}{\mu}\frac{dp}{dz}\right)$$

and

$$a = 1$$

Next, the dimensionless governing equation of the right rectangle can be expressed as follows:

$$\nabla^2 w_2(x,y) = -1 \tag{5}$$

with the following boundary conditions:

$$w_2(x,0) = 0$$

$$w_2(x,a-b) = u$$

$$\frac{\partial w_2}{\partial x}(1,y) = 0 \tag{6}$$

$$w_1(c,y) = w_2(c,y), \quad 0 \le y < a-b$$

$$\frac{\partial w_1(c,y)}{\partial x} = \frac{\partial w_2(c,y)}{\partial x}, \quad 0 \le y < a-b$$

With the boundary conditions of Eqs. (4) and (6), Eqs. (3) and (5) can be solved and obtained as follows:

$$w_1(x,y) = y\left(a - \frac{y}{2}\right) + \sum_n A_n \sin(\alpha_n y)(e^{\alpha_n(x-c)} + e^{-\alpha_n(x+c)}) \tag{7}$$

$$w_2(x,y) = \frac{-y^2}{2} + \frac{y}{a-b}\left(u + \frac{1}{2}(a-b)^2\right) + \sum_m B_m \sin(\beta_m y) \times (e^{\beta_m(x-2+c)} + e^{-\beta_m(x-c)}) \tag{8}$$

Here, the A_n and B_m are constant coefficients, and the eigenvalues, respectively, are

$$\alpha_n = \frac{(2n-1)\pi}{2a}, \quad \beta_m = \frac{m\pi}{a-b} \tag{9}$$

It is further assumed that the velocity of bars has the same order with the pressure gradient and is specified in the range of $-1 \le u \le 1$.

Substituting the boundary condition (4) into Eq. (7), the following equation can be obtained:

$$\sum_n A_n \sin(\alpha_n y_i)(1 + e^{-2\alpha c}) = u + y_i\left(\frac{y_i}{2} - a\right) \tag{10}$$

where $i = M+1$ to N and $y_i = y_{M+1}$ to y_N.

Next, the velocity and the shear stress of the two regions of the L-shaped domain can be matched along the common boundary in Eq. (6).

Substituting the boundary conditions into Eqs. (7) and (8) yields

$$\sum_n A_n \sin(\alpha_n y_i)(1 + e^{-2c\alpha}) - \sum_m B_m \sin(\beta_m y_i)(1 + e^{-2(1-c)\beta}) = \left\{\frac{1}{a-b}\left[u + \frac{(a-b)^2}{2}\right] - a\right\} y_i \tag{11}$$

where $i = 1$ to M and $y_i = y_1$ to y_M.

$$\sum_n A_n \alpha_n \sin(\alpha_n y_i)(1 - e^{-2c\alpha}) + \sum_m B_m \beta_m \sin(\beta_m y_i)(1 - e^{-2(1-c)\beta_m}) = 0 \tag{12}$$

where $i = 1$ to M and $y_i = y_1$ to y_M.

Choosing N points along the boundary at $y = c$, we obtain

$$y_i = (i-1)a/(2N), \quad i = 1, \ldots, N \tag{13}$$

where $N = 40$ in this study.

We truncate A_n to N terms and B_m to M terms. Note that M can be calculated from the equation below

$$M = \text{floor function } [N(1 - 2b/a)] + 1 \tag{14}$$

The linear system of $M+N$ equations with $M+N$ unknowns are solved for the coefficients of A_n and B_m.

The mean value for $w(x,y)$ is derived as follows:

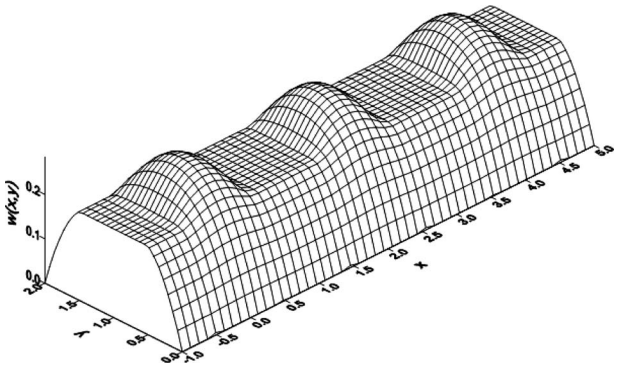

Fig. 2 Local velocity distributions for $u=0.2$, $a=1.0$, $b=0.5$, $c=0.5$, and $A=0.25$

$$w_{\text{mean}} = \frac{1}{a-b(1-c)}\left[\int_0^c \int_0^a w_1 dy dx + \int_c^1 \int_0^{a-b} w_2 dy dx\right] \tag{15}$$

Integrating Eq. (15) gives

$$w_{\text{mean}} = \frac{1}{a-b(1-c)}\left\{\frac{ca^3}{3} + \sum_n A_n \frac{1}{\alpha_n^2}\left(1 - \cos\frac{(2n-1)\pi}{2}\right)(1 - e^{-2c\alpha_n}) + (1-c) \times \left[\frac{(a-b)^3}{12} + \frac{(a-b)}{2}u\right] + \sum_m B_m \frac{1}{\beta_m^2}[\cos m\pi - 1] \times [e^{-2\beta_m(1-c)} - 1]\right\} \tag{16}$$

Furthermore, the f Re can be expressed as the function of the volumetric flow rate. According to the definition and the work of Wang [5], f Re can be derived in the form

$$f \text{ Re} = \frac{8[a-b(1-c)]^2}{(2+b-c)^2 w_{\text{mean}}} \tag{17}$$

The coefficients A_n and B_m in Eqs. (7) and (8) can be evaluated with the aid of Eqs. (10)–(12), and then $w_1(x,y)$ and $w_2(x,y)$ are obtained. The numerical calculation is obtained by using VISUAL C++ 6.0.

3 Results and Discussion

Figure 2 depicts the local velocity profile of flow in the channel for $u=0.2$, $a=1.0$, $b=0.5$, $c=0.5$, and $A=0.25$. As can be clearly seen in the figure, the local velocities of the bottom and the top of the channel are all zero under the no-slip boundary conditions and the velocity gradually increases away from the bottom and the top of the channel. The maximum value of w falls on w_1 and occurs at $x=0$ and $y=a$. Also, note that the bars move forward with a velocity u of 0.2 in the channel. Because the onward movement of the bars is slow, and the top and the bottom plates are fixed, the velocity distribution appears as $(w_1(x,y)) > u > (w_2(x,y))$. Then, Fig. 3 describes fluid velocity in the channel when the bars move forward under a larger velocity than the case in Fig. 2, i.e., $u=1.0$. In this case, the bars are moving in a larger speed than the fluid velocity in all regions of the channel, i.e., $u > w(x,y)$.

Figure 4 depicts velocity of flow in the channel when the bars move in the reverse direction slowly, $u=-0.1$. The fluid flows along with the $+z$-direction due to the positive pressure gradient, $dp/dz > 0$. On the other hand, the bars move in the opposite direction, the $-z$-direction. This condition leads to the adverse shear

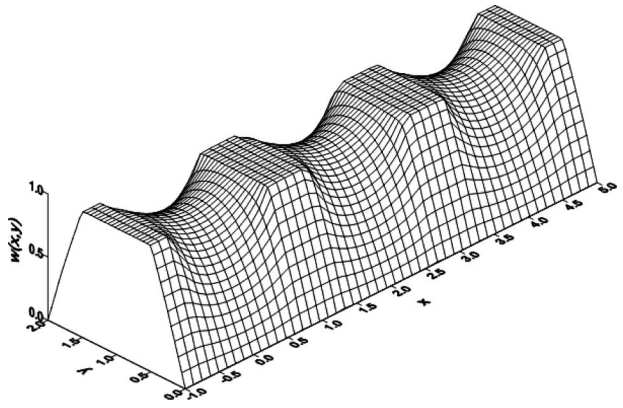

Fig. 3 Local velocity distributions for $u=1.0$, $a=1.0$, $b=0.5$, $c=0.7$, and $A=0.15$

stress, and a reverse flow occurs in the channel. Under this circumstance, both the forward flow and backward flow are observed to coexist in the channel. For a larger adverse velocity of the bars in the reverse direction, $u=-1.0$, the fluid velocities are displayed in Fig. 5. It is shown that the velocity of the adverse flow induced by shear stress is greater than the velocity of the positive flow induced by the fluid pressure gradient. In this situation, a reverse flow takes place in the entire channel, i.e., $w(x,y)<0$.

Figure 6 presents the effects of the velocity of bars on the mean fluid velocity under five different A's with the velocity of bars in the range of $-1.0 \le u \le 1.0$. In order to evaluate the influence of the cross-section area and the velocity of bars on the mean fluid velocity, the value of b in the figure is set at a fixed value, $b=0.5$. When the velocity of bars increases from -1 to 1, the mean fluid velocity will gradually increase. Also, the effects of the cross-section areas of the bars A on the mean fluid velocity are observed in the figure. When A is larger, the velocity of bars will influence both the shear stress and mean fluid velocity significantly. Besides, when A is larger, the mean velocity is also larger.

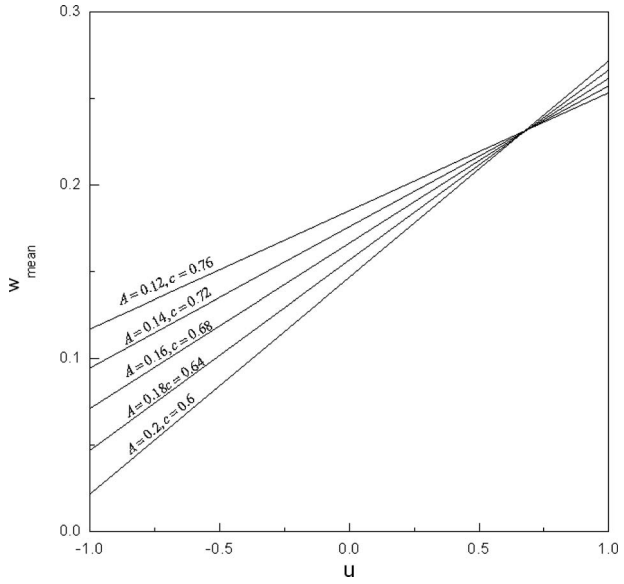

Fig. 6 Mean fluid velocity for bars with different velocities, $b=0.5$

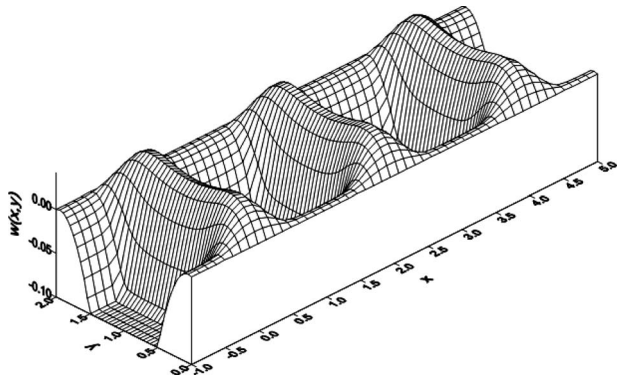

Fig. 4 Local velocity distributions for $u=-0.1$, $a=1.0$, $b=0.5$, $c=0.5$, and $A=0.25$—partial reverse flow under the negative velocity of bars

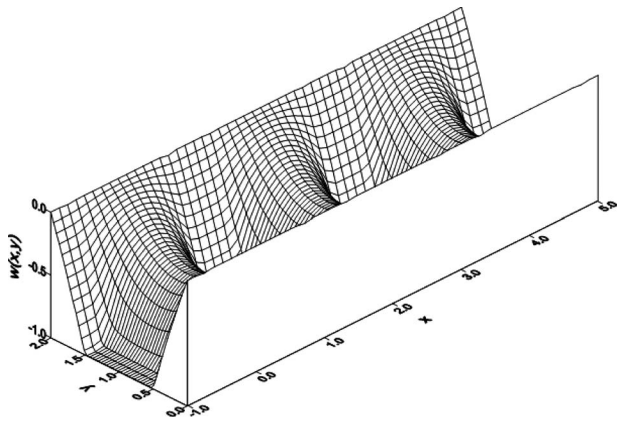

Fig. 5 Local velocity distributions for $u=-1.0$, $a=1.0$, $b=0.5$, $c=0.7$, and $A=0.15$—full reverse flow under the negative velocity of bars

Figure 7 plots the effects of different u on f Re under five bars with different cross-section areas. The f Re gradually decreases when the velocity of bars varies from -1 to 1. Besides, when the velocity of bars is a negative number, f Re will increase with an increasing A. Conversely, a larger A will lead to a decrease in f Re when the velocity of bars is a positive number. The f Re value is not a constant similar to a classical channel without mov-

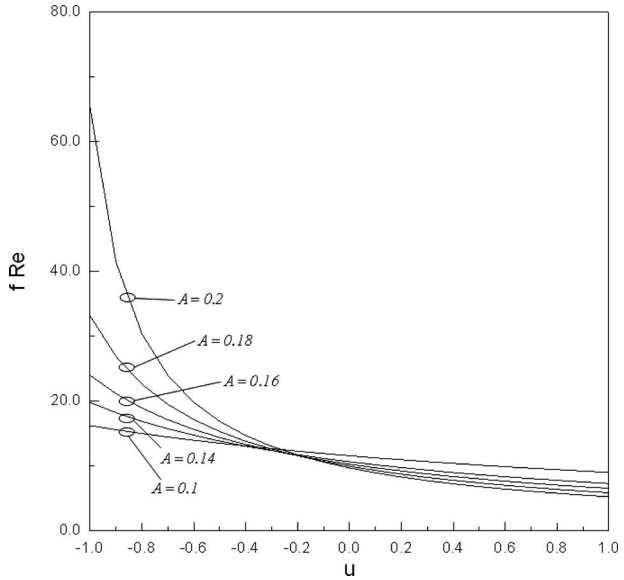

Fig. 7 The f Re values for bars with different velocities, $b=0.5$

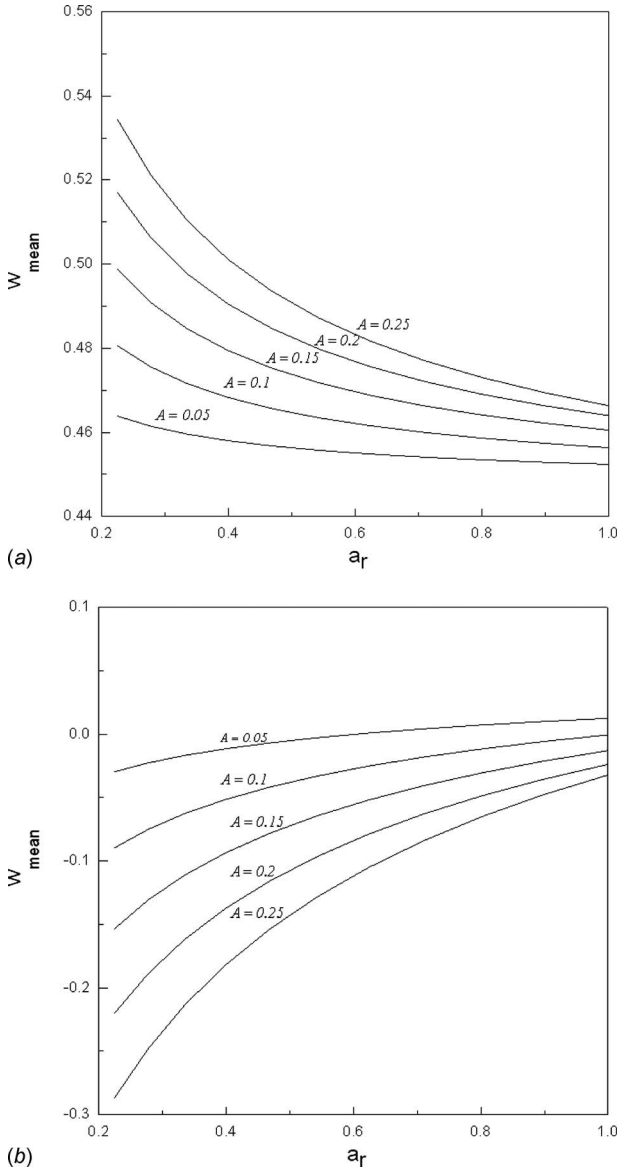

Fig. 8 (*a*) Mean fluid velocity for bars with different aspect ratios, $u=1.0$; and (*b*) mean fluid velocity for bars with different aspect ratios, $u=-1.0$

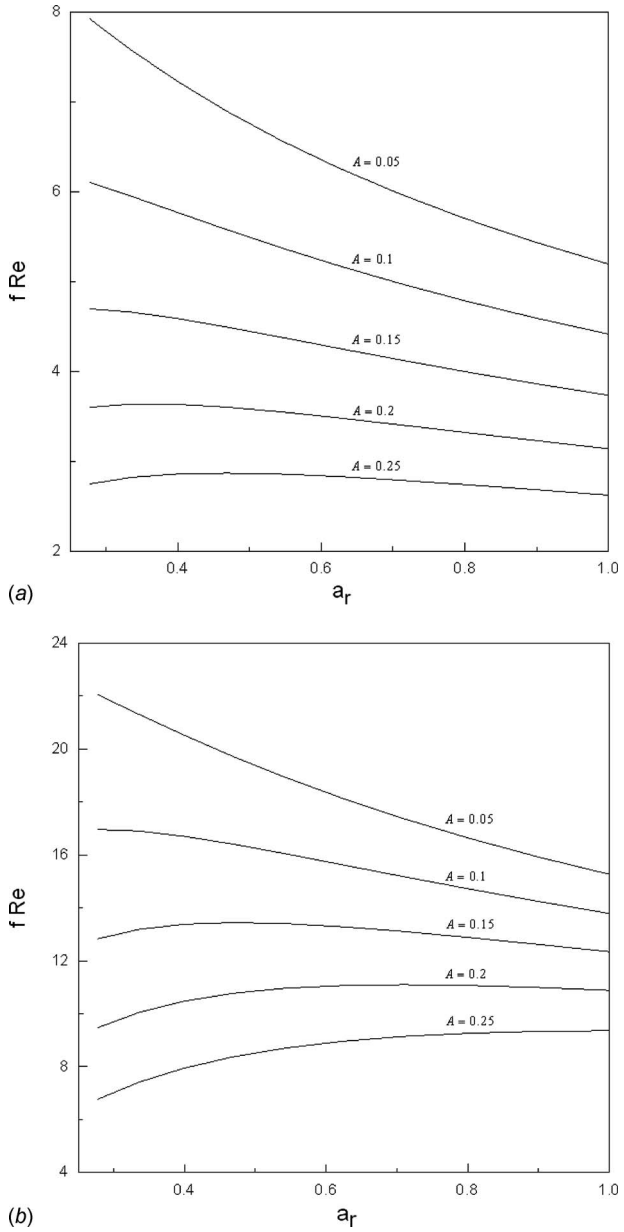

Fig. 9 (*a*) The *f* Re values on different aspect ratios of bars, $u=0.5$; and (*b*) the *f* Re values on different aspect ratios of bars, $u=-0.5$

ing bars. Figures 8(*a*) and 8(*b*) show the influence of different aspect ratios a_r on the mean velocity of flow. In Fig. 8(*a*), u is 1.0 and in Fig. 8(*b*), u is −1.0. The aspect ratio of the bar is defined as the ratio of height to width. To normalize the aspect ratio, a parameter a_r is defined as follows:

$$a_r = \frac{b/(1-c)}{[b/(1-c)]_{\max}}$$

or in an alternative form

$$a_r = \frac{b/(1-c)}{1/A}$$

$$[b/(1-c)]_{\max} = 1/(1-c)$$

and

$$b(1-c) = 1(1-c) = A$$

since $0 < b \leqq 1$. For $u=1.0$, an increase in the aspect ratio, proportional to an increase in the height b will cause an increase in w_1 and a decrease in w_2. The mean velocity is affected mainly by w_1; thus, an increase in b will result in an increase in the mean velocity of flow. Furthermore, for the bars with a smaller cross-section area, e.g., $A=0.05$, the effect of the aspect ratio on the mean velocity becomes less significant. However, for the bars with a larger cross-section area, e.g., $A=0.25$, the mean velocity will increase with a larger rate of variation. This is because an increase in A will lead to a decrease in the area of the channel flow, and then that brings about an increase in the mean velocity. For $u=-1.0$, it is seen that an increase in a_r will cause an increase in the mean velocity of flow. Besides, since the adverse bars are moving opposite to the flow direction, a larger A bears a higher shear and the mean velocity of flow will decrease eventually. Figure 9(*a*) presents the product of the friction factor and Reynolds number for different aspect ratios under the condition of $u=0.5$. When the aspect ratio increases, f Re will decrease. Besides, an increase in the cross-section area of the bars will result in a decrease in f Re.

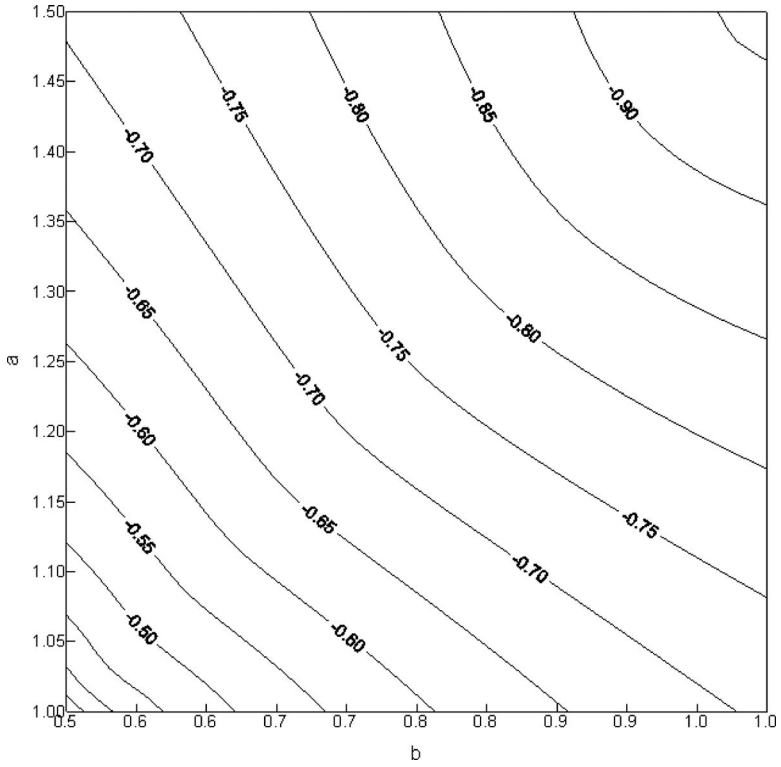

Fig. 10 The contour plot of the velocity of bars under $w_{mean}=0$ and $A=0.25$

A larger A will cause a larger w_{mean} and a smaller f Re. Figure 9(b) shows f Re on different aspect ratios a_r under the condition of $u=-0.5$. Due to the positive pressure gradient, the direction of fluid flows is frontward, but if the bars move in the adverse direction, the friction between the two motions of opposite directions will increase. As a result, the values of f Re in Fig. 9(b) are higher than those in Fig. 9(a).

Figure 10 shows the contour plot of u when w_{mean} is zero for different a and b values, and the case of the figure is $A=0.25$. As observed in the figure, the increase in a will lead to an increase in the volumetric flow rate; therefore, for obtaining $w_{mean}=0$, the reverse velocity of the bars have to be increased. Besides, the increase in b will decrease $(1-c)$, and leads to an increase in the shear stress in the $-z$-direction. Therefore, the smaller adverse velocity of the bars can help obtain $w_{mean}=0$.

Finally, the analytical solution in this study can be easily computed by the point-match methods. For realizing coefficients A_n and B_m, the values of A_n and B_m are listed in Table 1.

4 Conclusions

The following conclusions can be drawn from the foregoing results of this study.

(1) Under the case of the negative velocity of the bars, the reverse flow will be opposite to the positive velocity of flow, i.e., a reverse fluid flow will occur and the mean fluid velocity will decrease.

(2.) The increase in the positive velocity of the bars brings about a larger mean fluid velocity.

(3.) The curve of w_{mean} versus u shows a larger rate as A is larger. Besides, a larger A will lead to an increase in f Re when the bar moves adversely. However, a larger A will cause a decrease in f Re under the positive velocity bars.

(4.) The coefficients A_n and B_m in velocities $w_1(x,y)$ and $w_2(x,y)$ of the semi-analytical solution in this study can be

Table 1 The coefficients of A_n and B_m for $A=0.15$, $a=1$, and $b=0.5$

A_1-A_{40}							
$A_1=-0.45639$	$A_2=-0.00015$	$A_3=0.00998$	$A_4=0.00200$	$A_5=-0.00213$	$A_6=-0.00029$	$A_7=0.00148$	$A_8=0.00054$
$A_9=-0.00052$	$A_{10}=0.00001$	$A_{11}=0.00063$	$A_{12}=0.00021$	$A_{13}=-0.00024$	$A_{14}=0.00007$	$A_{15}=0.00036$	$A_{16}=0.00009$
$A_{17}=-0.00015$	$A_{18}=0.00008$	$A_{19}=0.00023$	$A_{20}=0.00002$	$A_{21}=-0.00011$	$A_{22}=0.00008$	$A_{23}=0.00016$	$A_{24}=-0.00003$
$A_{25}=-0.00009$	$A_{26}=0.00008$	$A_{27}=0.00011$	$A_{28}=-0.00007$	$A_{29}=-0.00008$	$A_{30}=0.00000$	$A_{31}=-0.00000$	$A_{32}=-0.00000$
$A_{33}=-0.00000$	$A_{34}=0.00000$	$A_{35}=-0.00000$	$A_{36}=0.00000$	$A_{37}=-0.00000$	$A_{38}=0.00000$	$A_{39}=-0.00000$	$A_{40}=0.00000$
B_1-B_{20}							
$B_1=0.00394$	$B_2=-0.00001$	$B_3=0.00127$	$B_4=-0.00009$	$B_5=0.00074$	$B_6=-0.00012$	$B_7=0.00051$	$B_8=-0.00014$
$B_9=0.00039$	$B_{10}=-0.00017$	$B_{11}=0.00031$	$B_{12}=-0.00019$	$B_{13}=0.00025$	$B_{14}=-0.00021$	$B_{15}=0.00011$	$B_{16}=0.00000$
$B_{17}=-0.00006$	$B_{18}=0.00000$	$B_{19}=-0.00000$	$B_{20}=0.00000$				

easily computed by the point-match method than by the direct integral method.

Nomenclature

a = normalized distance between plates
a_r = aspect ratio parameter ($=b/(1-c)/1/A$)
A = dimensionless area of the cross section of a beam ($=b(1-c)$)
A_n = coefficient of the function
b = dimensionless half height of the beam
B_m = coefficient of the function
c = dimensionless half spacing between width of the beams
D_h = hydraulic diameter ($=4[a-b(1-c)]H/2+b-c$) (m)
f Re = friction factor, product of the friction factor and the Reynolds number
H = half span of the selected domain (m)
p = pressure (N/m^2)
Re = Reynolds number ($=W_z D_h/\nu$)
u = dimensionless velocity of bars ($=-U/(H^2/\mu dp/dz)$)
U = velocity of bars (m/s)
W_z = velocity in the z-direction (m/s)
w = dimensionless velocity in the z-direction ($=-W_z/(H^2 dp/\mu dz)$)
w_{mean} = dimensionless mean velocity of the flow
x = dimensionless horizontal axis ($=X/H$)
X = horizontal axis (m)
y = dimensionless vertical axis ($=Y/H$)
Y = vertical axis (m)
Z = axis normal to the paper (m)
z = dimensionless axis normal to the paper ($=Z/H$)
μ = viscosity ($N\,s/m^2$)
ν = kinematic viscosity (m^2/s)

References

[1] Sparrow, E. M., and Loeffler, A. L., 1959, "Longitudinal Laminar Flow Between Cylinders Arranged in Regular Array," AIChE J., **5**, pp. 325–330.
[2] Cheng, K. C., 1966, "Analog Solution of Laminar Heat Transfer in Noncircular Ducts by Moiré Method and Point-Matching," ASME J. Heat Transfer, **88**, pp. 175–182.
[3] Trogdon, S. A., and Joseph, D. D., 1982, "Matched Eigenfunction Expansions for a Slow Flow Over a Slot," J. Non-Newtonian Fluid Mech., **10**, pp. 185–213.
[4] Zarling, J. P., 1976, "An Analysis of Laminar Flow and Pressure Drop in Complex Shaped Ducts," ASME J. Fluids Eng., **21**, pp. 702–706.
[5] Wang, C. Y., 1994, "Flow in a Channel With Longitudinal Ribs," ASME J. Fluids Eng., **116**, pp. 233–237.
[6] Wang, C. Y., 1976, "Parallel Flow Between Corrugated Plates," J. Engrg. Mech. Div., **102**, pp. 1088–1090.
[7] Achiq, A., and Naciri, J. K., 2001, "Asymptotic Solutions of the Wake Induced by a Streamwise Moving Flat Plate in a Channel," Int. J. Eng. Sci., **39**, pp. 1499–1507.
[8] Fu, W. S., Ke, W. W., and Wang, K. N., 2001, "Laminar Forced Convection in a Channel With a Moving Block," Int. J. Heat Mass Transfer, **44**, pp. 2385–2394.
[9] Fu, W. S., Tseng, C. C., Huang, C. P., and Wang, K. N., 2007, "An Experimental Investigation of a Block Moving Back and Forth on a Heat Plate Under a Slot Jet," Int. J. Heat Mass Transfer, **50**, pp. 3224–3233.
[10] Luo, X. Y., and Pedley, T. J., 1995, "A Numerical Simulation of Steady Flow in a 2-D Collapsible Channel," J. Fluids Struct., **9**, pp. 149–174.
[11] Bahrami, M., Yovanovich, M. M., and Culham, J. R., 2006, "Pressure Drop of Fully-Developed, Laminar Flow in Microchannels of Arbitrary Cross-Section," ASME J. Fluids Eng., **128**, pp. 1036–1044.

2D Numerical Simulations of Blade-Vortex Interaction in a Darrieus Turbine

E. Amet
Laboratoire des Ecoulements Géophysiques Industriels (LEGI), Grenoble 38041, France

T. Maître
Research Scientist
Institut National Polytechnique de Grenoble (INPG), Grenoble 38031,France

C. Pellone
Research Scientist

J.-L. Achard
Research Scientist

Centre National de la Recherche Scientifique (CNRS), Grenoble 38042, France

*The aim of this work is to provide a detailed two-dimensional numerical analysis of the physical phenomena occurring during dynamic stall of a Darrieus wind turbine. The flow is particularly complex because as the turbine rotates, the incidence angle and the blade Reynolds number vary, causing unsteady effects in the flow field. At low tip speed ratio, a deep dynamic stall occurs on blades, leading to large hysteresis lift and drag loops (primary effects). On the other hand, high tip speed ratio corresponds to attached boundary layers on blades (secondary effects). The optimal efficiency occurs in the middle range of the tip speed ratio where primary and secondary effects cohabit. To prove the capacity of the modeling to handle the physics in the whole range of operating condition, it is chosen to consider two tip speed ratios ($\lambda = 2$ and $\lambda = 7$), the first in the primary effect region and the second in the secondary effect region. The numerical analysis is performed with an explicit, compressible RANS k-ω code TURBFLOW, in a multiblock structured mesh configuration. The time step and grid refinement sensitivities are examined. Results are compared qualitatively with the visualization of the vortex shedding of Brochier (1986, "Water channel experiments of dynamic stall on Darrieus wind turbine blades," J. Propul. Power, **2**(5), pp. 445–449). Hysteresis lift and drag curves are compared with the data of Laneville and Vitecoq (1986, "Dynamic stall: the case of the vertical axis wind turbine," Prog. Aerosp. Sci., **32**, pp. 523–573).*
[DOI: 10.1115/1.4000258]

Keywords: VAWT, RANS modeling, dynamic stall, hysteresis

1 Introduction

Basically, wind turbines can be divided in two groups depending on their rotational axis direction: horizontal axis wind turbine (HAWT, or axial flow turbine), and vertical axis wind turbine (VAWT, or cross-flow turbine). VAWT has a smaller efficiency than HAWT, but did not benefit from the years of development undergone by the HAWT. A typical Darrieus turbine is a fixed pitch VAWT with straight blades and its simplicity lies in the absence of the yawing mechanism. On the other hand, the rotor aerodynamics is far from being simple since it involves highly unsteady flow fields. This unsteadiness is due to large variations in the angle of attack on the blades during their rotation.

Figure 1 presents a typical performance curve in term of power coefficient C_P versus the tip speed ratio λ. This curve is divided in three regions according to the importance of the primary (dynamic) and secondary (viscous) effects. At low tip speed ratios, blades undergo deep stall, leading to large dynamic loadings. Losses come from the large scale vortices detached from blades and convected in the wake. These dynamic effects are strongly influenced by the solidity σ of the turbine. At higher tip speed ratio, the shaft, the added mass effects, and the viscosity friction prevail due to smaller angles of attack. Between the two zones, there is a narrow optimal transition zone, corresponding to a balance between primary and secondary effects.

Since 1970, several aerodynamic prediction models have been formulated for Darrieus machines. The momentum models (single streamtube model [1], multiple streamtubes model [2], double-multiple streamtubes model [3,4], and other variants are all derived from the actuator disk theory. They are limited to small tip speed ratio and for solidity parameter below 0.2, because the Glauert momentum theory is not valid outside this range [5,6]. Also, the flow is assumed quasisteady and predicted blade loads are inaccurate. The normal component to the free-stream flow is neglected. The momentum models are inadequate to model the wake developed downstream of a wind turbine farm [7].

The vortex methods applied to rotor wake problems ranges from "prescribed" (fixed) to "free" vortex techniques. The development of a vortex wake model is based on the assumption of an incompressible potential flow with all vorticity being assumed concentrated within the vortex filaments [8]. In the vortex models, based on the vorticity equation, the blade element is replaced with a lifting line or surfaces that depend on the azimuthal position. The advantage is that the pressure does not explicitly appear in the vorticity equation and the pressure field is not needed to compute for the velocity field [5]. The fluid velocity is obtained by adding the undisturbed fluid velocity and the vortex induced velocity. On the other hand, lift and drag static coefficients are needed to compute the bound element vortex strength. The vortex models are relatively higher in computational overhead, mainly because the Biot–Savart law is computed for every vortex shed in the flow but they are more realistic than the momentum models.

Ponta and Jacovkis [9] combined a free vortex model with a finite element analysis (FEVDTM). The free vortex model acts as a macromodel, whose results are used as a boundary condition on the boundary of the micromodel (the finite elements area which include the airfoil). The bound vortex strength is obtained by integrating the velocity obtained with the finite element analysis. Once converged, the surface pressure distribution over the airfoil is obtained by integrating the momentum equation model. Knowing the pressure and velocity distributions, a boundary layer model is used to compute for the viscous shear stress over the airfoil surface. Then, the instantaneous forces are calculated by integrating the pressure distribution and shear stress. This method is attractive because it is free of empirical data; rotational effects

Contributed by the Fluids Engineering Division of ASME for publication in the JOURNAL OF FLUIDS ENGINEERING. Manuscript received July 2, 2008; final manuscript received August 31, 2009; published online October 21, 2009. Assoc. Editor: Joseph Katz.

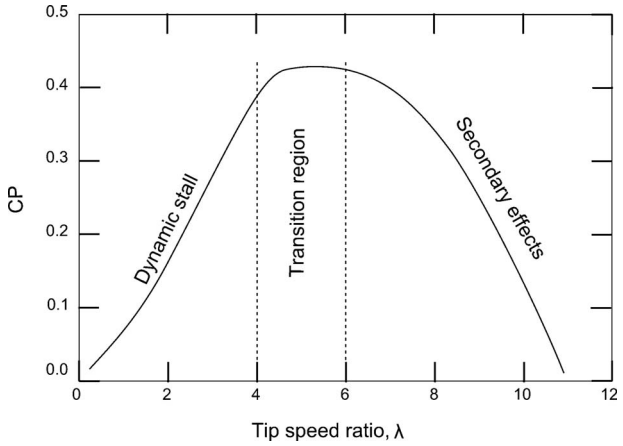

Fig. 1 Typical Darrieus rotor performance C_P as a function of the tip speed ratio [7]

are introduced in the finite elements analysis and static airfoil data are not needed. It does not cover the stall phenomena but provides instantaneous data at the border of the boundary layer that could be used to detect the dynamic stall appearance.

All these aforementioned methods (momentum and vortex) are not able to predict accurately the physics beyond the stall angle. That is why dynamic stall models have been incorporated in the analysis. These methods may be divided in theoretical and (semi)-empirical methods [10]. The theoretical models are derived from experimental air load measurements in two-dimensional flows for oscillating airfoils and then the loads are described using a few key parameters, depending on the method used. In this category falls the "UTRC, α, A, B" method [11], Boeing–Vertol "Gamma" function method [12], Beddoes' Time Delay method [13], Gangwani's method [14], etc.

The semi-empirical methods are derived from the thin-airfoil theory by using a set of linear and nonlinear equations for lift, drag, and pitching coefficients, with several empirical coefficients, mostly deduced from unsteady airfoil measurements. In this category, there are the Johnson's method (MIT method) [15], ONERA method [16], Leishman–Beddoes method [17], Gormont method [12], etc.

The advantages of the momentum and vortex models are their flexibility to include a wide range of empirically subcomponent models representing various physical effects. These are hindered by two aspects: first, by the strong hypotheses discussed above, and second, by the fact that they are nondeterminist. Validation of this approach with experimental measurements is essential. For further details, see Refs. [8,5,18]. The CFD codes arise as a better choice to overcome these limitations.

The basis of all CFD codes is the numerical schemes for solution of the flow equations, grid generation technique, and modeling the boundary layer turbulence. The most affordable is the RANS method. Allet et al. [19] performed a two-dimensional CFD computation of a single-bladed VAWT turbine using a NACA 0015 airfoil. A finite element turbulent solver based on a stream function-vorticity formulation has been used with two turbulence models, i.e., Cebeci–Smith and Johnson–King. The shape of the instantaneous normal and tangential forces was similar with the experimental curve but the maximum values were overpredicted. Moreover, the stall vortices visualized in the corresponding experiments are not obtained in the computed results.

More elaborated modeling combine RANS method for the boundary layers regions and the LES method in the outer regions (the so-called detached eddie simulation (DES)). Simão Ferreira et al. [20] compared two URANS models (with Spalart–Allmaras and k-ε turbulence models), and the LES and DES models with experimental vorticity visualization for a single-bladed NACA 0015 VAWT with infinite aspect ratio. DES models give the most accurate description of the generation and shedding of the vorticity and an acceptable sensitivity to grid refinement (both in time and space). LES models perform worse than DES models, probably because they model the wall region less accurately. DES and LES models present large force oscillations at frequencies higher than the frequency of the turbine rotation, due to either a continuous shedding of small vortices or either due to some numerical convergence effects. A nonzero value of the normal force for a zero geometric angle was found for both URANS models, while for DES and LES models, a zero normal force was found. It is more likely that, for a zero geometric angle, a symmetric airfoil in circular motion develops a nonzero lift, unlike a symmetric airfoil in pure translation, which has a zero lift for a zero geometric angle. This could be explained by the apparent camber as the turbine rotates (virtual camber) and the inertia of the fluid in the boundary layer [21].

Observe that for large scale wind turbines, compressibility effects should not be neglected when an accurate solution is needed. Even if the upwind flow has a low Mach number, local Mach numbers >0.3 are to be expected, due to local velocities acceleration. McCroskey et al. [22] observed sonic velocities on the surface of an airfoil every time the Mach number exceeded 0.2.

The present work examines two operating conditions for the turbine corresponding to the primary and secondary effects regions. This analysis is performed with the 2D URANS compressible solver TURBFLOW (Ecole Centrale de Lyon, France). This CFD code was chosen not for the compressibility equations, but for its higher order discretization schemes, which are expected to provide a better description of the flow unsteadiness. The chosen test case, corresponding to the experiment of Laneville and Vittecoq [23], on a two bladed Darrieus air turbine, is incompressible. This experimental work highlights the strong dependence of the lift and drag hysteresis curves of a blade with the tip speed ratio λ. Two tip speed ratios are considered in this study: a low tip speed ratio $\lambda=2$ for the primary effects analysis and a higher tip speed ratio $\lambda=7$ for the secondary effects analysis. The time step and grid refinement sensitivities for $\lambda=2$ are examined. At $\lambda=2$, results are compared qualitatively with the visualization of the vortex shedding of Brochier et al. [24] (on a very close configuration). Hysteresis lift and drag curves are also quantitatively compared with the data of Laneville and Vittecoq. The case $\lambda=7$ is not covered by these experiments.

2 Turbine Parameters

The two-dimensional cross section of a Darrieus blade is shown in Fig. 2. As the turbine rotates with the angular velocity Ω, in the upstream flow U_∞, the attack velocity field changes during a revolution, given by

$$\vec{W} = \vec{U}_\infty - \vec{\Omega}_\wedge \overrightarrow{OM} \tag{1}$$

Notice that this velocity acts upon the blade side exposed to the upstream flow. Consequently, the inner suction side in the upstream half disk becomes the inner pressure side in the downstream half disk. At the same time, the incidence angle varies from positive to negative values.

From geometric considerations, the velocity modulus W and the incidence angle α are given by

$$W = U_\infty \sqrt{1 + 2\lambda \cos\theta + \lambda^2} \tag{2}$$

$$\alpha = \tan^{-1}\left(\frac{\sin\theta}{\cos\theta + \lambda}\right) \tag{3}$$

where θ is measured from the tip position in the counterclockwise direction (Fig. 2).

The maximum incidence angle is given by

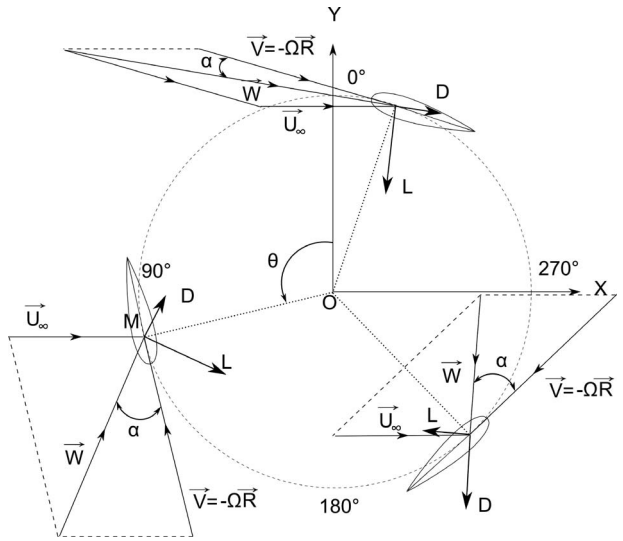

Fig. 2 Forces and velocities in a Darrieus turbine [20]

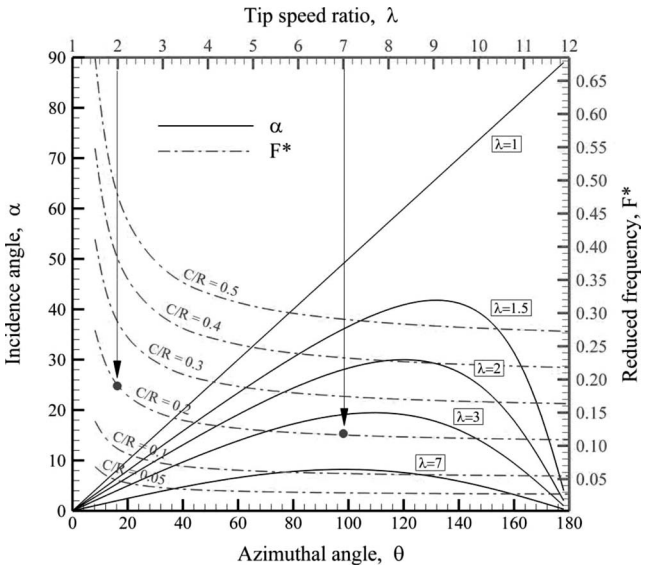

Fig. 3 Tip speed ratio effect on $\alpha(\theta)$ curves; curvature parameter effect on $F^*(\alpha)$

$$\alpha_{\max} = \tan^{-1}(1/\sqrt{\lambda^2 - 1}) \tag{4}$$

Laneville and Vittecoq [23] defined a reduced frequency for a Darrieus turbine, derived from that of helicopter blades for a mean zero incidence, as follows:

$$F^* = \frac{C\dot{\alpha}_{\max}}{\Omega R \times 2\alpha_{\max}} \tag{5}$$

The reduced frequency can be seen as the ratio between a time scale of the fluid motion along the blade $C/\Omega R$ on a time scale $2\alpha_{\max}/\dot{\alpha}_{\max}$ of the incidence angle variation. As stated by McCroskey [25], for reduced frequencies in excess of 0.05, the machine is prone to strong dynamic stall with the presence of vortex shedding if the angle of attack exceeds the one for static stall. For F^* values smaller than 0.05, the flow is assumed quasisteady. The equivalent expression of Eq. (5) for a Darrieus turbine is obtained by setting $\theta = \Omega t$ in Eq. (3) as

$$F^* = \left(\frac{C}{R}\right)\left(\frac{1}{\lambda - 1}\right)\frac{1}{2\alpha_{\max}} \tag{6}$$

Figure 3 is a plot on a same graph of two sets of curves: the incidence angle α versus the azimuthal angle θ for various tip speed ratios λ and the reduced frequency F^* versus the tip speed ratio λ for various curvature parameters C/R. The first set shows that for $\lambda = 2$ to 6, typical optimal values for water and wind Darrieus turbines (depending on solidity), the maximum angle of incidence varies from 30 deg to 9.5 deg. These angles are large compared with classical turbo machines applications. The static stall angle $\alpha = 12$ deg is obtained for $\lambda = 5$. Consequently, for all λ values less than 5, dynamic stall potentially occurs. The second set of curves show that for $C/R > 0.1$, F^* is in excess of 0.05, whatever the value of the tip speed ratio. So, if the two conditions $\lambda < 5$ and $C/R > 0.1$ are fulfilled, strong dynamic stall is to be expected.

In practice, a distinction between air and water Darrieus turbines is necessary. For water applications, because of their high solidity (0.5–2) and their low tip speed ratio, Darrieus turbines are always associated with dynamic stall phenomena. For air, the Darrieus turbine is less affected because of a smaller solidity (0.1–0.5) and higher tip speed ratios.

The forces acting on a blade, commonly applied at the quarter chord (thrust center) are depicted on the Fig. 4. The aerodynamic force on a blade is projected on three reference frames, as follows:

- An absolute reference frame (X, Y) with the origin in the center of rotation O;
- Lift-drag relative reference frame (l, d), with the origin at the thrust center M and the tangential and normal forces acting respectively in the W and perpendicular to W directions;
- Normal-tangential relative reference frame (n, t) called Lithental frame, with the origin at the thrust center and the tangential and normal forces acting respectively in the chord and perpendicular to chord directions.

As seen from Fig. 4, when the t-direction is tangential to the circle of rotation (blade without pitch angle), the thrust is given by the tangential component of the aerodynamic force in the Lithental reference frame.

The force coefficients are normalized (the unitary cross-dimension is 1 m) as follows:

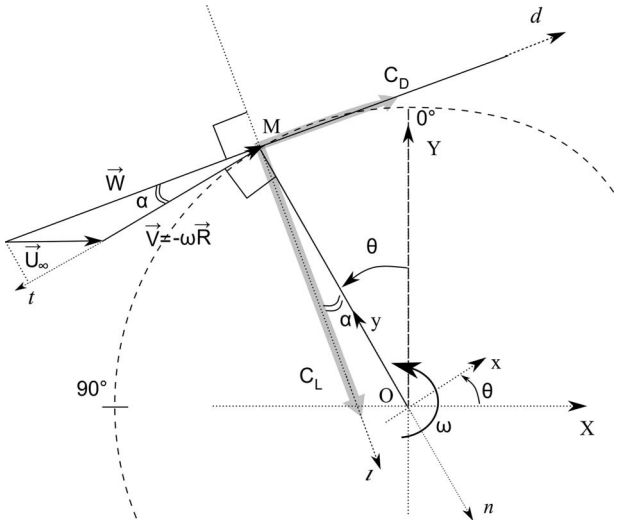

Fig. 4 Velocities and forces acting on a blade and their conventional positive directions

Table 1 Characteristics for the three experimental setups

Parameter	Brochier et al., 1986	Fujisawa and Shibuya, 2001	Laneville and Vitecoq, 1986
Technique	LDV in water channel	PIV in water channel	Separately measurements of N and T by strain gauge (air)
Blade profile	NACA 0018	NACA 0018	NACA 0018
Number of blades n_b	2	1	2
Blade chord C	0.02 m	0.01 m	0.061 m
Turbine radius R	0.06 m	0.03 m	0.3 m
Curvature C/R	0.33	0.33	0.20
Blade length ℓ	0.2 m	0.135 m	0.6 m
Reynolds number	Re_D=10,000 (fixed)	Re_D=3000(fixed)	Re_C=38,000(fixed)
Angular velocity Ω	variable	variable	300 rpm (fixed)
Undisturbed flow velocity U_∞	0.15 m/s (fixed)	0.05 m/s (fixed)	variable
Tip speed ratio λ	2.14 3.85	1; 2; 3	2; 2.5; 3; 4; 5
Reduced frequency F^*	0.3 0.22	∞; 0.32; 0.24	0.194; 0.164; 0.134; 0.124; 0.119
Central column diameter	0.01 m	Not used	0.0381 m
Blade fixation	End plates	Bottom=disk Up=free	Bottom=horizontal arm with force transducers Up=wires
Aspect ratio	$\approx\infty$	Relatively low	Relatively low

$$\left.\begin{aligned} C_L &= \frac{L}{0.5\rho C1(\Omega R)^2} \\ C_D &= \frac{D}{0.5\rho C1(\Omega R)^2} \end{aligned}\right\} \tag{7}$$

3 Numerical Study

Numerical simulations on a Darrieus turbine were carried out, the hysteretic behavior of which was investigated experimentally by Laneville and Vittecoq [23]. The various parameters are shown in Table 1.

The two blades have a NACA 0018 foil shape and are attached to the rotor radius at the quarter point from the leading edge in an infinite flow field. The offset pitch angle is set to zero (α_0=0). Due to some numerical instabilities at the trailing edge, the sharp edge was transformed into a round edge with a ratio radius/chord of 0.1%. The results are not affected by this tiny transformation.

3.1 Grid Setup. The computational domain extends 30 blade chord lengths from the center. The mesh is a multiblock structured grid composed by a mix of "O" blocks near the blades and near the frontier and a "H" bloc in the center (Fig. 5). The whole domain was meshed with the GAMBIT software (version 2.4) of FLUENT and then divided in 12 blocks, roughly of the same number of grid points, to take advantage of the parallel virtual machine (PVM) parallel programming. The computations were performed on two Dell PowerEdge 1950 machines equipped with two Intel Xeon dual core processors.

The reference grid contains 160,000 points and will be referenced as grid N1. Two blocks contain each blade and extend half a chord, meshed with a ratio of a maximum of 1.15 between two adjacent cells, with 188 nodes on each blade face. The ratio for the other zones is incremented from 1.15 to 3 at the boundary. To properly resolve the viscous affected region, an O mesh is used around the airfoils and $y+$ at the wall adjacent cell is chosen around 1, corresponding to a size of 25 μm. Grid sensitivity study presented in Appendix A show that a finer grid provide very similar results.

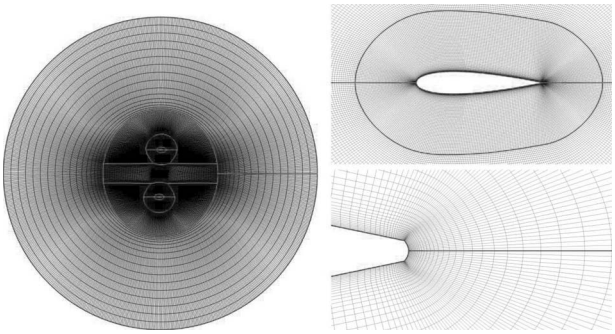

Fig. 5 Overview of the grid mesh N1

3.2 Numerical Governing Equations. The flow solver TURBFLOW is used to perform computations on the Darrieus turbine. The equations solved here are the full unsteady compressible RANS equations in the absolute frame, where the laminar viscosity is assumed constant. The equations are solved for the conservative (Favre mass-averaged) variable density ρ, momentum vector components ρu_i, and total energy ρE. In the present study, the turbulence model k-ω of Kok [26] is used. To avoid unphysical production of eddy viscosity, the production of kinetic energy is limited with a limiter relating the maximum allowable production to the double of the dissipation of turbulent kinetic energy.

To take into account the blades rotation, an arbitrary Lagrangian–Euler (ALE) method was used [27], with an adiabatic zero normal velocity condition on the blade surface. At the outlet, the atmospheric pressure was imposed, and at the inlet, the upstream velocity was used.

The space discretization is based on a monotone upstream-centered schemes for conservation laws (MUSCL) [27] finite volume formulation, with a third-order upwind scheme [28] for the convective terms. To advance the solution in time, a dual-time step procedure was used. Also, due to the stiffness and low convergence of the compressible solvers when low Mach numbers are encountered [29], a low Mach preconditioning is employed [30]. The solution is advanced in pseudotime with a three-step Runge–Kutta method until a pseudosteady-state is reached. The following numerical parameters come from a study presented in Appendix B. The physical time step was limited to 1.38×10^{-4} s, which corresponds to 0.25 deg of incremental azimuthal angle. To cover a chord, 48 time steps are necessary. For the inner time step, a local time step was employed with CFL=1, which gives a pseudotime step of 10^{-8} s near the blade region. To ensure stability at the beginning of a time step, a linear slope of the CFL number was imposed for the first 300 pseudotime steps, ranging from 10^{-3} to 1. A maximum number of 3000 inner-iterations was used (see Appendix A). In the following simulations, a transient behavior is noticed, with large differences between the first and the second revolutions, and negligible differences between the second and the third revolutions. Similar transient behaviors are found in Refs. [31,32]. The presented results correspond to the second revolution.

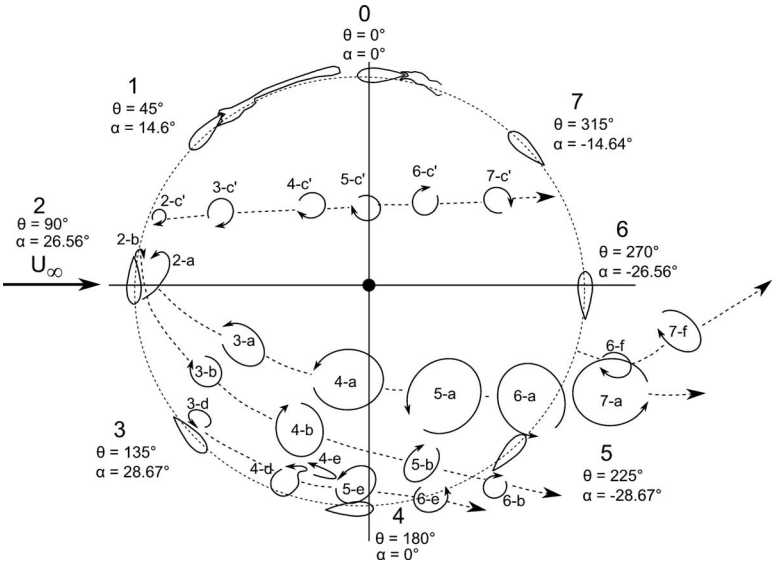

Fig. 6 Computed vortices trajectories for λ=2, using Q criterion, nondimensionalized by $(C/(\Omega R))^2$

4 Results

4.1 Case λ=2. Figure 6 shows the main vortices trajectories inside the turbine. The map has been obtained using the Q criterion, well adapted to identify traveling vortices (i.e., high vorticity and low shear strain rate regions) [33,34]. The numbers 0 to 7 refer to the foil positions and the letters to the vortex. The figure shows that only the clockwise ($\boldsymbol{c}'$) vortex goes through the upper part of the turbine, following a straight trajectory. On the other hand, the ($\boldsymbol{a}$-$\boldsymbol{b}$) pair of vortices and the clockwise ($\boldsymbol{e}$) vortex cross also the turbine, following curvilinear trajectories.

In Fig. 7, isocontours of vorticity and streamlines in a relative frame of reference are plotted for 24 azimuthal blade positions. The main coherent vortices are identified with letters as done in Refs. [24,35]. (the vortex field was not analyzed in Ref. [23]). Because the present configuration is close to the Brochier one, a similar vortex marking out is used. For convenience, the main characteristics of the three aforementioned experimental works are gathered in Table 1.

From Fig. 6, it appears that three regions are potentially concerned with blade vortex interactions, as follows:

(1) a large region from positions 2 to 6 (θ=90−270 deg), where the foil interacts with its own vortices, essentially $\boldsymbol{a}$ and $\boldsymbol{b}$ (Fig. 7.19)
(2) a narrow region about position 7 (θ=315 deg), where the foil interacts with its own vortex $\boldsymbol{c}'$ (Figs. 7.22–7.24)
(3) a narrow region between positions 0 and 1 (θ=0–45 deg) where the foil interacts with the $\boldsymbol{c}'$ vortex shed by the other blade (Figs. 7.1 and 7.2)

To check the real influence of $\boldsymbol{a}$, $\boldsymbol{b}$ and $\boldsymbol{c}'$ vortices in the three cases, their circulation have been evaluated by computing their vorticity flux Γ. The induced velocity on the blade is obtained using the Kelvin vortex model. Following this model, the azimuthal induced velocity at a point situated at a distance r from the vortex center, lying in the outer vortex region, is given by $v_\theta = \Gamma/(2\pi r)$. The vortex influence is calculated at the quarter chord blade point.

In the first aforementioned case, the position corresponding to Fig. 7.19 is chosen because, as it will be shown in the next paragraph, it reveals a strong interaction. The induced velocities of vortices $\boldsymbol{a}$ and $\boldsymbol{b}$ are equal to 2m/s and 0.5m/s, respectively, corresponding to 21% and 5% of the blade rotational speed (9.42 m/s). This result confirms the strong interaction of the vortex $\boldsymbol{a}$ when its trajectory intersects the blade trajectory at the beginning of the second half disk of rotation. The influence of the vortex $\boldsymbol{b}$ is weaker because of a smaller circulation and a larger distance from the blade.

In the two other cases (Figs. 7.23 and 7.1) the induced velocities are found equal to 2.5% and 1% of the rotational speed, respectively. This shows that the $\boldsymbol{c}'$ vortex influence on the two blades is negligible.

At θ=0 (Fig. 7.1), the flow recovers an attached boundary layer. The alternated vortices, seen at the rear of the wake, come from higher incidences undergone at the end of the preceding revolution. At θ=45 deg (Fig. 7.2), a counterclockwise vortex $\boldsymbol{c}$ appears at the trailing edge. As this vortex grows, a new counterclockwise vortex $\boldsymbol{a}$ develops at the leading edge (Figs. 7.3 and 7.4). At θ=71.25 deg (Fig. 7.5), $\boldsymbol{c}$ vortex is shed in the wake simultaneously with a clockwise vortex $\boldsymbol{c}'$ coming from the outer side boundary layer. As vortices $\boldsymbol{c}$ and $\boldsymbol{c}'$ are convected in the wake, the $\boldsymbol{a}$ vortex continues to develop and detaches from the leading edge (Figs. 7.6 and 7.7). From θ=90 deg to θ=105 deg (Figs. 7.8–7.12), the detachment of the $\boldsymbol{a}$ vortex is strongly coupled with the growth of a clockwise $\boldsymbol{b}$ vortex at the trailing edge (similar to $\boldsymbol{c}'$). As vortices $\boldsymbol{a}$ and $\boldsymbol{b}$ are shed in the wake (Figs. 7.13–7.15) a counterclockwise $\boldsymbol{d}$ vortex develops at the leading edge. At this position, the incidence angle reaches the maximum α=29.92 deg. In a similar way than for ($\boldsymbol{c}$-$\boldsymbol{c}'$) vortices and ($\boldsymbol{a}$-$\boldsymbol{b}$) vortices, the detachment of the $\boldsymbol{d}$ vortex corresponds to the growth of a clockwise $\boldsymbol{e}$ vortex at the trailing edge coming from the outer side boundary layer (Figs. 7.16–7.18). At this position, the foil enters in the second half disk of rotation and the incidence angle becomes negative. When approaching the maximum negative angle of incidence, (θ=225 deg, Fig. 7.19) a clockwise vortex $\boldsymbol{f}$ is seen at leading edge. Figures 7.19 and 7.20 depict the blade positions at two close angles of incidence −28.68 and −28.02, before and after the maximum, respectively. Figure 7.19 shows that the local angle of attack exceeds by far the geometrical one. This can be explained by the proximity of the $\boldsymbol{a}$ vortex that creates a blockage effect leading to a flow deflection in the outer direction. This effect is not seen on the Fig. 7.20 due to the convection of the $\boldsymbol{a}$ vortex in the downstream region. As seen in the first half disk, the $\boldsymbol{f}$ vortex detachment leads to the devel-

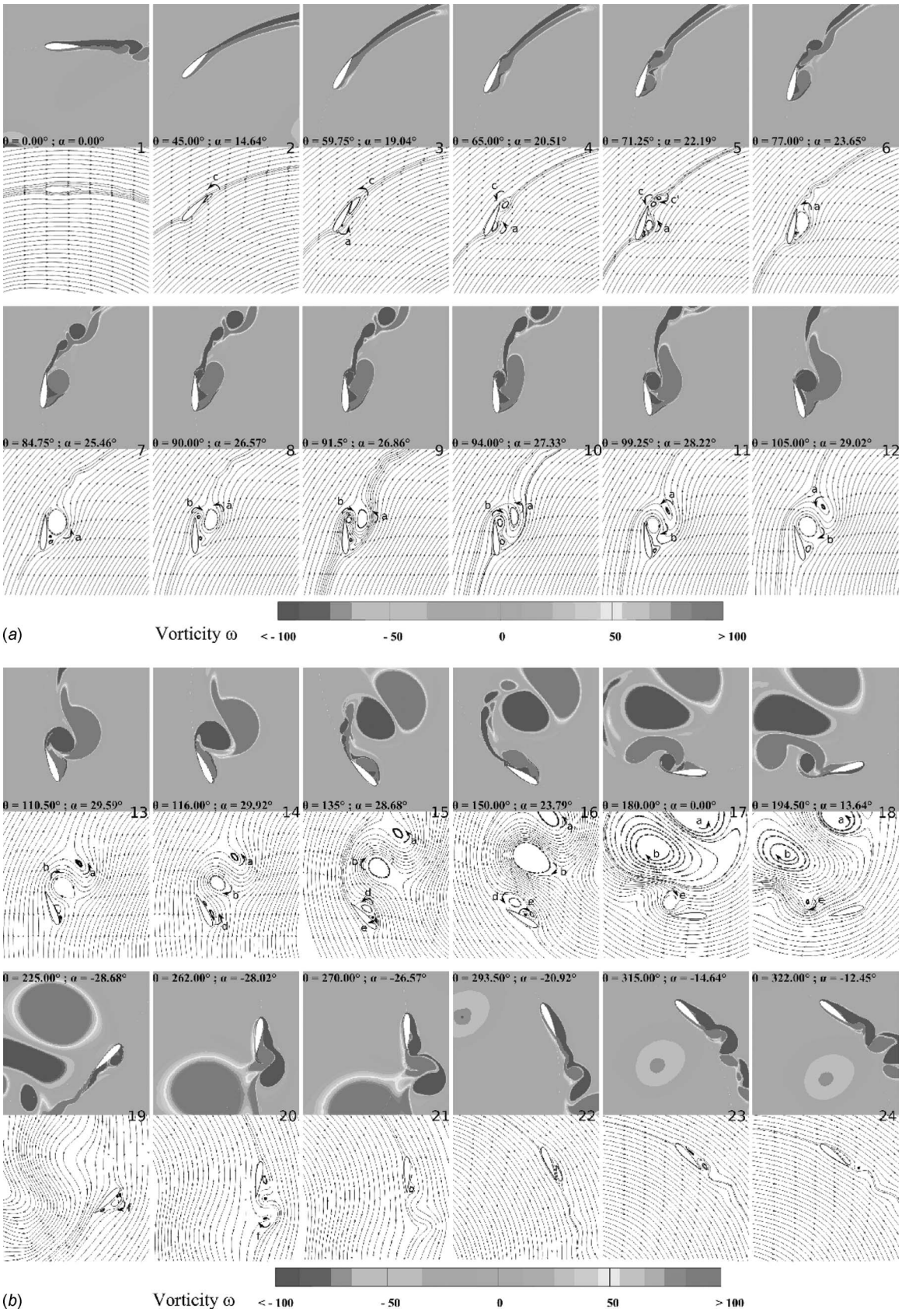

Fig. 7 Vorticity vector isocontours and relative streamlines

opment and the shedding of a counter-rotative vortex ***g*** (Figs. 7.20 and 7.21). As the incidence angle decreases (θ=293–322 deg, Figs. 7.21–7.24) many other pairs of alternate counter-rotating vortices, detaching from leading and trailing edges, are shed in the wake. These pairs of vortices appear weaker than the ones observed in the first half disk.

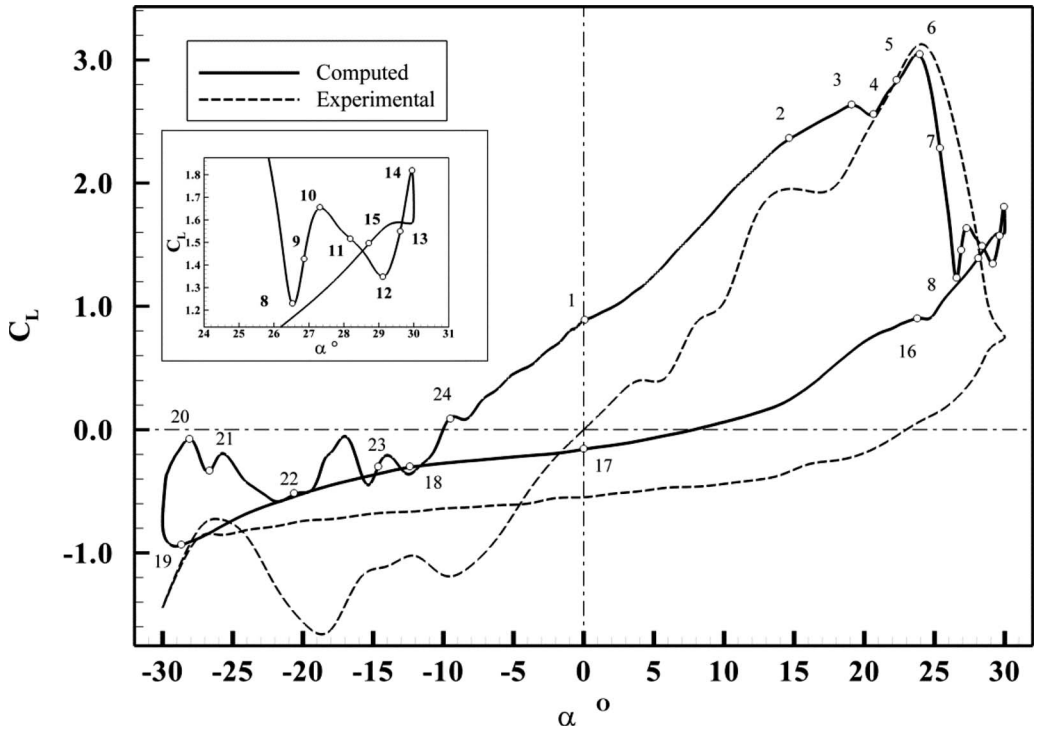

Fig. 8 Lift coefficient for one revolution, λ=2

Figures 8 and 9 show the lift and drag coefficients on one blade versus the geometrical angle of attack α. The black and dotted lines correspond to the calculated and experimental coefficients, respectively. The number plotted on the calculated curves corresponds to the picture number in Fig. 7. Though the global numerical and experimental curve shapes are similar (some global translations are observed between the two curves), some significant differences exist. They can come from four factors, as follows:

(1) The first one is the grid sensitivity, or more generally, the influence of the numerical parameters of the solver like the time step, the number of inner-iterations of the dual-time

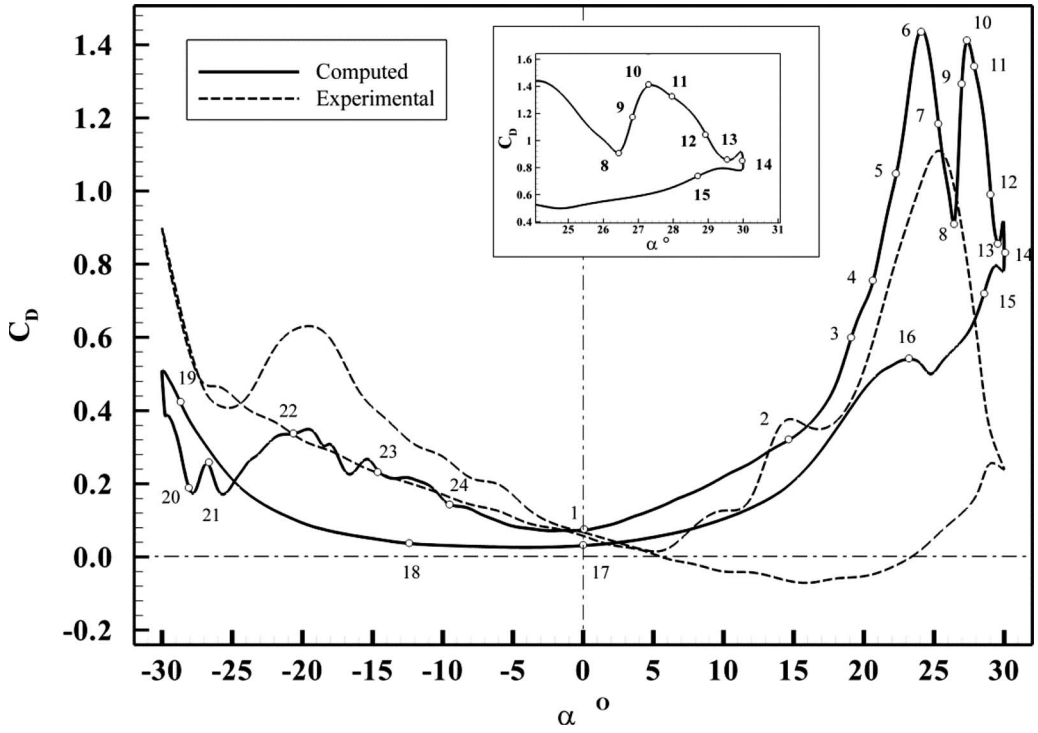

Fig. 9 Drag coefficient for one revolution, λ=2

stepping, and the order of the numerical schemes. A detailed study reported in Appendix A shows that a more refined grid do not produce remarkable differences on the hysteresis lift and drag loops. It is also demonstrated that the chosen physical and dual-time steps are small enough to produce no influence on the results.

(2) The second one is the two-dimensional approximation. In the experimental work, the blade aspect ratio, equal to 10, seems to be too large to explain the mentioned gap. Nevertheless, this point should be further investigated.

(3) The third one is the physical model relevance. Several works, as mentioned in the introduction, show that the URANS model based on classical isotropic turbulent model is satisfying in the blade boundary layer. The main weakness of this approach concerns actually the convection of the large eddies that are detached from the blade and convected inside the turbine. For this reason it is surprising that the main gap between the calculated and experimental coefficients concerns the blade positions between $\theta = 332$ deg and $\theta = 60$ deg (positions 24 to 3) corresponding to moderate flow incidences ($\alpha = -12$ deg to 20 deg), where no or only moderate stall takes place. A theoretical inviscid model reported in Appendix B shows that the flow curvature effect (due to the blade rotation) leads to a strong positive lift coefficient $C_L = 1$ for $\theta = 0°$ Fig. 21, close to the numerical coefficient $C_L = 0.85$, though the experimental one is 0. Also, data concerning the turbulence intensity upstream are not provided in the experimental work.

(4) Finally, the last factor concerns the accuracy of the experimental data. The above considerations make these data questionable in some respects. Unfortunately, no sufficient detail are found in the experimental study to quantify the uncertainties relative to the measured forces acting on the blades. Since the blades are built with balsa wood and maintained with wires at the tip, a possible cause of discrepancy could be the blade torsion. If a twist is considered only, numerical simulations (viscid and inviscid) show that an offset pitch angle of the order of 3 deg (trailing edge orientated toward the rotor) is sufficient to cause a zero lift coefficient for a null incidence.

In the following the calculated lift variations presented in Fig. 8 are linked to the dynamic of the main vortices highlighted in Figs. 6 and 7. The drag is not commented because its variations are in phase with the lift ones.

From positions 1 to 2 the boundary layer is attached and the lift curve is linear. The slope is about the half of the one given by the theoretical inviscid model of Appendix B. This difference is attributed to the delay due to the strong unsteadiness of the flow. The first lift drop corresponds to the detachment of the ***c*** vortex (positions 3 and 4). Then, a new raise is observed when the ***a*** vortex develops along the inner part of the foil (positions 5 and 6). The second drop corresponds to passage of the ***a*** vortex at the blade trailing edge (positions 7 and 8). This drop is attributed to the streamlines that separate strongly from the chord direction at trailing edge. From positions 9 to 14, though the incidence reaches its maximum, the lift stabilizes (oscillates) due to the strong and complex interactions of the two main vortices ***a*** and ***b*** with the blade. From position 15 to 17, the lift decreases smoothly following the flow incidence decrease. For position 17 ($\theta = 180$ deg, $\alpha = 0$ deg) the negative value of the lift is attributed to the influence of the ***d*** vortex, which obviously interacts with the blade. The inviscid model, which does not take into account these vortices, gives a positive lift coefficient of 0.31 coherent with the curvature effect (Appendix B, Fig. 21). From positions 18 to 19, the blade has undergone a negative lift due to the negative flow incidence. The increase in the lift slope, in this part, is probably

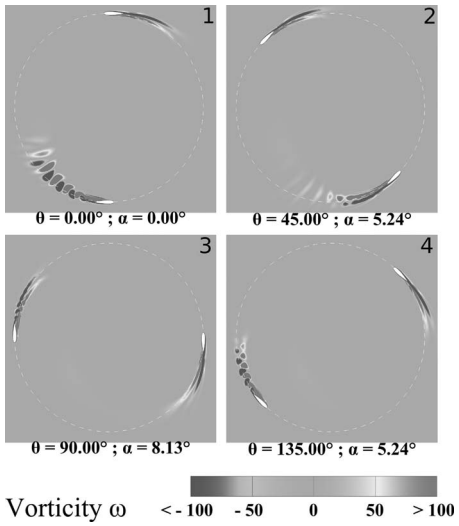

Fig. 10 Vorticity vector for λ=7 (black color-counterclock rotating)

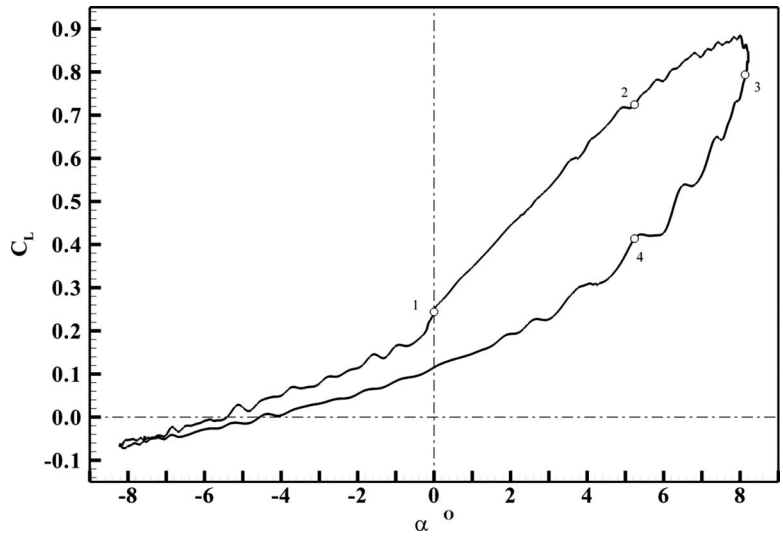

Fig. 11 Computed lift coefficient for one revolution, λ=7

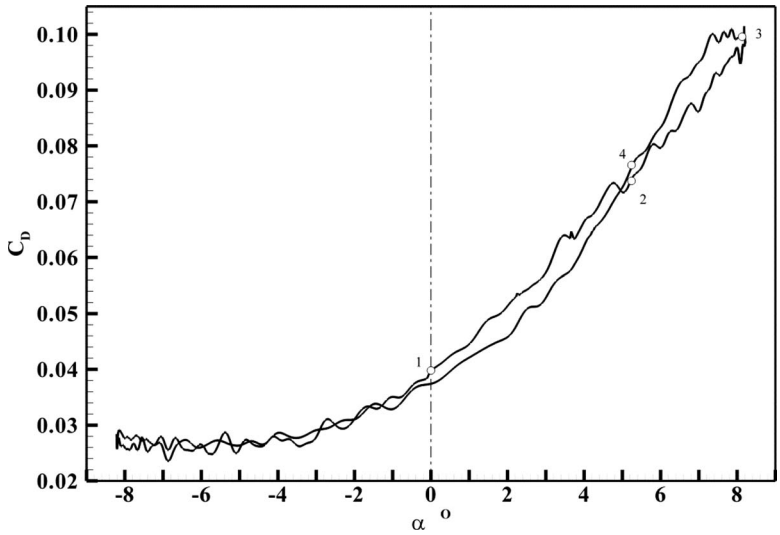

Fig. 12 Computed drag coefficient for one revolution, λ=7

due to the influence of the ***a*** and ***b*** vortices as they get closer to the blade. Position 20 confirms this influence; as the incidence keeps its maximum between positions 19 and 20 (−28 deg), the lift coefficient changes from −1 to about 0. The corresponding streamlines presented on Fig. 7 show that the counterclockwise ***a*** vortex induces a flow blockage at position 19, which increases locally the negative incidence. At position 20, this flow blockage is completely removed due to the convection of the ***a*** vortex downstream. From position 21 to position 24 incidence decreases as the blade revolution completes. The oscillating behavior of the lift during this phase is a direct consequence of the alternate vortices developing at the leading and trailing edges and sheds in the blade wake. Finally, the large hysteresis loops obtained for the lift and the drag curves show the aforementioned strong influence of the vortex structures on the blade.

The vortex formation and its convection downstream are found also in visualizations by Brochier et al. [24] or by Fujisawa and Shibuya [35]. For low tip speed ratios (λ=1,2,3), the counter pair of vortices ***a***-***b*** is mentioned in the two articles and the convection mechanism is similar. Fujisawa and Shibuya [35] mentioned the presence of two pairs of counter-rotating vortices, one at the small incidence angle and the other one at the higher incidence angle. The present computed results confirm the existence of two pairs of such counter-rotating vortices, (***c***-***c′***) and (***a***-***b***), although the pair generated at low incidence angle is more quickly dissipated than the (***a***-***b***) pair of vortices.

4.2 Case λ=7. Figure 10 presents the vorticity field for four blades positions, actually eight positions if one blade is considered. The flow field appears much less complicated than in the case λ=2. In the first half of the revolution alternate vortices, very similar to those observed in the second half of the revolution for λ=2, are observed. In the second half of the revolution, the alternate vortices are replaced by an attached boundary layer. Figures 11 and 12 present the corresponding lift and drag coefficients. The experimental coefficients are not available for this tip speed ratio. It is important to notice that flow incidences are now less than 8 deg compared with 30 deg in the case λ=2. This explains the light

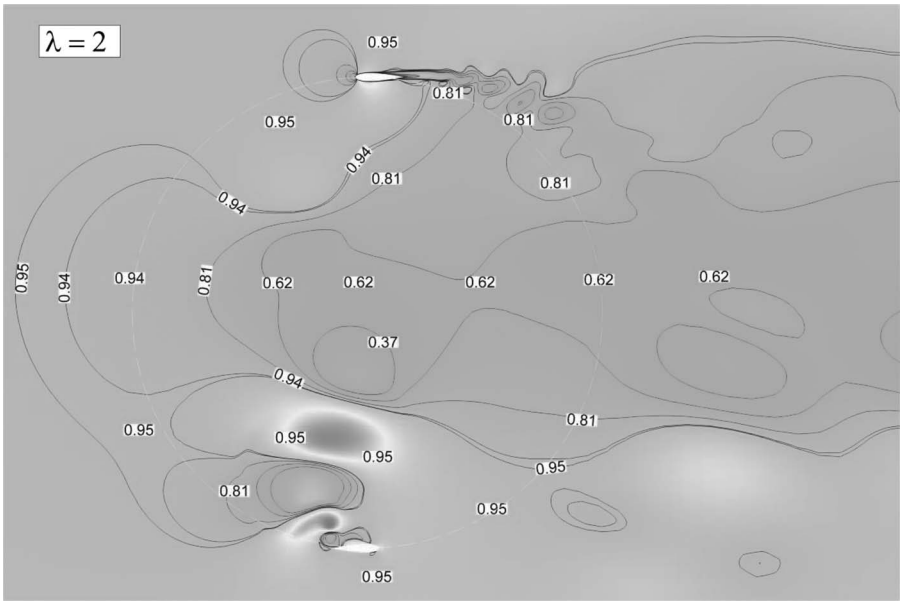

Fig. 13 Isovalues of axial velocity ratio U_X/U_∞ for θ=0 deg, λ=2

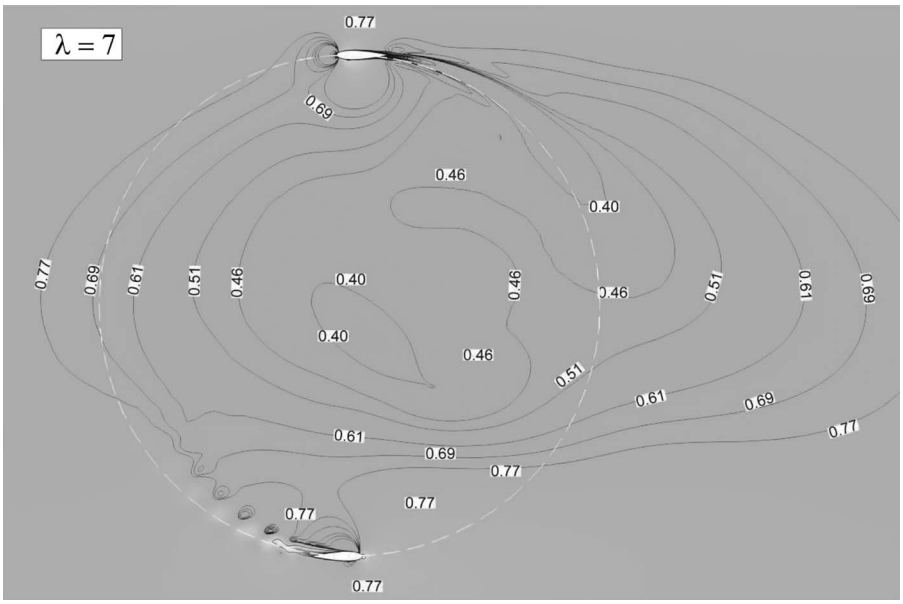

Fig. 14 Isovalues of axial velocity ratio U_X/U_∞ for θ=0 deg, λ=7

stall regime observed. The figures also show a small hysteresis for the lift and practically no hysteresis for the drag. The hysteresis is restricted to the first half of the revolution where a light stall is observed. This demonstrates that the importance of the hysteresis directly depends on the dynamic stall strength. Figure 11 also shows a remarkable slope change between the first and second half disks. The slope for a negative α is about half of the one for a positive α. This curve behavior can be explained by the variation in the main flow velocity shown in Figs. 13 and 14 for λ =2 and 7, respectively. The flow velocity decreases along the turbine, particularly for λ=7. As a result, the local tip speed ratio at the blade position, based on the local flow field, is strongly increased for downstream blade positions. This leads to smaller local flow incidences in this region and consequently to smaller lifts values. The flow slowing down in front of the turbine comes from the turbine drag and is associated to a global turbine bypassing. Figure 15 presents the drag turbine coefficient versus the azimuthal blade position. It confirms that the drag for λ=7 is larger than for λ=2, the corresponding mean drags being 2.2 and 0.64, respectively. It must also be noticed that for the θ=0 deg position, the turbine drag is practically zero though the flow slowing down, found at the same position in Figs. 13 and 14, is important. This explains why the behavior of the macroscopic flow field around the turbine depends not only of the current flow inside but also of the flow time history.

5 Conclusion

The unsteady flow field in a cross-flow turbine was numerically computed with a 2D URANS method and a k-ω turbulence model. Two extreme tip speed ratios λ=2 and 7, of the straight two bladed Darrieus turbine investigated experimentally by Laneville

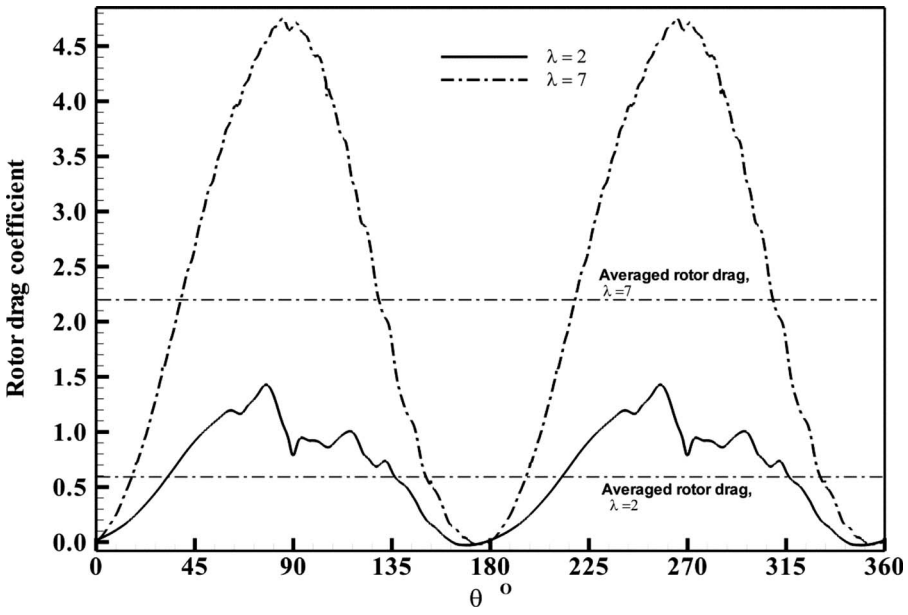

Fig. 15 Rotor drag coefficient

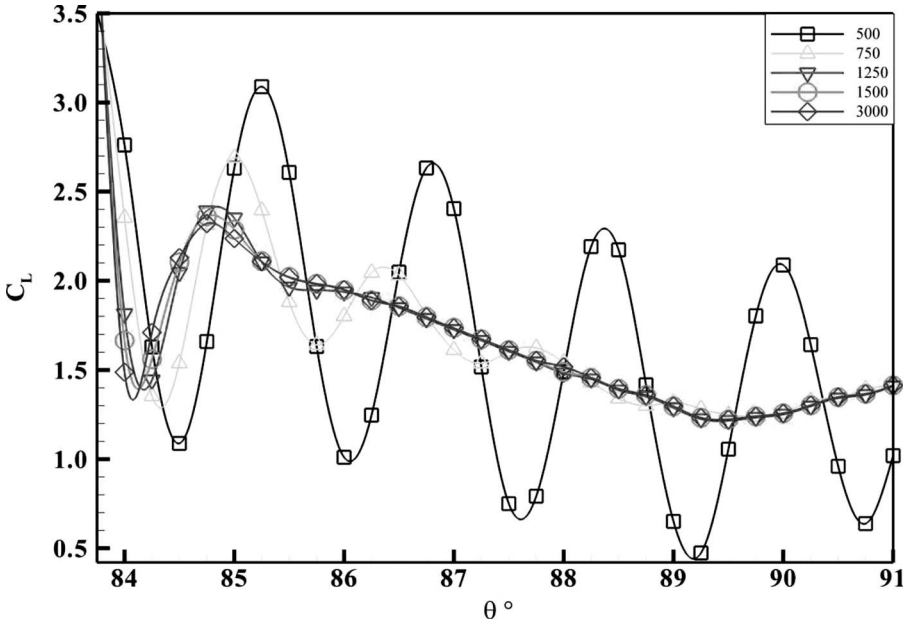

Fig. 16 Influence of inner-iterations on the lift coefficient at the beginning of the dynamic stall

and Vittecoq [23], have been considered. The grid and numerical parameters have been chosen to avoid any sensitivity effects on the results.

(1) The comparison with the experiment is made at $\lambda=2$ on the basis of the lift and drag coefficients. Though the global numerical and experimental curve shapes are similar, some significant differences exist. Several arguments lead to ask oneself about the experimental data. Unfortunately, the uncertainties of the lift and drag measurements are not precisely provided.

(2) The dynamic stall undergone by the blades has been studied in detail using the numerical results. For $\lambda=2$, pairs of counterclockwise vortices close to those observed in experimental works are sequentially shed from the blade. The (***a***-***b***) pair, created near the maximum incidence angle in the upstream half disk, is the strongest. The maximum lift coefficient corresponds to the convection of the ***a*** vortex from the leading edge to the trailing edge of the blade. The sudden lift drop is caused by the vortex passage at the trailing edge. It is shown that this vortex continues to influence the same blade at ulterior positions. It is responsible for the strong increase in the negative lift in the downstream half disk and then for its drop at the maximum negative incidence angle. The drag varies practically in phase with the lift during the blade rotation. The large hysteresis loops obtained for the lift and the drag curves express the strong influence of the vortex structures on the blade.

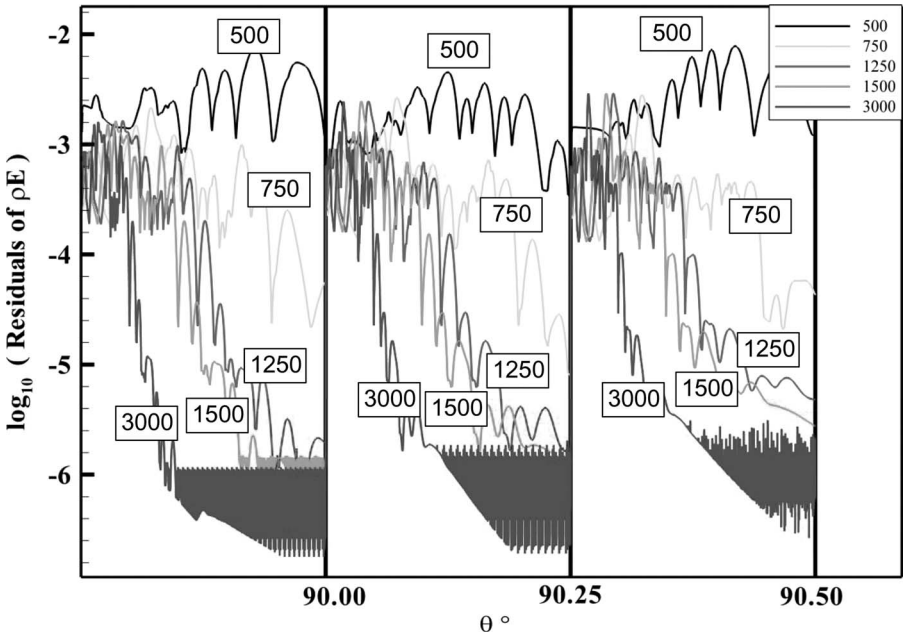

Fig. 17 Residuals of ρE for three time steps and various inner-iterations

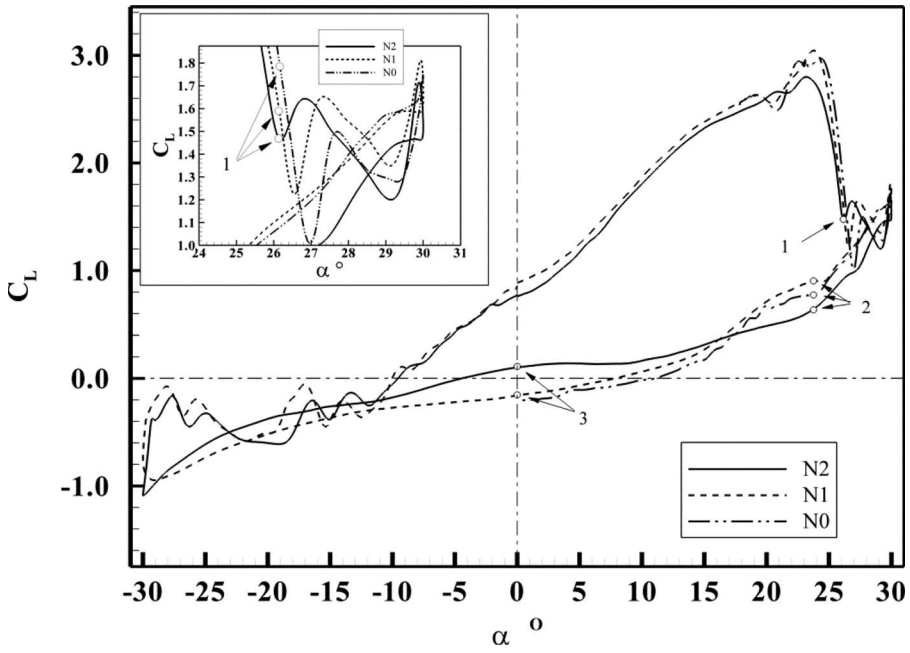

Fig. 18 Lift coefficients for the three meshes

(3) The $\lambda = 7$ case is characterized by a weak shedding of alternated vortices in the upstream half disk and by an attached flow in the downstream half disk. This light stall regime, due to smaller incidence angles, tends to flatten the hysteresis loops of the lift and drag curves. A strong decrease in the main flow is also found inside the turbine. This explains the smaller slope of the lift curve in the downstream half disk. It is shown that the flow blockage, addressing the macroscopic flow around the turbine, is induced not only by the current turbine drag but also by its time history.

A new experimental setup is being built in the Laboratoire des Ecoulements Géophysiques Industriels (LEGI) hydrodynamic tunnel. It will allow measurement of average and instantaneous turbine torques and powers on cross-flow turbine models. Flow visualizations and velocity measurements will also be possible. Further numerical works will focus especially on the comparison with the experimental data obtained.

Once fully validated, this modeling will allow to obtain the optimal foil section of the turbine, particularly its camber-line. Indeed, an inverse camber-line leads to a power increase in the half upwind disk of rotation, but to a power decrease in the half downwind disk. The choice of the optimal camber-line could be obtained only using CFD calculations.

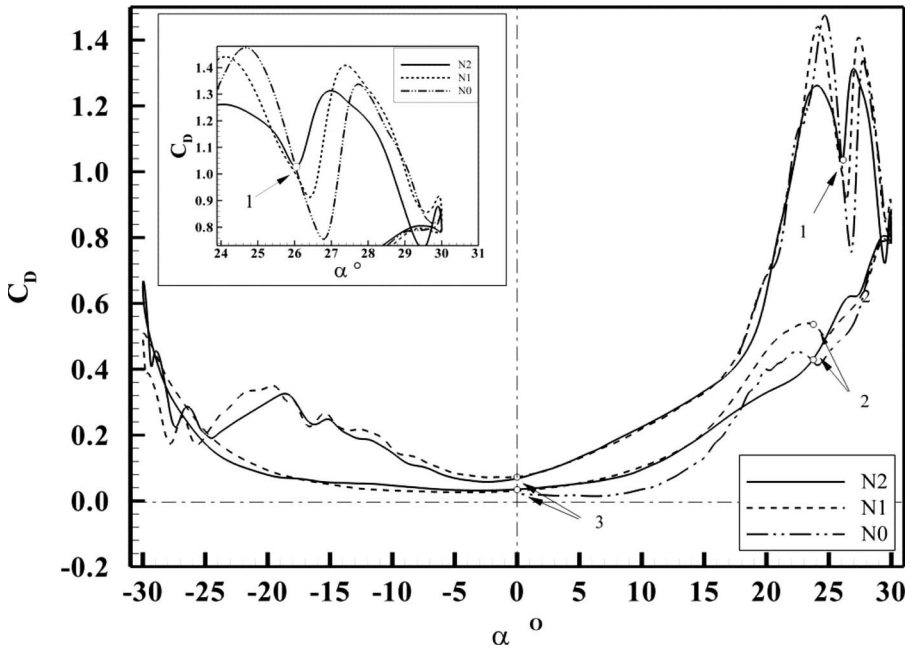

Fig. 19 Drag coefficients for the three meshes

Nomenclature

D = drag force (N)
L = lift force (N)
R = turbine radius (m)
F^* = reduced frequency
n_b = number of blades
ℓ = blade length (m)
C = chord of the foil (m)
$S=2R\ell$ = swept area (m^2)
U_∞ = upstream fluid velocity (m/s)
W = relative velocity (m/s)
μ = water molecular viscosity (Kg/m s)
α = incidence angle (deg)
α_0 = offset pitch angle (deg)
$\dot{\alpha}=d\alpha/dt$ = rate of change in the incidence angle (s^{-1})
$\theta=\Omega t$ = azimuthal angle (deg)
$\Delta\theta$ = azimuthal increment angle (deg)
$\lambda=\Omega R/U_\infty$ = tip speed ratio
$\sigma=n_bC/R$ = solidity
ρ = water density (Kg/m^3)
Ω = angular velocity (rad/s)
$C_P=\text{Torque}\times\Omega/1/2\rho SU_\infty^3$ = power coefficient
$\text{Re}_C=\rho\Omega RC/\mu$ = blade Reynolds number
$\text{Re}_D=\rho U_\infty 2R/\mu$ = machine Reynolds number
rpm = revolutions per minute (rpm)

Appendix A: Numerical Convergence and Grid Sensitivity

Preliminary tests showed that a maximum of 3000 inner-loops by time step combined with 10^{-7} for the residuals is sufficient enough to ensure the overall convergence of the computation. A specific test to check the influence of the inner-loops on the solution was carried out. The converged solution with the previous parameters at a particular azimuthal position (88 deg, corresponding to the deep dynamic stall regime) was chosen using 500, 750, 1250, 1500, and 3000 inner-iterations and the solution was advanced in time for 40 time steps. The lift coefficient is plotted in Fig. 16 and the residuals of (ρE) for three time steps are plotted in Fig. 17. An insufficient number of inner-loops is reflected in an oscillatory behavior of lift coefficient, while from 1250 of inner-loops the lift remains unchanged. A closer look at the convergence rate inside a physical time step (Fig. 17) shows that the oscillatory lift coefficient comes from an insufficiently convergence rate. From 1500 inner-iterations, no supplementary gain is obtained. The peaks present at the end of a time step for 1500 and 3000 inner-iterations are a consequence of the filtering operator, which limits the turbulent variables k and sometimes ω. It should be noted that either a lower CFL or a smaller physical time step activates less often the filtering operator. In the attached flow regime (0 ± 45 deg), the filtering operator is not activated and the residuals have a steep linear descent. The choice of a CFL=1 and a time step corresponding to 0.25 deg and a maximum of 3000 inner-iterations is a good compromise between convergence and stability.

To check the grid sensitivity, two other grids were chosen, systematically dividing or multiplying in each direction by two (multiplying or dividing by four the total number of cells) referred as N0 (the finer mesh) and N2 (the coarser grid). It should be noted that for a block structured mesh with collocated grid points, this technique becomes highly prohibitive because the computational time is multiplied by a factor of four for the finer mesh. To overcome this problem, for the finer mesh, a linear interpolation from the reference solution ($\lambda=2$) was done for an azimuthal position of 55 deg and the test was stopped at 180 deg. Also, a rigorous test was not possible, due to the explicit CFL restrictions; for the finer mesh an azimuthal increment of 0.1 deg and a five-step Runge–Kutta method was used instead of 0.25 deg and three-step Runge–Kutta for the other two cases.

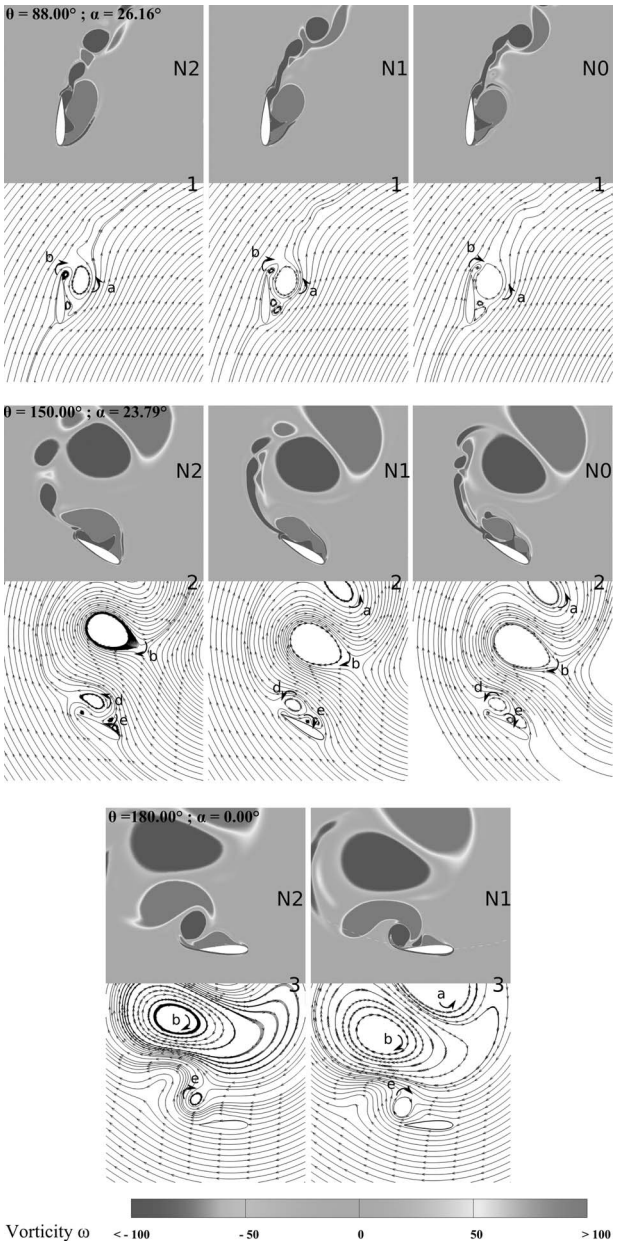

Fig. 20 Vorticity isocontours and relative streamlines for the three meshes and three azimuthal angles; numbers 1 to 3 refer to positions indicated on Figs. 18 and 19

The results for the lift and drag coefficients are presented in Figs. 18 and 19, respectively. Seen from these figures, the difference between the lift and drag coefficients, for the finer mesh N0 and the reference mesh N1 is negligible, even though the time step is smaller for the N0 mesh. It can be concluded that for the reference mesh, the solution is relatively time step independent.

The following remarks concern the three meshes:

(a) From $\theta=0$ deg until the beginning of the dynamic stall, the coarser mesh N2 gives satisfactory results compared with the other two meshes, although the maximum lift and drag coefficient is under predicted.
(b) A deeper decrease in both lift and drag coefficients occurs for the N0 and N1 meshes, compared with the N2 mesh, which corresponds to the passage of the ***a*** vortex

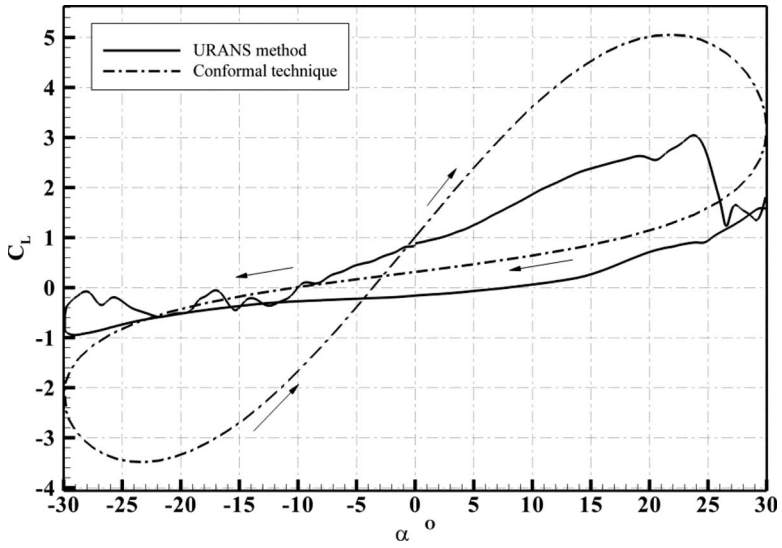

Fig. 21 Computed lift coefficient, λ=2

toward the trailing edge. From the relative stream traces in Fig. 20.1, the decrease is a consequence of a larger ***a*** vortex on the inner-surface of the foil.

(c) The main difference between the coarse mesh and the other two meshes appears in the zone corresponding to the convection downstream in the inner part of the rotor of the counter-rotating pair of vortices (***a***-***b***). The (***a***-***b***) pair of vortices follows more closely the blade in the case of the finer grid (Figs. 20.2 and 20.3). Their influence is particularly obvious. At $\theta=180$ deg, the coarser mesh indicates a positive lift (as predicted by the theoretical model, Appendix B), while the other two meshes produce a negative lift coefficient.

(d) At the end of the revolution, the N2 and the N1 meshes produce similar results.

Appendix B: Conformal Transformation

A conformal mapping technique was used which transforms the complex plane $z=x+iy$ into a complex plane z^T. In the complex plane $z^T=f(z,t)$, the entrainment velocity of a point belonging to the moving complex plane $z=x+iy$ (Figure 4) becomes zero relative to the transformed frame of reference z^T. Thus, the transformed foil is at rest. It is easy to demonstrate that z^T has the following form (characteristics theory)

$$z^T = f(z,t) = U_\infty t + F_1[ze^{-i\theta}] \tag{B1}$$

F_1 is an arbitrary holomorphic complex function. F_1 is determined so that the velocity at infinity vanishes. A class of functions which have this property is the complex logarithm function

$$z^T = A_0 \log B_0(z - z_0) \tag{B2}$$

The complex constants are chosen so that the foil leading edge is located at the origin of the plane z^T. The transformation has to respect the domain topology. In fact, z_0 should not be taken inside the foil. It is selected simply at the origin of coordinates ($z_0=0$). With these restrictions the transformation becomes

$$z^T = A_0 \log(z/z_L) \tag{B3}$$

where $A_0=C^T e^{i\phi_0}/|\log(z_F/z_L)|$, and z_F and z_L designate the affixes of the trailing and leading edges points in the complex plane z, respectively, and C^T is the chord. Under the assumptions of nonviscous fluid and irrotational flow, the complex velocity V of the physical plane is transformed into the complex velocity V^T

$$V^T = Vz/A_0 \tag{B4}$$

The slip condition in the physical plane for one point i, located on the airfoil (affix z_P), has the following form in the transformed plane:

$$\mathrm{Im}\left[e^{i\chi}V_P^T + e^{i\chi}U_\infty\left(e^{i\theta} + i\lambda\frac{\bar{z}_P}{R}\right)\frac{z_P}{A_0}\right] = 0 \tag{B5}$$

where Im is the imaginary part of a complex function, and χ is the tangent angle at the point P of the transformed foil. At instant t, in the transformed plane, the static foil is attacked by the complex velocity $V_0^T=U_\infty(e^{i\theta}+i\lambda(\bar{z}_P/R))(z_P/A_0)$. The velocity is a function of time and point position in the transformed plane. To simplify the calculation, a steady flow is considered and the attack velocity is the average velocity on the foil. The magnitude of ϕ_0 is calculated in order to provide a positive real value of the mean velocity V_m^T. Thus, in the transformed plane, the velocity at infinity upstream is always directed along the positive x^T axis.

In the physical plane, at any time, the flow has a period of 2π. In the transformed plane, a space periodicity of direction $\phi_0 + \pi/2$ is, thus, obtained. The potential flow is calculated in a two-dimensional cascade of transformed foils. The method is the boundary elements method (singularities methods). The pressure integrations along the foil provide the efforts that the fluid exerts on the foil. For the calculation of the pressure p, the Lagrange equation is written in the physical moving plane (generalized Bernouilli equation) as

$$p + \frac{1}{2}\rho|V|^2 + \rho\frac{\partial^{oxy}\Phi}{\partial t} + \rho\Omega\ \mathrm{Im}(Vz) = p_\infty \tag{B6}$$

where p_∞ stands for the upstream pressure. The nonstationary term $\partial^{oxy}\Phi/\partial t$ due to the partial derivative of the velocity potential relative to the moving plane is neglected. The results are presented in Fig. 21.

References

[1] Templin, R. J., 1974, "Aerodynamic Performance Theory for the NRC Vertical Axis Wind Turbine," National Research Council of Canada, Report No. LTR-LA-160.

[2] Strickland, J. H., 1975, "The Darrieus Turbine: A Performance Prediction Model Using Multiple Streamtubes," SANDIA Laboratory, Report No. SAND 75-041.

[3] Loth, J. L., and McCoy, H., 1983, "Optimisation of Darrieus Turbine With an Upwind and Downwind Momentum Model," J. Energy, **7**, pp. 313–318.

[4] Paraschivoiu, I., and Delclaux, F., 1983, "Double Multiple Streamtubes. Model

With Recent Improvement," J. Energy, **7**(3), pp. 250–255.
[5] Paraschivoiu, I., 2002, *Wind Turbine Design With Emphasis on Darrieus Concept*, Polytechnic, Brooklyn, NY.
[6] Pawsey, N. C. K., 2002, "Development and Evaluation of Passive Variable-Pitch Vertical Axis Wind Turbine," Ph.D. thesis, University of New South Wales, Sydney, Australia.
[7] Strickland, J. H., Webster, B. T., and Nguyen, T., 1979, "A Vortex Model of the Darrieus Turbine: An Analytical and Experimental Study," ASME J. Fluids Eng., **101**, pp. 500–505.
[8] Leishman, G. J., 2002, "Challenges in Modelling the Unsteady Aerodynamics of Wind Turbines," Wind Energy, **5**, pp. 85–132.
[9] Ponta, F. L., and Jacovkis, M., 2001, "A Vortex Model for Darrieus Turbine Using Finite Element Techniques," Renewable Energy, **24**, pp. 1–18.
[10] Leishman, G. J., 2002, *Principles of Helicopter Aerodynamics*, Cambridge University Press, New York.
[11] Bielawa, R. L., 1975, "Synthesized Unsteady Airfoil Data With Applications to Stall Flutter Calculations," 31st Annual Forum of the American Helicopter Society, Washington, DC, May 13–15.
[12] Gormont, R. E., 1973, "A Mathematical Model of Unsteady Aerodynamics and Radial Flow for Application to Helicopter Rotor," USAAVLABS, Technical Report No. 72-67.
[13] Beddoes, T. S., 1978, "Onset of Leading Edge Separation Effects Under Dynamic Conditions and Low Mach Number," 34th Annual Forum of the American Helicopter Society, Washington, DC, May 15–17.
[14] Gangwani, S. T., 1981, "Prediction on Dynamic Stall and Unsteady Airloads for Rotor Blades," 37th Annual Forum of the American Helicopter Society, LA, May 17–20.
[15] Johnson, W., 1980, *Helicopter Theory*, Princeton University Press, Princeton, NJ.
[16] Pitot, D., 1989, "Differential Equation Modelling of Dynamic Stall," La Recherche Aerospatiale, Paper No. 1989-6.
[17] Leishman, G. J., and Beddoes, T. S., 1989, "A Semi-Empirical Model for Dynamic Stall," J. Am. Helicopter Soc., **34**(3), pp. 3–17.
[18] Claessens, M. C., 2006, "The Design and Testing of Airfoils for Application in Small Vertical Axis Wind Turbines," Ph.D. thesis, Delft University of Technology, Delft, The Netherlands.
[19] Allet, A., Hall, É. S., and Paraschivoiu, I., 1999, "Numerical Simulation of Dynamic Stall Around an Airfoil in Darrieus Motion," ASME J. Sol. Energy Eng., **121**, pp. 69–76.
[20] Simão Ferreira, C. J., Bijl, L., van Bussel, G., and van Kuik, G., 2007, "Simulating Dynamic Stall in a 2D VAWT: Modeling Strategy, Verification and Validation With Particle Image Velocimetry Data," J. Phys.: Conf. Ser., **75**, p. 012023.
[21] Migliore, P. G., Wolfe, W. P., and Fanucci, J. B., 1980, "Flow Curvature Effects on Darrieus Turbine Blade Aerodynamics," J. Energy, **4**(2), pp. 49–55.
[22] McCroskey, W. J., McAllistair, K. W., Carr, L., Pucci, L. W., Lambert, O., and Indengard, R., 1981, "Dynamic Stall on Advanced Airfoils Sections," J. Am. Helicopter Soc., **26**(7), pp. 40–50.
[23] Laneville, A., and Vittecoq, P., 1986, "Dynamic Stall: The Case of the Vertical Axis Wind Turbine," Prog. Aerosp. Sci., **32**, pp. 523–573.
[24] Fraunié, P., Brochier, G., Béguier, C., and Paraschivoiu, I., 1986, "Water Channel Experiments of Dynamic Stall on Darrieus Wind Turbine Blades," J. Propul. Power, **2**(5), pp. 445–449.
[25] McCroskey, W. J., 1972, "Dynamic Stall on Airfoils and Helicopters Rotors," AGARD Paper No. R595.
[26] Kok, J. C., 1999, "Resolving the Dependence on Free-Stream Values for the k-ω Turbulence Model," National Aerospace Laboratory NLR, Paper No. NLR-TP-99295.
[27] Donea, J., Giuliani, S., and Halleux, J. P., 1982, "An Arbitrary Lagrangian–Euler Finite Element Method for Transient Dynamic Fluid-Structure Interactions," Comput. Methods Appl. Mech. Eng., **33**, pp. 689–723.
[28] Edwards, J. R., and Liou, M. S., 1998, "Low-Diffusion Flux-Splitting Methods for Flows at All Speeds," AIAA J., **36**(9), pp. 1610–1617.
[29] Turkel, E., and Vatsa Veer, N., 2003, "Choice of Variables and Preconditioning for Time Dependent Problems," 16th AIAA Computational Fluid Dynamics Conference, Orlando, FL, Jun. 23–26.
[30] Weiss, J. M., and Smith, W. A., 1995, "Preconditioning Applied to Variable and Constant Density Flows," AIAA J., **33**(11), pp. 2050–2057.
[31] Ploesteanu, C., 2004, "Etude Hydrodynamique d'un Type d'Hydrolienne à axe Vertical pour les Courants Marins," Ph.D. thesis, Institut National Polytechnique de Grenoble, France.
[32] Ekaterinas, J. A., and Platzer, M. F., 1998, "Computational Prediction of Airfoil Dynamic Stall," Prog. Aerosp. Sci., **33**, pp. 759–846.
[33] Chong, M. S., and Perry, A. E., 1990, "A General Classification of Three-Dimensional Flow Fields," Phys. Fluids A, **2**(5), pp. 765–777.
[34] Jeong, J., and Hussain, F., 1995, "On the Identification of a Vortex," J. Fluid Mech., **285**, pp. 69–94.
[35] Fujisawa, N., and Shibuya, S., 2001, "Observations of Dynamic Stall on Darrieus Wind Turbine Blades," J. Wind Eng. Ind. Aerodyn., **89**, pp. 201–214.

Modification of Axial Fan Flow by Trailing Edge Self-Induced Blowing

Matjaž Eberlinc
e-mail: matjaz.eberlinc@fs.uni-lj.si

Brane Širok
e-mail: brane.sirok@fs.uni-lj.si

Matevž Dular
e-mail: matevz.dular@fs.uni-lj.si

Marko Hočevar
e-mail: marko.hocevar@fs.uni-lj.si

Faculty of Mechanical Engineering,
University of Ljubljana,
Aškerčeva 6,
Ljubljana SI-1000, Slovenia

Axial fans often show adverse flow conditions at the fan hub and at the tip of the blade. The modification of conventional axial fan blade is presented. Hollow blade was manufactured from the hub to the tip. It enables the formation of self-induced internal flow through internal passages. The internal flow enters the passage of the hollow blade through the opening near the fan hub and exits through the trailing edge slots at the tip of the hollow blade. The study of the influence of internal flow on the flow field of axial fan and modifications of axial fan aerodynamic characteristics is presented. The characteristics of the axial fan with the internal flow were compared to characteristics of a geometrically equivalent fan without internal flow. The results show integral measurements of performance testing using standardized test rig and the measurements of local characteristics. The measurements of local characteristics were performed with a hot-wire anemometry and a five-hole probe. Reduction in adverse flow conditions near the trailing edge at the tip of the hollow blade, boundary-layer reduction in the hollow blade suction side, and reduction in flow separation were attained. The introduction of the self-induced blowing led to the preservation of external flow direction defined by the blade geometry, which enabled maximal local energy conversion. The integral characteristic reached a higher degree of efficiency. [DOI: 10.1115/1.4000345]

Keywords: axial fan, hollow blade, self-induced blowing, hot-wire anemometry, five-hole probe

1 Introduction

Axial fans often show adverse flow conditions at the fan hub and at the tip of the blade. Near the axial fan hub, at the inlet slot location, recirculation flow occurs. Here, the attachment of the blade onto the fan motor is optimized for easy manufacturing, which affects aerodynamic properties. Consequently, a decrease in flow velocity and increase in pressure is present. As a result, radial flow passing from the hub to the tip of the blade has negative effects on the fan efficiency. On the entire blade, the separation of flow on the suction side of the blade occurs. External flow is not able to follow the path of the blades' profile; therefore, it separates from the profile. The thickness of the boundary layer is increased.

A method to reduce these adverse flow conditions by introducing hollow blades is presented. The internal flow enters the hollow blade near the fan hub, and exits it as a free jet at the trailing edge at the tip of the hollow blade (Fig. 1). The internal flow is self-induced as no energy is required and the only driving force is the fan rotation. The internal flow is mainly driven by the centrifugal forces resulting from the fan rotation. The internal flow passage is mainly radial while the flow exits in the axial direction, although the direction of the internal flow is defined by the shape of the hollow blade. Using these modifications, reduction in adverse flow conditions near the trailing edge at the tip of the blade, boundary-layer reduction in the blade suction side, and reduction in flow separation was achieved. The modifications also enable increased local energy conversion and improve fan characteristics. It is to be understood that due to the centrifugal forces acting on the air in the hollow blade, the overpressure is built up on the tip of the hollow blades in the internal passage. This overpressure enables the air to blow from the trailing edge slot into the external flow. The increased velocity at the location of the trailing edge slot reduces the static pressure in the external flow. This prevents the formation of adverse pressure gradient in the boundary layer.

Internal flow adds energy to the external flow and consequently contributes to the preservation of the flow direction. As a direct result, flow separation from the blade suction side and the thickness of the boundary layer are reduced, which leads to higher fan efficiency. It can be assumed that at the trailing edge of the hollow blade, where mixing of the external and internal flows takes place, stabilization of flow structures is expected.

The concept of reducing the blade wake through trailing edge blowing has been investigated in the literature, where different explanations were proposed. Schlichting [1] developed a method for preventing separation, where additional energy is supplied to the particles of fluid. Suction was applied in the design of aircraft wings [2], where much larger maximum lift values were obtained. Garg [3] presented the use of hollow blades in gas turbines with induced secondary flow circulation, where the main purpose was blade cooling. Murphy et al. [4] experimentally and numerically described the system used in chemical industry for mixing of multiphase fluids. In their research, gas is supplied through the hollow impeller shaft. Gas continues along to every individual blade, where exit slots on the impeller blades in low pressure regions are drilled. Gas mixes with external fluid and influences the flow field in the vicinity. Sutliff et al. [5] and Woodward et al. [6] presented turbofan noise reduction with full-span trailing edge blowing with hollow blades and internal flow in internal radial flow passages.

To understand flow conditions near the blade trailing edge where internal flow mixes with external flow, the boundary-layer theory of Schlichting [1] and free-jet flow theory [1] were used. This theory was compared with the theory of Batchelor [7] and Hinze [8]. It is expected that the external flow better follows the blade shape near the trailing edge at the tip of the hollow blade and that the fan integral characteristic reaches a higher degree of static pressure difference.

Contributed by the Fluids Engineering Division of ASME for publication in the JOURNAL OF FLUIDS ENGINEERING. Manuscript received February 7, 2008; final manuscript received September 28, 2009; published online October 23, 2009. Editor: Joseph Katz.

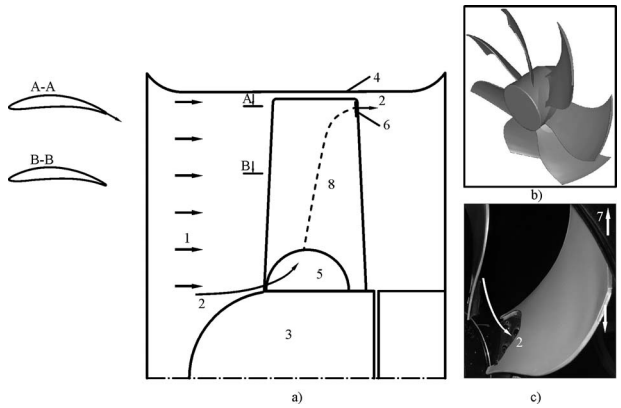

Fig. 1 Axial fan with self-induced trailing edge blowing: (*a*) schematic diagram of the axial fan, (*b*) axial fan, and (*c*) hollow blade (1. external flow; 2. internal flow; 3. fan rotor; 4. fan casing; 5. inlet opening for internal flow; 6. trailing edge slot at the tip of the hollow blade for internal flow; 7. rotation of the axial fan; 8. hollow blade) [12]

Changes in the flow field near the fan hub are also expected. They mostly result from the internal flow flowing into the internal radial flow passage; consequently, a reduction in radial flow in the cascade near the fan hub is expected [9–11].

To confirm the above assumptions, two versions were compared differing only in the presence or the absence of blade internal flow. Measurements of the integral characteristic were performed. Both versions were compared by the experimental analysis of local velocity field measurements with a hot-wire anemometry and a five-hole probe. All measurements were performed at equal operating and known ambient conditions.

The results show that the introduction of internal flow improved the fan characteristics and reduced the flow separation on the suction side of the blade.

2 Experimental Setup

The tested axial fan had a diameter of 500 mm and was manufactured with seven hollow blades [11,12]. The hub radius of the axial fan was 140 mm and the slot between the hollow blade and influx was 4 mm. The hollow blades were manufactured from serially produced ∅500 mm axial fan blades upon several modifications. The original/conventional axial fan blade was made from the profile NACA 63A series, where only the suction side of the blade was used with 2 mm thickness on the whole surface. Hollow blade had the same profile as the original blade—on the suction side of the hollow blade with 1 mm thickness on the whole surface. For the presented hollow blade, an additional layer of the NACA 63A series suction side with 1 mm thickness on the pressure side of the blade was added. The pressure side of the hollow blade had the same aspect ratio, but smaller curvature, enabling the gap between the suction and pressure sides for internal flow passage. At the tip of the hollow blade, the maximum thickness was 5 mm.

The internal flow enters the internal radial flow passage of the hollow blade through the openings near the fan hub. The inlet slot of the hollow blades has a semicircle opening with a diameter of 40 mm (Fig. 1). The outlet slot on the trailing edge at the tip of the hollow blade, where the internal flow exits the blade internal passages, has a size of 20×1 mm (Fig. 1). Therefore, the inlet/outlet surface ratio was approximately 30.

The selection of the fan was based on the results of the flow kinematics analysis of the internal [1] and external flows, as shown in Fig. 2 [13]. Calculations were made for three axial fan operating points at volume flow coefficients of $\varphi_1=0.24$, $\varphi_2=0.26$, and $\varphi_3=0.28$ (Table 1).

In order to estimate the external flow velocity, relative velocity w was calculated from the velocity vector triangle (Fig. 2(*b*)). Relative velocity w is calculated from the axial velocity c_{a2} and relative velocity angle β_2 (Fig. 2(*b*)). Relative velocity w is compared with the velocity of the internal flow u_j.

The estimation of velocity of the internal flow is based on the following three assumptions: (i) internal channel is large enough that no losses inside the hollow blade occur and the pressure at the trailing edge slot is only a result of centrifugal forces; (ii) the pressure at the location of the trailing edge slot is transformed into velocity and the pressure loss coefficient ξ due to narrowing can be used; and (iii) the velocity at the location of the hot-wire anemometer can be estimated from the velocity in the trailing edge slot using equations from the boundary-layer theory and published experimental results.

For the internal flow, first the determination of pressure and velocity of internal flow in the internal passage was taken into consideration. Pressure in the internal passage is a result of centrifugal forces. The internal passage is large enough that no pressure inside is lost. Through the internal radial flow passage, the

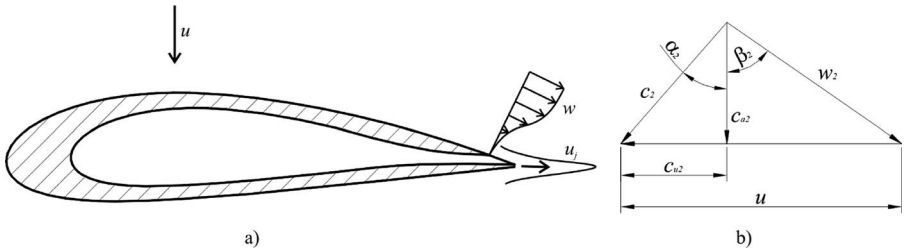

Fig. 2 (a) Direction and size of the internal u_j and external w flow velocities at the blade trailing edge; (b) external flow velocity vector triangle on the blade trailing edge: absolute c_2, axial c_{a2}, and tangential u velocities

Table 1 Analytically determined axial fan velocities

N	Volume flow coefficient φ	Air density ρ (kg/m^3)	Axial fan motor rotations per minute n (rpm)	External flow velocity w (m/s)	Internal flow pressure p_j (Pa)	Internal flow velocity u_j (m/s)
1	0.24	1.2	1133	25.7	544	29.1
2	0.26	1.2	1129	24.9	541	29.0
3	0.28	1.2	1123	23.7	535	28.8

passage cross section narrows all the way to the tip trailing edge, where the internal flow exits through the trailing edge slot at the tip of the hollow blade. A presumption was made that the internal flow is unimpeded and ideally follows the internal flow passage. In the slot, the pressure is transformed into kinetic energy. Therefore, only loss due to narrowing was considered. Because of narrowing, loss coefficient ξ is selected analytically [14]. At the exit, where the internal flow from the trailing edge slot at the tip of the hollow blade mixes with the external flow, local velocity is increased and pressure is decreased. Due to the comparison of mathematical analyses of external and internal flows with the measurement results attained from the local measurements with a hot-wire anemometry and a five-hole probe, which were performed 5 mm from the trailing edge of the hollow blade, the theory of Schlichting [1] was used to estimate the velocity at the location where the measurements took place.

When the internal flow exits the trailing edge slot at the tip of the hollow blade, a jet boundary occurs between two streams, which move at different speeds in the same direction. The width of this mixing region increases in a downstream direction. The emerging jet becomes mixed with the surrounding fluid. Particles of fluid from the surroundings are carried away by the jet so that the mass flow increases in the downstream direction. It is permissible to study such problems with the aid of the boundary-layer equations, and with the aid of semi-empirical assumptions, it is possible to apply Prandtl's mixing-length theory [1].

Experimental results on jets were given by the German Aerospace Center in Goettingen [1]. The assumption for shear stress leads to a considerably simpler calculation. The width of the jet is proportional to x and the center-line velocity $u_j \sim x^{-1}$. Thus, according to measurements, the virtual kinematic viscosity ε_0 is a function of the loss coefficient ξ, air density ρ, internal flow pressure p_j, and width of the jet x. The virtual kinematic viscosity ε_0 remains constant throughout the jet. The differential equation for the velocity distribution becomes formally identical with that for the laminar jet, the only difference being the virtual kinematic viscosity of the turbulent flow. The constant kinematic momentum K was introduced; according to the measurements K is a function of the loss coefficient ξ, air density ρ, internal flow pressure p_j, and width of the jet x. Kinematic momentum K, as a measure of the strength of the jet velocity u_j of exiting internal flow, was obtained [1] in Eq. (1) as

$$u_j = \text{const} \frac{K}{\varepsilon_0 x} \frac{1}{\left(1 + \frac{1}{4}\eta^2\right)^2} \tag{1}$$

where η in Eq. (2) is defined as [1]

$$\eta = \text{const} \frac{\sqrt{K}}{\varepsilon_0} \frac{y}{x} \tag{2}$$

According to the measurement performed by the German Aerospace Center in Goettingen and Reichardt [1], the empirical solutions of constant values for K^{-2}/ε_0 were determined.

Table 1 presents analytically determined external flow velocity w and internal flow velocity u_j at the exit from the trailing edge slot at the tip of the hollow blade.

Table 1 shows that the internal flow velocity u_j is greater compared with the external jet flow w ($u_j > w$), meaning that the internal flow forces the external flow in its direction. At this point, it is important to emphasize that the external flow velocity w obtained from the velocity vectors presents the velocity in the far-field region from the blade wall (Fig. 2(a)) and proportionally reduces in directions toward the blade wall [1]. Consequently, it can be assumed that the internal flow in the near wall region has an even higher influence toward the external flow; therefore, it is assumed that velocity $u_j \gg w$.

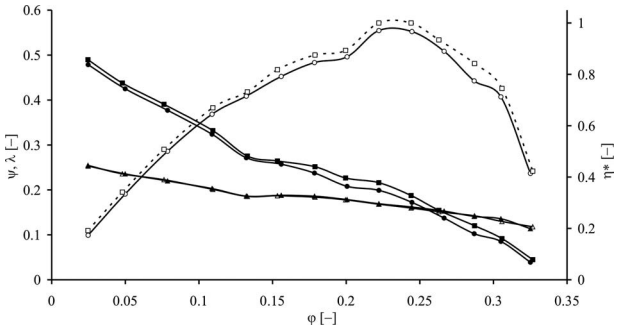

Fig. 3 Comparison of the integral characteristic of the axial fan at local properties and normalized efficiency for the cases with and without internal flow: (■) total pressure coefficient ψ for the case with internal flow; (●) total pressure coefficient ψ for the case without internal flow; (□) normalized efficiency η^* for the case with internal flow; (○) normalized efficiency η^* for the case without internal flow; (▲) power coefficient λ for the case with internal flow; and (△) power coefficient λ for the case without internal flow

3 Experimental Analysis

The experimental part includes measurements of integral characteristics of the fan and measurements of the local properties. The latter were performed with a hot-wire anemometry and a five-hole probe. All measurements were carried out in accordance with standards and under equal ambient conditions. Measurements of both versions with and without internal flows were performed immediately one after another, in a way, which allows achieving minimal measurement uncertainty.

3.1 Measurements of Integral Characteristics. Measurements were performed for both versions. To obtain comparable results, the measurements of integral characteristics were performed in accordance with standards [15,16] under equal operating and ambient conditions and at the same fan operating points, with the same measurement equipment, which was calibrated before measurement and were performed immediately one after another. The motor used was the same for both versions and with the following specifications: $U=400$ V, $f=50$ Hz, $P_w=770$ W, and $I=1.45$ A. The measurements for both versions were performed with the motor's constant speed. Prior to the measurements was the motor being calibrated according to the instructions of the International Organization for Standardization [15]. Measurements on the axial fan with hollow blades were conducted on a specially designed test station for the measurements of integral characteristics at the Hidria Institute Klima. The volume flow was measured on measurement nozzles with a sensor of differential pressure and static pressure in front of the nozzle. The Mensor 6100 sensor was used in both cases. The static pressure difference Δp_s was measured with the same sensor. The Vaisala HMT 330 measuring device for temperature and relative humidity was used to determine the ambient conditions and pertaining air density, while the barometric pressure was measured with the Vaisala PTB 220 measuring device. The connecting electrical power P_w and the rotating frequency of the fan's rotor were measured in addition to the aerodynamic parameters. Electrical power was measured with the Zimmer LGM450 digital power analyzer and the rotating frequency n was measured with an HIK IJ measuring device. The main sources of total measurement uncertainty [9,10,17] are uncertainties of the measuring rotating frequency, volume flow, pressure difference, temperature correction, humidity, etc. Overall measuring uncertainty is estimated to be 2.8% from the measured value and is in accordance with the International Organization for Standardization [16].

The integral characteristic of axial fan is presented in Fig. 3. In Fig. 3, measurements of the pressure difference (ψ=total pressure

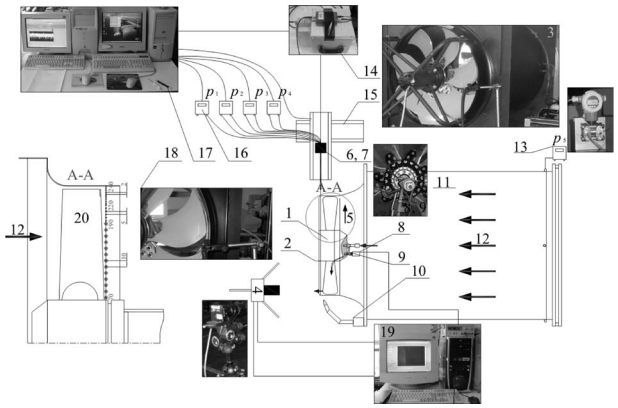

Fig. 4 Measuring station scheme for measuring local flow properties: 1. axial flow fan; 2. axial flow fan mesh; 3. wind tunnel with measured axial flow fan; 4. high-speed camera; 5. rotation direction of axial flow fan; 6. five-hole probe; 7. hot-wire anemometer; 8. inductive sensor; 9. rotational speed sensor; 10. illumination, 11. wind tunnel; 12. flow direction indication; 13. differential pressure transmitter 5; 14. signal conditioning module; 15. positioning table; 16. differential pressure transmitter 1–4; 17. PC for control, acquisition, and data storage 1; 18. axial flow fan with hollow blades and detail; 19. PC for control, acquisition, and data storage 2; and 20. detail (presenting measurement points on a line perpendicular to the axis at a distance of 5 mm behind the trailing edge of the hollow blade)

coefficient), power (λ=power coefficient), and normalized efficiency η^* attained with Eq. (3) are presented. Parameters in the integral characteristic were defined by Eq. (3) as

$$\varphi = \frac{4q_v}{\pi D^2 u}, \quad \psi = \frac{2\Delta p_t}{\rho u^2}, \quad \lambda = \frac{8P_w}{\pi \rho D^2 u^3}, \quad \eta = \frac{\varphi\psi}{\lambda}, \quad \eta^* = \frac{\eta}{\eta_{\max}} \tag{3}$$

where φ is the flow coefficient, ψ is the total pressure coefficient, Δp_t is the total pressure, λ is the power coefficient, P_w is the input power from a motor (kW), η is the efficiency, η^* is the normalized efficiency, D is the diameter, ρ is the air density, and $u = \pi D n/60$ is the velocity.

Figure 3 shows results for the integral characteristics of the axial fan in local properties with and without internal flows. When the internal flow was introduced, an increase in normalized efficiency η^* and pressure coefficient ψ was observed. A difference in pressure coefficient ψ (up to 6%) is present through the complete operating range. The power coefficient λ is comparable for both versions.

It can be assumed that the blade wake is reduced, which consequently leads to shifting of the characteristic toward larger values of flow in the complete operating range of the axial fan.

3.2 Measurements of Local Flow Properties. Measurements of the local flow properties were performed with a hot-wire anemometer and a five-hole probe. Local measurements were performed in three operating points, at axial fan rotating frequency $n=1124$ rpm, and at volume flow coefficients of $\varphi_1=0.24$, $\varphi_2=0.26$, and $\varphi_3=0.28$ (Fig. 3).

Figure 4 shows the scheme of the measuring station for measuring the local flow properties. Measurements of the local flow properties were performed at the outlet of the fan. At the each selected operating point of the axial fan, local flow measurements in 29 measuring points on blade radius were performed. Measurement points were selected on a line perpendicular to the axis at a distance of 5 mm behind the trailing edge of the hollow blade (Fig. 4, detail A-A). This allowed measurements across the entire trailing edge from the rotor hub to the tip of the hollow blade. Measurement results in every measuring point were compared for the case with and without internal flows.

3.2.1 Velocity Measurements With Hot-Wire Anemometry. A hot-wire anemometer was used to measure the instantaneous velocity fluctuations, phase average velocities, and turbulence intensity. Measurements were performed in accordance with Bruun [18] and Jørgensen [19].

For measurements with hot-wire anemometry, a Dantec MiniCTA anemometer with wire sensor Dantec 55P11 (diameter of ∅5 μm and length of 1.25 mm) was used. The hot-wire anemometer working temperature was 250°C. The positioning of the hot-wire anemometer sensor on the measurement station allowed measurements of the instantaneous meridian velocity. Positioning of the hot-wire anemometer sensor was performed by using a PC controlled precision positioning device. For the acquisition of the hot-wire anemometer signal, a 16-bit data acquisition board from National Instruments was used. The acquisition frequency was 50 kHz. Prior to analog/digital (A/D) conversion, the output of the hot-wire anemometer was filtered with SCXI module by using low pass fourth order Bessel filter with a frequency of 10 kHz. LABVIEW software was used for data acquisition and storage. Calibration of the hot-wire anemometer was performed on the measuring station for the calibration of anemometers. In accordance with King's law [18], the constants $A=1.9132$, $B=0.8744$, and $n=0.4476$ were determined. Temperature correction was applied during calibration and measurements. Temperature was measured using a Pt-100 class A resistance thermometer with four wire connections and Agilent 34970A instrument. Actual velocity was calculated from the hot-wire anemometer output according to King's law equation [18].

Measurements were performed for both versions with the same measurement equipment, which was calibrated before measurement and were performed immediately one after another. The main sources of the total measurement uncertainty [9,10,17] result from the uncertainty of selecting the operating point and the fluctuations, selecting the starting point of positioning, rotational speed of the fan, calibration, positioning of the hot-wire anemometer sensor with a positioning table, linearization, A/D resolution, data acquisition, temperature correction and humidity, and hot-wire anemometer limited frequency response. The adjustments of the main voltage, fan electric motor temperature variations during measurements, and measurement time uncertainty were selected in accordance with recommendations in Ref. [20]. A separating transformer was used to separate the fan power supply from the measurements' power supply. Overall measuring uncertainty of instantaneous velocity was estimated to be 2.8% of the measured value.

3.2.2 Velocity Vector Measurements With Five-Hole Probe. Average velocity vectors were measured using a five-hole probe and were performed on a measuring station, as shown in Fig. 4. Operating and measuring points are the same as for the hot-wire anemometer measurements and are described in Sec. 3.2. The response time of the five-hole probe is very slow, while the velocity fluctuations in the fan are very rapid; therefore, the method allows only measurement of time-averaged velocity vectors. All velocity fluctuations from periodic blade movements and pressure pulsations are averaged.

Two presumptions were considered for time averaging, i.e., stationary fluid flow, for each selected operating point, and fluid flow on the fan inlet and outlet is axisymmetrical regarding the axis of fan rotation. In order to satisfy the axisymmetrical conditions, large unimpeded inlet and outlet flow fields had to be assured. The measuring station has a straight inlet flow section of $1.5D$ and is selected in accordance with the International Organization for Standardization [15].

United Sensor Co. (New Hamphire, USA) type DA-187 probe was used. The measurement procedure using a five-hole probe

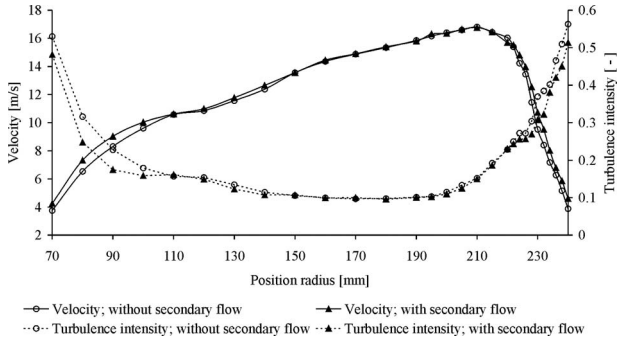

Fig. 5 Average velocity and turbulence intensity in operating point $\varphi_1=0.24$

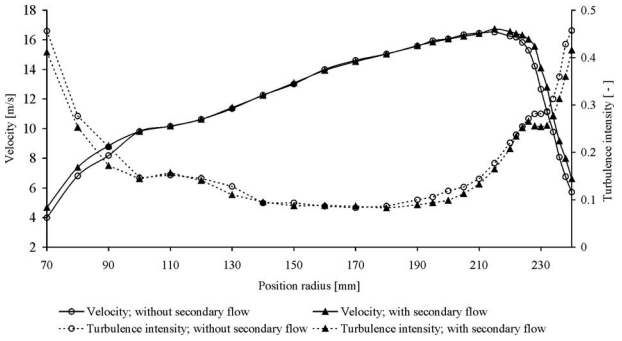

Fig. 7 Average velocity and turbulence intensity in operating point $\varphi_3=0.28$

requires the manual rotation of the probe around its axis until the yaw angle α between the axial and tangential velocities of the flow is reached and the pressure difference on the yaw holes is zero. All later measurement steps are performed automatically by reading the measurement transmitters and using calibration curves provided by the manufacturer. From the absolute velocity c and corresponding angles, axial c_a, tangential u, and radial v_r velocities are calculated.

For differential pressure measurements, a differential pressure transmitter Endress+Hauser Deltabar S PMD75 was used. Absolute pressure was measured with Vaisala PTB 220 while Vaisala HMT 331 transmitter was used for measuring the temperature and relative humidity. Differential pressure transmitters had the current output of 4–20 mA, digitalized with an A/D data acquisition board with 16-bit resolution and sampling frequency of 1 kHz. Sampling data time was 1 min and the measured data from each separate differential pressure transmitter was averaged.

The main sources of the total measurement uncertainty are the uncertainties of the yaw angle measurement [17,21], measurements of ambient conditions, probe positioning, selection of starting position, selection of operating points, velocity and pressure fluctuations, pressure transmitters, data acquisition system, factory calibration curves for five-hole probe, etc. The overall measurement uncertainty was estimated to be 3% for the measurement of velocity and ± 1 deg for the measurement of flow angles.

4 Measurement Results

4.1 Velocity Measurement Results With Hot-Wire Anemometry. Figures 5–7 show the average velocities and turbulence intensities, defined as the ratio between the standard deviation and average velocity for the cases with and without internal flows for three different operating points ($\varphi_1=0.24$, $\varphi_2=0.26$, and $\varphi_3=0.28$). Measurements were performed using a hot-wire anemometer, as described in Sec. 3.2.1. Here, the velocity is equal to the sum of the axial and radial velocities. Measuring points (20) are positioned from the fan hub, at 70 mm from the fan axis, to the fan tip, at 240 mm from the fan axis. The distances between the measuring points are as follows: from 70 mm to 190 mm from the axis with a step of 10 mm, from 190 mm to 220 mm with a step of 5 mm, and from 220 mm to 240 mm with a step of 2 mm (Fig. 4, detail A-A). Measuring points near the tip of the hollow blade are closer to each other in order to better determine the local flow properties in the region where the internal flow exits the blade internal passage.

In Figs. 5–7, a distinctive difference in average velocity and turbulence intensity between the cases with and without internal flow was noticed.

The difference appears on the blade radius from 210 mm to 240 mm due to internal flow exiting from the trailing edge slot at the tip of the hollow blade and mixing with the external flow. In average, about 7.8% increase in velocity and about 9.1% reduction in turbulence intensity was achieved by the introduction of the internal flow. It is interesting that the introduction of the internal flow also resulted in more beneficial conditions near the hub of the fan (from 70 mm to 100 mm). Velocity is increased in the near hub region in average for about 6.9%. Turbulence intensity is reduced in average for 10%. This reduced the generation of vortices near the fan hub, which is usual for this fan type and used method of attachment of the blades to the hub by riveting.

In the middle of the blade, radius velocity remains practically unchanged while the turbulence intensity reduces in average for 4% in the case with internal flow.

In addition, phase average analysis was performed with MATLAB software. Phase average flow velocity was calculated in a way that velocity was cut into sections, corresponding to one fan blade. Signal was cut in accordance to the fan's rotational speed. Results are presented in Fig. 8. Velocity is presented for the operating point of the axial fan at $\varphi_2=0.26$ for cases with and without internal flow. Measuring point at a radius of 228 mm was selected. At this radius, the trailing edge slot is located. The velocity dis-

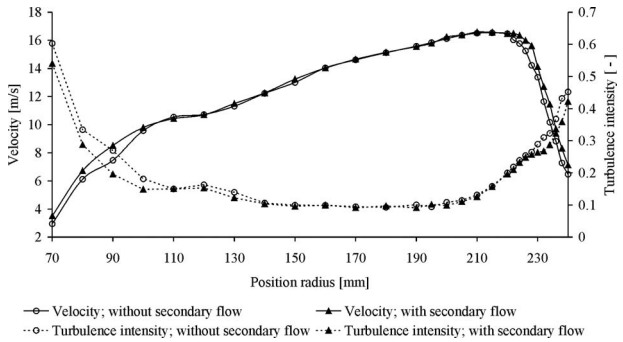

Fig. 6 Average velocity and turbulence intensity in operating point $\varphi_2=0.26$

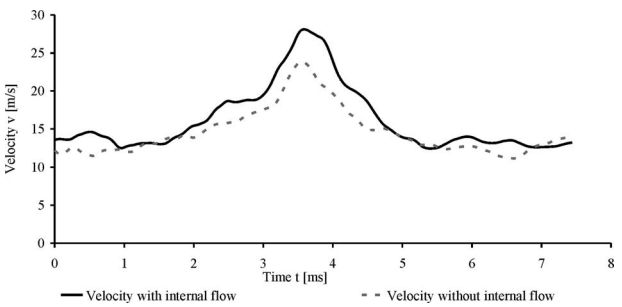

Fig. 8 Phase average of the axial relative velocity field for $\varphi_2=0.26$ and radius of 228 mm

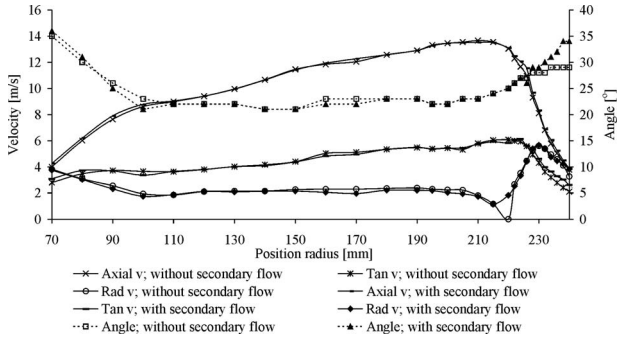

Fig. 9 Axial, tangential, and radial velocities, and yaw angle α for fan operating point $\varphi_1 = 0.24$

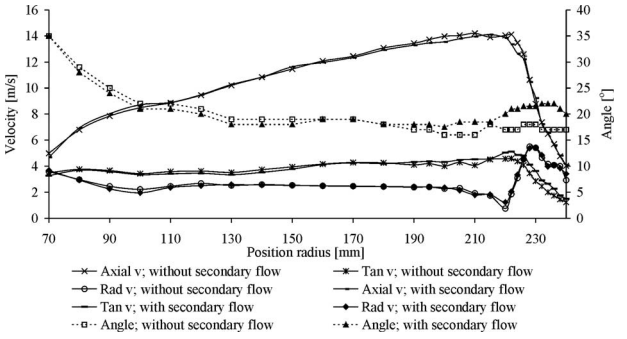

Fig. 11 Axial, tangential, and radial velocities, and yaw angle α for fan operating point $\varphi_3 = 0.28$

tributions for the other two operating points are comparable and are therefore not shown. In the case with internal flow, increased average velocity at the location of the trailing edge of the hollow blade was achieved. The peak of maximum velocity is shifted to the right, which corresponds to higher velocity on the suction side of the hollow blade. Higher velocity on the suction side of the hollow blade shows that the external flow better follows the angle of the hollow blade.

Introduction of the internal flow reduces the turbulence intensity and increases the average velocity in the regions close to the hub and tip of the hollow blade. This occurs because the internal flow adds energy to the external flow and consequently contributes to the preservation of flow direction. As a direct result, flow separation from the blade suction side and thickness of the boundary layer are reduced, which leads to higher fan efficiency.

4.2 Results of Velocity Measurements With Five-Hole Probe. Measurements with a five-hole probe were performed with and without internal flows in the same positions and operating points as measurements with hot-wire anemometry. The description of selecting operating and measuring points can be found in Sec. 4.1. Figures 9–11 present the axial c_a, tangential u, and radial v_r velocities and yaw angle α.

Figures 9–11 show that in the case with internal flow the tangential velocity on the blade trailing edge near the tip of the hollow blade increases in average by 11%. Also, a change in velocity yaw angle α is substantial as it increases to about 10%. Consequently, the flow direction is changed and that the air flow in the case of the internal flow better follows the contour of the fan blade.

When on a radius from 70–100 mm, a 3% reduction in radial velocity and yaw angle α is observed. These changes are a result of flow passing into the internal flow passage. As a consequence, external radial flow reduces.

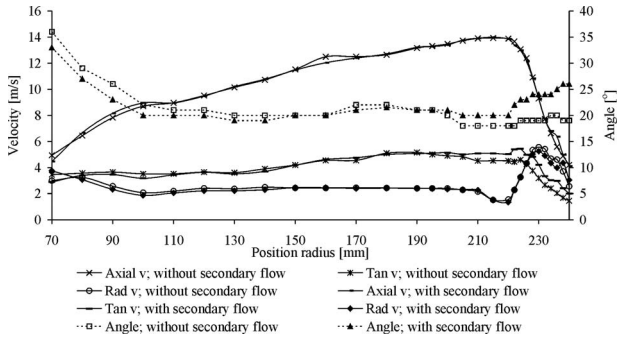

Fig. 10 Axial, tangential, and radial velocities, and yaw angle α for fan operating point $\varphi_2 = 0.26$

In the middle of the blade span (from 100 mm to 200 mm from the axis of the fan), deviations in velocity and yaw angle α are not distinctive.

Results of measurements with a five-hole probe are in agreement with the results obtained by hot-wire anemometry. Both measurements confirm that the introduction of the internal flow influences the flow through the axial fan with hollow blades.

5 Conclusions

This paper presented the introduction of flow through the hollow blades of the axial fan. With the help of different measuring techniques, the effects of the internal flow on the flow field of the hollow blade were determined. As a consequence, increased velocity, reduced turbulence intensity, and more uniform velocity distribution were obtained with the internal flow passing through the hollow blades. It is interesting to know that by introducing the internal flow, more beneficial conditions near the hub of the fan were achieved as well. Velocity increase in the region near the hub is a result of more plausible fluid flow as a part of the external flow, entering the hollow blade internal flow passage. This reduces the generation of vortices near the fan hub, which is usual for this type of fan and for the used method of attaching the blades to the hub by riveting. In the middle of the blade radius, velocity remains practically unchanged while the turbulence intensity reduces in the case with internal flow. Therefore, it is assumed that the external flow field changes and follows the blade contour better; the flow separation near the trailing edge on the suction side at the tip of the hollow blade minimizes. The beneficial influence also reflects in the integral characteristic, where increase in static pressure difference was achieved.

Nomenclature

A = King's law constants
B = King's law constants
c = velocity (m/s)
D = diameter (mm)
f = frequency (Hz)
I = current (A)
n = fan rotation (min^{-1})
n = King's law constants
p = pressure (Pa)
P = power (kW)
u = velocity (m/s)
U = voltage (V)
w = relative velocity (m/s)
q = flow (m^3/h)
v = velocity (m/s)
Δ = difference
α = jaw angle (deg)
β = pitch angle (deg)
η = efficiency

φ = flow coefficient
ρ = air density (kg/m^3)
ξ = loss coefficient
λ = power coefficient
ψ = total pressure coefficient

Subscripts

a = axial
j = internal jet flow pressure
r = radial
s = static
t = total
u = axial component of tangential velocity
v = volume

References

[1] Schlichting, H., 1979, *Boundary-Layer Theory*, Springer, Berlin.
[2] Rhee, S. H., Kim, S. E., Ahn, H., Oh, J., and Kim, H., 2003, "Analysis of a Jet-Controlled High-Lift Hydrofoil With a Flap," Ocean Eng., **30**, pp. 2117–2136.
[3] Garg, V. K., 2002, "Heat Transfer Research on Gas Turbine Airfoils at NASA GRC," Int. J. Heat Fluid Flow, **23**, pp. 109–136.
[4] Murthy, B. N., Deshmukh, N. A., Patwardhan, A. W., and Joshi, J. B., 2007, "Hollow Self-Inducing Impellers: Flow Visualization and CFD Simulation," Chem. Eng. Sci., **62**, pp. 3839–3848.
[5] Sutliff, D. L., Tweedt, D. L., Fite, B. E., and Envia, E., 2002, *Low-Speed Fan Noise Reduction With Trailing Edge Blowing*, Glenn Research Center, Cleveland, OH.
[6] Woodward, R. P., Fite, E. B., and Podboy, G. G., 2007, *Noise Benefits of Rotor Trailing Edge Blowing for a Model Turbofan*, Glenn Research Center, Cleveland, OH.
[7] Batchelor, G. K., 2000, *An Introduction to Fluid Dynamics*, Cambridge University Press, Cambridge.
[8] Hinze, J. O., 1959, *Turbulence: An Introduction to Its Mechanism and Theory*, McGraw-Hill, New York.
[9] Eberlinc, M., Širok, B., and Hočevar, M., 2009, "Experimental Investigation of the Interaction of Two Flows on the Axial Fan Hollow Blades by Flow Visualization and Hot-Wire Anemometry," Exp. Therm. Fluid Sci., **33**(5), pp. 929–937.
[10] Eberlinc, M., Širok, B., Hočevar, M., and Dular, M., 2009, "Numerical and Experimental Investigation of Axial Fan With Trailing Edge Self-Induced Blowing," Forsch. Ingenieurwes., **73**(3), pp. 129–138.
[11] Eberlinc, M., Širok, B., and Hočevar, M., 2009, "Patented Hollow Blades of the Axial Fan With Trailing Edge Self-Induced Blowing," Benthem Science Publishers Recent Patents on Mechanical Engineering, **2**(1), pp. 1–7.
[12] Eberlinc, M., Širok, B., Hočevar, M., and Dular, M., 2009, "Axial Turbine Machine Hollow Blade With Internal and External Flow Field," The Slovenian Intellectual Property Office, Patent No. 22635.
[13] Wallis, R. A., 1983, *Axial Fans and Ducts*, Wiley, New York.
[14] Idelčik, I. E., 1991, *Fluid Dynamics of Industrial Equipment: Flow Distribution Design Methods*, Hemisphere, New York.
[15] International Organization for Standardization, 2007, ISO 5801: 2007: Industrial Fans.
[16] International Organization for Standardization, 2003, ISO 5167: 2003: Measurement of Fluid Flow.
[17] Coleman, H. W., and Steele, W. G., 1989, *Experimentation and Uncertainty Analysis for Engineers*, Wiley, New York.
[18] Bruun, H. H., 1995, *Hot-Wire Anemometry Principles and Signal Analysis*, Oxford University Press, New York.
[19] Jørgensen, F. E., 2005, *How to Measure Turbulence With Hot-wire Anemometers*, Dantec Dynamics, Skovlunde.
[20] Verein Deutscher Ingenieure/Verband Deutscher Elektro-Techniker, 1993, "Netzmessungen in Strömungsquerschitten," Paper No. VDI/VDE 2640.
[21] Gonsalez, J. C., and Arrington, E. A., 1999, *Five-Hole Flow Angle Probe Calibration for the NASA Glenn Icing Research Tunnel*, Dynacs Engineering Company, Inc., Brook Park, OH.

Pressure Drop in Laminar Developing Flow in Noncircular Ducts: A Scaling and Modeling Approach

Y. S. Muzychka
Faculty of Engineering and Applied Science,
Memorial University of Newfoundland,
St. John's, NF, A1B 3X5, Canada

M. M. Yovanovich
Department of Mechanical and Mechatronics Engineering,
University of Waterloo,
Waterloo, ON, N2L 3G1, Canada

A detailed review and analysis of the hydrodynamic characteristics of laminar developing and fully developed flows in noncircular ducts is presented. New models are proposed, which simplify the prediction of the friction factor–Reynolds product f Re for developing and fully developed flows in most noncircular duct geometries found in heat exchanger applications. By means of scaling analysis it is shown that complete problem may be easily analyzed by combining the asymptotic results for the short and long ducts. Through the introduction of a new characteristic length scale, the square root of cross-sectional area, the effect of duct shape has been minimized. The new model has an accuracy of ±10% or better for most common duct shapes when nominal aspect ratios are used, and ±3% or better when effective aspect ratios are used. Both singly and doubly connected ducts are considered. [DOI: 10.1115/1.4000377]

Keywords: laminar flow, noncircular ducts, hydrodynamic entrance length, developing flow, modeling, pressure drop

1 Introduction

Laminar flow fluid friction and heat transfer in noncircular ducts occur quite frequently in low Reynolds number flow heat exchangers such as automotive coolers, cold plates, and microchannel heat sinks. It is now also occurring more frequently in a host of other energy conversion and reclamation devices, as a result of the miniaturization of modern technologies. While traditional approaches have relied heavily on the use of tabulated and/or graphical data, the ability to design thermal systems using robust models is much more desirable in the age of computer simulations and computer assisted design. Most modern fluid dynamics and heat transfer texts rarely present correlations or models for more complex geometries, which appear in many engineering systems. Rather, a subset of data for miscellaneous geometries is usually presented after detailed discussion and analysis of simple geometries such as the circular duct and parallel plate channel.

In the present paper, the hydrodynamic problem is considered in detail, and a new and much simpler model is developed for predicting the friction factor–Reynolds number product for developing laminar flow in noncircular ducts.

Laminar fully developed fluid flow in noncircular ducts of constant cross-sectional area results when the duct length L is sufficiently greater than the hydrodynamic entrance length L_h, i.e., $L \gg L_h$, or when the characteristic transversal scale is sufficiently small to ensure a very small Reynolds number. Under these conditions the flow through most of the duct or channel may be considered fully developed. However, in many engineering systems such as compact heat exchangers and microcoolers used in electronics packaging, while the characteristic dimension of the flow channel is small enough to give rise to laminar flow conditions, the flow length is generally not sufficiently large enough to give rise to fully developed flow, i.e., $L \sim L_h$ or $L \ll L_h$, and developing flow prevails over most of the duct length. In these situations, a model capable of predicting the hydrodynamic characteristic, usually denoted as f Re, the friction factor–Reynolds number product as a function of dimensionless duct length, is required.

Since the pressure drop in a developing flow is due to both wall shear and fluid acceleration, some references choose to denote it as the *apparent* friction factor–Reynolds number product f_{app} Re, in order to distinguish it from the fully developed flow value f Re. However, since dimensionless pressure drop or f_{app} Re in the entrance region transitions smoothly to f Re in fully developed flow, this distinction is dropped in favor of just f Re, which is implied to vary with dimensionless duct length, i.e., $f\,\text{Re}(L^+)$, where L^+ is the dimensionless duct length to be defined shortly.

2 Literature Review

A review of literature reveals that only two significant attempts at developing a general model have been undertaken. These are the work of Shah [1] and Yilmaz [2]. Both of these models are based on the earlier work of Bender [3]. Bender [3] combined the asymptotic result for a "short" duct [4], with the result for the "long" duct, to provide a model that is valid over the entire length of a circular duct. The demarcation between short and long being the duct length relative to the hydrodynamic entrance length as shown in Fig. 1, i.e.,

$$f\,\text{Re}_{D_h} = \begin{cases} \dfrac{3.44}{\sqrt{L^+}}, & L^+ < 0.001 \\ (f\,\text{Re})_{\text{fd}} + \dfrac{K_\infty}{4L^+}, & L^+ > 0.1 \end{cases} \tag{1}$$

where

$$L^+ = \frac{L/D_h}{\text{Re}_{D_h}} \tag{2}$$

is the dimensionless duct length.

As such, this formulation requires the use of the concept of the incremental pressure drop factor K_∞. Shah [1] later extended the model of Bender [3] to predict results for the equilateral triangle,

Contributed by the Fluids Engineering Division of ASME for publication in the JOURNAL OF FLUIDS ENGINEERING. Manuscript received March 19, 2009; final manuscript received September 23, 2009; published online October 27, 2009. Editor: Joseph Katz.

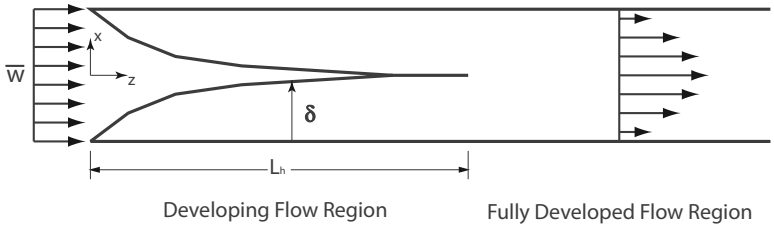

Fig. 1 Hydrodynamic entrance problem

the circular annulus, the rectangular duct, and parallel plate channel geometries. Shah [1] achieved this by generalizing the form of the model of Bender [3], and by tabulating coefficients for each particular geometry for a number of channel and annulus aspect ratios using

$$f\,\mathrm{Re}_{D_h} = \frac{3.44}{\sqrt{L^+}} + \frac{(f\,\mathrm{Re})_{\mathrm{fd}} + K_\infty/4L^+ - 3.44/\sqrt{L^+}}{1 + C/(L^+)^2} \tag{3}$$

Yilmaz [2] proposed a more general model of Shah [1]. Rather than tabulating coefficients, Yilmaz [2] developed a complex correlation scheme for the fully developed friction factor $(f\,\mathrm{Re})_{\mathrm{fd}}$, the incremental pressure drop K_∞, and a fitting coefficient C, which appears in the Shah [1] model. This model is more general than that of Shah [1] but is also quite complex since a base correlation has been augmented with three additional correlations.

Despite its complexity, the model of Yilmaz [2] is accurate over the entire range of the entrance and fully developed regions for many duct cross sections. The primary drawback of the simple model proposed by Shah [1] is the requirement of tabulated coefficients and parameters for each geometry, i.e., $(f\,\mathrm{Re})_{\mathrm{fd}}$, K_∞, and C, thus limiting interpolation for geometries such as the rectangular duct and circular annulus, whose solution varies with aspect ratio. In the case of the model developed by Yilmaz [2], interpolation is no longer a problem; however, this is achieved at the cost of simplicity.

The two models discussed above represent the current state of the art for internal flow problems. Both models are based on the combination of the short duct and long duct solutions using the correlating method of Bender [3]. In this approach the incremental pressure drop factor K_∞ is required in the long duct solution (see Eq. (1)). As a result of the complex correlating equations for K_∞ developed by Yilmaz [2], the simple physical behavior of the hydrodynamic entrance problem is lost. In both cases, however, the models are based on the proposed form put forth by Bender [3]. Unfortunately, this form of correlation is more complicated than need be for this problem. It was formulated as a nonlinear superposition of two asymptotes. However, only one of these asymptotes is a true asymptote. The other asymptote represents a transitional one, which contains the true fully developed asymptote. As such, the model introduces the incremental pressure drop, which is not actually required. It is apparent from the available data that smooth transition occurs from the entrance region to that of fully developed flow.

Since the solution obtained by Shapiro et al. [4] accounts for the increase in momentum of the accelerating core and the wall shear, the use of the term K_∞ in a hydrodynamic entrance model such as that proposed by Bender [3] is redundant. The model presented in this paper does not require this parameter and is significantly simpler in composition.

3 Governing Equations

The governing equations for steady incompressible flow in the hydrodynamic entrance region in a noncircular duct or channel are

$$\nabla \cdot \vec{V} = 0 \tag{4}$$

and

$$\rho \vec{V} \cdot \nabla \vec{V} = -\nabla p + \mu \nabla^2 \vec{V} \tag{5}$$

Simultaneous solution to the continuity, Eq. (4), and momentum, Eq. (5), equations subject to the no slip condition at the duct wall, $\vec{V}=0$, the boundedness condition along the duct axis, $\vec{V} \neq \infty$, and a constant initial velocity, $\vec{V}=U\vec{k}$, is required to characterize the flow. However, most available data are a result of solution to a much simpler set of equations, which result from boundary layer type assumptions [4].

In the case of cross sections that can be characterized by a single variable, these yield the continuity equation and momentum equation in the direction of the flow, i.e., the z-momentum equation. For two dimensional cross sections, an additional closure equation is required for relating transverse velocity components. Additional discussion on special issues pertaining to the solution of this problem is discussed in Ref. [4].

In Sec. 4, scaling analysis is used to show the appropriate form of the solution for both short and long ducts. Later, asymptotic analysis is used to develop a new model. Several of the duct shapes of interest are shown in Fig. 2.

Solutions to Eqs. (4) and (5) have been obtained using a host of methods including finite difference methods, variational methods, integral methods, and theoretical approaches, which ultimately require some form of numerical method. A simple modeling approach is presented, which predicts that all of the available data are now developed.

4 Scale Analysis

We now examine the momentum equation and consider the various force balances implied under particular flow conditions. The momentum equation represents a balance of three forces: inertia, pressure, and friction, i.e.,

$$\underbrace{\rho \vec{V} \cdot \nabla \vec{V}}_{\text{inertia}} = \underbrace{-\nabla p}_{\text{pressure}} + \underbrace{\mu \nabla^2 \vec{V}}_{\text{friction}} \tag{6}$$

Geometry	Shape	P/√A
Rectangle	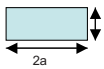	$\frac{2(\varepsilon+1)}{\sqrt{\varepsilon}}$
Ellipse		$\frac{4E(\varepsilon')}{\sqrt{\pi\varepsilon}}$
Annulus	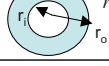	$\frac{2\sqrt{\pi}(1+r^*)}{\sqrt{(1-r^{*2})}}$
Polygons		$2\sqrt{N}\left(\tanh\left(\frac{\pi}{N}\right)\right)^{1/2}$
Isosceles Triangle	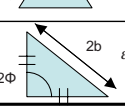	$\frac{2/\cos\phi + 2\tan\phi}{\sqrt{\tan\phi}}$

Fig. 2 Common duct shapes

We now consider three separate force balances. Each is examined below using the method of scale analysis advocated by Bejan [5]. Using Fig. 1 as a starting point, we will examine the various force balances implied by Eq. (5) in the two regions divided by L_h.

4.1 Long Duct Asymptote, $L \gg L_h$. Fully developed laminar flow in a duct of arbitrary, but constant cross section, is governed by the Poisson equation

$$\underbrace{\nabla p}_{\text{pressure}} = \underbrace{\mu \nabla^2 \vec{V}}_{\text{friction}} \tag{7}$$

which represents a balance between the friction and pressure forces. Thus we may write the following approximate relation using the characteristics of the flow and the geometry:

$$\frac{\Delta p}{L} \sim \mu \frac{U}{\mathcal{L}^2} \tag{8}$$

where $\mathcal{L}$ represents a characteristic transversal length scale of the duct cross section. The velocity scales according to the area mean value U, and the axial length scales according to L. Rearranging the above expression gives

$$\Delta p \sim \frac{\mu U L}{\mathcal{L}^2} \tag{9}$$

Next, we examine the shear stress at the wall. The shear stress may be approximated by

$$\vec{\tau} = \mu \nabla \vec{V} \sim \mu \frac{U}{\mathcal{L}} \tag{10}$$

Next, we may introduce the definition of the friction factor, defined as the dimensionless wall shear

$$f \sim \frac{\tau}{\rho U^2} \sim \frac{\mu U/\mathcal{L}}{\rho U^2} \sim \frac{1}{\mathrm{Re}_{\mathcal{L}}} \tag{11}$$

The above expression may be written such that the following relationship exists for all cross-sectional geometries:

$$f\,\mathrm{Re}_{\mathcal{L}} \sim \frac{\tau \mathcal{L}}{\mu U} \sim \mathcal{O}(1) \tag{12}$$

or

$$f\,\mathrm{Re}_{\mathcal{L}} = C_1 \tag{13}$$

Equation (12) is often denoted as the Poiseuille number Po in modern literature, such that $f\,\mathrm{Re}_{\mathcal{L}} = 2\,\mathrm{Po}_{\mathcal{L}}$. The factor of 2 results from the use of the kinetic or dynamic pressure in Eq. (11), i.e., $\frac{1}{2}\rho U^2$, which is omitted in the scaling analysis. The constant C_1 has been found to vary for most geometries in the range $12 < C_1 < 24$, when $\mathcal{L} = D_h$.

Finally, a control volume force balance gives

$$\tau = \frac{\Delta p}{L}\frac{A}{P} \tag{14}$$

and yields the following relationship when combined with the two scaling laws, Eqs. (10) and (14):

$$\mathcal{L} \sim \frac{A}{P} \sim \frac{D_h}{4} \tag{15}$$

We shall see later that this length scale, which results from the force balance, although convenient, is not the most appropriate choice. As a length scale it is fundamentally important in the relationship of Eq. (14), but this by no means implies necessity of its use in Eq. (12). Equation (12) represents a dimensionless mean wall shear, which gives us freedom to choose $\mathcal{L}$. It is in this definition that the appropriate choice of a characteristic length scale must be carefully considered.

4.2 Short Duct Asymptote, $L \ll L_h$. In the entrance region near the duct inlet two regions must be considered. One is the inviscid core and the other the viscous boundary layer. The flow within the boundary layer is very similar to laminar boundary layer development over a flat plate, except that the velocity at the edge of the boundary layer is no longer constant in the duct flow. The two regions are now examined beginning with the flow within the boundary layer.

The force balance within the boundary layer is governed strictly by inertia and friction forces

$$\underbrace{\rho \vec{V} \cdot \nabla \vec{V}}_{\text{inertia}} = \underbrace{\mu \nabla^2 \vec{V}}_{\text{friction}} \tag{16}$$

This balance yields

$$\rho \frac{U^2}{L} \sim \mu \frac{U}{\delta^2} \tag{17}$$

where δ is the boundary layer thickness (see Fig. 1). Thus,

$$\frac{\delta}{L} \sim \frac{1}{\sqrt{\mathrm{Re}_L}} \tag{18}$$

Although the flow in a confined channel is markedly different from that of a plate in streaming flow, both experience boundary layer growth, which is inversely proportional to the Reynolds number. The major distinction, as we shall see is the rate at which the boundary layer grows within a confined channel, is much slower than a plate in streaming flow, due to a favorable pressure gradient. Introducing the transversal length scale $\mathcal{L}$ we obtain

$$\frac{\delta}{\mathcal{L}} \sim \sqrt{\frac{L}{\mathcal{L}\,\mathrm{Re}_{\mathcal{L}}}} \sim \sqrt{L^+} \tag{19}$$

where L^+ is the dimensionless duct length defined by

$$L^+ = \frac{L}{\mathcal{L}\,\mathrm{Re}_{\mathcal{L}}} \tag{20}$$

Next, considering the relationship for the wall shear

$$\vec{\tau} = \mu \nabla \vec{V} \sim \mu \frac{U}{\delta} \tag{21}$$

and the friction factor, we obtain

$$f \sim \frac{\tau}{\rho U^2} \sim \frac{\mu U/\delta}{\rho U^2} \sim \frac{\mu \sqrt{\mathrm{Re}_L}}{\rho U L} \sim \frac{1}{\sqrt{\mathrm{Re}_L}} \tag{22}$$

Rewriting the above expression in terms of the length scale $\mathcal{L}$, and defining the product of friction factor and Reynolds number yield the following expression for the entrance region:

$$f\,\mathrm{Re}_{\mathcal{L}} \sim \frac{\mathcal{O}(1)}{\sqrt{L^+}} \tag{23}$$

or

$$f\,\mathrm{Re}_{\mathcal{L}} = \frac{C_2}{\sqrt{L^+}} \tag{24}$$

Equation (19) illustrates an important point highlighted by Bejan [5], that hydrodynamically developing flows should be presented as a function of $\sqrt{L^+}$ rather than L^+, since the effective wall shear is inversely proportional to δ and hence a function of $\sqrt{L^+}$ as shown in Eq. (24).

Finally, in the inviscid core, the momentum equation represents a balance of inertia and pressure forces

$$\underbrace{\rho \vec{V} \cdot \nabla \vec{V}}_{\text{inertia}} = \underbrace{-\nabla p}_{\text{pressure}} \tag{25}$$

which scales according to

$$\rho U^2 \sim \Delta p \tag{26}$$

Since the boundary layer in the developing region will be thinner under a favorable pressure gradient in the core, the constant in Eq. (24) will be much larger than the value obtained for friction in a boundary layer flow over an isolated flat plate in streaming flow. The constant C_2 has been found theoretically by Siegel [6] for the circular duct to be $C_2=3.44$ for a mean friction factor and $C_2=1.72$ for a local friction factor. For an isolated plate in streaming flow, these are $C_2=1.328$ and $C_2=0.664$, respectively. As will be seen shortly, the boundary layer develops over a length four times greater than that predicted by the simple Blasius theory. Thus it is reasonable to expect that the friction factor would be greater by approximately the same value, given the inverse dependency of f on δ. In this case it is approximately 2.6 times greater.

In summary, we have found from scaling analysis the following relationships for the friction factor–Reynolds number product:

$$f\,\mathrm{Re}_{\mathcal{L}}=\begin{cases} C_1, & L \gg L_h \\ \dfrac{C_2}{\sqrt{L^+}}, & L \ll L_h \end{cases} \tag{27}$$

This asymptotic behavior will be examined further and will form the basis for the new model developed for the hydrodynamic entrance problem, once the exact limits are formulated.

4.3 Hydrodynamic Entrance Lengths. The entrance length is traditionally defined as the point downstream of the inlet, where the centerline velocity is 99% of the maximum velocity. This measure of the development region is also utilized in the selection of an appropriate heat transfer model as well as ascertaining which type of friction model be utilized for pressure drop calculations. One may easily get an estimate for the entrance length using simple boundary layer theory.

If the entrance length is used as a criterion to measure the extent of the boundary layer region, then we shall refer to a *short duct* and *long duct* in the following manner:

$$L \ll L_h \quad \text{short duct}$$

$$L \gg L_h \quad \text{long duct} \tag{28}$$

We use the much greater and much less than notation, since a channel flow, which only marginally satisfies the entrance length criteria, i.e., $L \sim L_h$, experiences a significantly higher pressure drop than a fully developed flow. Care must be taken to ensure that fully developed flow prevails over most of a duct or channel. Merely stating that $L > L_h$ is not strictly valid for making an assumption of fully developed flow.

If we consider a simple channel formed by two plates separated by $2b$, the boundary layers on each plate in laminar flow will merge at a point $z \sim L_h$ downstream, when their thickness is of order of the half plate separation

$$\delta = \frac{5z}{\sqrt{\mathrm{Re}_z}} \sim b \tag{29}$$

or

$$L_h \sim 0.0025 D_h\,\mathrm{Re}_{D_h} \tag{30}$$

after introducing $D_h=4b$ for the channel. This estimate is much shorter than the actual length in a channel flow, as the favorable pressure gradient in the inviscid core leads to much slower boundary layer development than the case for Blasius flow. The actual solution for a channel is given by [4]

$$L_h \sim 0.011 D_h\,\mathrm{Re}_{D_h} \tag{31}$$

which is approximately four times greater. Thus, given that the boundary layer develops more slowly in a channel flow, we easily see from Eqs. (19), (21), and (24) that the constant $C_2 > 1.328$, owing to the acceleration within the inviscid core.

Depending on the channel or duct shape, the entrance length may be written more generally as

$$L_h = C_{0,D_h} D_h\,\mathrm{Re}_{D_h} \tag{32}$$

where C_{0,D_h} varies weakly with duct shape. It typically has an order of magnitude $0.01 < C_{0,D_h} < 0.06$, when $\mathcal{L}=D_h$.

A simple equation relating the approximate magnitude of the hydrodynamic entrance length may be obtained using scaling analysis, by considering an equality between the two asymptotic limits given in Eq. (27) when $L^+=L_h^+$,

$$C_1 = \frac{C_2}{\sqrt{L_h^+}} \tag{33}$$

or

$$L_h^+ = \left(\frac{C_2}{C_1}\right)^2 \sim C_{0,\mathcal{L}} \tag{34}$$

Later, it will be shown that this approximate scaling result compares well with more exact solutions. This solution represents the intersection of the asymptotic limits on a plot of the complete behavior of f Re versus L^+, whereas the traditional entrance length is defined on the basis of the centerline velocity.

4.4 Length Scales and Slenderness. One issue that has not been adequately addressed in literature is the selection of an appropriate characteristic length scale, i.e., $\mathcal{L}$. Traditionally, the hydraulic diameter has been chosen, $\mathcal{L}=4A/P$. However, in many texts, its use in laminar flow has been questioned [7–9]. In an earlier work [10], the authors addressed this issue using dimensional analysis. It was determined that the widely used concept of the hydraulic diameter was inappropriate for laminar flow and the authors proposed using $\mathcal{L}=\sqrt{A}$ as a characteristic length scale, by considering other problems in mathematical physics for which the Poisson equation applies. A more detailed discussion and analysis on the use of $\mathcal{L}=\sqrt{A}$ may be found in Refs. [11,12]. More recently, Duan and Muzychka [13] and Muzychka and Edge [14] showed that the square root of flow area is also more appropriate for nondimensionalizing gaseous slip flows and non-Newtonian flows.

The choice of an appropriate characteristic length, which minimizes the effect of duct shape on the numerical value of the dimensionless friction factor–Reynolds number product, defined by Eq. (13), will now be examined. Given an arbitrary duct of cross-sectional area A, perimeter P, and length L, one can choose several combinations of these generic characteristics to obtain a length scale

$$\mathcal{L} = \frac{4A}{P}, \sqrt{A}, P, L, \sqrt{PL}, (AL)^{1/3} \tag{35}$$

in addition to a host of other possibilities defined using the particular duct or channel dimensions, i.e., semi-axis lengths, etc. In the heat transfer and fluid flow literature the convention is to use the hydraulic diameter $4A/P$ or hydraulic radius $2A/P$. This characteristic length arises naturally from a simple control volume balance on an arbitrarily shaped straight duct, i.e., Eq. (15).

The use of the hydraulic diameter is often considered the most convenient as a result of the relationship defined by Eq. (15). However, when the hydraulic diameter is used, the dimensionless grouping $f\,\mathrm{Re}_{D_h}$ takes on values that vary between 12 and 24 for most common duct shapes. This requires the use of exact values for accurate prediction of the pressure drop. The basis for the use of the hydraulic diameter arose in the modeling of turbulent flows in noncircular ducts. In turbulent flows, the velocity gradient varies only in a region very near the wall and there is deeper penetration of the flow field into re-entrant corners. In a laminar flow the velocity gradient varies over most of the cross-sectional area and flow does not penetrate as deep into re-entrant corners. The result of these two effects is that a mismatch occurs between the true hydraulic equivalent duct and the hydraulic equivalent duct determined by the definition $4A/P$. However, a number of other

deficiencies in the hydraulic diameter concept should be addressed, namely, that the hydraulically equivalent circular area and perimeter based on the hydraulic diameter are not the same as the true area and perimeter of the noncircular duct. This mismatch in area and perimeter is often cited as the probable cause in the mismatch of dimensionless laminar flow data [7].

Other possibilities for $\mathcal{L}$ given above have a number of potential flaws. First, the perimeter and area are not definable for the parallel plate channel. This issue does not pose a problem for singly or doubly connected regions having finite area and perimeter. However, the parallel plate is merely an idealization for low aspect ratio ducts and channels. In principle it exists as a convenient limit; in practice, it is never truly realized. However, if one considers a duct of fixed area, the parallel plate channel is approached as the duct aspect ratio varied such that $a \gg b$, thus physically realizing the situation where $\sqrt{A}$ is a constant, but the duct aspect ratio $\epsilon \to 0$.

The use of perimeter may be considered from the point of view of constant shear stress or preservation of the retarding force and hence the surface area of the duct or channel. That is

$$(\bar{\tau}_w PL)_{\mathrm{nc}} = (\bar{\tau}_w PL)_c \tag{36}$$

If the mean shear stress at the wall is constant, then the following relationship holds:

$$P_{\mathrm{nc}} = P_c \tag{37}$$

and the effective circular diameter becomes

$$D_{\mathrm{eff}} = \frac{P_{\mathrm{nc}}}{\pi} \tag{38}$$

In other words, the characteristic length $\mathcal{L} = P \propto D_{\mathrm{eff}}$.

Finally, it may also be argued on physical grounds that the square root of the flow area is essentially the same as preserving the cross-sectional duct area or maintaining a constant mass flux. That is

$$(\rho \bar{w} A)_c = (\rho \bar{w} A)_{\mathrm{nc}} \tag{39}$$

Now if both the circular and noncircular ducts have the same mass flux $G = \rho \bar{w}$ then

$$A_c = A_{\mathrm{nc}} \tag{40}$$

and the effective circular diameter becomes

$$D_{\mathrm{eff}} = \sqrt{\frac{4A_{\mathrm{nc}}}{\pi}} \tag{41}$$

In other words, the characteristic length $\mathcal{L} = \sqrt{A} \propto D_{\mathrm{eff}}$.

It has been shown in Ref. [11] that $\mathcal{L} = \sqrt{A}$ succeeds in bringing the dimensionless results closer together for similar ducts, i.e., rectangular and elliptical or polygonal [10–14]. In all cases, better correlation of the laminar flow data was achieved versus an appropriate measure of duct slenderness, allowing a single approximate expression to be used for many duct shapes.

Finally, since it has been established that $\mathcal{L} = \sqrt{A}$ is more appropriate than the hydraulic diameter, we should consider its effect on the dimensionless duct length L^+. Using Eq. (20) we may write either

$$L^+ = \frac{L/D_h}{\mathrm{Re}_{D_h}} = \frac{\mu L P^2}{16 \dot{m} A} \tag{42}$$

or

$$L^+ = \frac{L/\sqrt{A}}{\mathrm{Re}_{\sqrt{A}}} = \frac{\mu L}{\dot{m}} \tag{43}$$

Clearly, Eq. (43) is more appropriate as it does not contain the transverse length scale. It is more fundamental than Eq. (42), since it contains only the mass flow rate, the viscosity, and the duct length.

Table 1 Definitions of aspect ratio

Geometry	Aspect ratio
Regular polygons	$\epsilon \approx 1$
Rectangle and ellipse	$\epsilon \approx \frac{b}{a}$
Miscellaneous shapes	$\epsilon \approx \frac{\ell_{\mathrm{short}}}{\ell_{\mathrm{long}}}$
Trapezoid	$\epsilon \approx \begin{cases} \frac{2h}{b_1+b_2}, & h < (b_1+b_2)/2 \\ \frac{b_1+b_2}{2h}, & h > (b_1+b_2)/2 \end{cases}$
Isosceles triangle	$\epsilon \approx \begin{cases} h/b & h < b \\ b/h & h > b \end{cases}$
Annular sector	$\epsilon \approx \frac{1-r^*}{(1+r^*)\Phi}$
Circular annulus	$\epsilon \approx \frac{(1-r^*)}{\pi(1+r^*)}$
Eccentric annulus	$\epsilon \approx \frac{(1+e^*)(1-r^*)}{\pi(1+r^*)}$

The measure of a duct's slenderness can be easily defined for most simple shapes. If we consider the rectangular and elliptical ducts, a simple measure of slenderness is the ratio of the minor and major axes. In the case of triangular ducts, a measure of slenderness may defined as the ratio of base to height or height to base, i.e.,

$$\epsilon \approx \frac{\ell_{\mathrm{short}}}{\ell_{\mathrm{long}}} \tag{44}$$

such that a simple intrinsic value falling in the range $0 < \epsilon < 1$ is obtained. However, even this simple measure requires some additional attention for ducts with small re-entrant corners.

In the case of the concentric annular duct, a simple measure of its proportions is traditionally the ratio of inner and outer radii. This measure is not compatible with that of most other shapes we consider, as slenderness is a combination of transverse lengths scales, while the radii ratio is a combination of parallel length scales. This issue can be overcome by defining a simple measure of slenderness

$$\epsilon \approx \frac{1-r^\star}{\pi(1+r^\star)} \tag{45}$$

This definition results from preserving the wall to wall spacing and defining a transverse length scale based on a rectangular duct of equivalent area. The issue becomes more complicated if one or both of the bounding ducts are polygons. But can be overcome if one defines

$$\epsilon \approx \frac{1-\sqrt{A_i/A_o}}{\pi(1+\sqrt{A_i/A_o})} \tag{46}$$

where A_i and A_o are the areas of the inner and outer polygons. The above formula is merely a generalized form where $\sqrt{A_i/A_o} = r^\star$ for the concentric annulus.

A summary of the nominal aspect ratios of typical ducts is given in Table 1.

5 Asymptotic Analysis

In this section, asymptotic analysis [15] is used to establish expressions for the characteristic long duct and short duct behaviors established through scaling analysis. First, the long duct limit is considered and a simple expression developed for predicting the constant $f\,\mathrm{Re}=C_1$. Additionally, the issue of an appropriate characteristic length scale is addressed and comparisons are made for both the hydraulic diameter D_h and square root of cross-sectional area $\sqrt{A}$ as characteristic length scales. Finally, the short duct limit is considered by re-examining the approximate solution obtained by Siegel [6] and Shapiro et al. [16].

5.1 Long Duct Asymptote, $L \gg L_h$. In order to establish the long duct limit, solutions for many ducts are examined. These solutions have been cataloged in Refs. [4,17]. The simplest duct shapes are the circular duct and the parallel plate channel. These important shapes also appear as limits in the elliptical duct, the rectangular duct, and the circular annulus.

We now examine a number of important results employing both $\mathcal{L}=4A/P$ and $\mathcal{L}=\sqrt{A}$. Starting with the *elliptical duct*, the dimensionless average wall shear is found to be [4]

$$f\,\mathrm{Re}_{D_h}=\frac{2\pi^2(1+\epsilon^2)}{\mathbf{E}(\epsilon')^2} \tag{47}$$

where $\epsilon=b/a$, the ratio of minor and major axes, and $\epsilon'=\sqrt{1-\epsilon^2}$. Equation (47) has the following limits:

$$f\,\mathrm{Re}_{D_h}=\begin{cases}16, & \epsilon\to 1\\ 19.76, & \epsilon\to 0\end{cases} \tag{48}$$

If the solution is recast using $\mathcal{L}=\sqrt{A}$, as a characteristic length scale, the following relationship is obtained:

$$f\,\mathrm{Re}_{\sqrt{A}}=\frac{2\pi^{3/2}(1+\epsilon^2)}{\sqrt{\epsilon}\mathbf{E}(\epsilon')} \tag{49}$$

Equation (49) now has the following limits:

$$f\,\mathrm{Re}_{\sqrt{A}}=\begin{cases}8\sqrt{\pi}\approx 14.18, & \epsilon\to 1\\ \dfrac{2\pi^{3/2}}{\sqrt{\epsilon}}\approx\dfrac{11.14}{\sqrt{\epsilon}}, & \epsilon\to 0\end{cases} \tag{50}$$

Next, we examine the *rectangular duct*. The solution for the dimensionless average wall shear [4], considering only the first term of the series, gives

$$f\,\mathrm{Re}_{D_h}=\frac{24}{(1+\epsilon)^2\left[1-\dfrac{192\epsilon}{\pi^5}\tanh\left(\dfrac{\pi}{2\epsilon}\right)\right]} \tag{51}$$

Equation (51) has the following limits:

$$f\,\mathrm{Re}_{D_h}=\begin{cases}14.13, & \epsilon\to 1\\ 24, & \epsilon\to 0\end{cases} \tag{52}$$

Examination of the single term solution reveals that the greatest error occurs when $\epsilon=1$, which gives a $f\,\mathrm{Re}$ value 0.7% below the exact value of $f\,\mathrm{Re}=14.23$. The results for a wide range of aspect ratios are tabulated in Ref. [4] using a 30 term series, which provided 7 digit precision. A sample is provided in Table 2 for comparison with the simpler one term approximation.

If the solution is recast using $\mathcal{L}=\sqrt{A}$, as a characteristic length scale, the following expression is obtained:

$$f\,\mathrm{Re}_{\sqrt{A}}=\frac{12}{\sqrt{\epsilon}(1+\epsilon)\left[1-\dfrac{192\epsilon}{\pi^5}\tanh\left(\dfrac{\pi}{2\epsilon}\right)\right]} \tag{53}$$

Equation (53) now has the following limits:

Table 2 Comparison of single term approximation for $f\,\mathrm{Re}$

	$f\,\mathrm{Re}_{D_h}$		$f\,\mathrm{Re}_{\sqrt{A}}$		
$\epsilon=b/a$	Exact	Equation (51)	Exact	Equation (53)	$12/\sqrt{\epsilon}$
0.001	23.97	23.97	379.33	379.33	379.47
0.01	23.68	23.68	119.56	119.56	120.00
0.05	22.48	22.47	52.77	52.77	53.66
0.1	21.17	21.16	36.82	36.81	37.95
0.2	19.07	19.06	25.59	25.57	26.83
0.3	17.51	17.49	20.78	20.76	21.91
0.4	16.37	16.34	18.12	18.09	18.97
0.5	15.55	15.51	16.49	16.46	16.97
0.6	14.98	14.94	15.47	15.43	15.49
0.7	14.61	14.55	14.84	14.79	14.34
0.8	14.38	14.31	14.47	14.40	13.42
0.9	14.26	14.18	14.28	14.20	12.65
1	14.23	14.13	14.23	14.13	12.00

$$f\,\mathrm{Re}_{\sqrt{A}}=\begin{cases}14.13, & \epsilon\to 1\\ \dfrac{12}{\sqrt{\epsilon}}, & \epsilon\to 0\end{cases} \tag{54}$$

Table 2 presents a comparison of the exact values [4] with the single term approximation, Eqs. (51) and (53) for both characteristic length scales. Also presented are values that result from using the asymptotic solution for the parallel plate channel. Clearly, this asymptotic result does an adequate job of predicting the values of $f\,\mathrm{Re}_{\sqrt{A}}$ up to $\epsilon=0.7$. Beyond this aspect ratio, very little change is observed in the $f\,\mathrm{Re}$ values.

Next, a comparison is made between the elliptical and rectangular duct solutions. It is now apparent that the solutions for the circular duct and square duct have essentially collapsed to a single value, Eqs. (50) and (54). Further, in the limit of small aspect ratio, the results for the elliptic duct and the rectangular duct have also come closer together, Eqs. (50) and (54). It is also clear from this analysis that the square root of cross-sectional area is more appropriate than the hydraulic diameter for nondimensionalizing the laminar flow data. As seen in Table 3, the maximum difference between the values for $f\,\mathrm{Re}$ occur in the limit of $\epsilon\to 0$. Comparison of Eqs. (49) and (53) shows that this difference is only 7.7%. Thus, we may use the simpler expression, Eq. (53), to compute values for the elliptical duct. This way, the elliptic integral in Eq. (49) need not be evaluated.

The results for several other flat duct geometries are shown in Figs. 3 and 4. Excellent correlation is achieved with the single term solution for the rectangular duct, merely resulting from a

Table 3 $f\,\mathrm{Re}$ results for elliptical and rectangular geometries [4]

	$f\,\mathrm{Re}_{D_h}$			$f\,\mathrm{Re}_{\sqrt{A}}$		
$\epsilon=b/a$	Rectangular	Elliptical	$\dfrac{f\,\mathrm{Re}^R}{f\,\mathrm{Re}^E}$	Rectangular	Elliptical	$\dfrac{f\,\mathrm{Re}^R}{f\,\mathrm{Re}^E}$
0.01	23.67	19.73	1.200	119.56	111.35	1.074
0.05	22.48	19.60	1.147	52.77	49.69	1.062
0.10	21.17	19.31	1.096	36.82	35.01	1.052
0.20	19.07	18.60	1.025	25.59	24.65	1.038
0.30	17.51	17.90	0.978	20.78	20.21	1.028
0.40	16.37	17.29	0.947	18.12	17.75	1.021
0.50	15.55	16.82	0.924	16.49	16.26	1.014
0.60	14.98	16.48	0.909	15.47	15.32	1.010
0.70	14.61	16.24	0.900	14.84	14.74	1.007
0.80	14.38	16.10	0.893	14.47	14.40	1.005
0.90	14.26	16.02	0.890	14.28	14.23	1.004
1.00	14.23	16.00	0.889	14.23	14.18	1.004

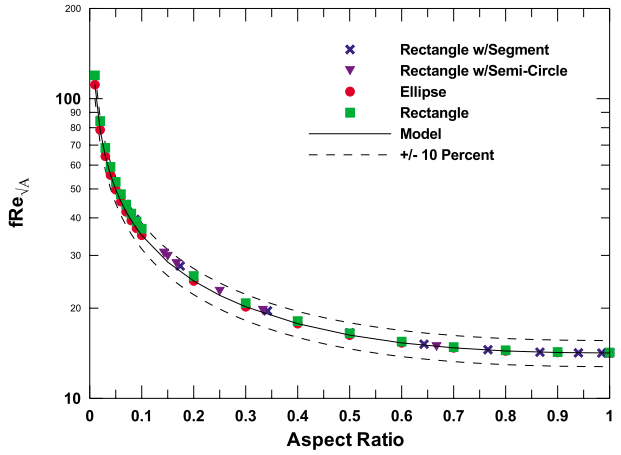

Fig. 3 $f\,\mathrm{Re}_{\sqrt{A}}$ **for regular flat ducts, data from Ref. [4]**

change in the characteristic length scale. In addition to the change in characteristic length scale, the appropriate aspect ratio as a measure of duct slenderness is also used. These are given in Table 1 and result from the intuitive definition of Eq. (44).

Next, we consider the regular polygons, which are essentially ducts of unity aspect ratio, a result of their ability to be circumscribed by the circular duct. Values for $f\,\mathrm{Re}_{D_h}$ fall in the range $13.33 \le f\,\mathrm{Re}_{D_h} \le 16$ for $3 \le N \le \infty$. The relative difference between the triangular and the circular ducts is approximately 16.7%. When the characteristic length scale is changed to $\mathcal{L} = \sqrt{A}$, the relative difference is reduced to 7.1% for the equilateral triangle, and less than 0.1% for the remaining polygons. The results are summarized in Table 4.

Finally we examine some simple doubly connected regions. The solution for a *concentric annular duct* is easily found in polar coordinates, and contains both the circular duct limit and the parallel plate channel limit. The solution for an annulus with inner radius r_i and outer radius r_i, such that $r^\star = r_i/r_o$, is found in most elementary fluids' texts as follows:

$$f\,\mathrm{Re}_{D_h} = \frac{16(1-r^\star)^2}{1+r^{\star 2}-(1-r^{\star 2})/\ln(1/r^\star)} \tag{55}$$

Equation (55) has the following limits:

$$f\,\mathrm{Re}_{D_h} = \begin{cases} 16, & r^\star \to 0 \\ 24, & r^\star \to 1 \end{cases} \tag{56}$$

Table 4 $f\,\mathrm{Re}$ **results for polygonal geometries [4]**

N	$f\,\mathrm{Re}_{D_h}$	$\frac{f\,\mathrm{Re}^P}{f\,\mathrm{Re}^C}$	$f\,\mathrm{Re}_{\sqrt{A}}$	$\frac{f\,\mathrm{Re}^P}{f\,\mathrm{Re}^C}$
3	13.33	0.833	15.19	1.071
4	14.23	0.889	14.23	1.004
5	14.73	0.921	14.04	0.990
6	15.05	0.941	14.01	0.988
7	15.31	0.957	14.05	0.991
8	15.41	0.963	14.03	0.989
9	15.52	0.970	14.04	0.990
10	15.60	0.975	14.06	0.992
20	15.88	0.993	14.13	0.996
∞	16	1.000	14.18	1.000

If the solution is recast using the square root of the cross-sectional area as a characteristic length scale, the following expression is obtained:

$$f\,\mathrm{Re}_{\sqrt{A}} = 8\sqrt{\pi}\left[\frac{(1-r^\star)\sqrt{1-r^{\star 2}}}{1+r^{\star 2}-(1-r^{\star 2})/\ln(1/r^\star)}\right] \tag{57}$$

Equation (57) has the following exact ($r^\star \to 0$) and approximate ($r^\star \to 1$) limits:

$$f\,\mathrm{Re}_{\sqrt{A}} = \begin{cases} 8\sqrt{\pi}, & r^\star \to 0 \\ 12\sqrt{\pi}\sqrt{\dfrac{1+r^\star}{1-r^\star}}, & r^\star \to 1 \end{cases} \tag{58}$$

The annulus now has limits comparable to Eq. (54) when Eq. (45) is used as an effective aspect ratio. In other words, there is little difference between a circular annulus and a rectangular duct. Figure 5 shows data for polygonal annular ducts [4] along with the result for the circular annulus. The results considered are those of the circular annulus and other annular ducts, which are bounded externally by a polygon or internally by a polygon [4]. As a result of defining an appropriate measure of slenderness and introducing the more appropriate characteristic length scale $\mathcal{L} = \sqrt{A}$, the data have collapsed onto a single curve. It is clear from Fig. 5 that excellent agreement is obtained when the results are rescaled according to $\mathcal{L} = \sqrt{A}$ and a new aspect ratio defined as $r^\star = \sqrt{A_i/A_o}$. This definition was chosen since it returns the same $r^\star$ ratio for the circular annular duct. Values for $f\,\mathrm{Re}$ for the circular annulus and other shapes have been examined by Muzychka [11]. It should be noted that as the inner boundary approaches the outer boundary, there is some departure from the circular annulus result

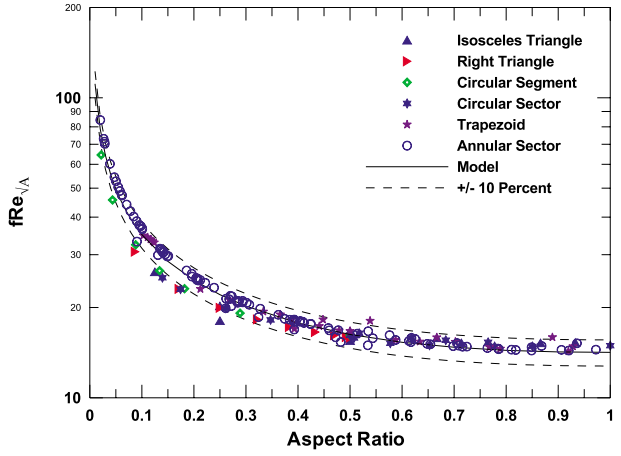

Fig. 4 $f\,\mathrm{Re}_{\sqrt{A}}$ **for other noncircular ducts, data from Ref. [4]**

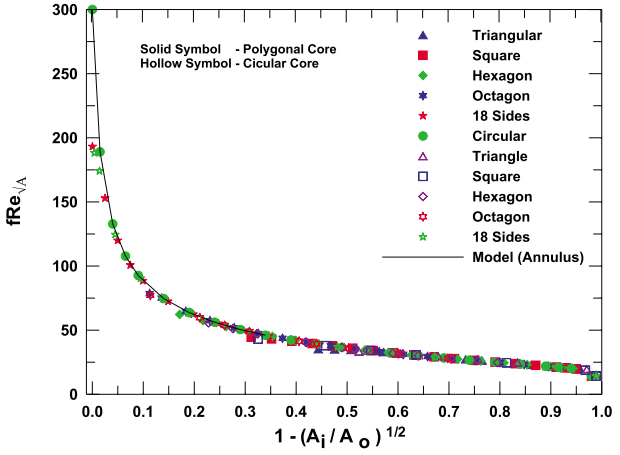

Fig. 5 $f\,\mathrm{Re}_{\sqrt{A}}$ **for annular ducts, data from Ref. [4]**

due to the flow field becoming multiply connected. These points have not been shown on the plot. Limiting values of $r^\star$ are provided in Ref. [11].

It is now clear that Eq. (53) fully characterizes the flow in the long duct limit for many ducts including doubly connected regions when the appropriate aspect ratio is used. The *maximum* deviation of exact values is of the order 7–10%. This result represents a seminal achievement in nondimensionalization. In a recent paper by Duan and Yovanovich [18], the authors introduce the idea of an effective aspect ratio, which further reduces the scatter of data points for ducts with re-entrant corners. This requires simple rules for each shape, but reduces the scatter to less than 3% in fully developed flows. A plot of over 700 data points in Ref. [18] is similar to Fig. 3.

5.2 Short Duct Asymptote, $L \ll L_h$. An analytical result for the friction factor in the entrance region of the circular duct was obtained by Siegel [6] using several methods. The solution begins with the definition of the short duct friction factor, which may be obtained by writing Bernoulli's equation in the entrance region. Since the pressure gradient is only a function of axial position, the following relationship may be written, which relates the friction factor to the velocity in the inviscid core

$$\frac{p_i - p_L}{\frac{1}{2}\rho U^2} = \left(\frac{u_c}{U}\right)^2 - 1 = 4f\left(\frac{L}{D}\right) \tag{59}$$

In order to determine the friction factor, a relationship for the dimensionless core velocity needs to be found. Siegel [6] applied several approximate analytical methods to obtain a solution for the velocity in the inviscid core. The most accurate method was the application of the method of Thwaites (see Ref. [19]). The Siegel [6] analysis begins with the integrated form of the continuity equation in the entrance region where the boundary layer is small relative to the duct diameter

$$\frac{\pi}{4}D^2U = \frac{\pi}{4}(D-2\delta)^2u_c + \pi\int_0^\delta (D-2y)u\,dy \tag{60}$$

where u is the velocity distribution in the boundary layer, u_c is the velocity in the core, and U is the mean velocity. Rearranging this expression leads to

$$\frac{U}{u_c} = 1 - \frac{4}{D}\int_0^\delta \left(1-\frac{u}{u_c}\right)dy + \frac{8}{D^2}\int_0^\delta \left(1-\frac{u}{u_c}\right)y\,dy \tag{61}$$

Next, using Pohlhausen's approximate velocity distribution, Siegel [6] developed an expression relating the boundary layer displacement thickness to the velocity in the core. Siegel [6] then obtained the following four term approximation for the velocity in the core near the entrance of a circular duct:

$$\frac{u_c}{U} = 1 + 6.88(L^+)^{1/2} - 43.5(L^+) + 1060(L^+)^{3/2}\cdots \tag{62}$$

Substitution of the above result into the expression for the friction factor yields

$$f\,\mathrm{Re}_D = \frac{3.44}{(L^+)^{1/2}}[1 - 2.88(L^+)^{1/2} + 111(L^+)\cdots] \tag{63}$$

Goldstein [19] obtained a solution for the core velocity using a method proposed in Schlichting [20], which solves for the velocity in the core using a series expansion. The results of Goldstein [19] yield similar results, with the leading term in the series being exactly the same. A similar analysis for the parallel channel [20] yields the same leading term as that for the circular duct. Analysis of the expressions developed by Siegel [6] and Goldstein [19] reveals that the leading term may be nondimensionalized using any characteristic length scale without introduction of scaling terms

$$f\,\mathrm{Re}_{\mathcal{L}} = \frac{3.44}{(L^+)^{1/2}}\left[1 - 2.88(L^+)^{1/2}\left(\frac{\mathcal{L}}{D}\right) + 111(L^+)\left(\frac{\mathcal{L}}{D}\right)^2\cdots\right] \tag{64}$$

where L^+ is defined by Eq. (2).

However, rescaling the additional terms in the expression results in scaling parameters, which are now functions of the duct geometry. Thus very near the inlet of any noncircular duct, the leading term of the solution is valid. As the boundary layer begins to grow further downstream, the effects of geometry become more pronounced and the solution for the circular duct is no longer valid. The leading term in the solution for any characteristic length $\mathcal{L}$ is

$$f\,\mathrm{Re}_{\mathcal{L}} = \frac{3.44}{\sqrt{L^+}} \tag{65}$$

which is valid for $L^+ = L/\mathcal{L}\ \mathrm{Re}_{\mathcal{L}} \le 0.001$. If a local friction factor is desired, the constant 3.44 is replaced with 1.72.

Equation (65) is independent of the duct shape and may be used to compute the friction factor for the short duct asymptote of most noncircular ducts.

6 Model Development and Comparisons

Having developed the simple expressions for large and small values of the dimensionless duct length, i.e.,

$$f\,\mathrm{Re}_{\sqrt{A}} = \frac{3.44}{\sqrt{L^+}}, \quad L^+ \to 0 \tag{66a}$$

$$f\,\mathrm{Re}_{\sqrt{A}} = \frac{12}{\sqrt{\epsilon}(1+\epsilon)\left[1 - \frac{192\epsilon}{\pi^5}\tanh\left(\frac{\pi}{2\epsilon}\right)\right]}, \quad L^+ \to \infty \tag{66b}$$

we shall proceed to develop a simple model for the apparent friction factor as a function of L^+, in addition to models for the hydrodynamic entrance length L_h^+, and a model for a new dimensionless fully developed flow length, which we will denote as L_{fd}^+.

6.1 Developing Flow Friction Factor. A general model is now proposed using the Churchill and Usagi [21] asymptotic correlation method. The model takes the form

$$y^\star = [(y_0^\star)^n + (y_\infty^\star)^n]^{1/n} \tag{67}$$

$$f\,\mathrm{Re}_{\sqrt{A}} = \left[\left(\frac{C_2}{\sqrt{L^+}}\right)^n + (C_1)^n\right]^{1/n} \tag{68}$$

where n is a superposition parameter determined by comparison with numerical data over the full range of L^+. Using the results provided by Eq. (66), and the general expression, Eq. (67), the following model is proposed:

$$f\,\mathrm{Re}_{\sqrt{A}} = \left[\left(\frac{3.44}{\sqrt{L^+}}\right)^2 + \left(\frac{12}{\sqrt{\epsilon}(1+\epsilon)\left[1 - \frac{192\epsilon}{\pi^5}\tanh\left(\frac{\pi}{2\epsilon}\right)\right]}\right)^2\right]^{1/2} \tag{69}$$

Using the available data [4,17], it is found that the value of n, which minimizes the root mean square (rms) difference, lies in the range $1.5 < n < 3.6$ with a mean value $n \approx 2$ [11,22,23]. Twenty-six data sets were examined from Refs. [4,17], and are summarized in Table 5. Comparisons of the model are presented in Figs. 6–8 for the most common duct shapes. Overall, the model when using the intrinsic aspect ratio yields very good agreement, with predictions lying in the range 1.16–8.72% rms error.

With the exception of the eccentric annular duct at large values of $r^\star$ and $e^\star$, i.e., a crescent shape, the proposed model predicts all of the developing flow data available in literature to within $\pm 10\%$ or better with few exceptions. The proposed model provides equal

Table 5 Comparison of rms and percent differences (%diff=(analytical −predicted)/(analytical)×100) in developing flow models

Geometry	Shah (1978) min/max	Yilmaz (1990) min/max	Proposed model min/max	Proposed model rms	Proposed model n [a]	Proposed model (n=2) rms
Circle	±1.9	−0.3/2.7	−2.73/1.05	1.20	2.01	1.71
Circular annulus r^*=0.05	±2.0	−17.0/1.2	−2.61/1.18	1.27	2.18	2.51
Circular annulus r^*=0.10	±1.9	−17.4/1.9	−1.97/1.09	0.77	2.14	1.73
Circular annulus r^*=0.50	±2.2	−10.2/0.9	−1.13/6.96	1.87	2.07	1.99
Circular annulus r^*=0.75	±2.1	−5.4/1.3	−1.44/7.17	2.12	2.04	2.16
Square b/a=1	±2.3	−2.4/1.6	−1.48/2.27	1.41	1.95	1.61
Rectangle b/a=0.5	±1.9	−2.1/6.7	−1.48/2.27	1.14	1.98	1.16
Rectangle b/a=0.2	±1.7	−1.5/5.0	−1.11/1.89	1.10	2.15	2.04
Parallel plates $b/a\rightarrow 0$	±2.4	−1.6/1.8	−1.22/0.86	0.60	2.32	3.33
Isosceles triangle 2ϕ=30 deg	-	−1.1/0.9	−1.30/4.41	1.75	1.71	4.91
Isosceles triangle 2ϕ=60 deg	±2.4	−0.6/1.1	−0.63/5.97	2.35	1.70	5.16
Isosceles triangle 2ϕ=90 deg	-	1.6/5.2	−7.28/0.85	2.04	2.03	2.08
Eccentric annulus e^*=0.5, r^*=0.5	-	−5.5/3.0	−2.06/1.97	1.71	1.50	8.72
Eccentric annulus e^*=0.5, r^*=0.1	-	−9.1/16	−2.22/2.29	1.66	1.66	5.08
Eccentric annulus e^*=0.7, r^*=0.3	-	−10.3/3.1	−10.89/8.39	7.56	1.86	7.72
Eccentric annulus e^*=0.9, r^*=0.1	-	−11.4/0.2	−13.96/5.87	5.94	2.38	7.30
Eccentric annulus e^*=0.9, r^*=0.5	-	−9.9/−3.5	−35.13/9.44	13.34	3.61	18.14
Ellipse b/a=1	-	-	−2.97/3.75	2.53	1.96	2.56
Ellipse b/a=0.5	-	-	−2.98/5.77	3.77	1.97	3.85
Ellipse b/a=0.2	-	-	−5.75/7.59	5.62	1.69	7.01
Circular sector 2ϕ=11.25 deg	-	-	−9.42/3.03	3.67	2.01	3.68
Circular sector 2ϕ=22.5 deg	-	-	−1.70/5.10	1.57	1.73	4.22
Circular sector 2ϕ=45 deg	-	-	−1.14/12.1	3.73	1.62	6.69
Circular sector 2ϕ=90 deg	-	-	−1.60/16.72	4.63	1.75	5.69
Pentagon	-	-	−3.46/12.75	5.79	1.76	6.41
Trapezoid ϕ=72 deg, b/a=1.123	-	-	−4.96/11.35	6.05	1.55	8.68

[a]Optimal value.

or better accuracy than the model of Yilmaz [2] and is also much simpler. A comparison of the model with the data for the parallel plate channel is also provided. For this geometry $\sqrt{A}\rightarrow\infty$. However, this geometry may be accurately modeled as a rectangular duct with ϵ=0.01 or a circular annular duct with $r^*>0.5$. Good agreement is obtained with the current model when the parallel plate channel is modeled as a finite area duct with small aspect ratio.

One notable feature of the new model is that it does not contain the incremental pressure drop term K_∞, which appears in the models of Bender [3], Shah [1], and Yilmaz [2]. Since the solution of Siegel [6] for the entrance region accounts for both the wall shear and the increase in momentum due to the accelerating core, there is no need to introduce the term K_∞.

Thus, the proposed model is now only a function of the dimensionless duct length L^+ and aspect ratio ϵ, whereas the models of Shah [1] and Yilmaz [2] are functions of many more parameters. It is both simple and accurate for most engineering calculations for microchannel and minichannel systems, or any other scale system where laminar flow prevails.

6.2 Hydrodynamic Entrance Lengths. Finally, it is desirable to develop a simple expression for the hydrodynamic entrance length. The hydrodynamic entrance length is useful for determining the extent to which the flow develops, particularly for selecting an appropriate heat transfer model. Traditionally, the length

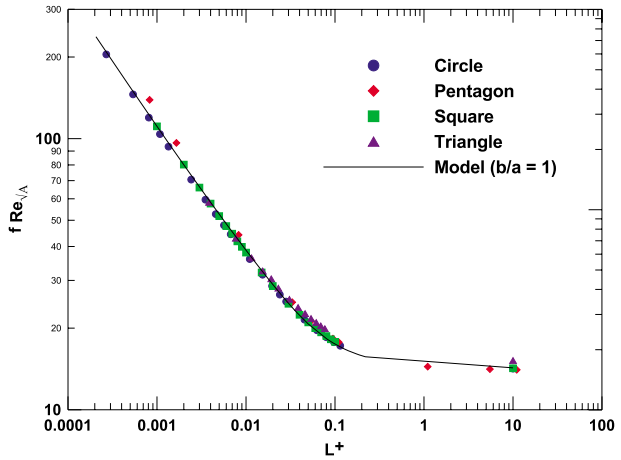

Fig. 6 $f\,\mathrm{Re}_{\sqrt{A}}$ **for developing laminar flow in polygonal ducts, data from Ref. [4]**

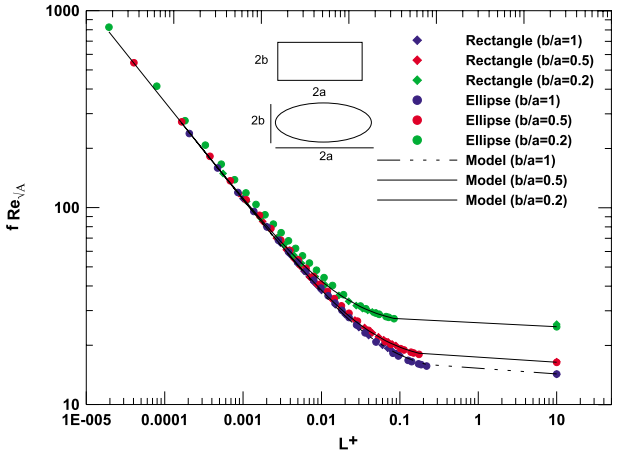

Fig. 7 $f\,\mathrm{Re}_{\sqrt{A}}$ **for developing laminar flow in regular flat ducts, data from Ref. [4]**

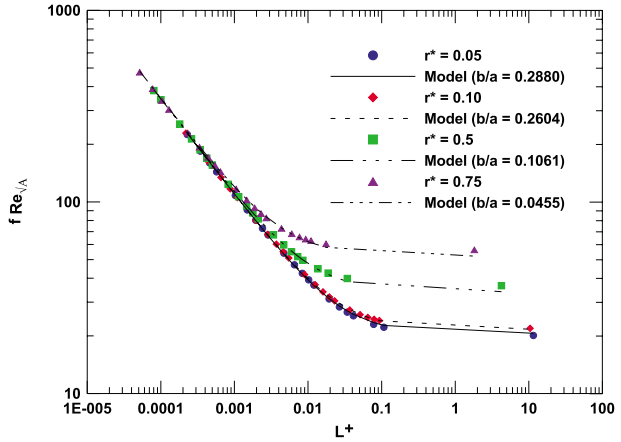

Fig. 8 $f\,\mathrm{Re}_{\sqrt{A}}$ **for developing laminar flow in the circular annular duct, data from Ref. [4]**

required for hydrodynamic boundary layer development in straight ducts of constant cross-sectional area is usually defined as the point where the centerline velocity is $0.99u_{\max}$ [4]. This is often followed with an assumption of fully developed flow downstream of the hydrodynamic entrance length.

An equation relating the approximate magnitude of the hydrodynamic entrance length may be obtained by considering an equality between the two asymptotic limits given in Eq. (33) with $L^+=L_h^+$; we obtain, when $\mathcal{L}=\sqrt{A}$,

$$L_h^+ \sim \left(\frac{C_2}{C_1}\right)^2 \sim C_{0,\sqrt{A}} \tag{70}$$

or

$$L_h = C_{0,\sqrt{A}}\sqrt{A}\,\mathrm{Re}_{\sqrt{A}} = C_{0,\sqrt{A}}\left(\frac{\dot{m}}{\mu}\right) \tag{71}$$

This solution represents the intersection of the asymptotic limits on a plot of the complete behavior of $f\,\mathrm{Re}$ versus L^+. Conveniently, it yields values that agree better than an order of magnitude guess. A new definition for the hydrodynamic entrance length may be obtained from Eq. (70). Substituting from Eq. (66*a*) for $C_2=3.44$ and Eq. (66*b*) for C_1, an approximate expression for the entrance length as a function of aspect ratio is obtained as follows:

$$L_h^+ = 0.0822\epsilon(1+\epsilon)^2\left[1-\frac{192\epsilon}{\pi^5}\tanh\left(\frac{\pi}{2\epsilon}\right)\right]^2 = C_{0,\sqrt{A}} \tag{72}$$

The above expression reduces to $L_h^+=0.059$ when $\epsilon=1$ and $L_h^+=0.00083$ when $\epsilon=0.01$. A complete tabulation is provided in Table 6, along with associated conversions for the rectangular duct and elliptical duct when using the hydraulic diameter as a length scale. These lengths when rescaled to be based on the hydraulic diameter take the values $L_h^+=0.047$ for a tube or square duct when $\epsilon=1$ and $L_h^+=0.021$ when $\epsilon=0.01$ for a channel. They compare well with the more exact results from Shah and London [4] for the circular duct, $L_h^+=0.056$, and parallel plate channel, $L_h^+=0.011$. Once again, we see that the order of magnitude is correctly and easily predicted. It should also be noted that a significant variation in data for L_{hy}^+ is found in literature. The advantage of Eq. (72) is that it provides a single universal expression, which can be applied to any duct shape, and also accounts for the aspect ratio effect, which tends to reduce entrance lengths for flatter ducts.

Table 6 Hydrodynamic entrance lengths

ϵ	Model $L_{h,\sqrt{A}}^+=C_{0,\sqrt{A}}$	Rectangle L_{h,D_h}^+	Ellipse L_{h,D_h}^+
0.01	0.000828	0.0211	0.0264
0.05	0.00424	0.0233	0.0269
0.1	0.00874	0.0263	0.0288
0.2	0.0181	0.0326	0.0316
0.3	0.0274	0.0387	0.0353
0.4	0.0361	0.0440	0.0379
0.5	0.0434	0.0485	0.0404
0.6	0.0499	0.0534	0.0435
0.7	0.0540	0.0556	0.0449
0.8	0.0564	0.0570	0.0453
0.9	0.0582	0.0582	0.0456
1	0.0586	0.0586	0.0459

Another useful expression may be developed from the asymptotic limits for determining the extent of a duct length, which is required for making a valid assumption of fully developed flow, i.e., one in which the pressure drop may be wholly determined using only Eq. (53) with small error. This hydrodynamic length can be considered the required dimensionless duct length for which fully developed flow prevails, in such a manner that boundary layer region contributes little to the overall pressure drop. In this case we propose a criterion that a duct length, which yields a dimensionless pressure drop, which is 5% greater than that predicted by Eq. (53) be adopted, i.e.,

$$f\,\mathrm{Re}(L^+) \sim 1.05C_1 \tag{73}$$

This yields a result of

$$L_{\mathrm{fd}}^+ \sim 9.75\left(\frac{C_2}{C_1}\right)^2 \sim 10L_h^+ \tag{74}$$

Equation (74) clearly shows that a duct having a dimensionless duct length of order ten times the hydrodynamic entrance length is required for all boundary layer effects to be lost in the pressure drop calculation, in a fully developed laminar flow (see Figs. 6–8). This is in marked contradiction to the many fluid mechanics texts, which state that fully developed flow pressure drop may be predicted using a Hagen–Poiseuille law result for $f\,\mathrm{Re}$ when $L > L_h$.

7 Summary and Conclusions

A simple model was developed for predicting the friction factor–Reynolds number product in noncircular ducts for developing laminar flow. The present study took advantage of scale analysis, asymptotic analysis, and the selection of a more appropriate characteristic length scale to develop a simple model. This model only requires two parameters: the aspect ratio of the duct and the dimensionless duct length; whereas the model of Shah [1] requires tabulated values of three parameters, and the model of Yilmaz [2] consists of several equations. The present model predicts most of the developing flow data within ±10% or better and 1.16–8.72% rms for eight singly connected ducts and two doubly connected ducts.

Additional models were also developed using the asymptotic results for both the hydrodynamic entrance length and the fully developed flow length, which is related to the hydrodynamic entrance length. These expressions can be used to determine the size of the hydrodynamic entrance region for use with appropriate heat transfer models, and for determining the extent of a duct for which entrance effects are negligible.

Finally these models may also be used to predict results for ducts for which no solutions or tabulated data exist. It was also shown that this is possible, since the use of the of the square root of the cross-sectional flow area was a more effective characteristic length scale than the hydraulic diameter for collapsing the numerical results of geometries having similar shape and aspect ratio.

Acknowledgment

The authors acknowledge the financial support of the Natural Sciences and Engineering Research Council of Canada (NSERC).

Nomenclature

A = flow area, m^2
a, b = major and minor axes of ellipse or rectangle, m
C = constant
C_0, C_1, C_2 = scaling constants
c = linear dimension, m
D = diameter of circular duct, m
D_h = hydraulic diameter, $\equiv 4A/P$
$\mathbf{E}(\cdot)$ = complete elliptic integral of the second kind
e = eccentricity, m
$e^\star$ = dimensionless eccentricity, $\equiv e/(r_o - r_i)$
f = Fanning friction factor $\equiv \tau/\left(\frac{1}{2}\rho U^2\right)$
G = mass flux, kg/s m^2
K = incremental pressure drop factor
ℓ = arbitrary dimension
L = duct length, m
L^+ = dimensionless duct length, $\equiv L/\mathcal{L}\ \mathrm{Re}_{\mathcal{L}}$
$\dot{m}$ = mass flow rate, kg/s
N = number of sides of a polygon
n = correlation parameter
P = perimeter, m
p = pressure, N/m^2
r = radius, m
$r^\star$ = dimensionless radius ratio, $\equiv r_i/r_o$
$\mathrm{Re}_{\mathcal{L}}$ = Reynolds number, $\equiv U\mathcal{L}/\nu$
Re_L = Reynolds number based on L
$\vec{V}$ = velocity vector, m/s
u, v, w = velocity components, m/s
U = average velocity, m/s
x, y, z = Cartesian coordinates, m

Greek Symbols

δ = boundary layer thickness, m
ϵ = nominal aspect ratio, $\equiv b/a$
Φ = half angle, rad
μ = dynamic viscosity, N s/m^2
ρ = fluid density, kg/m^3
τ = wall shear stress, N/m^2

Subscripts

$\sqrt{A}$ = based on square root of flow area
c = core
c = circular
D_h = based on hydraulic diameter
eff = effective
fd = fully developed
h = hydrodynamic
i = inner
long = longest perpendicular
$\mathcal{L}$ = based on the arbitrary length scale $\mathcal{L}$
nc = noncircular
o = outer
short = shortest perpendicular
∞ = fully developed limit

Superscripts

C = circle
E = ellipse
P = polygon
R = rectangle
$\bar{(\cdot)}$ = mean value

References

[1] Shah, R. K., 1978, "A Correlation for Laminar Hydrodynamic Entry Length Solutions for Circular and Non-Circular Ducts," ASME J. Fluids Eng., **100**, pp. 177–179.
[2] Yilmaz, T., 1990, "General Equations for Pressure Drop for Laminar Flow in Ducts of Arbitrary Cross Sections," ASME J. Energy Resour. Technol., **112**, pp. 220–223.
[3] Bender, E., 1969, "Druckverlust bei Laminarer Stromung im Rohreinlauf," Chem.-Ing.-Tech., **41**, pp. 682–686.
[4] Shah, R. K., and London, A. L., 1978, *Laminar Flow Forced Convection in Ducts*, Academic, New York.
[5] Bejan, A., 1995, *Convection Heat Transfer*, 2nd ed., Wiley, New York.
[6] Siegel, R., 1953, "The Effect of Heating on Boundary Layer Transition for Liquid Flow in a Tube," Sc.D. thesis, Massachusetts Institute of Technology, Cambridge, MA.
[7] White, F. M., 1974, *Viscous Fluid Flow*, McGraw-Hill, New York.
[8] Denn, M., 1980, *Process Fluid Mechanics*, Prentice-Hall, Upper Saddle River, NJ.
[9] Mironer, A., 1979, *Fluid Mechanics*, McGraw-Hill, New York.
[10] Yovanovich, M. M., and Muzychka, Y. S., 1997, "Solutions of Poisson Equation Within Singly and Doubly Connected Domains," 1997 National Heat Transfer Conference, Baltimore, MD, Aug. 10–12, Paper No. AIAA 97-3880.
[11] Muzychka, Y. S., 1999, "Analytical and Experimental Study of Fluid Friction and Heat Transfer in Low Reynolds Number Flow Heat Exchangers," Ph.D. thesis, University of Waterloo, Waterloo, ON, Canada.
[12] Bahrami, M., Yovanovich, M. M., and Culham, J. R., 2006, "Pressure Drop of Fully Developed, Laminar Flow in Microchannel of Arbitrary Cross-Section," ASME J. Fluids Eng., **128**, pp. 1036–1044.
[13] Duan, Z. P., and Muzychka, Y. S., 2007, "Slip Flow in Non-Circular Micro-Channels," Microfluid. Nanofluid., **3**(4), pp. 473–484.
[14] Muzychka, Y. S., and Edge, J., 2008, "Laminar Non-Newtonian Fluid Flow in Non-Circular Ducts and Micro-Channels," ASME J. Fluids Eng., **130**, p. 111201.
[15] Leal, L. G., 1992, *Laminar Flow and Convective Transport*, Butterworth-Heinemann, Boston, MA.
[16] Shapiro, A. H., Siegel, R., and Kline, S. J., 1954, "Friction Factor in the Laminar Entry Region of a Smooth Tube," *Proceedings of the Second U.S. National Congress of Applied Mechanics*, pp. 733–741.
[17] Shah, R. K., and Bhatti, M. S., 1987, "Laminar Convective Heat Transfer in Ducts," *Handbook of Single Phase Convective Heat Transfer*, S. Kakac, R. K. Shah, and W. Aung, eds., Wiley, New York, Chap. 3.
[18] Duan, Z. P., and Yovanovich, M. M., 2009, "Pressure Drop for Laminar Flow in Micro-Channels of Arbitrary Cross-Sections," IEEE Semi-Therm Symposium, San Jose, CA, Mar. 15–19.
[19] R. Goldstein, ed., 1938, *Modern Developments in Fluid Dynamics*, Oxford University Press, Oxford.
[20] Schlichting, H., 1979, *Boundary Layer Theory*, McGraw-Hill, New York.
[21] Churchill, S. W., and Usagi, R., 1972, "A General Expression for the Correlation of Rates of Transfer and Other Phenomena," AIChE J., **18**, pp. 1121–1128.
[22] Muzychka, Y. S., and Yovanovich, M. M., 1998, "Modelling Friction Factors in Non-Circular Ducts for Developing Laminar Flow," Second AIAA Theoretical Fluid Mechanics Meeting, Albuquerque, NM, Jun. 15–18, AIAA Paper No. 98-2492.
[23] Muzychka, Y. S., and Yovanovich, M. M., 2002, "Laminar Flow Friction and Heat Transfer in Non-Circular Ducts and Channels Part I Hydrodynamic Problem," *Compact Heat Exchangers: A Festschrift on the 60th Birthday of Ramesh K. Shah*, G. P. Clelata, B. Thonon, A. Bontemps, and S. Kandlikar, eds., Edizioni ETS, Italy, pp. 123–130.

Direct Simulation Based Model-Predictive Control of Flow Maldistribution in Parallel Microchannels

Mathieu Martin

Chris Patton

John Schmitt

Sourabh V. Apte[1]
e-mail: sva@engr.orst.edu

School of Mechanical, Industrial and Manufacturing Engineering,
Oregon State University,
Corvallis, OR 97331

Flow maldistribution, resulting from bubbles or other particulate matter, can lead to drastic performance degradation in devices that employ parallel microchannels for heat transfer. In this work, direct numerical simulations of fluid flow through a prescribed parallel microchannel geometry are performed and coupled with active control of actuated microvalves to effectively identify and reduce flow maldistribution. Accurate simulation of fluid flow through a set of three parallel microchannels is achieved utilizing a fictitious-domain representation of immersed objects such as microvalves and artificially introduced bubbles. Flow simulations are validated against experimental results obtained for flow through a single high-aspect ratio microchannel, flow around an oscillating cylinder, and flow with a bubble rising in an inclined channel. Results of these simulations compare very well to those obtained experimentally, and validate the use of the solver for the parallel microchannel configuration of this study. System identification techniques are employed on numerical simulations of fluid flow through the geometry to produce a lower dimensional model that captures the essential dynamics of the full nonlinear flow, in terms of a relationship between valve angles and the exit flow rate for each channel. A model-predictive controller is developed, which employs this reduced order model to identify flow maldistribution from exit flow velocities and to prescribe actuation of channel valves to effectively redistribute the flow. Flow simulations with active control are subsequently conducted with artificially introduced bubbles. The model-predictive control methodology is shown to adequately reduce flow maldistribution by quickly varying channel valves to remove bubbles and to equalize flow rates in each channel. [DOI: 10.1115/1.3216519]

1 Introduction

Microchannels are employed in a variety of devices, such as heat sinks and heat exchangers, to improve heat transfer effectiveness. For improved efficiency and cooling of high heat loads, two-phase flows involving convective boiling of high latent heat fluids are often used. Formation of vapor bubbles inside the microchannel geometry can lead to blocking effects, resulting in flow maldistribution with nonuniform spatial and temporal conditions. Such flow maldistribution reduces the effectiveness of the heat transfer, leading to decreased performance of the devices under consideration.

Previous investigations into multiphase flow in microchannels [1,2] have shown that the vapor phase can take different forms, each yielding qualitatively different flow behavior. For two-phase flow in a square channel, Cubaud [3] classified flow regimes by the size and occupation of the channel by the vapor phase. In bubbly flow, small bubbles comprise a vapor phase that is relatively small in comparison to the channel dimensions. In this flow regime, bubbles are mainly spherical and flow with the fluid at a similar velocity. Sharp and Adrian [4] investigated clogging or arching structures inside microchannels or in sharp corners due to interaction of rigid particles. Bubble-laden flows may also lead to similar blocking effects in microchannel geometries.

In microchannel geometries using a liquid as a coolant for the removal of high heat fluxes, bubbles may form and grow at nucleation sites. These bubbles remain attached to channel walls due to surface tension effects [5]. Existence of the bubble in a channel affects the fluid flow not only in that channel, but also in all of the connected channels, leading to flow maldistribution. As the bubble grows, eventually the surface tension forces keeping the bubble attached to the wall are lowered, and the hydrodynamic forces acting on the bubble may overcome any resistive forces detaching and moving the bubble [6,7]. Formation and growth of bubbles inside parallel microchannel geometries can lead to flow instabilities and flow reversals and can affect the flow distribution in a network of channels [8]. To mitigate these flow instabilities, Mukherjee and Kandlikar [8] proposed the use of variable size microchannels with increased cross-sectional areas in the downstream direction. Increasing areas in the downstream directions result in higher pressures locally, which tend to reduce the flow reversal, and is an example of a *passive control* to mitigate flow distribution problems. Active control, based on the model-predictive control algorithm, has been used by Bleris et al. [9] in order to improve mixing of chemical species in parallel microchannels. By regulating the mass-flow rates in each channel, they showed how active control can be used to improve mixing and chemical reaction processes.

In the present work, we investigate an active control strategy as applied to the two-phase flow in parallel microchannels in order to mitigate flow maldistributions due to the presence of single or multiple bubbles in one or more branches of the channels. We consider the bubbly flow regime with one or more bubbles present in a parallel microchannel configuration, as shown in Fig. 1. As the first step, the bubbles are modeled as rigid spherical particles in a two-dimensional (2D) simulation. Bubble growth is not simulated; instead, bubbles are injected into the domain close to a

[1]Corresponding author.

Contributed by the Fluids Engineering Division of ASME for publication in the JOURNAL OF FLUIDS ENGINEERING. Manuscript received February 17, 2009; final manuscript received July 17, 2009; published online October 8, 2009. Reviewed by Joseph Katz.

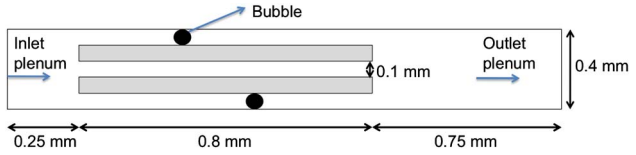

Fig. 1 Schematic of parallel microchannels with bubbly flow

microchannel wall. Bubbles are held fixed until the hydrodynamic force applied by the flow reaches a critical threshold, at which point the bubble is released into the flow. The threshold force that must be overcome by the hydrodynamic forces is estimated by approximating surface tension forces based on the analysis performed by Lee et al. [6]. Flow maldistribution resulting from bubble injection is regulated through the actuation of valves at the entrance of each microchannel.

The paper is structured as follows. Section 2 provides the mathematical foundation of the direct numerical simulations employed in this study. Details regarding the implementation of the numerical algorithm employed are presented in Sec. 3. The control design methodology, including the means by which reduced order models are produced from direct numerical simulations and the use of such models in a model-predictive control (MPC) scheme, is detailed in Sec. 4. Section 6 presents results of validation cases for the flow solver. Controlled flow simulations of bubbly flow are examined in Sec. 7, with conclusions and avenues for future work presented in Sec. 8.

2 Mathematical Formulation

The computations carried out in this work utilize direct numerical simulation (DNS) with fictitious-domain representation of arbitrary shaped immersed objects such as microvalves and bubbles. The fictitious-domain approach of Glowinski et al. [10], Patankar [11], and Apte et al. [12] allows accurate representation of moving boundaries embedded in a fluid flow. Two types of moving boundaries are considered in this study: (i) specified motion of the immersed object and (ii) freely moving objects. The motion of the microvalves is a *specified* rigid body motion (RBM) consisting of translation and rotational velocities. The bubbles or particles are allowed to move *freely*. Their motion is obtained by directly computing the forces acting on them. As the first step, we assume the bubbles as *rigid* objects immersed in a surrounding viscous fluid. As shown later, such an assumption is reasonable for low Reynolds numbers and low Weber numbers. For small Weber numbers, the inertial shearing forces acting on the bubble are much smaller than the surface tension forces. Under these conditions bubble deformation is minimal, and the shape of the bubble is preserved. One consequence of this assumption is that modeling the motion of the bubble is much easier; the region occupied by the bubble is forced to undergo rigid body motion consisting of only translation and rotation. The bubble motion is then obtained directly by using a novel algorithm based on fictitious-domain method for high-density ratios between the fluid and the immersed object. In this fully resolved simulation approach, models for drag, lift, or added mass forces on the bubble are not required, but such forces are directly computed. Below we describe in detail the computational approach for freely moving rigid objects immersed in a viscous, incompressible fluid. Details of the numerical scheme and several verification and validation test cases are also presented to show good predictive capability of the numerical solver.

Let Γ be the computational domain, which includes both the fluid ($\Gamma_F(t)$) and the particle ($\Gamma_P(t)$) domains. Let the fluid boundary not shared with the particle be denoted by $\mathcal{B}$ and have a Dirichlet condition (generalization of boundary conditions is possible). For simplicity, let there be a single rigid object in the domain and the body force be assumed constant so that there is no net torque acting on the object. The basis of the fictitious-domain based approach [10] is to extend the Navier–Stokes equations for fluid motion over the entire domain Γ inclusive of the immersed object. The natural choice is to assume that the immersed object region is filled with a Newtonian *fluid* of density equal to the object density (ρ_P) and some fluid viscosity (μ_F). Both the real and fictitious fluid regions will be assumed as incompressible and thus the incompressibility constraint applies over the entire region. In addition, as the immersed objects are assumed rigid, the motion of the material inside the object is constrained to be a rigid body motion. Several ways of obtaining the rigidity constraint have been proposed [10,13,11]. We follow the formulation developed by Patankar [11], which was also applied by Sharma and Patankar [14] for freely moving rigid objects in laminar flows. Apte et al. [12] extended the formulation to colocated grid finite volume schemes with good conservative properties necessary for turbulent flows. Details of the numerical algorithm are described in detail by Apte et al. [12]. A brief description is given here for completeness.

The momentum equation for fluid motion applicable in the entire domain Γ is given by

$$\rho\left(\frac{\partial \mathbf{u}}{\partial t} + (\mathbf{u}\cdot\nabla)\mathbf{u}\right) = -\nabla p + \nabla\cdot(\mu_F(\nabla\mathbf{u} + (\nabla\mathbf{u})^T)) + \rho\mathbf{g} + \mathbf{f} \quad (1)$$

where ρ is the density field, $\mathbf{u}$ is the velocity vector, p is the pressure, μ_F is the fluid viscosity, $\mathbf{g}$ is the gravitational acceleration, and $\mathbf{f}$ is an additional body force that enforces rigid body motion within the immersed object region Γ_P. The fluid velocity field is constrained by the conservation of mass, which for an incompressible fluid simply becomes $\nabla\cdot\mathbf{u}=0$.

In order to enforce that the material inside the immersed object moves in a rigid fashion, a rigidity constraint is required that leads to a nonzero forcing function $\mathbf{f}$. Inside the particle region, the rigid body motion implies vanishing deformation rate tensor

$$\left.\begin{aligned} &\frac{1}{2}(\nabla\mathbf{u} + (\nabla\mathbf{u})^T) = \mathbf{D}[\mathbf{u}] = 0 \\ &\Rightarrow \mathbf{u} = \mathbf{u}^{\mathrm{RBM}} = \mathbf{U} + \Omega\times\mathbf{r} \end{aligned}\right\} \text{in } \Gamma_P \quad (2)$$

where $\mathbf{U}$ and Ω are the translation and angular velocities of the object, and $\mathbf{r}$ is the position vector of a point inside the object from its centroid.

The vanishing deformation rate tensor for the rigidity constraint automatically ensures the incompressibility constraint inside the particle region. The incompressibility constraint gives rise to the scalar field (the pressure, p) in a fluid. Similarly, the tensor constraint $\mathbf{D}[\mathbf{u}]=0$ for rigid motion gives rise to a tensor field inside the particle region. A fractional-step algorithm can be devised to solve the moving boundary problem [11,12]. Knowing the solution at time level t^n, the goal is to find $\mathbf{u}$ at time t^{n+1}.

1. In this first step, the rigidity constraint force $\mathbf{f}$ in Eq. (1) is set to zero, and the equation together with the incompressibility constraint (Eq. (2)) is solved by standard fractional-step schemes over the entire domain. Accordingly, a pressure Poisson equation is derived and used to project the velocity field onto an incompressible solution. The obtained velocity field is denoted as $\mathbf{u}^{n+1}$ inside the fluid domain and $\hat{\mathbf{u}}$ inside the object.
2. The velocity field for a freely moving object is obtained in a second step by projecting the flow field onto a rigid body motion. Inside the object

$$\rho_P\left(\frac{\mathbf{u}^{n+1} - \hat{\mathbf{u}}}{\Delta t}\right) = \mathbf{f} \quad (3)$$

To solve for $\mathbf{u}^{n+1}$ inside the particle region we require $\mathbf{f}$. The constraint on the deformation rate tensor given by Eq. (2) can be reformulated to obtain

$$\nabla \cdot (\mathbf{D}[\mathbf{u}^{n+1}]) = \nabla \cdot \left(\mathbf{D}\left[\hat{\mathbf{u}} + \frac{\mathbf{f}\Delta t}{\rho} \right] \right) = 0 \tag{4}$$

$$\mathbf{D}[\mathbf{u}^{n+1}] \cdot \mathbf{n} = \mathbf{D}\left[\hat{\mathbf{u}} + \frac{\mathbf{f}\Delta t}{\rho} \right] \cdot \mathbf{n} = 0 \tag{5}$$

The velocity field in the particle domain involves only translation and angular velocities. Thus $\hat{\mathbf{u}}$ is split into a rigid body motion ($\mathbf{u}^{\mathrm{RBM}} = \mathbf{U} + \Omega \times \mathbf{r}$) and residual nonrigid motion ($\mathbf{u}'$). The translational and rotational components of the rigid body motion are obtained by conserving the linear and angular momenta and are given as

$$M_P \mathbf{U} = \int_{\Gamma_P} \rho_P \hat{\mathbf{u}} d\mathbf{x} \tag{6}$$

$$\mathcal{I}_P \Omega = \int_{\Gamma_P} \mathbf{r} \times \rho_P \hat{\mathbf{u}} d\mathbf{x} \tag{7}$$

where M_P is the mass of the particle, and $\mathcal{I}_P = \int_{\Gamma_P} \rho_P [(\mathbf{r} \cdot \mathbf{r})\mathbf{I} - \mathbf{r} \otimes \mathbf{r}] d\mathbf{x}$ is the moment of inertia tensor. Knowing $\mathbf{U}$ and Ω for each particle, the rigid body motion inside the particle region $\mathbf{u}^{\mathrm{RBM}}$ can be calculated.

3. The rigidity constraint force is then simply obtained as $\mathbf{f} = \rho(\mathbf{u}^{\mathrm{RBM}} - \hat{\mathbf{u}})/\Delta t$. This sets $\mathbf{u}^{n+1} = \mathbf{u}^{\mathrm{RBM}}$ in the particle domain. Note that the rigidity constraint is nonzero only inside the particle domain and zero everywhere else. This constraint is then imposed in a third fractional step.

In practice, the fluid flow near the boundary of the particle (over a length scale on the order of the grid size) is altered by the above procedure owing to the smearing of the particle boundary. The key advantage of the above formulation is that the projection step only involves straightforward integrations in the particle domain.

The above formulation can be easily generalized to particles with *specified motion* (such as the microvalves) by directly setting $\mathbf{u}^{\mathrm{RBM}}$ to the specified velocity. In this case, the integrations (Eq. (6)) in the particle domain are not necessary.

3 Numerical Approach

The preceding mathematical formulation is implemented in a colocated structured grid three-dimensional (3D) flow solver based on a fractional-step scheme developed by Apte et al. [12]. Modifications to the original scheme for freely moving objects were made in order to handle large-density ratios ($\mathcal{O}(1000)$) representative of water-to-air bubbles. Accordingly, in the present work the fluid-particle system is solved by a *three-level fractional-step scheme*. First the momentum equations (without the pressure and the rigidity constraint terms) are solved. The incompressibility constraint is then imposed by solving a *variable-coefficient Poisson equation* for pressure. Finally, the rigid body motion is then enforced by constraining the flow inside the immersed object to translational and rotational motion. The main steps of the numerical approach are given below.

3.1 Immersed Object Representation. In the numerical implementation, we create small material volumes of cubic shape that completely occupy the immersed object (see Fig. 2). Each material volume is assigned the properties of the immersed object (e.g., density, etc.). The shape of the object can be reconstructed from these material volumes by computing an indicator or color function (with value of unity inside the object and zero outside) on a fixed background mesh used for the flow solution. In this work, the material volumes are forced to undergo rigid motion, based on the translational and rotational velocities of the object, resulting in no relative motion among them. At each time-step the material volumes are advanced to new locations. In the present approach, the boundary of the object is represented in a stair-stepped fashion, and it is straightforward to create the material volumes using a bounding-box algorithm [14,12] as follows.

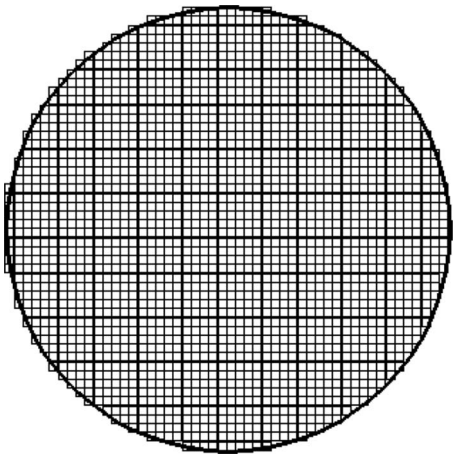

Fig. 2 Schematic of material volumes for a circular object

1. Determine the bounding box for the particle based on its surface representation.
2. Generate cubic grid within the bounding box.
3. Use distance searches to determine if the centroid of the control volume lies within the bounding surface of the particle.
4. Eliminate points outside the particle domain.

The total mass of the material volumes generated will be exactly equal to the mass of the particle if the surface of the particle aligns with the grid. The stair-stepped surface representation, however, results in an error in the total mass of the material volumes compared with the original shape. This error reduces with an increase in the total number of material volumes per object. A more complex grid generation process based on the Delaunay triangulation can be used to accurately represent the surface of the object by using standard body-fitted grid generation tools. In the present work, however, we use a sufficient number of material volumes to represent the object boundary and to follow the stair-stepped approach owing to its simplicity.

3.2 Discretized Equations and Numerical Algorithm. Figure 3 shows the schematic of variable storage in time and space. All variables are stored at the control volume (cv) center with the exception of the face-normal velocity u_N, located at the face centers. The face-normal velocity is used to enforce continuity equation. Capital letters are used to denote particle fields. The time-staggering is done so that the variables are located most conveniently for the time-advancement scheme. We follow the collocated spatial arrangement for velocity and pressure field [15,16]. Accordingly, the particle positions (X_i), density (ρ), volume fraction (Θ), viscosity (μ), and the pressure (p) are located at time levels $t^{n-1/2}$ and $t^{n+1/2}$, whereas the velocity fields (u_i, u_N, and U_i) and the rigid body constraint force $f_{i,R}$ are located at time levels t^n and t^{n+1}. This makes the discretization symmetric in time a feature important to obtain good conservation properties.

The semidiscretization of the governing equations in each time-step is given below.

Step 1. Starting with a solution at t^n and $t^{n-1/2}$, the centroids of material volumes ($X_{i,M}$) representing immersed objects are first advanced explicitly

$$X_{i,M}^{n+1/2} = X_{i,P}^{n-1/2} + \mathcal{R}_{ij}(X_{j,M}^{n-1/2} - X_{j,P}^{n-1/2}) + U_{i,M}^{n} \Delta t \tag{8}$$

where $X_{i,M}$ is the position vector of the material volume center, $X_{i,P}$ is the position vector of the immersed object centroid, $U_{i,M}$ is

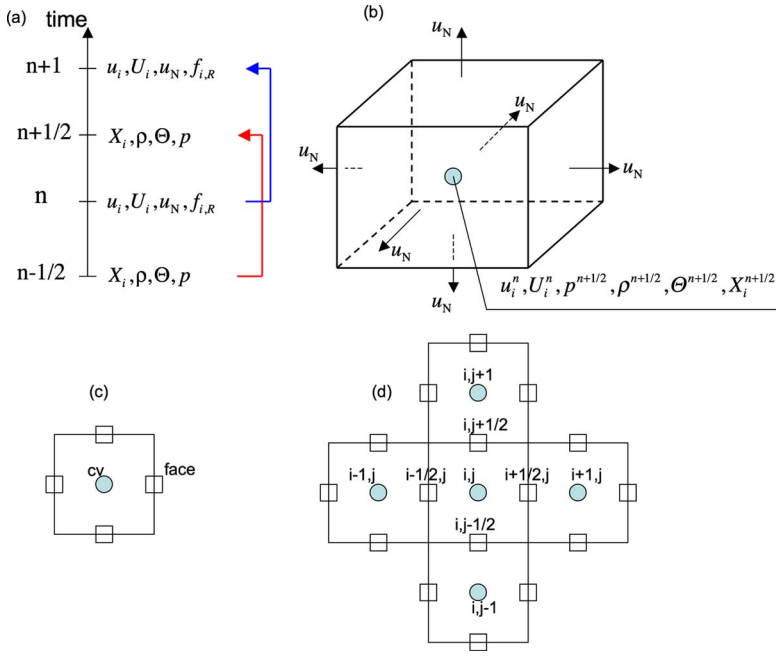

Fig. 3 Schematic of the variable storage in time and space: (*a*) time-staggering, (*b*) three-dimensional variable storage, (*c*) *cv* and face notation, and (*d*) index notation for a given *k*-index in the *z* direction. The velocity fields (u_i and u_N) are staggered in time with respect to the volume fraction (Θ), density (ρ), particle position (X_i), the pressure field (p), and the rigid body force ($f_{i,R}$). All variables are collocated in space at the centroid of a control volume except the face-normal velocity u_N, which is stored at the centroid of the faces of the control volume.

the translation velocity, $\Omega_{i,M}$ is the angular velocity, and Δt is the time-step. Here $\mathcal{R}_{ij}$ is the rotation matrix evaluated using particle locations at $t^{n-1/2}$. The details of the particle update and the rotation matrix are given in the Appendix.

Step 2. Knowing the new positions of the material volumes and particle centroid, an indicator function (color function) $\Theta^{n+1/2}$ is evaluated at the *cv*-center of the fixed background grid. We use a discrete delta-function [17] to compute the color function. The color function is unity inside the particle region and vanishes outside with smooth variation near the boundary. This thus allows identification of the particle on the background mesh. Details of the interpolation between the material volume centers and the *cv* center are given in the Appendix. The density and the viscosity are then calculated over the entire domain as

$$\rho_{cv}^{n+1/2} = \rho_P \Theta_{cv}^{n+1/2} + \rho_F (1 - \Theta_{cv}^{n+1/2}) \tag{9}$$

$$\mu_{cv}^{n+1/2} = \mu_P \Theta_{cv}^{n+1/2} + \mu_F (1 - \Theta_{cv}^{n+1/2}) \tag{10}$$

where ρ_P is the density of the immersed particle and ρ_F is the density of the surrounding fluid. Likewise μ_P is dynamic viscosity of the fictitious fluid inside the particle region, and μ_F is the dynamic viscosity of the surrounding fluid. For particles with specified motion (microvalves) μ_P is assumed equal to the fluid viscosity (μ_F). For bubbles, appropriate viscosity of the air bubble is specified.

Step 3. Advance the momentum equations using the fractional-step method [18]. First, obtain a predicted velocity field over the entire domain. We advance the velocity field from t^n to t^{n+1}. The predicted velocity fields may not satisfy the continuity or the rigidity constraints. These are enforced later

$$\frac{u_{i,cv}^* - u_{i,cv}^n}{\Delta t} + \frac{1}{V_{cv}} \sum_{\text{faces of } cv} u_{i,\text{face}}^{*n+1/2} u_N^n A_{\text{face}} = \frac{1}{\rho_{cv}^{n+1/2}} \left(\frac{1}{V_{cv}} \sum_{\text{faces of } cv} \tau_{ij,\text{face}}^{*n+1/2} N_{j,\text{face}} A_{\text{face}} \right) + g_i \tag{11}$$

where g_i is the gravitational acceleration, V_{cv} is the volume of the *cv*, A_{face} is the area of the face of a control volume, $N_{j,\text{face}}$ is the face-normal vector, and

$$u_{i,\text{face}}^{*n+1/2} = \tfrac{1}{2}(u_{i,\text{face}}^n + u_{i,\text{face}}^*)$$

$$\tau_{ij,\text{face}}^{*n+1/2} = \mu_{cv}^{n+1/2} \left[\frac{1}{2} \left(\frac{\partial u_i^n}{\partial x_j} + \frac{\partial u_i^*}{\partial x_j} \right) + \left(\frac{\partial u_j^n}{\partial x_i} \right) \right]_{\text{face}}$$

In the above expressions, the velocities at the "face" are obtained by using arithmetic averages of the neighboring *cv*s attached to the face. For the viscous terms, the velocity gradients in the direction of the momentum component are obtained implicitly using the Crank–Nicholson scheme. A centered discretization scheme is used for spatial gradients. Evaluation of the pressure gradients at the *cv* centers is explained below.

Step 4. Solve the variable-coefficient Poisson equation for pressure

$$\frac{1}{\Delta t} \sum_{\text{faces of } cv} u_N^* A_{\text{face}} = \sum_{\text{faces of } cv} \frac{1}{\rho_{\text{face}}^{n+1/2}} A_{\text{face}} \frac{\delta p}{\delta N}^{n+1/2} \tag{12}$$

where ρ_{face} is obtained using arithmetic averages of density in the neighboring *cv*s. The face-normal velocity u_N^* and the face-normal pressure gradient are obtained as

$$u_N^* = \tfrac{1}{2}(u_{i,\text{nbr}}^* + u_{i,cv}^*) N_{i,\text{face}}$$

$$\frac{\delta p}{\delta N}_{n+1/2} = \frac{p_{\text{nbr}}^{n+1/2} - p_{cv}^{n+1/2}}{|\mathbf{s}_{cv,\text{nbr}}|}$$

where nbr represents neighboring *cv* associated with the *face* of the *cv*, and $|\mathbf{s}_{cv,\text{nbr}}|$ is the distance between the two *cv*s. The variable-coefficient pressure equation is solved using a biconjugate gradient algorithm [19].

Step 5. Reconstruct the pressure gradient at the *cv* centers using density and face-area weighting first proposed by Ham and Young [20]

$$\frac{1}{\rho_{cv}^{n+1/2}} \frac{\delta p^{n+1/2}}{\delta x_i} = \frac{\sum_{\text{faces of } cv} \frac{1}{\rho_{\text{face}}^{n+1/2}} \frac{\delta p^{n+1/2}}{\delta N} \cdot \boldsymbol{i} |N_{i,\text{face}} A_{\text{face}}|}{\sum_{\text{faces of } cv} |N_{i,\text{face}} A_{\text{face}}|} \tag{13}$$

Step 6. Update the *cv*-center and face-normal velocities to satisfy the incompressibility constraint

$$\hat{u}_{i,cv} = u_{i,cv}^{*} - \Delta t \frac{\delta p_{cv}^{n+1/2}}{\delta x_i} \tag{14}$$

$$\hat{u}_N = u_N^{*} - \Delta t \frac{\delta p^{n+1/2}}{\delta N} \tag{15}$$

The face-normal velocity field $\hat{u}_N$ will satisfy the incompressibility constraint, however, the *cv*-based velocity may not satisfy the rigid body constraint inside the particle region. Note that in the absence of any rigid body, $\rho = \rho_F$, throughout the domain, the algorithm reduces to the standard fractional-step scheme for single-phase incompressible flow. The above velocity field will then be denoted as $u_{i,cv}^{n+1}$. In the presence of rigid bodies, the following steps are performed to enforce the rigidity constraint within the particle domain.

Step 7. First interpolate the velocity field $\hat{u}_{i,cv}$ from the grid *cv*s to the material volume centroids to obtain $\hat{U}_{i,M}$ using the kernel interpolation outlined in the Appendix. Solve for the translational and rotational velocity fields

$$\mathcal{M}_P \mathbf{U}_P^T = \sum_{M=1}^{N} V_M \rho_M \mathbf{U}_M \tag{16}$$

$$\mathcal{I}_P \boldsymbol{\Omega}_P = \sum_{M=1}^{N} \rho_M V_M (\mathbf{r} \times \mathbf{U}_M) \tag{17}$$

where subscripts P and M denote the particle and the material volume centroids respectively, V_M is the volume and ρ_M the density of each material volume, $\mathcal{M}_P = \Sigma_{M=1}^{N} \rho_M V_M$ is the total mass of the particle, $\mathcal{I}_P$ is the moment of inertia of the particle about the coordinate axes fixed to the particle centroid, and $\mathbf{r}$ is the position vector of a point within the particle region with respect to the particle centroid. The moment of inertia is given as

$$\mathcal{I}_P = \sum_{M=1}^{N} \rho_M V_M [(\mathbf{r} \cdot \mathbf{r})\mathbf{I} - \mathbf{r} \otimes \mathbf{r}] \tag{18}$$

where $\mathbf{I}$ represents the identity matrix. The rigid body motion is then obtained as

$$\mathbf{U}_M^{\text{RBM}} = \mathbf{U}_M^T + \boldsymbol{\Omega}_P \times (\mathbf{X}_M - \mathbf{X}_P) \tag{19}$$

Step 8. Compute the rigid body constraint force and correct the velocity field to satisfy this constraint within the particle region

$$F_{i,M}^{n+1} = -\frac{(U_{i,M} - U_{i,M}^{\text{RBM},n+1})}{\Delta t} \tag{20}$$

The force on the grid control volumes ($f_{i,cv}$) is obtained from $F_{i,M}$ by using the interpolation scheme discussed in the Appendix. The velocity field inside the particle region is then modified as

$$u_{i,cv}^{n+1} = \hat{u}_{i,cv} + \Delta t f_{i,cv}^{n+1} \tag{21}$$

4 Controller Design

Model-based control design requires a reduced order model of the flow dynamics that relates individual channel valve openings with the exit flow velocities for each channel. While direct numerical simulations of the flow field produce the most accurate relationship between these quantities, the computationally intensive nature of these simulations precludes their use in any real-time physical realization. However, many real-time control methodologies have been developed to control linear multiple-input multiple-output (MIMO) systems. The development of a reduced order linear MIMO model is therefore motivated both by the ability of linear models to adequately represent nonlinear flow dynamics in certain flow regimes and the relative success of linear control methodologies in controlling nonlinear systems.

4.1 System Identification. As a result, standard system identification techniques [21] are employed to produce a linear model of the flow dynamics, which relates channel valve openings (inputs) to channel exit flow velocities (outputs). Specifically, an autoregressive exogenous (ARX) model [22] of the flow dynamics is developed from direct numerical simulations of the flow regime, in which channel valve openings are varied in a prescribed fashion, and the resulting output flow velocities are recorded. While a linear MIMO ARX model is developed, the relationship between inputs and outputs in the ARX formulation is most easily illustrated for the single-input single-output case. In this instance a linear difference equation relates the input and output

$$\begin{aligned} y(t) = &- a_1 y(t-1) - a_2 y(t-2) - \cdots - a_{n_a} y(t-n_a) + b_1 u(t-n_k) \\ &+ b_2 u(t-n_k-1) + \cdots + b_{n_b} u(t-n_k-n_b+1) \end{aligned} \tag{22}$$

where $y(t)$ is the output, $u(t)$ is the input, n_k is the time delay, n_a is the number of poles, n_b is the number of zeros plus one, and a_i and b_j are constants to be determined via the identification process. The equation for the current output is therefore a function of both values of the output and the input at previous sampling instants. The choice of how many previous input and output values to retain is driven by the model validation procedure, in which the output prediction of the model is compared with the results obtained from direct numerical simulations of the flow for data not utilized in the identification process. In the multivariable case, the coefficients a_i and b_i become $n_o \times n_o$ and $n_o \times n_i$ matrices, respectively, where n_o and n_i represent the number of model outputs and inputs.

System identification is conducted following the procedure presented in Ref. [22]. Uncontrolled simulations are utilized to determine the system settling time, which informs the choice of both the sampling interval and the duration of the identification tests. Identification tests are subsequently conducted via numerical simulations of the flow field, in which channel valve angles are randomly varied to excite all modes of the flow dynamics. Flow velocities at the exit of each channel are recorded and this output data, in conjunction with the recorded variation in the input valve orientations, are processed within the MATLAB system identification toolbox to produce multiple linear ARX models of varying orders. Models are validated against numerical simulation data not used in the identification procedure. Channel exit flow velocities are generated by each model from the prescribed variation of the input valves used to produce the validation data set. These velocities are compared with those obtained by direct numerical simulation of the flow field. Model selection is governed by output accuracy, as balanced with model simplicity. The selected linear MIMO system model is subsequently employed as a substitute for the actual flow dynamics in the model-predictive controller design.

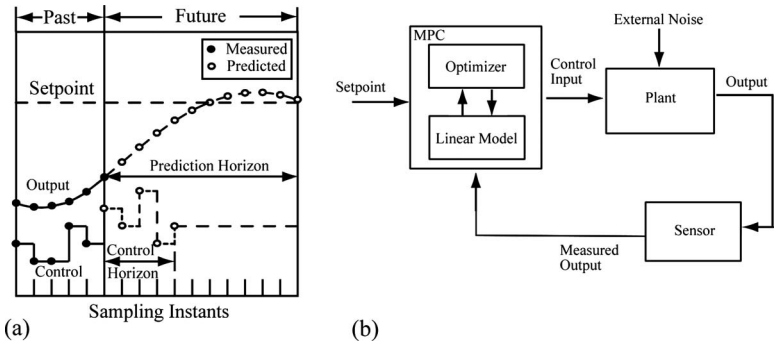

Fig. 4 Model-predictive control scheme: (*a*) inputs and outputs and their relation to the control and prediction horizon's (*b*) control system diagram including the model-predictive controller

4.2 Model-Predictive Control. A model-predictive control methodology [23] is employed to equalize flow velocities in a parallel microchannel configuration in the presence of bubble disturbances. Benefits of model-predictive control include real-time optimization of control outputs, direct incorporation of constraints on both manipulated and controlled variables, successful system operation closer to constraints, and robustness to model uncertainty and external disturbances. An overview of the functionality of a model-predictive controller is illustrated in Fig. 4 and summarized below.

For the parallel microchannel configuration studied, the model-predictive controller prescribes the valve openings for each channel (control inputs) from knowledge of the desired flow velocity at the exit of each channel (system setpoints) and the actual flow velocities (measured outputs). To determine the valve openings that will result in the measured flow velocities reaching the desired values in the future, the model-predictive controller utilizes the linear system model produced by the system identification procedure. Predictions of the exit flow velocities are generated using the model for a user-specified duration into the future (prediction horizon) from a sequence of channel valve openings over a user-specified control horizon. Optimal values for the valve openings are determined, via solution of a quadratic programming problem, over the control horizon such that a cost function involving the deviation from the desired setpoints is minimized over the prediction horizon. Once the optimal sequence of valve openings is determined, only the first set of openings is provided to the flow solver (plant). At the next sampling instant, the resulting exit flow velocities are measured and sent to the model-predictive control scheme. Utilizing this new information regarding the actual flow velocities achieved as a result of the valve openings, as opposed to those predicted by the linear model, the process repeats.

Realization of the model-predictive control design is achieved by through the MATLAB model-predictive control toolbox. The system model, control horizon, prediction horizon, cost function structure and associated weighting matrices, setpoint values, and the measured outputs are input into the MPC toolbox. The quadratic programming problem is solved within the toolbox to produce the channel valve openings utilized by the flow solver. The resulting strategy is computationally lightweight, enabling future physical implementation with small microcontrollers.

5 CFD-Controller Interface

To perform the coupled computational fluid dynamics (CFD)-controller simulations, we have developed a simple communication interface between the MATLAB-based control algorithms and FORTRAN-based CFD solver. The controller algorithms are run on a single processor, whereas the direct numerical simulations are performed on multiple processors. Figure 5 shows the schematic of the communication interface between the two packages.

An external communication interface, developed in FORTRAN, is created to manage execution of both the CFD simulation and the MATLAB-based model-predictive controller. Direct numerical simulations are executed as directed by the communication interface, and at each sampling instant, produce an American Standard Code for Information Interchange (ASCII) text file containing the outlet flow velocities of each channel. This file is read by the MATLAB-based control program, and system states are employed by the model-predictive control algorithm to produce a new set of valve openings written to an external file. Once written, the file of valve openings is read by the CFD solver and the process repeats. Valve openings are not instantaneously changed in the direct numerical simulations, rather a maximum rate of change is prescribed and the valves move from their prior position to the prescribed openings at this rate.

The direct numerical simulations mainly govern the total simulation time mainly due to the details of the flow captured. The MATLAB-based controller takes a negligible amount of time compared with CFD. This framework is efficient and is applicable to several other physics problems requiring coupling of CFD and model-predictive control.

6 Validation Cases

The numerical formulation and the control algorithm are first used to perform basic validation and verification studies. The numerical test cases were chosen to validate the basic incompressible flow algorithm applied to high-aspect ratio channel flows, flow developed by objects undergoing specified motion to test the capability of the solver to handle moving microvalves, motion of freely moving particles and bubbles, and finally testing of the coupled CFD-control algorithm. Accordingly, the following tests are performed: (i) single-phase incompressible flow in a high-aspect ratio microchannel at different Reynolds numbers corresponding to the experimental data of Qu et al. [24], (ii) flow over a fixed cylinder at different Reynolds number, (iii) flow developed by an oscillating sphere corresponding to experiments by Dütsch et al. [25], (iv) rising of a small bubble in an inclined channel corresponding to experiments by [26], and (v) equalizing mass-flow rates in parallel microchannels using model-predictive con-

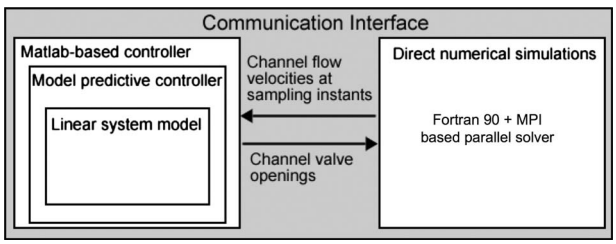

Fig. 5 Schematic of CFD-controller interface

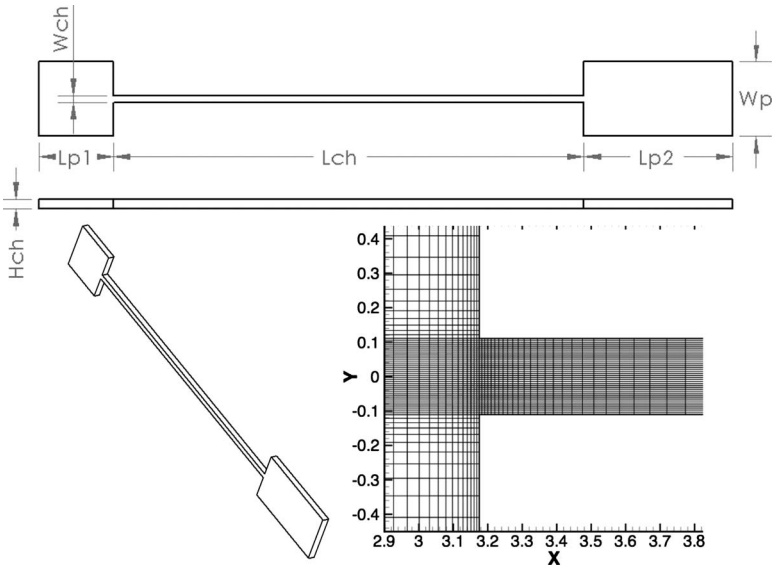

Fig. 6 Schematic and grid for the single channel geometry. The grid used consists of around 1.5×10^6 grid elements. Only a small section of the grid is shown.

trol. After these extensive validation studies, the coupled solver is applied to mitigate flow maldistribution in parallel microchannels.

6.1 Microchannel Channel Case. Simple flow in a 3D channel, as studied by Qu et al. [24], serves as the initial test case. Validation of the flow solver for this test case is a critical step toward our simulation goal, since the parallel microchannel geometry of interest involves flow through microchannels with a high-aspect ratio (see Fig. 6).

Channel dimensions are given in Table 1. As seen from the schematic, the ratio of plenum to microchannel height is very large. The computational grid consists of around 1.5×10^6 grid points with roughly 30 cells inside the microchannel in the vertical direction. The grid cells are refined near the walls and near the entrance region to resolve the flow accurately. Fluid flow through the channel is simulated for different Reynolds numbers (Re = 196 and Re = 1895), and the resulting velocity profiles and pressure drops are compared with the experimental and numerical results presented in Ref. [24]. In these simulations, two large plenums are used at the inlet and outlet of the domain to ensure that the boundary conditions do not perturb the solution inside the channel. A fully-developed velocity profile for a three-dimensional rectangular channel [24] is applied at the inlet of the domain, and data are only collected after the flow in the channel reaches steady state.

Table 1 Dimensions (in millimeters) for the single microchannel [24]

Wch	Wp	Hch	Lp1	Lpch	Lp2
0.222	6.35	0.694	6.35	120	12.7

Figure 7 illustrates the comparison of the simulated velocity profile over the cross section at different locations within the channel to the numerical and experimental data in Ref. [24]. The simulations produce a parabolic profile and good agreement with the both the numerical and experimental results. For larger Reynolds numbers, the numerical velocity at the center of the channel is slightly larger than the experimental data; however, it agrees with the simulations conducted by Qu et al. [24]. These deviations are within the uncertainties in maintaining constant flow rates, as well as velocity measurements. As illustrated in Fig. 8, the velocity along the center line of the channel, for the length of the channel, shows very good agreement with the experimental data.

Table 2 presents the comparison of numerically obtained pres-

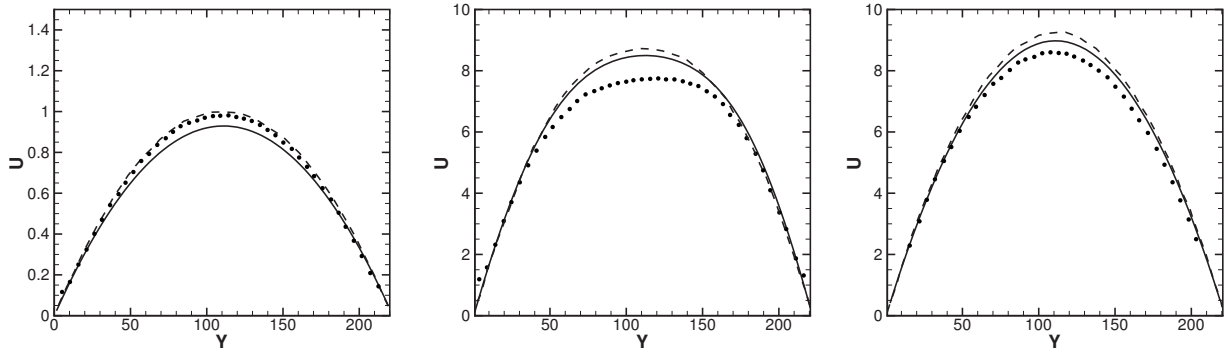

(*a*) $Re = 196, x' = 1\ cm$ (*b*) $Re = 1895, x' = 1\ cm$ (*c*) $Re = 1895, x' = 10\ cm$

Fig. 7 Velocity profiles in the center plane of the channel taken at $x'=1$ cm and $x'=10$ cm from the entrance of the channel. ● shows the experimental data, – – – shows the numerical simulation from Ref. [24], and — shows the present study. The velocity is expressed in m/s and the *y* location is expressed in microns.

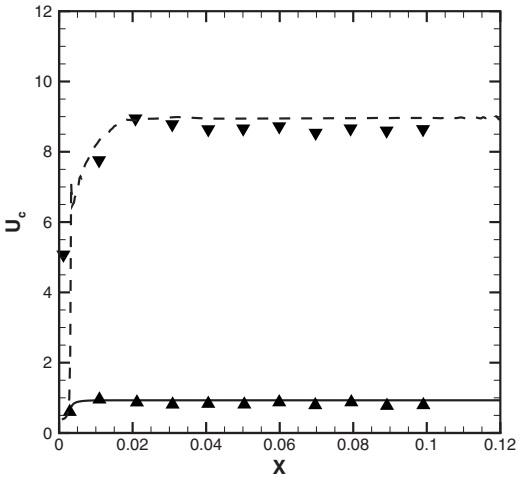

Fig. 8 Velocity distribution along the central line of the channel. Re=196: ▲ shows the experimental data from Ref. [24], and — shows the present simulation; Re=1895: ▼ is the experimental data, and – – – shows the present simulation. Velocity is expressed in m/s and the *x* location is expressed in meters.

sure drop inside the microchannel with the theoretical pressure drop in a square microchannel (excluding the plenums). A good agreement is achieved for low Reynolds number (up to $Re_{ch}=1021$). For $Re_{ch}=1895$ the pressure drop is underpredicted by the simulation. This is attributed to the effects of sudden changes in aspect ratios near the inlet and outlet plenums. Flow separations are possible near the entrance, modifying the flow evolution to fully-developed velocity profile and thus affecting the overall pressure drop. To test the accuracy of the solver, we have also simulated flow through the microchannel duct (without the plenums) with uniform inlet on a grid similar to the grid used for the case with plenums. The pressure drop values for the same mass-flow rates are shown in Table 2 and agree well with the theoretical estimates.

Table 2 Comparison between computed and theoretical pressure drops at different Reynolds numbers

	Pressure drop (bar)		
Re_{ch}	DNS (with plenum)	DNS (without plenum)	Theory (without plenum)
196	0.189	0.195	0.20
1021	1.09	1.06	1.04
1895	1.33	1.87	1.93

6.2 Flow Induced by an Oscillating Cylinder. Simulation of a periodic oscillating cylinder in a fluid at rest has often been used to test the accuracy of immersed boundary techniques and serves as our second test case. Numerical simulation results are validated against those of Kim and Choi [27], as well as experimental data available from Ref. [25].

Two nondimensional numbers characterize a periodic oscillating cylinder: the Reynolds number $Re=U_m d/\nu$ and the Keulegan–Carpenter number $KC=U_m/fd$, where $U_m=0.01$ m/s is the maximum velocity of the cylinder, $f=0.2$ Hz is the frequency of the oscillations, $d=0.01$ m is the diameter of the cylinder, and ν is the kinematic viscosity. The position of the cylinder in the x-direction is defined by the equation

$$x_p(t) = -A_p \sin \omega t \tag{23}$$

where $x_p(t)$ is the location of the centroid of the cylinder in the x-direction, and A_p is the maximum amplitude of the oscillations. Because the oscillation frequency is given by $\omega=2\pi f$, the Keulegan–Carpenter number can be rewritten as $KC=2\pi A_p/d$. Simulations are conducted with $Re_d=100$ and $KC=5$, as in Ref. [27]. The computational domain is comprised of a square box $100d\times 100d\times d$, respectively, in the axial, vertical, and spanwise directions. The grid is refined and uniform in the region of motion of the cylinder and stretched toward the walls. Grid resolution in the cylinder region is refined so that 20 grid points are always located along the cylinder diameter. Neumann boundary conditions are applied in the x and y directions. Simulations begin with the both the flow and cylinder at rest, with the cylinder positioned in the center of the domain. Simulation data regarding fluid flow are collected after the cylinder has gone through ten cycles.

The normalized velocity in the wake of the cylinder at three different phases of the cycle is compared with numerical and experimental results in Fig. 9. As illustrated, our results show excellent agreement with both the experimental [25] and numerical simulation data [27].

6.3 Rising Spherical Bubbles. We test the numerical algorithm for bubbles rising in a stationary fluid. Two test cases are considered: (i) a single spherical bubble rising in an inclined channel corresponding to the study of Lumholt et al. [26] at a low density ratio ($\rho_f/\rho_p\sim 1.03$), and (ii) a spherical bubble rising in a straight channel at high-density ratio ($\rho_f/\rho_p=1000$). The first case is important to show that the present approach correctly captures the hydrodynamics of the rising bubble and the thin layer between the bubble and the channel wall. The second case tests the stability of the solver at high-density ratios.

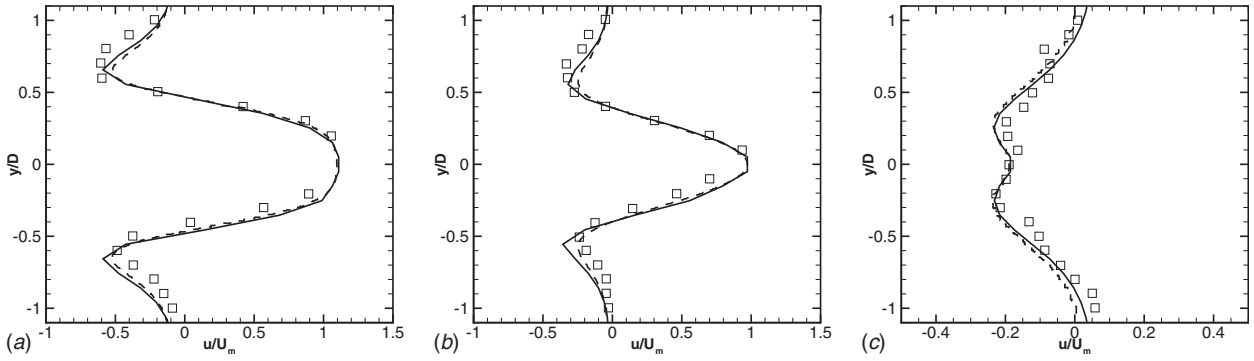

Fig. 9 Normalized axial velocity (u/U_m) at three different phase positions. The velocity is measured at a fixed *x* location ($x=-0.6d$) relative to the initial location of the particle center: □ shows the experimental data from Ref. [25], — shows the present simulation, and – – – shows the numerical results from Ref. [27].

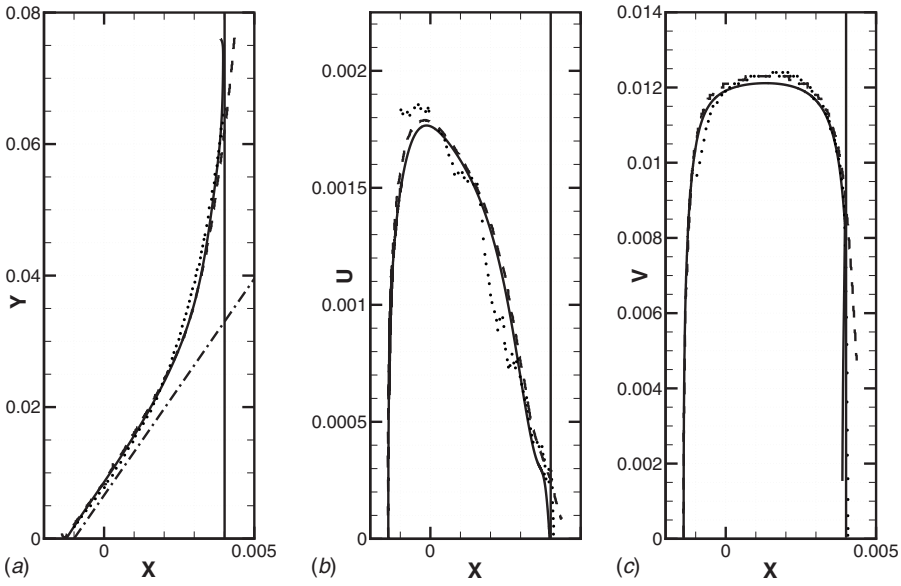

Fig. 10 Comparison of experimental ● and numerical simulations – – – [26] with the current simulation —. (*a*) shows the particle trajectory inside the domain (the –·– line shows the initial trajectory due only to the effect of gravity), (*b*) shows the velocity of the particle in the lateral direction, and (*c*) shows the velocity on the vertical direction. The particle position is expressed in meters and the velocities are expressed in m/s.

6.3.1 Sphere Rising in Inclined Channel. Flow solver performance is also examined for another case of particle motion: a bubble rising in an inclined channel. In the simulation, the bubble is modeled as a rigid spherical particle flowing in an inclined channel. The simulation is conducted with a fluid density of $\rho_f = 1115$ kg/m^3, a bubble density of $\rho_p = 1081$ kg/m^3, and a fluid viscosity of $\nu = 3.125$ mm^2/s. The Reynolds number $\mathrm{Re}_p^{\mathrm{Stokes}}$ based on the Stokes settling velocity W is defined as

$$\mathrm{Re}_p^{\mathrm{Stokes}} = \frac{2aW}{\nu} = \frac{4a^3}{9\nu^2}\left|\frac{\rho_p}{\rho_f} - 1\right| g \tag{24}$$

where $g = 9.82$ m/s^2 is the gravitational acceleration, and $a = 2$ mm is the diameter of the particle. The channel is inclined at an angle of 8.23 deg with the vertical. This is simulated by adding components of gravitational forces in the horizontal and vertical directions.

The computational domain consists of a rectangular box with dimensions 10 mm in the x direction, 80 mm in the y direction, and 40 mm in the z direction. The grid is Cartesian and uniform over the domain with $40 \times 320 \times 160$ grid points, respectively in the x, y, and z directions so that $\Delta = 0.25 \times 10^{-3}$ m. The bubble is injected at $x = -1.4$ mm, $y = -1.0$ mm, and $z = 20.0$ mm. Simulation results for a Reynolds number of $\mathrm{Re}_p^{\mathrm{Stokes}} = 13.6$ are compared with experimental and numerical data from Ref. [26]. As illustrated in Fig. 10, the numerical simulation exhibits excellent agreement with both experimental and numerical results. Buoyancy forces cause the bubble to rise and travel alongside the right wall of the domain. Ultimately, the particle follows the right wall without touching it, keeping a very thin lubrication layer between the particle and the wall. This simulation validates that the numerical approach is capable of simulating freely moving rigid objects.

6.3.2 Rising Sphere With High Density Ratio. We consider a sphere (diameter 6.66 mm, $\rho_p = 1$ kg/m^3) rising in a quiescent fluid ($\rho_f = 1000$ kg/m^3, $\mu_f = 0.0422$ kg/m s) in a vertical channel of size $0.02 \times 0.02 \times 0.09$ m^3. Initially the spherical bubble is placed at the center of the channel and a height of 0.01 m from the bottom wall. The bubble starts rising due to buoyancy force ($g = 9.8$ m/s^2) and reaches a terminal velocity. The computation is performed on a uniform grid ($80 \times 80 \times 360$ giving approximately 26 points within the sphere) and the time-step is 25 μs.

Mordant and Pinton [28] performed experiments on freely falling spherical particles in a large water tank for various density ratios (maximum density ratio considered was $\rho_p/\rho_f = 14.6$). They showed that for small particles falling in a large tank (that is, for small values of the ratio of particle diameter to tank width $D_p/L \sim 0.005$) the temporal evolution of the particle velocity can be well predicted by the curve

$$U^* = 1 - \exp\left(-\frac{3t}{\tau_{95}}\right) \tag{25}$$

where U^* is the velocity of the particle normalized by its terminal velocity, τ_{95} is the time it takes for the sphere to reach 95% of its terminal velocity, and t is the time. We compare the temporal evolution of the rising spherical particle to this curve in Fig. 11. The present simulations are performed for a much higher density ratio $\rho_f/\rho_p = 1000$. The domain size in simulations is small ($D_p/L = 0.333$) and thus wall effects become important. This test case confirms the stability of the numerical solver when applied to large-density ratio fluid-particle systems.

Additional test cases of the present approach for large-density ratio fluid-particle systems were also performed to show code stability and accuracy [29].

6.4 Equalizing Flow Rates in a Parallel Microchannel Geometry. The coupling and coordination between the control system design and the flow solver are examined via flow equalization in a parallel microchannel geometry. In this test case, a fully-developed parabolic velocity profile is imposed at the inlet. This inflow condition combined with the nonsymmetric geometry of the parallel microchannels produces different mass-flow rates in each of the channels. Because the mass-flow rate is imposed at the inlet, the amount of fluid entering the geometry is known. As a result, without any bubble in the geometry, the controller regulates the flow in each channel by varying channel valve openings to achieve equal mass-flow rates in each channel. Simulation de-

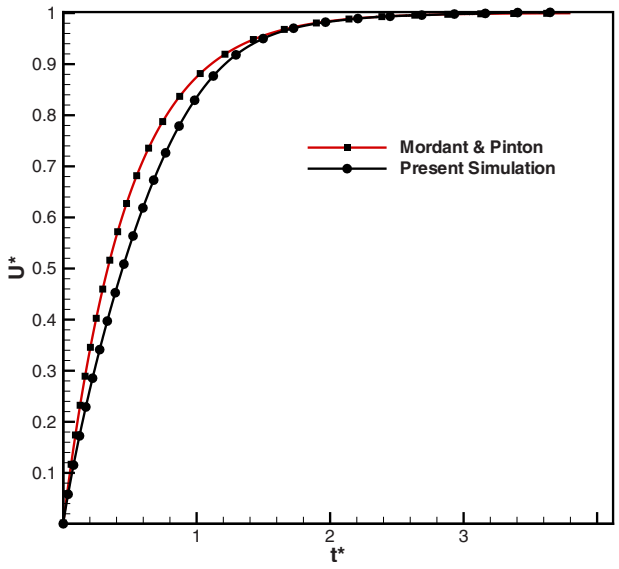

Fig. 11 Temporal evolution of a spherical bubble rising in a water column: $U^* = U/U_{terminal}$ and $t^* = t/\tau_{95}$. Square symbols are for Ref. [28] and circle is for the present simulation.

tails, including the geometry, boundary conditions, grid, and controller design are detailed in Sec. 7.

Figure 12 shows the velocity contour of the fluid inside a three-channel microchannel once the steady state has been achieved and the flow has been equalized by the controller. As illustrated, mass-flow rates are equalized in each channel through partial closure of each valve. The maximum amount of closure occurs for the center channel valve due to the increased flow velocity that occurs as a result of the inlet boundary condition and the asymmetry of the geometry.

Figure 13(*a*) shows the mass-flow rate history in each channel, and Fig. 13(*b*) illustrates the corresponding history of the controller actions. Initially, different mass-flow rates exist in each channel, with the maximum flow rate occurring in the middle channel. Valve actuation, as prescribed by the controller, partially closes the valves in each of the channels, reducing the flow rate in the center channel while increasing it in both the upper and lower channels until equal flow rates are achieved. The maximum difference between the mass-flow rates in the three channels is 0.12%, and the error in the steady-state flow rates to the theoretically computed value for the inlet flow rate is 0.16%.

7 Flow Simulation Through Parallel Microchannels

In this section the results for a three-channel microchannel are presented. The schematic of the geometry and the model used for these simulations are presented in Fig. 1. A single bubble is introduced in the top channel, and the resultant flow distribution is first examined. A control algorithm is developed that senses the presence of the bubble and resultant flow maldistribution, activates microvalves, and facilitates effective removal of the bubble. Details of these coupled CFD-control simulations are discussed here.

7.1 Geometry and Model. The parallel microchannel geometry considered consists of three microchannels, and two plenums for the inlet and outlet (see Fig. 1). The dimensions of the domain are 0.8 mm in the x direction, 0.4 mm in the y direction, and 0.025 mm in the spanwise direction. The spanwise dimension remains constant for the entire geometry. The inlet plenum is 0.25 mm and 0.4 mm in the x and y directions, respectively. The outlet plenum

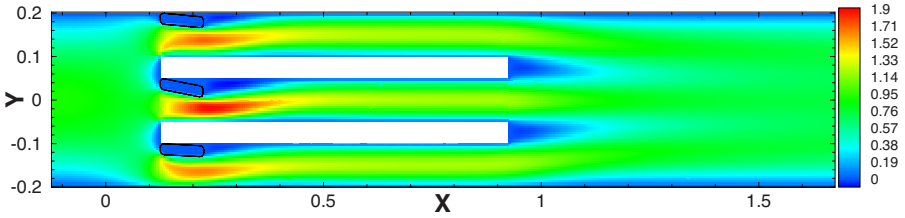

Fig. 12 Steady state velocity contours in a parallel microchannel after flow rates in each channel are made equal. Also shown are the steady-state position of the microvalves. Lengths are expressed in millimeters and the velocity contours are in m/s.

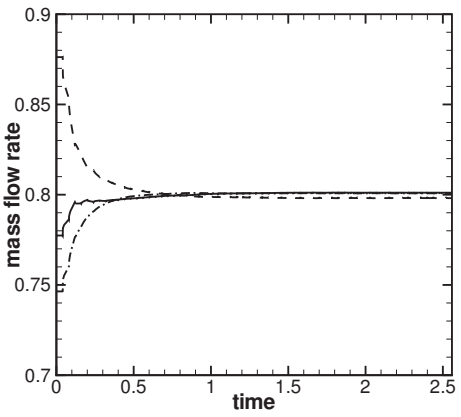

(*a*) Velocity history in each channel

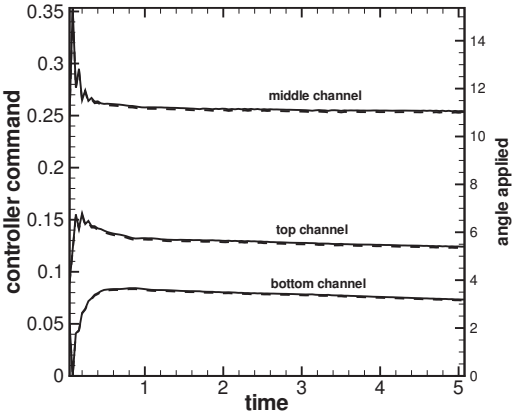

(*b*) Controller output history correlated with angle applied to each valve.

Fig. 13 Time evolution of the flow rates (*a*) and controller input (*b*) to the flow solver: – – – shows the data for the top channel; — shows the middle channel; – – shows the bottom channel. The mass-flow rate is expressed in kg/s, time is expressed in milliseconds, and angles are expressed in degrees.

Table 3 Control parameters used for controller design and system ID tests

Control parameters	
Control horizon	Five sampling periods 0.2 ms
Prediction horizon	Ten sampling periods 0.4 ms
Valve position weighting matrix	Diagonal 3×3 matrix, 0.001 on diagonal
Valve rate weighting matrix	Diagonal 3×3 matrix, 1.0 on diagonal
Output error weighting matrix	Diagonal 3×3 matrix, 10 on diagonal
Valve opening constraint	Constrained to remain between 0 and 1
Valve rate constraint	Constrained to remain within -0.15 and 0.15

is 0.75 mm and 0.4 mm in the x and y directions, respectively. The outlet plenum is longer than the inlet to prevent the outflow boundary from perturbing the flow inside the channels. Dimensions of all three channels are equal: 0.8 mm in the x direction and 0.1 mm in the y direction. The fluid used in this study is water with fluid properties at room temperature. The density ratio between the fluid and the rigid vapor bubble was held fixed at 10. Simulations with higher density ratios (on the order of 100) revealed similar results, as presented below.

The grid is cubic and uniform in each direction so that $\Delta = 0.005$ mm, therefore, there are five grid points in the z direction all over the domain. Each channel contains 20 grid points in the y direction and 160 grid points in the x direction. Over the entire domain there are 128,000 grid points.

At the inlet boundary of the domain a 2D fully-developed parabolic profile is applied, the fluid used having the same properties as water. The maximum velocity at the center of the parabolic profile is defined by $3/2U_p$, where $U_p=0.6$ m/s so that the global mass-flow rate entering the computational domain is $\dot{m} = 2.4$ mg/s.

7.2 System Identification and Controller Development. The system settling time in response to a step change in a valve position was numerically determined as approximately 0.8 ms, which was the time required for the channel flow velocities to reach 98% of their steady-state values. A sampling interval of one twentieth of the settling time, or 0.04 ms, was chosen for both the identification tests and the control design. A generalized binary noise (GBN) signal was generated to prescribe the closure of each of the valves between fully open and 50% closed for the system identification test. The GBN signal was created with a mean switching time of one-third the settling time and a minimum switching time equal to the sampling rate. The duration of the test was twelve times the settling time or 9.6 ms.

Input and output data generated by the numerical system identification test were processed in the MATLAB system identification toolbox to produce ARX models of varying complexities. Model validation was performed for each model, with model quality judged by a "best fit" criterion

$$\text{best fit} = \left(1 - \frac{\|y - \hat{y}\|}{\|y - \bar{y}\|}\right) \times 100 \tag{26}$$

where y is the measured output, $\hat{y}$ is the predicted output, and $\bar{y}$ is mean of the measured output. A model has a perfect best fit value of 100% if $\hat{y}$ is equal to y. A best fit value of zero represents a fit, which is no better than picking a constant value of $\bar{y}$ for the model output. A model with three poles, two zeros, and one delay produced best fit values of 86.5%, 87.6%, and 83.7% for channels one, two, and three, respectively. Models of lower order were significantly less accurate, while higher order models were only marginally more accurate. The model identified by this process, and subsequently utilized in the controller design, was

$$\begin{aligned} I\mathbf{y}(t) = &- \begin{bmatrix} -2.09 & -0.91 & -0.74 \\ -1.70 & -3.00 & -1.87 \\ 3.13 & 3.21 & 1.96 \end{bmatrix} \mathbf{y}(t-1) \\ &- \begin{bmatrix} 2.15 & 1.92 & 1.69 \\ -1.00 & -0.72 & -0.76 \\ -0.99 & -1.04 & -0.77 \end{bmatrix} \mathbf{y}(t-2) \\ &- \begin{bmatrix} -1.82 & -1.85 & -1.79 \\ 1.99 & 2.04 & 1.92 \\ -0.03 & -0.05 & 0.01 \end{bmatrix} \mathbf{y}(t-3) \\ &+ \begin{bmatrix} 0.05 & -0.02 & -0.02 \\ -0.02 & 0.05 & -0.02 \\ -0.03 & -0.03 & 0.04 \end{bmatrix} \mathbf{u}(t-1) \\ &+ \begin{bmatrix} 0.01 & -0.03 & -0.01 \\ -0.01 & 0.03 & -0.02 \\ -0.01 & -0.00 & 0.02 \end{bmatrix} \mathbf{u}(t-2) \\ &+ \begin{bmatrix} -0.02 & 0.02 & 0.01 \\ 0.01 & -0.04 & 0.01 \\ 0.01 & 0.02 & -0.02 \end{bmatrix} \mathbf{u}(t-3) \end{aligned} \tag{27}$$

where $\mathbf{y}(t)=[y_1(t)y_2(t)y_3(t)]^T$ represents the flow velocity in each channel, and $\mathbf{u}(t)=[u_1(t)u_2(t)u_3(t)]^T$ represents the valve closure for each channel.

Controller design required specification of the control horizon, prediction horizon, and the cost function form and associated weighting parameters. In this study, a quadratic cost function was constructed in terms of a vector of valve positions, a vector comprised of the change in the valve positions in one sampling period, and a vector representing the difference between the exit flow rates and the desired values. Selection of the values in the weighting matrices of the cost function provided a means to balance the magnitude and rate of the valve closures with the attainment of the desired exit flow rates. Initial values for the control horizon, prediction horizon, and weighting matrices were computed via the tuning strategy detailed in Ref. [30]. These parameters were subsequently refined based on simulation results of the controlled performance. Final values utilized in the simulation results are presented in Table 3.

7.3 Effect of a Single Bubble on the Flow Distribution. First, the effect of a single bubble present in the top channel of the three-channel geometry on the flow distribution is investigated. A 60 μm bubble is introduced in the top channel close to the bottom side of the channel wall. The bubble plugs 60% of the channel height. The bubble is held fixed at this location, and its effect on the flow distribution and pressure drop are presented below. In this work, we do not simulate the physics of bubble nucleation and bubble growth. Instead, a bubble is introduced initially and held fixed. This represents a practical situation wherein the sur-

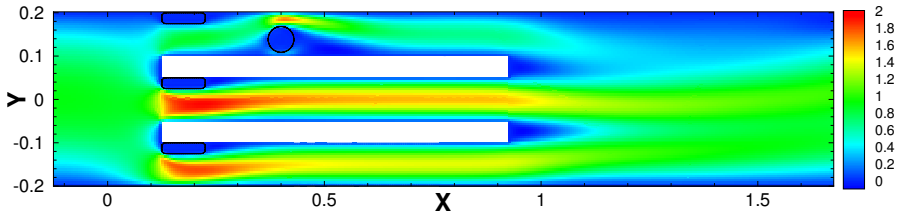

(*a*) Velocity contour

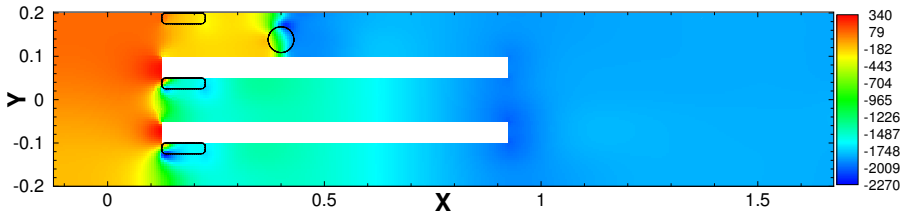

(*b*) Pressure contour

Fig. 14 Velocity and pressure contours inside the parallel microchannel with presence of a stationary bubble in the top channel. The lengths are expressed in millimeters, the velocity is expressed in m/s, and the pressure is expressed in pascals.

face tension and viscous forces on the bubble are greater than the hydrodynamic forces, and the bubble remains attached to one side of the channel wall.

Figures 14(*a*) and 14(*b*) show contours of axial flow velocity and pressure inside the parallel microchannel in the presence of a bubble in the top channel. For this configuration the microvalves are completely open and controller is not activated, and the flow maldistribution is clearly visible. Figure 15(*a*) shows the history of flow rates in each channel after the bubble is injected into the top channel, whereas Fig. 15(*b*) shows the steady-state pressure drop in each branch of the microchannel in the presence of the bubble, indicating a higher pressure drop in the top channel.

Next, we estimate the range of forces acting on the bubble held fixed in the top channel by varying the microvalve configurations. We consider two extreme cases: (a) all microvalves are completely open, and (b) the middle and bottom channel are completely closed by microvalves. In the first case, majority of the flow goes through the middle and bottom branches, whereas in the latter case all flow goes through the top channel. Figure 16 shows the time history of the forces on the bubble in these two extreme configurations. It is found that when the bottom and middle channels are completely closed, the entire inflow goes through the top channel, increasing the hydrodynamic forces on the bubble. The range of the forces applied to the bubble in these extreme configurations varies from 0.013 μN to 0.19 μN. The magnitude of the force, when the bottom and middle channels are closed, is larger than the forces necessary to hold the bubble fixed, estimated based on the surface tension forces, and thus the bubble can be removed by increasing mass-flow rate in the top channel. Without any actuation (i.e., all valves are completely open), the hydrodynamic force on the bubble is insufficient to overcome the estimated surface tension forces, and thus the bubble will remain fixed inside the top channel. The goal of the controller then is to

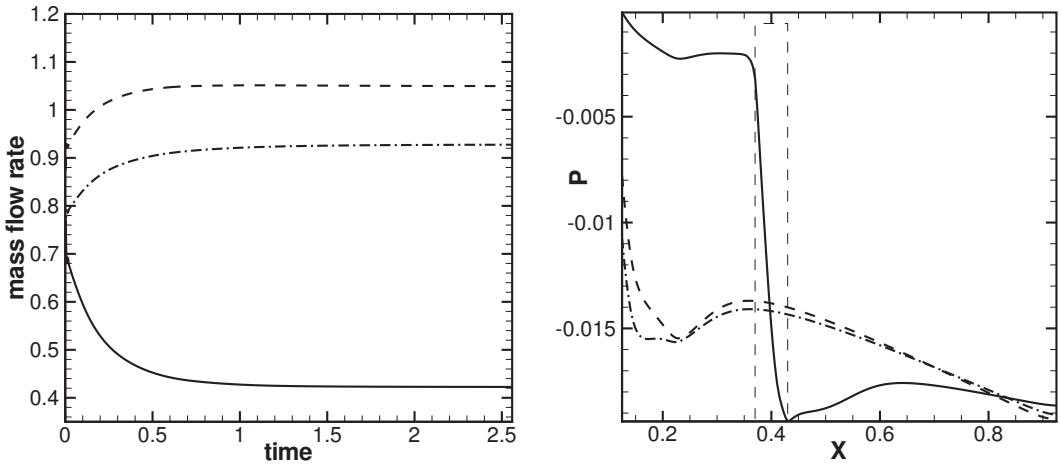

(*a*) Mass Flow Rate (*b*) Pressure Drop

Fig. 15 Temporal evolution of mass-flow rate (*a*) in each channel and steady-state pressure drops (*b*) in each branch: — shows the top channel; – – – shows the middle channel; – – – shows the bottom channel. The mass-flow rates are expressed in mg/s, time in milliseconds, length in millimeters, and pressure in bars. The dashed rectangle in right panel represents the location of the bubble.

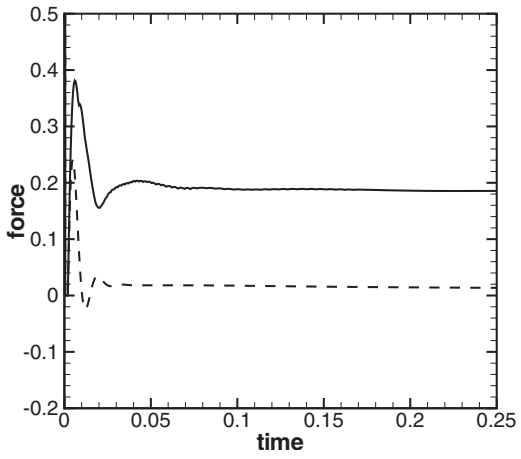

Fig. 16 Temporal evolution of the total force acting on the bubble: – – – shows that all channels are open, and — shows that the middle and bottom channels are completely closed. The forces are expressed in μN and the time is expressed in milliseconds. *The horizontal dashed line represents the threshold inertial force necessary to set the bubble in motion.*

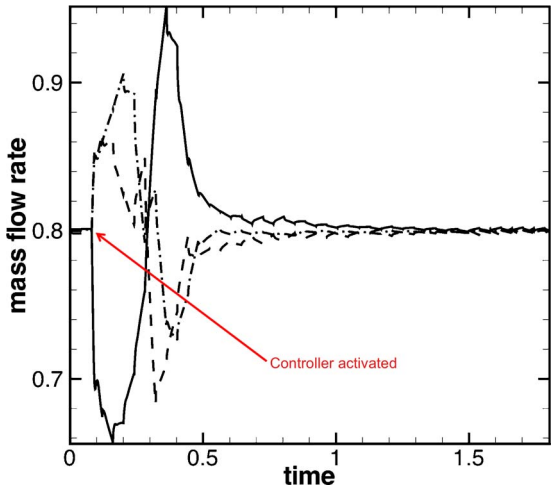

Fig. 17 History of the flow in each channel with injection of the bubble at t=0.04 ms. — shows the data for the top channel; – – – shows the middle channel; – – shows the bottom channel. The time is expressed in milliseconds and the mass-flow rate is expressed in mg/s.

first detect flow maldistribution and then to activate microvalves such that the flow rate inside the top channel is increased sufficiently to remove the bubble. This is achieved by slowly activating the microvalves in the middle and the bottom channel.

7.4 Coupled CFD-Controller Simulations. The model-predictive control algorithm developed above is applied to mitigate flow maldistribution due to presence of bubbles in branches of parallel microchannels shown in Fig. 1. Two cases are investigated to show the effectiveness of the controlled simulations: (i) the presence of a single bubble in the top channel and (ii) the presence of one bubble in the top and bottom channels. The history of the controller commands, evolution of the flow rates in each branch, and the trajectory of the bubble are presented below.

7.4.1 Single Bubble Simulation. We start with a steady-state solution for the three-channel geometry (see Fig. 1) with valve configurations set such that flow rates are equalized in branch of the channel. A single bubble of diameter 60 μm blocking the upper channel 60% is then introduced in the upper channel. The controller sensor and actuator are activated to first sense the flow maldistribution and then to provide inputs to the microvalves to regulate the flow rates in each channel such that the bubble is effectively removed.

As a sensor, we monitor the flow rates at the exit of each branch of the microchannel. Figure 17 shows the history of the mass-flow rates in each branch of the microchannel starting with initial equal rates. With the presence of the bubble in the top branch, the mass-flow rate in the top channel decreases, whereas those in the bottom and middle channels increase. This disparity in the flow rates is detected by the sensor, and the controller provides a series of commands to each microvalve such that equal flow rates are restored in each channel.

Figures 18(*a*)–18(*c*) provide the temporal history of the controller command and the location and velocities of the bubble. As the sensor senses flow maldistribution, it starts to close the middle and bottom channels, thus, increasing the flow rate in the top channel. This increase in flow increases the hydrodynamic forces on the bubble, and the bubble is set in motion as soon as the hydrodynamic force exceeds a precalculated resistive force (due to surface tension forces) on the bubble. Once in motion, the bubble quickly acquires the velocity of the fluid flow as its Stokes number is very small. The bubble is slowly moved out of the top branch. The controller then starts to close the top channel such that the flow rates in all channels are equalized.

7.4.2 Multiple Bubble Simulation. To test the controller on multiple bubbles, we introduce bubbles in the top and the bottom channels. The bubbles are placed close to the bottom walls of respective branches. The bubble in the bottom channel is farther downstream as compared with the bubble present in the top channel. Figure 19 shows the pressure drop distribution inside the microchannel after the bubbles are introduced and before the controller is activated. It clearly shows large pressure drops in branches with bubbles, and correspondingly the flow rates are also reduced in those channels.

Once the controller is activated, the sensors sense flow maldistributions with lower flow rates in the bottom and the top channels and a high flow rate in the middle channel. The controller starts closing the middle valve while keeping the others fully open. This diverts the flow in the other two channels. Figure 20(*a*) shows temporal history of the controller command correlated with the angular positions of the microvalves. Large variations in the microvalve positions are observed initially during the initial transient after introduction of the bubbles. A time history of the flow rates in each branch of the channel is shown in Fig. 20(*b*). With the increase in flow rates in the top and bottom channels, the net force on the bubbles in respective branches also increases. Figure 20(*c*) shows the history of the force acting on the bubbles in the top and bottom channels. For this simulation, the force on the bottom bubble exceeds the threshold required to obtain an attached bubble, releasing the bubble in the bottom channel first. As soon as the bubble starts moving, it quickly reaches its terminal velocity (owing to the small Stokes number), and the total force on the bubble reduces. Once the hydrodynamic forces on the bubble in the top channel overcome the estimated resistive forces, the bubble starts moving downstream. Finally, the bubbles move out of the channel branches to the exit plenum, and the controller acts on all microvalves in order to equate the flow rates in each branch of the parallel microchannel.

Figures 21(*a*)–21(*c*) show the velocity contours at three different stages during this coupled simulation: (i) before activation of the controller indicating flow maldistribution, (ii) after the controller is activated, the time at which the bubble in the bottom channel starts moving, and (iii) the time at which the bubble in the top channel is released. Before the controller is activated, the flow rate in the middle channel is much larger compared with the other two branches. Once the controller is activated, it closes the microvalve for the middle channel and fully opens the valves in the top

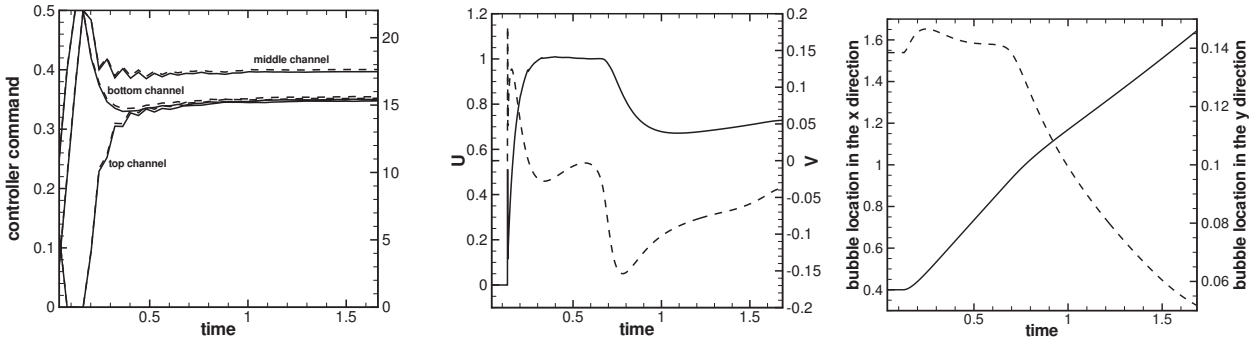

(*a*) Controller command (*b*) Bubble velocity (*c*) Bubble location

Fig. 18 Temporal evolution of the bubble motion and the controller commands: (*a*) controller command —— history correlated with angular location – – – – for each microvalve, (b): axial — and vertical – – – – velocities of the bubble, and (c) axial —— and vertical – – – – locations of the bubble. Time is expressed in milliseconds, velocities are expressed in m/s, bubble locations are expressed in millimeters, and angles are expressed in degrees.

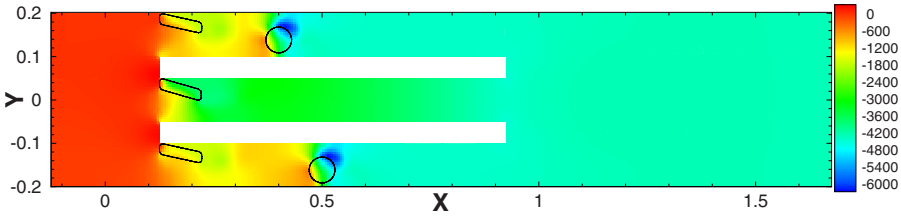

Fig. 19 Pressure contours in the presence of two bubbles before the controller is activated. The pressure is expressed in pascals and lengths are in millimeters.

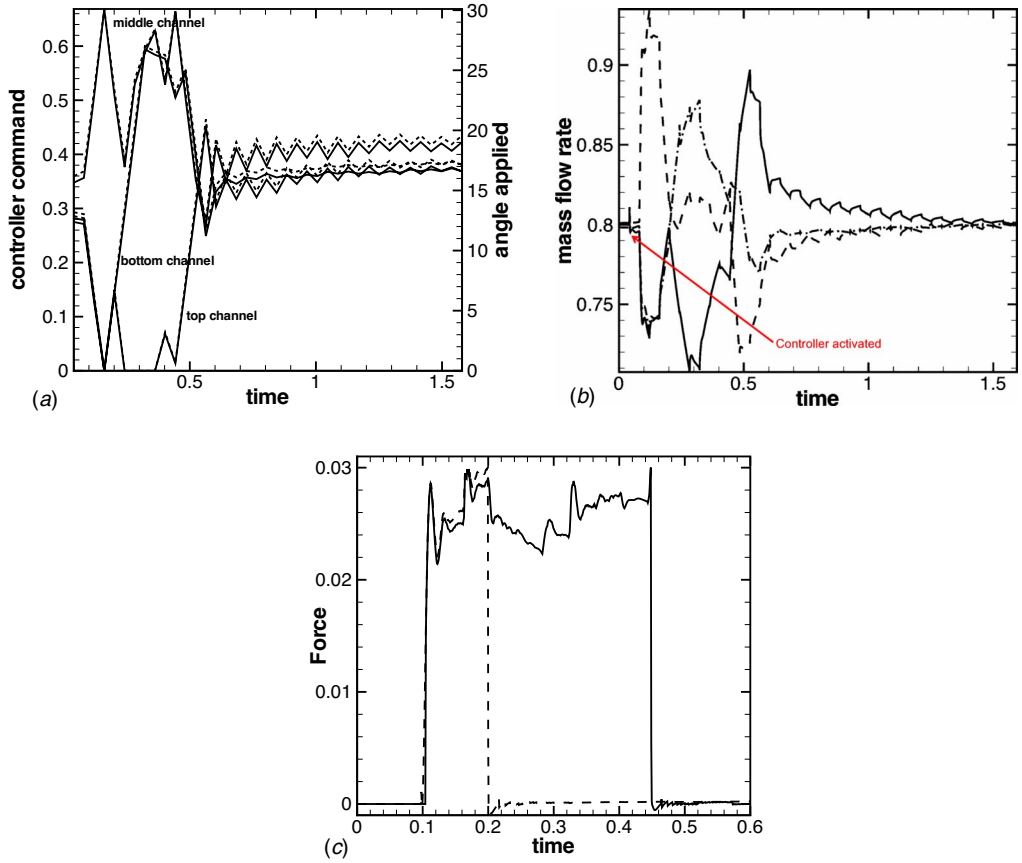

Fig. 20 Temporal histories of controller command, mass-flow rates, and forces on the bubbles: (*a*) history of controller commands — correlated with angular positions of microvalves – – – ; (*b*) mass-flow rates measured at the end of each channel:— shows the top channel, – – – shows the middle channel, and –·–·– shows the bottom channel; (*c*) history of total forces acting on the bubbles: — shows the bubble initially in the top channel, and – – – shows the bubble initially in the bottom channel. Time is expressed in milliseconds, angles are expressed in degrees, force is expressed in μN, and mass-flow rates are expressed in kg/s.

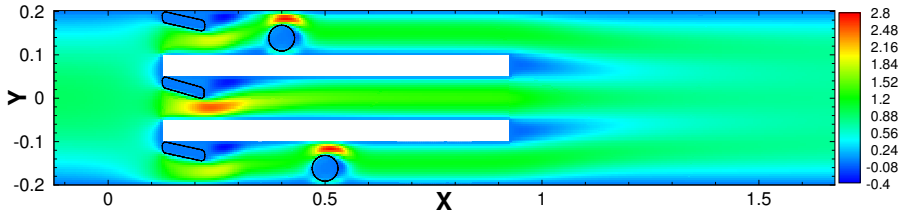

(*a*) Before action of the controller.

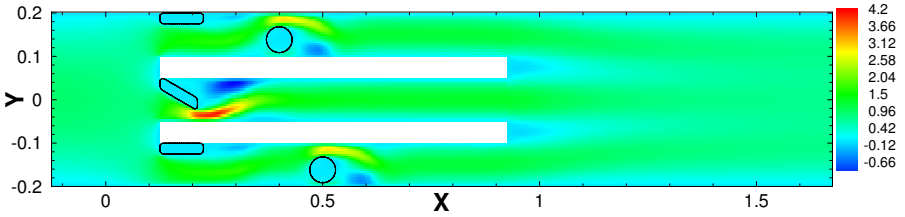

(*b*) Before the bottom bubble has been released.

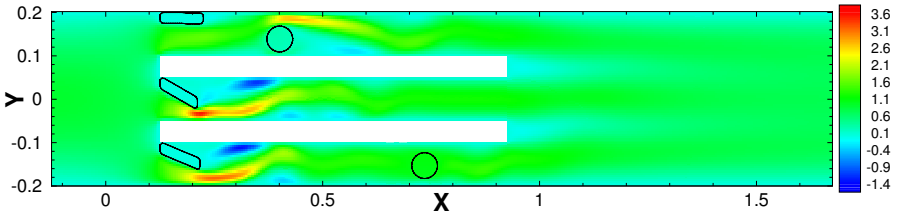

(*c*) Before the top bubble has been released.

Fig. 21 Temporal evolution of velocity contours and bubble trajectories in the coupled CFD-controller simulation for two bubbles. The lengths are expressed in millimeters, and the velocity is expressed in m/s.

and bottom channels. The bubbles are then set in motion and finally escape into the exit plenum, reducing the flow maldistribution.

8 Conclusion

We investigated flow maldistribution occurring in parallel microchannels due to presence of vapor bubbles in certain branches of the channel. In the present work, the bubbly flow regime consisting of small bubbles inside the microchannels was simulated at low Reynolds numbers. Neglecting any deformation of the vapor bubble, the bubbles were treated as rigid particles of density lower than the surrounding fluid. This assumption is reasonable for low Weber and Reynolds numbers. A novel fictitious-domain based direct numerical simulation approach was developed to simulate from first principles the motion of freely moving rigid objects with large-density ratios between the object and the surrounding fluid. The approach is also applicable to model flow around rigid microvalves with specified rotational motion. The numerical approach was thoroughly validated over a range of standard numerical tests for freely moving and specified motion of particles to show good agreements with available experimental data. The parallel numerical solver was integrated with a MATLAB-based model-predictive control algorithm to perform coupled CFD-controller simulations wherein the flow rates in different branches of the microchannels are controlled by activating microvalves at the entrance to the channels.

The goal of these coupled simulations was to first detect flow maldistribution in the presence of bubbles, and then eliminate any disparity in the flow rates through microvalve actuation. Accordingly, the flow rates in each branch of the microchannel were used as sensor input. System identification techniques were first employed on numerical simulations of fluid flow through the parallel microchannel in the absence of any bubbles. These studies produced a lower dimensional model that captures the essential dynamics of the full nonlinear flow in terms of a relationship between valve angles and the exit flow rate for each channel. A model-predictive controller was then developed by utilizing this reduced order model to identify flow maldistribution from exit flow velocities and prescribe actuation of channel valves to effectively redistribute the flow. Coupled simulations were first applied to single-phase flow in three-channel geometry that equates the flow rates in each branch of the channel. The approach was then applied to two-phase flow, with artificially introduced bubbles in certain branches. The model-predictive control methodology was shown to adequately reduce flow maldistribution by quickly varying channel valves to remove bubbles and to equalize flow rates in each channel. The approach developed is general in the sense that it is also applicable to fouling and clogging of microchannels to presence of rigid particulates. The numerical model is efficient, and simulations involving particle clusters are feasible due to its parallel implementation.

Acknowledgment

This work was supported under the U.S. Army's Tactical Energy Systems program at Ft. Belvoir. The funding was received through the Oregon Nano and Microtechnology Institute (ONAMI) at Oregon State University. All simulations were conducted at the in-house high performance computing cluster. SVA also acknowledges Dr. Ki-Han Kim of the Office of Naval Research for the support provided under the ONR Grant No.

N000140610697. This resulted in successful implementation of the DNS algorithm for freely moving particles.

Appendix

1 Interphase Interpolations. Any property defined at the material volumes within the particle can be projected onto the background grid by using interpolation functions. Use of simple linear interpolations may give rise to unphysical values within the particle domain (e.g., volume fractions greater than unity) [14] and may give rise to numerical oscillations in the particle velocity. In order to overcome this, a smooth approximation of the quantity can be constructed from the material volumes using interpolation kernels typically used in particle methods [31]

$$\Phi^{\Delta}(\mathbf{x}) = \int \Phi(\mathbf{y})\xi^{\Delta}(\mathbf{x}-\mathbf{y})d\mathbf{y} \tag{A1}$$

where Δ denotes grid resolution. The interpolation operator can be discretized using the material volume centroids as the quadrature points to give

$$\Phi^{\Delta}(\mathbf{x}) = \sum_{M=1}^{N} V_M \Phi(\mathbf{X}_M)\xi^{\Delta}(\mathbf{x}-\mathbf{X}_M) \tag{A2}$$

where $\mathbf{X}_M$ and V_M denote the coordinates and volume of the material volumes, respectively, and the summation is over all material volumes for a particle. For example, in order to compute particle volume fraction, $\Phi(\mathbf{X}_M)$ will be unity at all material points. This gives the unity volume fraction within the particle domain and zero outside the particle. In order to conserve the total volume of the particle, as well as the total force/torque exerted by the particle on the fluid, the interpolation kernel should at least satisfy

$$\sum_{M=1}^{N} V_M \xi^{\Delta}(\mathbf{x}-\mathbf{X}_M) = 1 \tag{A3}$$

$$\sum_{M=1}^{N} V_M (\mathbf{x}-\mathbf{X}_M)\xi^{\Delta}(\mathbf{x}-\mathbf{X}_M) = 0 \tag{A4}$$

Several kernels with second-order accuracy include Gaussian, quartic splines, etc. A kernel with compact support requiring only the immediate neighbors of a control volume has been designed and used in immersed boundary methods [17]. For uniform meshes with resolution Δ, it utilizes only three points in one dimension and gives the sharpest representation of the particle onto the background mesh

$$\xi^{\Delta}(\mathbf{x}-\mathbf{X}_M) = \frac{1}{\Delta^3}\delta\left(\frac{x-X_M}{\Delta}\right)\delta\left(\frac{y-Y_M}{\Delta}\right)\delta\left(\frac{z-Z_M}{\Delta}\right) \tag{A5}$$

where

$$\delta(r) = \begin{cases} \frac{1}{6}(5-3|r|-\sqrt{-3(1-|r|)^2+1} & 0.5 \le |r| \le 1.5, \quad r = \dfrac{(x-x_0)}{\Delta} \\ \frac{1}{3}(1+\sqrt{-3r^2+1} & |r| \le 0.5 \\ 0 & \text{otherwise} \end{cases} \tag{A6}$$

The same interpolation kernel can be used to interpolate a Eulerian quantity defined at the grid centroids to the material volume centroids. The interpolation kernel is second-order accurate for smoothly varying fields [32]. The effect of these interpolations is that the surface of the particle is smoothed over the scale proportional to the kernel length. Note that in order to reduce the spreading of the interfacial region, it is necessary to use compact support, as well as finer background grids and material volumes.

2 Updating the Particle Position. The rigid body motion of a particle can be decomposed into translational ($\mathbf{U}^T$) and rotational ($\mathbf{U}^R$) components. The total velocity field at each point within the particle is given as

$$\mathbf{U}^{\mathrm{RBM}} = \mathbf{U}^T + \boldsymbol{\Omega} \times \mathbf{r} \tag{A7}$$

where $\mathbf{U}^T$ is the translational velocity, $\boldsymbol{\Omega}$ is the angular velocity, and $\mathbf{r}$ is the position vector of the material volume centroid with respect to the particle centroid. All the material volumes have the same translational velocity as the particle centroid ($\mathbf{U}^T = \mathbf{U}_P$).

Given a velocity field and the positions ($\mathbf{X}_M^0$) of the material volume centroids and the particle centroid ($\mathbf{X}_P$) at $t=t_0$, the new positions ($\mathbf{X}_M^t$) at $t=t_0+\Delta t$ are obtained by linear superposition of the rotational and translational components of the velocity. The axis of rotation passing through the rigid body centroid $\mathbf{X}_P$ is given as $\hat{\sigma} = \boldsymbol{\Omega}/|\boldsymbol{\Omega}|$. The new coordinates due to rotation around $\hat{\sigma}$ are given as

$$\mathbf{X}' = \mathcal{R}(\mathbf{X}_M^0 - \mathbf{X}_P) + \mathbf{X}_P \tag{A8}$$

where the rotation matrix is

$$\mathcal{R} = \begin{bmatrix} t\hat{\sigma}_x\hat{\sigma}_x + c & t\hat{\sigma}_x\hat{\sigma}_y - s\hat{\sigma}_z & t\hat{\sigma}_x\hat{\sigma}_z + s\hat{\sigma}_y \\ t\hat{\sigma}_x\hat{\sigma}_y + s\hat{\sigma}_z & t\hat{\sigma}_y\hat{\sigma}_y + c & t\hat{\sigma}_y\hat{\sigma}_z - s\hat{\sigma}_x \\ t\hat{\sigma}_x\hat{\sigma}_z - s\hat{\sigma}_y & t\hat{\sigma}_y\hat{\sigma}_z + s\hat{\sigma}_x & t\hat{\sigma}_z\hat{\sigma}_z + c \end{bmatrix} \tag{A9}$$

Here $c=\cos(\alpha)$, $s=\sin(\alpha)$, $t=1-\cos(\alpha)$, and $\alpha=|\boldsymbol{\Omega}|dt$. The material volume centroids are all uniformly translated to give the final positions

$$\mathbf{X}_M^t = \mathbf{X}' + \mathbf{U}^T dt \tag{A10}$$

References

[1] Qu, W., and Mudawar, I., 2003, "Flow Boiling Heat Transfer in Two-Phase Micro-Channel Heat Sinks—I. Experimental Investigation and Assessment of Correlation Methods," Int. J. Heat Mass Transfer, **46**(15), pp. 2755–2771.

[2] Triplett, K., Ghiaasiaan, S., Abdel-Khalik, S., and Sadowski, D., 1999, "Gas-Liquid Two-Phase Flow in Microchannels Part I: Two-Phase Flow Patterns," Int. J. Multiphase Flow, **25**(3), pp. 377–394.

[3] Cubaud, T., 2004, "Transport of Bubbles in Square Microchannels," Phys. Fluids, **16**(12), pp. 4575–4585.

[4] Sharp, K., and Adrian, R., 2005, "On Flow-Blocking Particle Structures in Microtubes," Microfluid. Nanofluid., **1**(4), pp. 376–380.

[5] Wang, E., Shankar, D., Hidroo, D., Fogg, C. H., Koo, J., Santiago, J., Goodson, K., and Kenny, T., 2004, "Liquid Velocity Field Measurements in Two-Phase Microchannel Convection," Proceedings of the Third International Symposium on Two-Phase Flow Modeling and Experimentation, Pisa, Italy.

[6] Lee, P., Tseng, F., and Pan, C., 2004, "Bubble Dynamics in Microchannels. Part I: Single Microchannel," Int. J. Heat Mass Transfer, **47**(25), pp. 5575–5589.

[7] Li, H., Tseng, F., and Pan, C., 2004, "Bubble Dynamics in Microchannels. Part II: Two Parallel Microchannels," Int. J. Heat Mass Transfer, **47**(25), pp. 5591–5601.

[8] Mukherjee, A., and Kandlikar, S., 2005, "Numerical Study of the Effect of Inlet Constriction on Bubble Growth During Flow Boiling in Microchannels," Proceedings of the ICMM05, Third International Conference on Microchan-

nels and Minichannels, Toronto, Canada, Vol. 75143.
[9] Bleris, L., Garcia, J., Arnold, M., and Kothare, M., 2006, "Model Predictive Hydrodynamic Regulation of Microflows," J. Micromech. Microeng., **16**(9), pp. 1792–1799.
[10] Glowinski, R., Pan, T., Hesla, T., Joseph, D., and Periaux, J., 2001, "A Fictitious Domain Approach to the Direct Numerical Simulation of Incompressible Viscous Flow Past Moving Rigid Bodies-Application to Particulate Flow," J. Comput. Phys., **169**(2), pp. 363–426.
[11] Patankar, N., 2001, "A Formulation for Fast Computations of Rigid Particulate Flows," Center for Turbulence Research Annual Research Briefs 2001, pp. 185–196.
[12] Apte, S. V., Martin, M., and Patankar, N., 2009, "A Numerical Method for Fully Resolved Simulation (FRS) of Rigid Particle-Flow Interactions in Complex Flows," J. Comput. Phys., **228**(8), pp. 2712–2738.
[13] Patankar, N., Singh, P., Joseph, D., Glowinski, R., and Pan, T., 2000, "A New Formulation of the Distributed Lagrange Multiplier/Fictitious Domain Method for Particulate Flows," Int. J. Multiphase Flow, **26**(9), pp. 1509–1524.
[14] Sharma, N., and Patankar, N., 2005, "A Fast Computation Technique for the Direct Numerical Simulation of Rigid Particulate Flows," J. Comput. Phys., **205**(2), pp. 439–457.
[15] Kim, D., and Choi, H., 2000, "A Second-Order Time-Accurate Finite Volume Method for Unsteady Incompressible Flow on Hybrid Unstructured Grids," J. Comput. Phys., **162**(2), pp. 411–428.
[16] Mahesh, K., Constantinescu, G., Apte, S., Iaccarino, G., Ham, F., and Moin, P., 2006, "Large-Eddy Simulation of Reacting Turbulent Flows in Complex Geometries," ASME J. Appl. Mech., **73**, pp. 374–381.
[17] Roma, A., Peskin, C., and Berger, M., 1999, "An Adaptive Version of the Immersed Boundary Method," J. Comput. Phys., **153**(2), pp. 509–534.
[18] Ferziger, J., and Perić, M., 2002, *Computational Methods for Fluid Dynamics*, Springer, New York.
[19] van der Vorst, H., 2003, *Iterative Krylov Methods for Large Linear Systems*, Cambridge University Press, Cambridge, England.
[20] Ham, F., and Young, Y., 2003, "A Cartesian Adaptive Level Set Method for Two-Phase Flows," Center for Turbulence Research Annual Research Briefs, pp. 227–237.
[21] Leung, L., 1999, *System Identification-Theory for the User*, Prentice- Hall, Englewood Cliffs, NJ.
[22] Zhu, Y., 2001, *Multivariable System Identification for Process Control*, Elsevier, New York.
[23] Camacho, E., and Bordons, C., 2004, *Model Predictive Control*, Springer-Verlag, Berlin.
[24] Qu, W., Mudawar, I., Lee, S., and Wereley, S., 2006, "Experimental and Computational Investigation of Flow Development and Pressure Drop in a Rectangular Micro-Channel," ASME J. Electron. Packag., **128**, pp. 1–9.
[25] Dütsch, H., Durst, F., Becker, S., and Lienhart, H., 1998, "Low-Reynolds-Number Flow Around an Oscillating Circular Cylinder at Low Keulegan–Carpenter Numbers," J. Fluid Mech., **360**, pp. 249–271.
[26] Lomholt, S., Stenum, B., and Maxey, M., 2002, "Experimental Verification of the Force Coupling Method for Particulate Flows," Int. J. Multiphase Flow, **28**(2), pp. 225–246.
[27] Kim, D., and Choi, H., 2006, "Immersed Boundary Method for Flow Around an Arbitrarily Moving Body," J. Comput. Phys., **212**(2), pp. 662–680.
[28] Mordant, N., and Pinton, J., 2000, "Velocity Measurement of a Settling Sphere," Eur. Phys. J. B, **18**(2), pp. 343–352.
[29] Finn, J., 2009, "A Multiscale Modeling Approach for Bubble-Vortex Interactions in Hydropropulsion Systems," MS thesis, Oregon State University, Corvallis, OR.
[30] Shridhar, R., and Cooper, D., 1998, "A Tuning Strategy for Unconstrained Multivariable Model Predictive Control," Ind. Eng. Chem. Res., **37**, pp. 4003–4016.
[31] Koumoutsakos, P., 2005, "Multiscale Flow Simulations Using Particles," Annu. Rev. Fluid Mech., **37**(1), pp. 457–487.
[32] Peskin, C., 2003, "The Immersed Boundary Method," Acta Numerica, **11**, pp. 479–517.

Control of Vortex Shedding From a Plate at Incidence Angles in the Range of 0–90 Deg

Chuan Ping Shao
Associate Professor
e-mail: shaocp2005@yahoo.com.cn

Jian Zhong Lin
Professor
e-mail: mecjzlin@public.zju.edu.cn

China Jiliang University,
Hangzhou 100080,
China

A thin strip cross-sectional element is used to suppress vortex shedding from a plate with a width to thickness ratio of 4.0 at incidence angles in the range of 0–90 deg and a Reynolds number of 1.1×10^4. The axes of the element and plate are parallel. The incidence angle of the element is 90 deg and the ratio of strip width to plate thickness is 0.5. Extensive measurements of wake velocities, together with flow visualization, show that vortex shedding from both sides of the plate is suppressed at incidence angles in the range of 0–55 deg if the element is placed at points in effective zones. Unilateral vortex shedding occurs if the element is applied at points in unilateral effective zones. The changes in sizes and locations of the effective and unilateral effective zones with the change in plate incidence are investigated, and the mechanism of the control is discussed. Two patterns of unilateral vortex shedding are observed. Pattern I occurs on the side where there is no element, and oppositely, pattern II occurs on the side where the element resides. A resonance model is proposed to illustrate the occurrence of pattern II unilateral shedding. The phenomenon of unilateral vortex shedding means that the vortex can be generated without strong interaction between the shear layers separated from the bluff body. [DOI: 10.1115/1.4000303]

1 Introduction

The phenomenon of vortex shedding naturally occurs behind bluff bodies. Vortex shedding induces structure vibration, increases fluid resistance, and generates noise. The control of vortex shedding has been frequently studied in the past few decades and a number of passive and active control techniques have been developed [1,2]. However, most of the efforts are devoted to bluff bodies of circular or square cross sections. The control of vortex shedding from an inclined plate is of theoretical importance and engineering significance in bridge deck and airfoil designs, but only a few documented research works can be found on this subject [3–6].

The passive control of vortex shedding from a bluff body by an additional small element has attracted great attention in recent years [7–16] due to its simplicity and effectiveness. These methods can be classified into two categories. The first category places the element upstream of the bluff body [7–16]. The second one, which originated with the work of Strykowski and Sreenivasan [17], applies the element downstream of the body.

In Strykowski and Sreenivasan's study [17], a small circular cylinder element was used and set parallel to the main circular cylinder. Vortex shedding from both sides of the main body can be suppressed if the circular element is set in an effective zone downstream of the main body. However, results show that their method was ineffective at Reynolds numbers above 150.

In our recent study [18–22], a strip or a square cross-sectional element was used to improve the effect. Vortex shedding from both sides of a cylinder can be suppressed at much higher Reynolds numbers if the element is set in a certain region quite similar to the effective zone shown in Ref. [17]. The element's bluffness is shown to play an important role in the suppression [18,19].

Though the improved element method is effective in suppressing vortex shedding from circular and square cylinders [18–22], whether or not it can suppress vortex shedding from other bodies, especially those of asymmetrical geometry and those of cross sections of larger streamwise to lateral dimension ratios, remains an open question.

To answer this question, a thin strip cross-sectional element is used in the present study to control vortex shedding from a plate at various incidence angles.

2 Experimental Setup

The experiment was conducted in a wind tunnel with test section of 5 m long, 1.0 m high, and 1.2 m wide. The test section could supply uniform free-stream with speed of 2.0–15.0 m/s with turbulence intensity of 1.0–1.2%.

The plate and element were all made of stainless steel. The plate has a length of 1.0 m, width $B=120$ mm, and thickness $H=30$ mm. The element has a length of 1.0 m, width $b=15$ mm, and thickness $h=2$ mm. As shown in Fig. 1, the plate is located at the center and spanned the height of the test section. The axes of the plate and element were parallel. The plate was allowed to turn around its axis to adjust the angle of incidence α. The main surface of the element was kept at right angles to the oncoming stream. The position of the element was varied to be below or above, and upstream or downstream of the plate. The test velocity of oncoming flow was restricted to less than 5 m/s so that no vibrations of the plate and element were excited during the test.

The smoke wire technique was used to visualize the wake flow. A detailed description of this technique was shown in Ref. [20]. The fluctuations of streamwise velocities in the plate wake were detected by a 55P11 sensor of a DANTEC streamline hot-wire anemometer. The flow unit 90H02 and calibration module 90H01 were used to regulate the voltage-velocity relation. The temperature compensation system was applied during the measurement, and the uncertainty of the measured velocity was less than 1.0%. Measurements were carried out at downstream stations $X/B=2.5$, 3.5, 5.0, 7.0, and 10.0 on the plane of midspan. Points at each X-station were measured from $Y/H=-6.0$ to $Y/H=6.0$ at intervals $\Delta(Y/H)=0.67$. The sampling frequency and sampling time were 1024 Hz and 65 s, respectively.

Contributed by the Fluids Engineering Division of ASME for publication in the JOURNAL OF FLUIDS ENGINEERING. Manuscript received November 24, 2008; final manuscript received June 27, 2009; published online October 27, 2009. Editor: Joseph Katz.

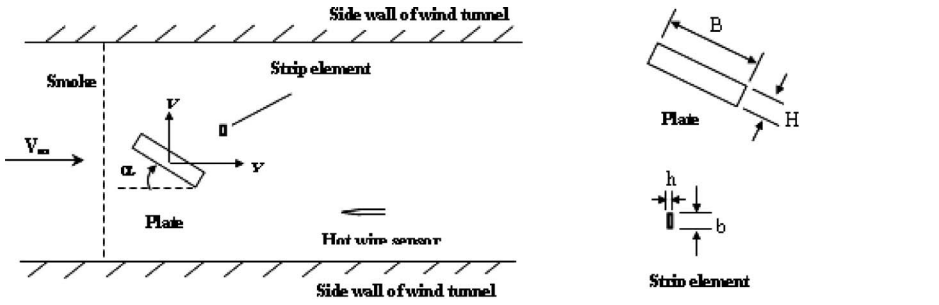

(a) Arrangements of the model test

(b) Dimensions of the plate and strip element

Fig. 1 Sketch of geometrical arrangements of the plate and control element: (*a*) arrangement of the model test; (*b*) dimensions of the plate and strip element

3 Results

The test range of the plate incidence is $\alpha=0-90$ deg, the test range of the element position at each α angle is $X/H=-4.0-8.0$ and $Y/H=-7.0-7.0$. The Reynolds number is $\mathrm{Re}=1.1\times10^4$, and the width of the strip element is $b/H=0.5$ (or $b/B=0.125$).

3.1 Flow Visualization. Figure 2 shows the control effect at $\alpha=0$ deg. Vortex shedding naturally occurs if no element is present (Fig. 2(*a*)). Vortex shedding from both sides of the plate is suppressed if the element is applied at $X/H=2.0$ and $Y/H=1.2$, a point directly above the trailing edge of the plate (Fig. 2(*b*)). In this case the flow in the gap between the plate and element looks like a jet shooting into the wake of the plate. Vortex shedding is also suppressed if the element is set at $X/H=-2.0$ and $Y/H=1.0$, a point directly above the leading edge of the plate (Fig. 2(*c*)), or at certain points upstream of the leading edge. In these cases the gap flow is decelerated before it interferes with the plate wake.

In our previous study [18,19], the phenomenon of unilateral vortex shedding was observed if an element was applied at certain points in the wake of a circular or square cylinder. The phenomenon is also observed in the present study if the distance between the element and plate is in a certain range. As shown in Figs. 2(*d*), 2(*e*), and 2(*h*), large-scale vortex shedding is suppressed on the side where the element resides. However, large-scale vortex shedding is still present on the side there is no element. Small-scale vortices can be seen downstream of the element, but they are so blurred as to be undistinguishable after a short distance.

The element and plate behave like an integrated single body if

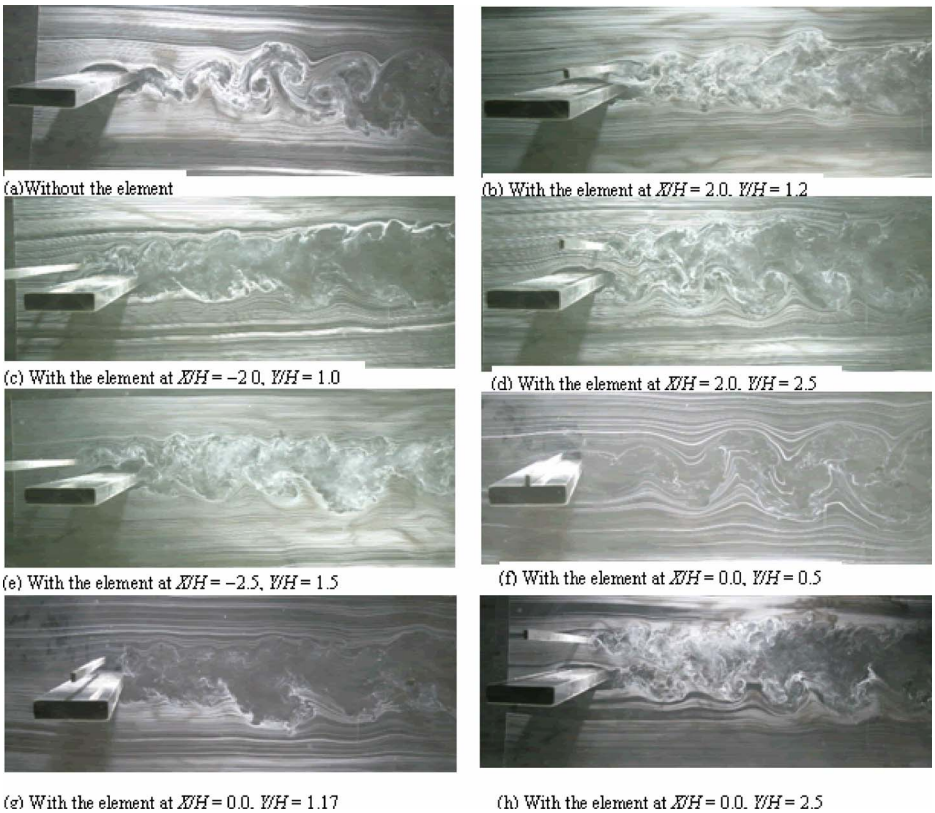

Fig. 2 The control effect at $\alpha=0$ deg: (*a*) without element; (*b*) with the element at $X/H=2.0$ and $Y/H=1.2$; (*c*) with the element at $X/H=-2.0$ and $Y/H=1.0$; (*d*) with the element at $X/H=2.0$ and $Y/H=2.5$; (*e*) with the element at $X/H=-2.5$ and $Y/H=1.5$; (*f*) with the element at $X/H=0.0$ and $Y/H=0.5$; (*g*) with the element at $X/H=0.0$ and $Y/H=1.17$; and (*h*) with the element at $X/H=0.0$ and $Y/H=2.5$

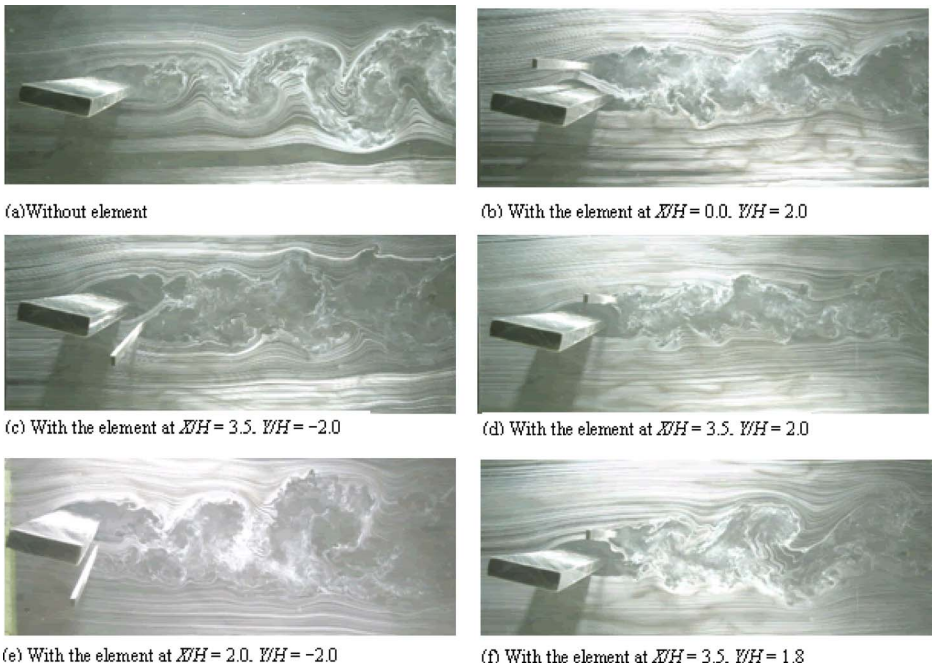

Fig. 3 The control effect at $\alpha=20$ deg: (*a*) without element; (*b*) with the element at $X/H=0.0$ and $Y/H=2.0$; (*c*) with the element at $X/H=3.5$ and $Y/H=-2.0$; (*d*) with the element at $X/H=3.5$ and $Y/H=2.0$; (*e*) with the element at $X/H=2.0$ and $Y/H=-2.0$; and (*f*) with the element at $X/H=3.5$ and $Y/H=1.8$

the element is applied very close to or directly contacting the plate. Vortex shedding occurs downstream of the integrated body (Fig. 2(*f*)).

A central barrier was used to reduce flow induced vibration of a long-span bridge deck [4], and the geometric arrangement of the barrier and deck is the same as that of the element and plate shown in Fig. 2(*f*). The result at $\mathrm{Re}=1.1\times10^4$ indicates that the suppression of vortex shedding by the central barrier is poor. The suppression can be improved if the barrier is a little above the deck (Fig. 2(*g*)). Regular vortex shedding is replaced by irregular oscillations of the shear layers on both sides. Further investigation is necessary to clarify whether or not the improvement can be extended to higher Reynolds numbers.

As shown in Fig. 2(*h*), regular unilateral vortex shedding occurs on the lower side if the distance between the element and plate is increased to a certain value.

Figure 3 examines the suppression effect at $\alpha=20$ deg. Vortex shedding is observed downstream of the plate if no element is applied (Fig. 3(*a*)). Vortex shedding on both sides of the plate is effectively suppressed if the element is set at some typical positions on both the upper and lower sides (Figs. 3(*b*)–3(*d*)). In cases shown in Figs. 3(*b*) and 3(*c*), the jetlike gap flow shoots directly into the plate wake. In the case shown in Fig. 3(*d*), however, no obvious gap flow can be seen.

Unilateral vortex shedding is also observed at $\alpha=20$ deg when the element is set at certain positions on either side of the plate. It is interesting to note that unilateral vortex shedding occurs not only on the side where there is no element (Fig. 3(*e*)), but also on the side where the element resides. As shown in Fig. 3(*f*), large-scale vortex shedding occurs on the upper side. On the lower side, however, only shear layer fluctuation is observed. The lower side shear layer fluctuation is induced by the vortices on the upper side.

To differentiate the two kinds of unilateral vortex shedding, we may call the one shown in Fig. 3(*e*) as pattern I and the one shown in Fig. 3(*f*) as pattern II.

Figure 4 demonstrates the control effect at $\alpha=30$ deg. Vortex shedding occurs on both sides if no element is applied (Fig. 4(*a*)), or if the element is applied at a point inside the wake (Fig. 4(*b*)). Vortex shedding is suppressed if the element is shifted away from the wake to the point $X/H=3.7$, $Y/H=-1.9$, and pattern I unilateral vortex shedding occurs if the element is further shifted away to the point $X/H=3.7$, $Y/H=-3.0$.

Figure 5 shows the suppression at $\alpha=40$ deg. Vortex shedding occurs and a broad wake appears downstream of the plate if no element is applied (Fig. 5(*a*)). Vortex shedding on both sides can be suppressed and the wake narrowed if the element is set at certain points on either the upper or lower sides (Figs. 5(*b*) and 5(*c*)). Pattern I unilateral vortex shedding is observed when the element is applied at a certain position (Fig. 4(*d*)).

The suppression at $\alpha=55$ deg is shown in Fig. 6. Vortex shedding on both sides of the plate can be suppressed if the element is fixed at points within a very small region.

At incidence angles $\alpha\geq60$ deg, no element position can be found to suppress the vortex shedding from both sides of the plate. On the other hand, the phenomenon of pattern I unilateral vortex shedding is observed at angles $\alpha=55$ deg, 60 deg, 75 deg, and 90 deg. Figure 7 shows the typical case at $\alpha=90$ deg.

3.2 Spectra of Fluctuating Velocities. Hot-wire measurements have been carried out at incidence angles of interval $\Delta\alpha=5$ deg over the range of $\alpha=0-55$ deg and of interval $\Delta\alpha=15$ deg over the range of $\alpha=60-90$ deg.

Figure 8 shows the power spectra of fluctuating velocities measured at different X-stations downstream of the plate at $\alpha=0$ deg without and with the element at typical positions. In the case without the element (Fig. 2(*a*)), a sharp peak appears in each of the spectra of fluctuating velocities at points on the upper and lower sides of the wake (Figs. 8(*a*) and 8(*b*)). The peak value varies with the measuring position, and the highest peaks are obtained at points in the range of $Y/H=-2.0--1.0$ (or 1.0–2.0) at $X/B=3.5$ and in the range of $Y/H=-4.5--2.5$ (or 2.5–4.5) at $X/B=10.0$. When the element is applied at $X/H=0.0$, $Y/H=1.17$ (Fig. 2(*g*)), the sharp peaks in the spectra of velocities at all the measured points are eliminated (Figs. 8(*c*) and 8(*d*)). The spectrum criterion proposed in our previous papers [18,19] tells us

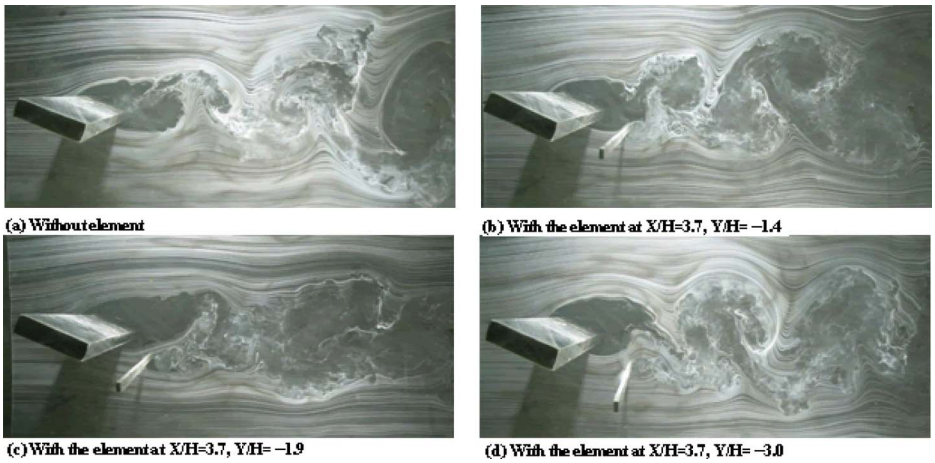

Fig. 4 The control effect at $\alpha=30$ deg: (*a*) without element; (*b*) with the element at $X/H=3.7$ and $Y/H=-1.4$; (*c*) with the element at $X/H=3.7$ and $Y/H=-1.9$; and (*d*) with the element at $X/H=3.7$ and $Y/H=-3.0$

that vortex shedding on both sides of the wake is suppressed.

The phenomenon of pattern I unilateral vortex shedding shown in Fig. 2(*h*) was rediscovered by hot-wire measurements and the power spectra of fluctuating velocities in a typical wake are shown in Fig. 8(*e*). There appears no sharp peak in the spectra at points on the upper side ($Y/H>0$) of the wake. On the lower side ($Y/H<0$), however, a sharp peak appears in the spectrum measured at $Y/H=-1.5$. The peak frequency is $fB/V_\infty \approx 0.64$, nearly the same as the frequency of vortex shedding without the element. With the increase in distance between the plate and the measuring position, the sharp peak in the spectrum of fluctuating velocity induced by unilateral vortex shedding declines. As shown in Fig. 8(*f*), the peak can hardly be recognized in the spectra measured at station $X/B=10.0$.

The phenomenon of pattern II unilateral vortex shedding shown in Fig. 3(*f*) was confirmed by fluctuating velocity measurements and a typical example is shown in Fig. 9. When the element is placed at $X/H=3.5$, $Y/H=1.8$ on the upper side of the wake (Figs. 3(*f*) and 9(*b*)), a sharp peak appears in each of the spectra at points $X/B=7.0$, $Y/H=2.0-5.0$ on the upper side, but no sharp peaks

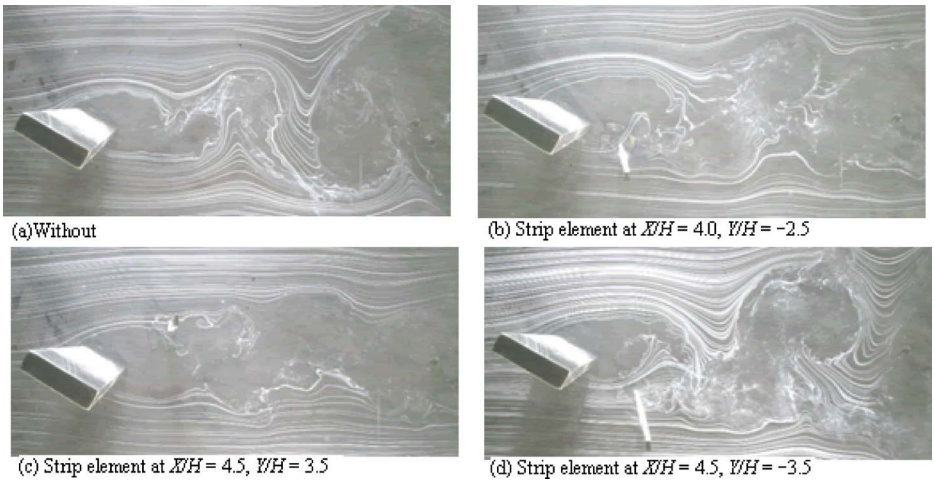

Fig. 5 The suppression effect at $\alpha=40$ deg: (*a*) without element; (*b*) strip element at $X/H=4.0$ and $Y/H=-2.5$; (*c*) strip element at $X/H=4.5$ and $Y/H=3.5$; and (*d*) strip element at $X/H=4.5$ and $Y/H=-3.5$

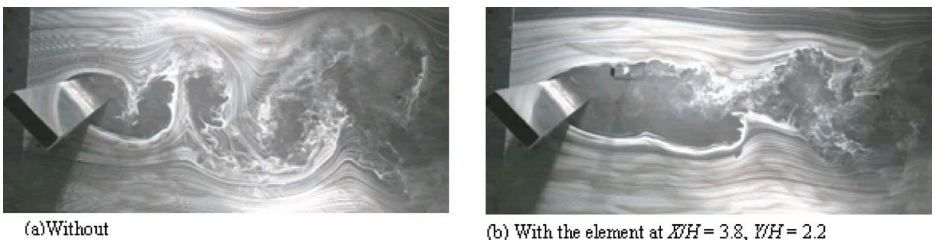

Fig. 6 The suppression effect at $\alpha=55$ deg: (*a*) without element; (*b*) with the element at $X/H=3.8$ and $Y/H=2.2$

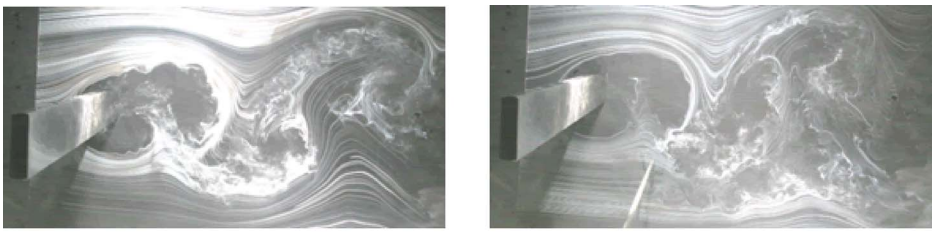

Fig. 7 The suppression effect at α=90 deg and Re=1.1×10^4: (*a*) without element; (*b*) with the element at *X*/*H*=4.0 and *Y*/*H*=5.0

appear in the spectra at points X/B=7.0, Y/H=−2.0−−5.0 on the lower side of the wake. The pattern II unilateral vortex shedding can be detected only when the element is in a laterally very narrow area. A slight lateral deviation of the position from Y/H =1.8 to Y/H=2.0 will change the flow into the state of vortex suppression on both sides (Figs. 3(*d*) and 9(*c*)), and a slight deviation from Y/H=1.8 to Y/H=1.6 will change the flow into the state of alternative vortex shedding from both sides of the plate (Figs. 3(*a*) and 9(*a*)).

Pattern II unilateral vortex shedding can also be detected if the element is set at certain points in a laterally very narrow area on the lower side.

The occurrence of pattern II unilateral vortex shedding depends not only on the element position, but also on the incidence angle of the plate. The range of this phenomenon in the present study is 10 deg≤α≤25 deg.

Figure 10 demonstrates the typical spectra measured in the wakes of the plate at α=30 deg with the element applied at positions on the lower side of the wake, corresponding to the visualization results shown in Fig. 4. A sharp peak appears in each of the spectra at points on both sides of the wake when the element is at X/H=3.7 and Y/H=−1.4, which is the case of alternative vortex shedding from both sides of the plate (Fig. 4(*b*)). There is no sharp peak in each of the spectra when the element is at X/H=3.7, Y/H=−1.9, which is the case where the vortex shedding from both sides of the plate is suppressed (Fig. 4(*c*)). When the element is set at X/H=3.7, Y/H=−3.0, a sharp peak is observed in the spectrum at a point on the upper side of the wake, but no sharp peak can be seen in the spectrum at a point on the lower side. This is the pattern I unilateral vortex shedding (Fig. 4(*d*)).

From the results of visualization and velocity measurements, we may deduce that effective zones of element position exist in which vortex shedding from both sides of the plate can be suppressed, and unilaterally effective zones of element position exist in which unilateral vortex shedding of pattern I or pattern II occurs. In principle, the effective and unilaterally effective zones can be identified by using the spectrum criterion [18,19]. However, the example shown in Fig. 11 reminds us that we should be very careful in using this criterion. As indicated in Fig. 11, if we apply

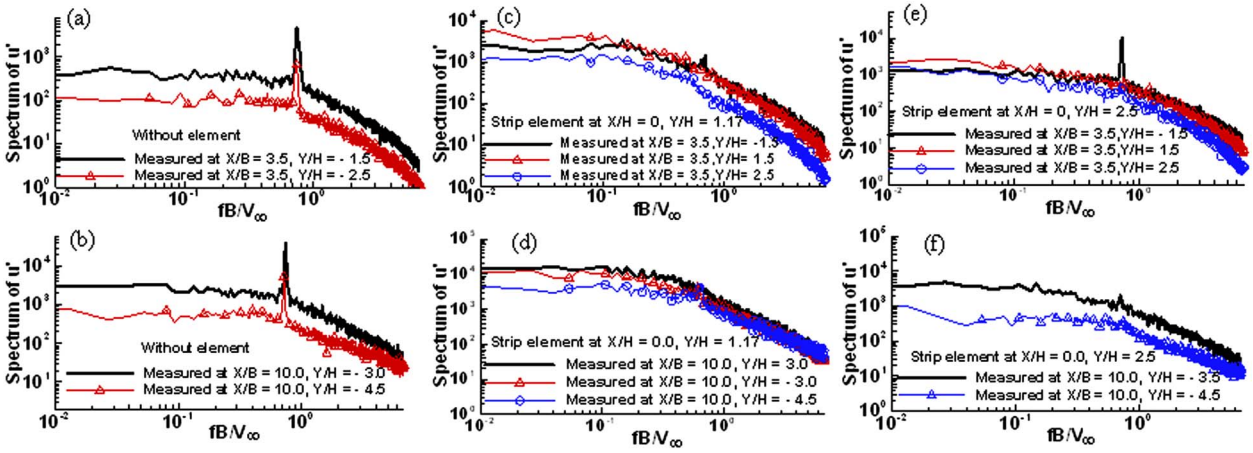

Fig. 8 Power spectra of fluctuating velocities at points downstream the plate at α=0 deg with and without element

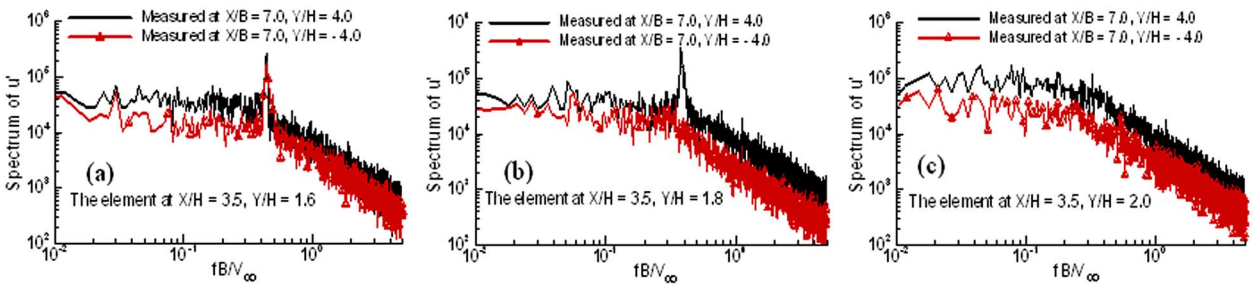

Fig. 9 Power spectra of fluctuating velocities downstream the plate at α=20 deg without element and with the element at *X*/*H*=3.5 and *Y*/*H*=1.6–2.0

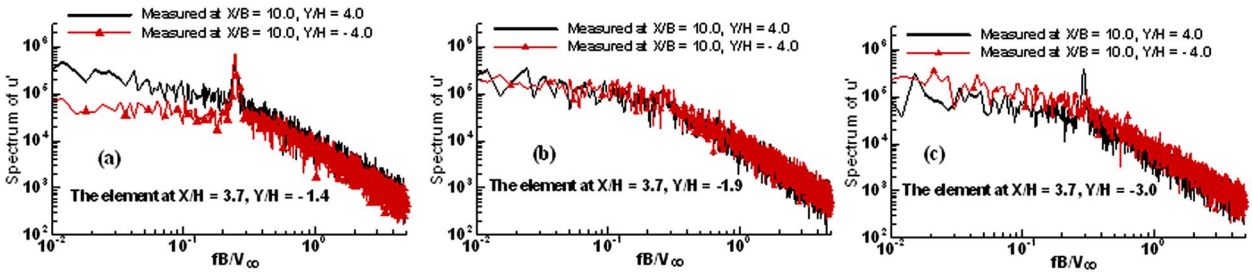

Fig. 10 Power spectra of fluctuating velocities at points downstream the plate at α=30 deg with the element applied at points X/H=3.7 and Y/H=−1.4−−3.0

the criterion to the spectra measured at $X/H=5.0$, $Y/B=\pm 2.0$ and ± 4.0, we may form an opinion that vortex shedding from both sides of the plate is suppressed when the element is set at $X/H=2.7$, $Y/H=3.1$. On the other hand, if we apply the criterion to the spectra measured at points $X/B=2.5$, $Y/H=\pm 2.7$ and ± 4.0, we may estimate that pattern I unilateral vortex shedding is induced when the element is placed at the same point. Detailed measurements have been conducted to eliminate this oddity. We note that the peak frequency in each of the spectra at Y-points at section $X/B=2.5$ is much higher than the peak frequencies at Y-points at section $X/B=5.0$. The peak frequency in the spectra measured at section $X/B=2.5$ is not the frequency of vortex shedding from the plate; it is actually the frequency of vortex shedding from the element. This means station $X/B=2.5$ is not far enough downstream for the plate wake signal detection. The element wake has a strong influence at this position.

The signal of unilateral vortex shedding decays rapidly as the distance from the plate to the downstream measuring station increases. A station too far downstream is also unsuitable for the plate wake signal detection. As shown in Figs. 8(*e*) and 8(*f*), pattern I unilateral vortex shedding, induced by the element set at $X/H=0$ and $Y/H=2.5$, can be detected at station $X/B=3.5$; however, it can hardly be distinguished at station $X/B=10.0$.

The suitable range of X-station for the plate wake signal detection changes with the change in α angle. Test results show that the suitable ranges for the cases in $\alpha=0-40$ deg and $\alpha=45-90$ deg are $X/B=3.5-7.0$ and $X/B=5.0-10.0$, respectively.

3.3 Effective Zones and Unilateral Effective Zones. For convenience of expression, the effective zone is simplified as E zone, the pattern I unilateral effective zone as I-UE zone, and the pattern II unilateral effective zone as II-UE zone.

The E zone is defined as a region of element position in which vortex shedding from both sides of the plate is suppressed [18–22], and vortex suppression at both sides is identified when no sharp peak appears in the spectrum of fluctuating velocity at any suitable measurement point in the wake.

The I-UE or II-UE zone is defined as a region of element position in which pattern I or II unilateral vortex shedding occurs. The pattern I unilateral shedding is identified when a sharp peak appears in each of the spectra at Y-points on the side where no element resides, and no sharp peak appears in each of the spectra at Y-points on the side where the element is placed. Conversely, the pattern II unilateral shedding is defined when a sharp peak appears in each of the spectra at Y-points on the side where the element resides, and no sharp peak appears in each of the spectra at Y-points on the side there is no element. The measuring points in the definitions are at a certain X-station within the range of $X/B=3.5-10.0$.

Hot-wire measurements were performed twice to determine the E and I-UE zones at each α angle. For the first measurement, the tested element positions form a net with intervals $\Delta(X/H)=\Delta(Y/H)=0.33-0.67$ over the area $-4.0\leq X/H\leq 8.0$ and $-7.0\leq Y/H\leq 7.0$. The sizes and locations of the zones were roughly measured on the first run. The element positions in the second measurement were located in narrow areas near the boundary lines of the zones determined by the first measurement. The accuracy in the second measurement was basically $\Delta(X/H)=\Delta(Y/H)=0.167$. The accuracy was promoted to $\Delta(X/H)=\Delta(Y/H)=0.083$ in cases when the E and UE zones were very small.

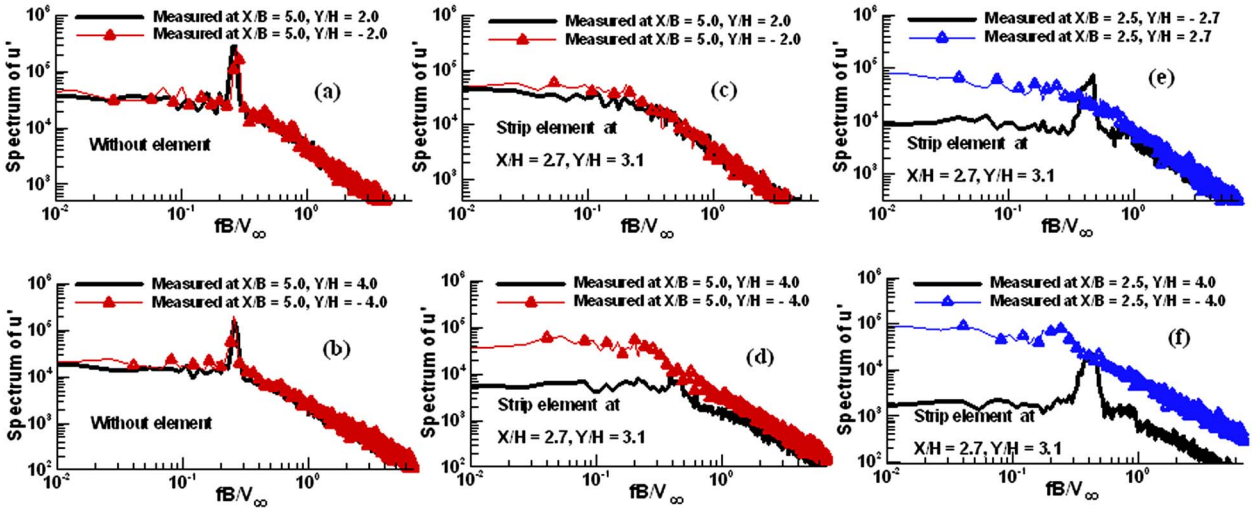

Fig. 11 Power spectra of fluctuating velocities at points downstream the plate at α=30 deg without element and with the element at X/H=2.7 and Y/H=3.1

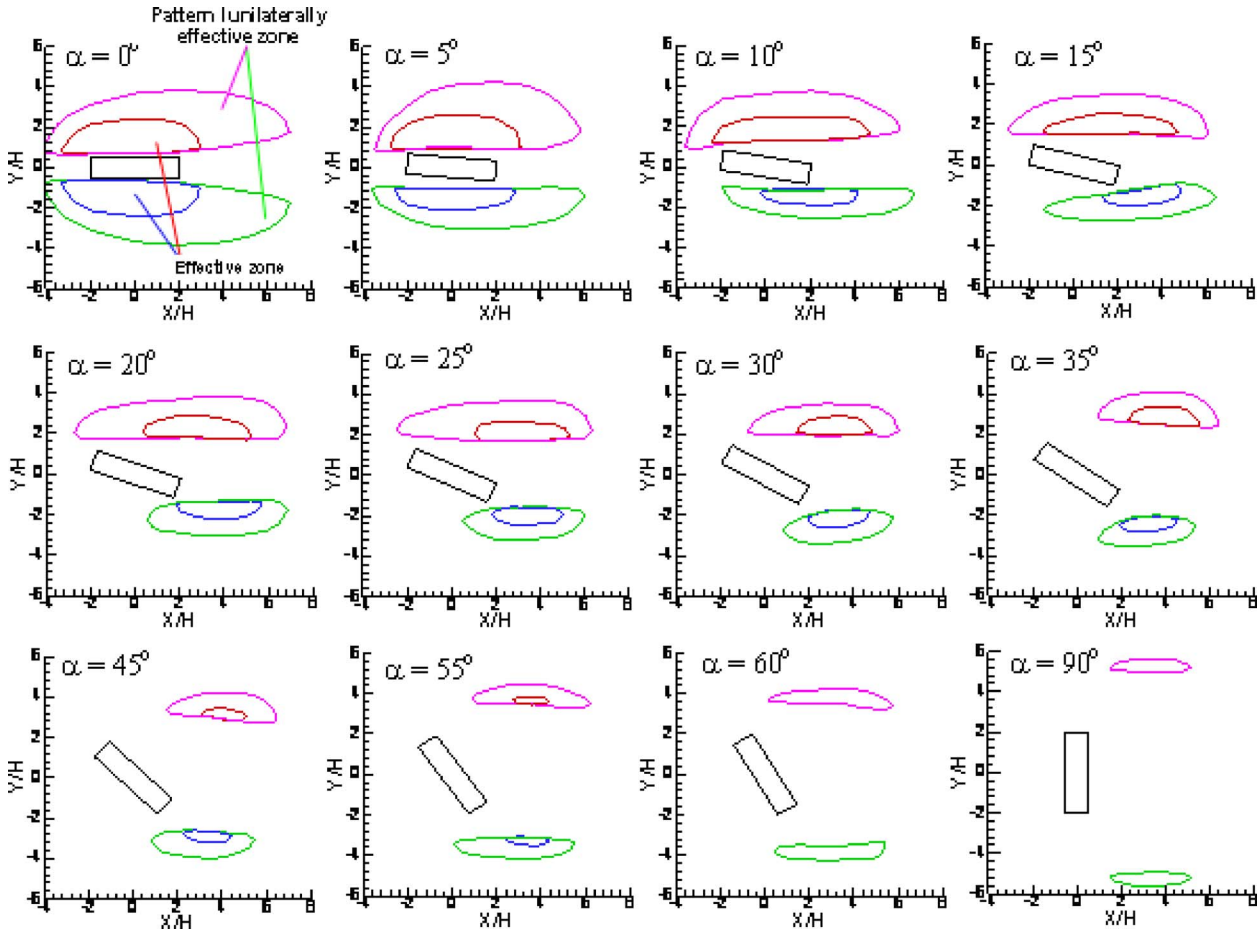

Fig. 12 E and I-UE zones at different angles α

The II-UE zones on both sides of the plate will not be discussed in the following because of their small sizes and the difficulties in accurately measuring them.

The measured E and I-UE zones at different angles α are shown in Fig. 12. On each side of the plate wake, there exists an E zone if angle α is within the range of 0–55 deg, and an I-UE zone at any α angle tested. The E zone is surrounded by the I-UE zone.

At α=0 deg, the E and I-UE zones symmetrically appear on the upper and lower sides of the plate. The streamwise dimension of the E zone measures from a station at X/H=2.8 downstream of the trailing edge of the plate to a station at X/H=−3.2 upstream of the leading edge of the plate, and the lateral dimension stretches from a point very close to the plate to a point 2.5H away from the plate. The streamwise dimension of the I-UE zone measures from X/H=6.8 to X/H=−4.5, and the lateral dimension measures from a point very close to the plate to a point 3.3H away from the plate.

The symmetrical geometries of the E and I-UE zones are heavily broken if α is even slightly deviated from 0 deg. With an increase in α, the lateral dimensions of the E and I-UE zones on both sides decrease, and the sizes of the E and I-UE zones on the upper and lower sides shrink at different rates.

On the upper side, the E zone moves downstream and its size shrinks gradually from a large area to a very small one with an increase in α from 0 deg to 55 deg, and it disappears if α exceeds a certain value between 55 deg and 60 deg. The I-UE zone shrinks gradually from a large region to a much smaller one with a change in α from 0 deg to 90 deg. The upstream tip of the I-UE zone moves downstream as α increases, but no obvious movement happens to the downstream tip of the I-UE zone.

On the lower side, the downstream movement of the E zone and the decrease in its size happen much more quickly as α is increased in the range of 0–15 deg, but these effects slow down as α is increased to more than 15 deg. The I-UE zone on the lower side shrinks much faster than the I-UE zone on the upper side as α is increased in the range of 0–30 deg. The upstream tip of the I-UE zone moves downstream rapidly in this α range, but no obvious movement happens to the downstream tip.

The difference between the sizes of E zones on the upper and lower sides and the difference between the sizes of I-UE zones on the upper and lower sides are small at angles α>40 deg.

4 Discussion

The role of the element's bluffness in the suppression was discussed in our previous paper [21]. It was shown that the higher the grade of element bluffness, the more effective the suppression. In the present study, the relative bluffness of the element is defined as the element width b divided by the frontal width of the plate. With the increase in α, the frontal area of the plate increases, and thus the relative bluffness of the element decreases. This may be the reason behind the differences in sizes between the E (or I-UE) zones at different α angles.

The frequency of vortex shedding from the element does not play an important role in the suppression. We note that at a fixed α angle, the frequency of vortex shedding from the plate is fixed. The frequency of vortex shedding from the element varies as the position of the element changes within the effective zone. Vortex shedding from the plate can be suppressed in cases of different frequencies of vortex shedding from the element. We also note that the point X/H=2.0, Y/H=−1.0 is inside the intersection area

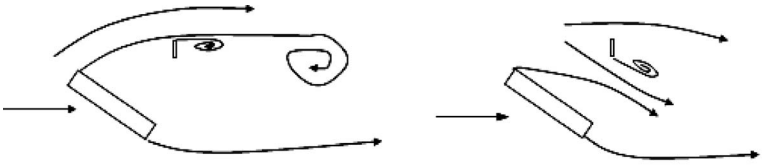

Fig. 13 Sketch of resonance model to show the pattern II unilateral vortex shedding: (*a*) flow in the first half period; (*b*) flow in the second half period

of the effective zones at angles $\alpha=0-10$ deg. With an increase in angle α from 0 deg to 10 deg, the local velocity of the flow coming to the element applied at the point is increased only by 7%, and the frequency of vortex shedding from the element is also increased only by 7%. However, the frequency of vortex shedding from the plate in case without suppression is decreased nearly by 40%. Vortex shedding from the plate is suppressed both at $\alpha=0$ deg and $\alpha=10$ deg. All the facts indicate that there is no coherence between the suppression and the frequency of vortex shedding from the element.

Gerrard and coworker [23,24] proposed two models to describe vortex generation from a bluff body: the shear layers interaction model and the vortex self cutoff model. The self cutoff mechanism was suggested to work at Reynolds numbers not larger than about 90 in the case of flow across a circular cylinder, and the interaction mechanism was said to work at much higher Reynolds numbers. However, the phenomenon of unilateral vortex shedding cannot be readily understood by Gerrard and coworker's models [23,24]. As was pointed out previously [18,19], the interaction mechanism has little opportunity to work, but the cutoff mechanism seems to work well in the case of pattern I unilateral vortex shedding at Reynolds numbers of order 10^4. As shown in Figs. 2–4, the rolledup unilateral vortex can cut itself off the supply of vorticity and propagates downstream one after another.

The pattern II unilateral vortex shedding occurs when the element is set in a very small II-UE zone close to the inner edge of the E zone. This phenomenon may be explained by a resonance mechanism. As shown in Ref. [25], regular oscillations of the shear layer separated from a circular cylinder can be detected at points slightly downstream the cylinder, even if vortex shedding on both sides of the cylinder is suppressed by a splitter plate, and the oscillating frequency is nearly the same as the frequency of vortex shedding without control. We suppose that vortex shedding from both sides of the plate is suppressed when the element is applied at a certain point in the plate wake. At the same time, the local flow across the element may induce vortex shedding. The element position is so chosen that the frequency of vortex shedding from the element is nearly the same as, or an integer multiple of, the frequency of fluctuation of the shear layer separated from the plate. A resonance is then excited. In the first half of the resonance oscillation period, as shown in Fig. 13(*a*), the small scale vortex shedding from the outer side of the element may induce large-scale vortex rolling up of the shear layer separated from the plate; thus, large-scale vortex shedding occurs on the side where the element resides. In the second half of the resonance oscillation period, as shown in Fig. 13(*b*), a gap flow between the plate and element is induced when vortex shedding occurs on the inner side of the element. The fluid in the gap may flow toward the shear layer on the opposite side, and help to diminish the rolling up of the shear layer and suppress vortex shedding on the side where there is no element.

This resonance occurs only when $f_e \approx nf$, where f_e and f are the frequency of vortex shedding from the element and from the plate, respectively, and $n=1,2,3,\ldots$. If we define the Strouhal numbers of the vortex shedding from the element and the plate as $\mathrm{St}_e = f_e b/U_e$ and $\mathrm{St}=fD/V_\infty$, respectively, where U_e is the local velocity coming to the element, and $D=B\sin\alpha+H\cos\alpha$ is the frontal width of the plate, then the two Strouhal numbers will be of approximately the same value [26] ($\mathrm{St}_e \approx \mathrm{St}$). So, we have $nb/U_e \approx D/V_\infty$. This severe restriction helps to explain why the II-UE zone is a laterally very narrow region close to the inner edge of the E zone.

The resonance mechanism means a regular vortex shedding can be generated from a single unstable shear layer by an actuation at a certain frequency applied at some certain positions. It also means that the interaction between the shear layers is not a necessary condition for the generation of vortex shedding.

5 Conclusions

The control of vortex shedding from a plate by a strip element is systematically studied at a Reynolds number of 1.1×10^4 and angles of plate incidence in the range of $0\sim90$ deg. Results of wind tunnel tests show that vortex shedding from both sides of the plate can be suppressed if the element is applied at points within two effective zones on both sides, and unilateral vortex shedding is observed if the element is placed in unilaterally effective zones on both sides of the plate. Two patterns of unilateral vortex shedding are observed. In pattern I, the unilateral shedding occurs on the side where there is no element, while in pattern II, it occurs on the side where the element resides. The effective and pattern I unilateral effective zones at different angles of plate incidence are shown in the paper. At small incidence angles, the effective and pattern I unilateral effective zones are large, and stretch from points upstream of the front edge to points downstream of the rear edge of the plate. The effective and pattern I unilateral effective zones on both sides shrink at different rates and move downstream with an increase in plate incidence. The pattern II unilateral vortex shedding is observed at incidence angles in the range of 10–25 deg, and the pattern II unilateral effective zones are very small areas downstream of the plate. The mechanism of the control is discussed and a resonance model is proposed to describe the occurrence of pattern II unilateral vortex shedding. The two patterns of unilateral vortex shedding are negative examples to Gerrard and coworker's model, which describes the main role of the shear layers interaction in vortex shedding generation.

Acknowledgment

This study was financially supported by the Natural Science Foundation of China (Grant Nos. 10472124 and 10872188). The experiment was carried out in the State Key Laboratory for Turbulence and Complex Systems Study at Peking University. The authors wish to thank Professor Qingding Wei and Senior Engineer Bin Liang for their help in preparing the experiment.

Nomenclature

b = width of the strip element
B = width of the plate
h = thickness of the strip element
H = thickness of the plate
Re = Reynolds number, $\mathrm{Re}=V_\infty B/\nu$
u' = streamwise component of fluctuating velocity
V_∞ = mean velocity of oncoming flow

X, Y = streamwise and lateral coordinates
α = angle of incidence of the plate
ν = kinematic viscosity of the air

References

[1] Zdravkovich, M. M., 1981, "Review and Classification of Various Aerodynamic and Hydrodynamic Means for Suppressing Vortex Shedding," J. Wind. Eng. Ind. Aerodyn., **7**, pp. 145–189.
[2] Ged-el Hak, M., 2000, *Flow Control—Passive, Active and Reactive Flow Management*, Cambridge University Press, Cambridge.
[3] Chen, J. M., and Fang, Y. C., 1996, "Strouhal Numbers of Inclined Flat Plates," J. Wind. Eng. Ind. Aerodyn., **61**, pp. 99–112.
[4] Sato, H., Kusuhara, S., Ogi, K.-I., and Matsufuji, H., 2000, "Aerodynamic Characteristics of Super Long-Span Bridges With Slotted Box Girder," J. Wind. Eng. Ind. Aerodyn., **88**, pp. 297–306.
[5] Roshko, A., 1955, "On the Wake and Drag of Bluff Bodies," J. Aeronaut. Sci., **22**, pp. 124–132.
[6] Munshi, S. R., Modi, V. J., and Yokomizo, T., 1999, "Fluid Dynamics of Flat Plates and Rectangular Prisms in the Presence of Moving Surface Boundary Layer Control," J. Wind. Eng. Ind. Aerodyn., **79**(1–2), pp. 37–60.
[7] Alam, M. M., Sakamoto, H., and Moriya, M., 2003, "Reduction of Fluid Forces Acting on a Single Circular Cylinder and Two Circular Cylinders," J. Fluids Struct., **18**, pp. 347–366.
[8] Bouak, F., and Lemay, J., 2001, "Use of the Wake of a Small Cylinder to Control Unsteady Loads on a Circular Cylinder," J. Visualization, **4**(1), pp. 61–72.
[9] Sarioglu, M., Akansu, Y. E., and Yavuz, T., 2005, "Control of Flow Around Square Cylinders at Incidence by Using a Rod," AIAA J., **43**(7), pp. 1419–1426.
[10] Lesage, F., and Gartshore, I. S., 1987, "A Method of Reducing Drag and Fluctuating Side Forces on Bluff Bodies," J. Wind. Eng. Ind. Aerodyn., **25**(2), pp. 229–245.
[11] Prasad, A., and Williamson, C. H. K., 1997, "A Method for the Reduction of Bluff Body Drag," J. Wind. Eng. Ind. Aerodyn., **69–71**, pp. 155–167.
[12] Igarashi, T., 1997, "Drag Reduction of a Square Prism by Flow Control Using a Small Rod," J. Wind Eng. Ind. Aerodyn., **69–71**, pp. 141–153.
[13] Tsutsui, T., and Igarashi, T., 2002, "Drag Reduction of a Circular Cylinder in an Air Stream," J. Wind. Eng. Ind. Aerodyn., **90**(4–5), pp. 527–541.
[14] Igarashi, T., and Nobuaki, T., 2002, "Drag Reduction of a Flat Plate Normal to air Stream by Flow Control Using a Rod," J. Wind. Eng. Ind. Aerodyn., **90**(4–5), pp. 359–376.
[15] Sakamoto, H., and Haniu, H., 1994, "Optimal Suppression of Fluid Forces Acting on a Circular Cylinder," ASME J. Fluids Eng., **116**, pp. 221–227.
[16] Wang, J. J., Zhang, P. F., Lu, S. F., and Wu, K., 2006, "Drag Reduction of a Circular Cylinder Using an Upstream Rod," Flow, Turbul. Combust., **76**(1), pp. 83–101.
[17] Strykowski, P. J., and Sreenivasan, K. R., 1990, "On the Formation and Suppression of Vortex Shedding at Low Reynolds Numbers," J. Fluid Mech., **218**, pp. 71–83.
[18] Shao, C. P., and Wang, J. M., 2007, "Control of Mean and Fluctuating Forces on a Circular Cylinder at High Reynolds Numbers," Acta Mech. Sin., **23**(2), pp. 133–143.
[19] Shao, C. P., and Wei, Q. D., 2008, "Control of Vortex Shedding From a Square Cylinder," AIAA J., **46**(2), pp. 397–407.
[20] Shao, C. P., Wang, J. M., and Wei, Q. D., 2007, "Visualization Study on Suppression of Vortex Shedding From a Cylinder," J. Visualization, **10**(1), pp. 57–64.
[21] Shao, C. P., and Wang, J. M., 2006, "Control of Vortex Shedding at Relatively High Reynolds Numbers," Chin. J. Theoret. Appl. Mech., **38**(2), pp. 153–161.
[22] Shao, C. P., 2008, "Advances in the Study of Methods and Mechanism of Bluff Body Wake Control," Adv. Mech., **38**(3), pp. 314–328.
[23] Gerrard, J. H., 1966, "The Mechanics of the Formation Region of Vortices Behind Bluff Bodies," J. Fluid Mech., **25**, pp. 401–413.
[24] Green, R. B., and Gerrard, J. H., 1993, "Vorticity Measurements in the Near Wake of a Circular Cylinder at Low Reynolds Numbers," J. Fluid Mech., **246**, pp. 675–691.
[25] Unal, M. F., and Rockwell, D., 1988, "On Vortex Formation From a Cylinder, Part 2: Control by Splitter-Plate Interference," J. Fluid Mech., **190**, pp. 491–512.
[26] Fage, A., and Johansen, F. C., 1927, "On the Flow of Air Behind an Inclined Flat Plate of Infinite Span," Proc. R. Soc. London, Ser. A, **116**, pp. 170–197.

Daniel C. Lyons
Hydraulic Engineer
VHCE York,
Voith Hydro, Inc.,
York, PA 17405
e-mail: daniel.lyons@voith.com

Leonard J. Peltier[1]
Senior Engineering Specialist in CFD
Bechtel National, Inc.,
Frederick, MD 21703
e-mail: ljpeltie@bechtel.com

Frank J. Zajaczkowski
Assistant Research Engineer
The Applied Research Laboratory,
The Pennsylvania State University,
University Park, PA 16804
e-mail: fxz101@psu.edu

Eric G. Paterson
Senior Research Associate
The Applied Research Laboratory,
The Pennsylvania State University,
University Park, PA 16802;
Associate Professor
Department of Mechanical and Nuclear Engineering,
The Pennsylvania State University,
University Park, PA 16802
e-mail: egp11@psu.edu

Assessment of DES Models for Separated Flow From a Hump in a Turbulent Boundary Layer

Separated flow past a hump in a turbulent boundary layer is studied numerically using detached-eddy simulation (DES), zonal detached-eddy simulation (ZDES), delayed detached-eddy simulation (DDES), and Reynolds-averaged Navier–Stokes (RANS) modeling. The geometry is smooth so the separation point is a function of the flow solution. Comparisons to experimental data show that RANS with the Spalart–Allmaras turbulence model predicts the mean-field statistics well. The ZDES and DDES methods perform better than the DES formulation and are comparable to RANS in most statistics. Analyses motivate that modeled-stress depletion near the separation point contributes to differences observed in the DES variants. The order of accuracy of the flow solver ACUSOLVE *is also documented.* [DOI: 10.1115/1.4000376]

Keywords: detached-eddy simulation, delayed detached-eddy simulation, zonal detached-eddy simulation, modeled-stress depletion, boundary-layer shielding, ACUSOLVE*, order of accuracy*

1 Introduction

Computational fluid dynamics (CFD) is today a primary analysis and design tool in engineering. The success of CFD is due not only to rapidly expanding computational resources but also to increased fidelity of modern numerical models. Recent advances in modeling turbulent flows have involved classes of eddy-resolving techniques that blend statistical Reynolds-averaged Navier–Stokes (RANS) modeling near walls with large-eddy simulation (LES) in outer regions of interest. Detached-eddy simulation (DES) [1] and its variants are perhaps the most common examples. Strelets [2] showed that DES of massively separated flows can yield improved flow statistics. The level of success of DES approaches for nonmassively separated flows, however, is not clear.

This work is motivated by the earlier study of Paterson and Peltier [3] who documented deficiencies of DES in modeling trailing-edge flows for airfoils where the separation point is not imposed by the geometry. They found that when the transition from RANS to LES occurs upstream of the separation point, resolved turbulence scales do not evolve quickly enough to compensate for the loss of statistical turbulence leading to a region of depleted turbulence stresses and unphysical flow that influences the flow downstream. Spalart et al. [4] used the term "modeled-stress depletion" to identify this difficulty and Menter et al. [5] discussed the resulting effect of "grid-induced separation." Variants of DES have been developed that shield attached boundary layers from transition to LES. Delayed detached-eddy simulation (DDES) [4] and zonal detached-eddy simulation (ZDES) [6] are examples.

The purpose of this work is to evaluate whether boundary-layer shielding techniques such as ZDES and DDES provide significantly improved modeling, over RANS and DES, of separated flow where the separation point is not prescribed by sharp edges in the geometry. The Glauert–Goldschmied body embedded in a turbulent boundary layer is our test case. The geometry comprises a nominally 2D hump in a channel with a smooth curved surface on the leeward side where separation occurs. A detailed experimental database is available from NASA.[2] These data and the corresponding computational studies have been extensively documented in literature, see Refs. [7,10], among others.

In Secs. 2–5, we present the geometry of the Glauert–Goldschmied body, then discuss the governing equations, turbulence closures, and domain discretization, and document the order of accuracy and other details of the CFD flow solver. Using comparisons to experimental data and by contrasting the DES, ZDES, DDES, and RANS models, we attempt to quantify the positive impacts of boundary-layer shielding on the flow solutions and to identify remaining modeling issues.

2 The Glauert–Goldschmied Body and Test Conditions

The Glauert–Goldschmied body is a 2D hump mounted in a parallel channel (see schematic in Fig. 1). End plates are used in the test section to remove the channel's side-wall boundary layers, and a splitter plate is used to place the configuration above the boundary layer at the floor of the channel and to provide a nearly

[1]Corresponding author.

Contributed by the Fluids Engineering Division of ASME for publication in the JOURNAL OF FLUIDS ENGINEERING. Manuscript received October 29, 2007; final manuscript received September 20, 2009; published online October 28, 2009. Editor: Joseph Katz.

[2]See http://cfdval2004.larc.nasa.gov/case3.html for code validation purposes.

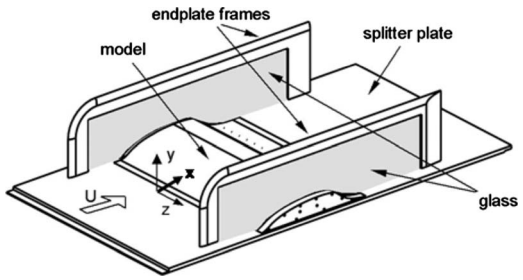

Fig. 1 Schematic of hump model used for CFD[2]

constant inflow velocity to the test section. The hump chord length is $c=0.42$ m (16.536 in.), and the hump height is 0.0537 m (2.116 in.). The distance from the splitter plate to the top wall of the channel is 0.382 m (15.032 in.).

A rich experimental database is available for this configuration.[3] The experimental measurements consist of x and y velocities in the recirculation region, documented by Greenblatt et al. [11], and pressure and shear stress measurements, documented by Naughton et al. [12], along the bottom surface of the hump. The results have been used for CFD validation during CFDVAL 2004. RANS, DES, LES, and DNS models were applied. The documentation of the validation exercises is available in the literature.

We consider the baseline case from the NASA test. The freestream velocity, U, is 34.6 m/s. The reported dynamic viscosity and density, μ and ρ, are 18.4×10^{-6} kg/ms and 1.184 kg/m^3, respectively, yielding a chord Reynolds number, Re, of 936,000. Experimental data show that the flow statistics are nominally 2D and that separation occurs on the leeward side of the hump at $x/c=0.665$, measured from the upstream edge of the hump geometry, creating a detached shear layer followed by reattachment downstream of the separation point at $x/c=1.11$.

3 Governing Equations

3.1 Navier–Stokes Equations. The equations governing fluid flow are the Navier–Stokes momentum conservation equations and continuity,

$$\frac{\partial\tilde{u}_i}{\partial t}+\tilde{u}_j\frac{\partial\tilde{u}_i}{\partial x_j}=-\frac{1}{\rho}\frac{\partial\tilde{p}}{\partial x_i}+\nu\frac{\partial^2\tilde{u}_i}{\partial x_j\,\partial x_j}\quad\text{and}\quad\frac{\partial\tilde{u}_i}{\partial x_i}=0 \tag{1}$$

The notation follows Tennekes and Lumley [13], where the overset tilde denotes a full variable $\tilde{u}_i$, one that has both a statistical mean value, U_i, and a fluctuating component, u_i: $\tilde{u}_i=U_i+u_i$.One can formally filter Eq. (1) to derive the equations solved by a CFD code:

$$\frac{\partial\tilde{u}_i^r}{\partial t}+\tilde{u}_j^r\frac{\partial\tilde{u}_i^r}{\partial x_j}=-\frac{1}{\rho}\frac{\partial\tilde{p}^r}{\partial x_i}+\nu\frac{\partial^2\tilde{u}_i^r}{\partial x_j\,\partial x_j}-\frac{\partial\tau_{ij}}{\partial x_j}\quad\text{and}\quad\frac{\partial\tilde{u}_i^r}{\partial x_i}=0 \tag{2}$$

where the "filtered/resolved" variables (superscript r, $\tilde{u}_i^r$, and $\tilde{p}^r$) are computed and the effects of the "subfilter" motions (superscript s and u_i^s) on the resolved field are collected in the subfilter stress, τ_{ij}, $\tau_{ij}\equiv(u_i^ru_j^s+u_i^su_j^r+u_i^su_j^s)^r+(u_i^ru_j^r)^r-(u_i^ru_j^r)$. Introducing an eddy-diffusion closure for the subfilter stress followed by collecting terms yields

$$\frac{\partial\tilde{u}_i^r}{\partial t}+\tilde{u}_j^r\frac{\partial\tilde{u}_i^r}{\partial x_j}=-\frac{1}{\rho}\frac{\partial\tilde{p}^r}{\partial x_i}+2\frac{\partial}{\partial x_j}[(\nu+\nu_T)\tilde{S}_{ij}^r] \tag{3}$$

where ν_T, the eddy diffusivity, must be modeled and $\tilde{S}_{ij}^r=(1/2)\times((\partial\tilde{u}_i^r/\partial x_j)+(\partial\tilde{u}_j^r/\partial x_i))$ is the strain rate tensor.

[3]http://cfdval2004.larc.nasa.gov/case3.html.

3.2 Modeling Strategies. The RANS, DES, DDES, and ZDES modeling approaches differ in their prescription for the eddy diffusivity. RANS closures model fully the effects of turbulence on the mean field. The DES variants allow some of the turbulence to be resolved explicitly, reducing the dependence on modeling. The original DES formulation transitions between LES and RANS based on local grid resolution, which may allow the transition to happen within attached boundary layers. The DDES and ZDES variants control the transition from the RANS to LES based on the local flow solution protecting attached boundary layers from transition to LES, thus providing boundary-layer shielding.

3.2.1 Spalart–Allmaras RANS. Our RANS closure is the Spalart–Allmaras (SA), one-equation turbulence model [14]. The SA model relates the eddy diffusivity, ν_T, to a computed diffusivity, $\tilde{\nu}$, that satisfies the transport equation:

$$\frac{\partial\tilde{\nu}}{\partial t}+U_j\frac{\partial\tilde{\nu}}{\partial x_j}=c_{b1}\tilde{S}\tilde{\nu}-c_{w1}f_w\left(\frac{\tilde{\nu}}{d}\right)^2+\frac{1}{\sigma}\frac{\partial}{\partial x_k}\left[(\nu+\tilde{\nu})\frac{\partial\tilde{\nu}}{\partial x_k}\right]+\frac{c_{b2}}{\sigma}\frac{\partial\tilde{\nu}}{\partial x_k}\frac{\partial\tilde{\nu}}{\partial x_k} \tag{4a}$$

where d is the distance to the nearest no-slip surface. The model constants are

$$c_{b1}=0.1355,\quad c_{b2}=0.622,\quad c_{v1}=7.1,\quad\sigma=\frac{2}{3}$$
$$c_{w1}=\frac{c_{b1}}{\kappa^2}+\frac{(1+c_{b2})}{\sigma},\quad c_{w2}=0.3,\quad c_{w3}=2,\quad\kappa=0.41 \tag{4b}$$

and the functional relationship of ν_T to $\tilde{\nu}$ is

$$f_{v1}=\frac{\chi^3}{\chi^3+c_{v1}^3},\quad f_{v2}=1-\frac{\chi}{1+\chi f_{v1}},\quad f_w=g\left(\frac{1+c_{w3}^6}{g^6+c_{w3}^6}\right)^{1/6}$$
$$\nu_T=\tilde{\nu}f_{v1}\quad\text{where}\quad\chi=\frac{\tilde{\nu}}{\nu},\quad g=r+c_{w2}(r^6-r),\quad r=\frac{\tilde{\nu}}{\tilde{S}(\kappa d)^2} \tag{4c}$$

$$S=\sqrt{2\Omega_{ij}\Omega_{ij}},\quad\tilde{S}=S+\frac{\tilde{\nu}}{(\kappa d)^2}f_{v2},\quad\Omega_{ij}=\frac{1}{2}\left(\frac{\partial U_i}{\partial x_j}-\frac{\partial U_j}{\partial x_i}\right)$$

The SA model diagnoses the time scale of the turbulence from the mean-field vorticity and chooses the characteristic length as maximum distance to the wall. The model constants and functions are tuned to data.

3.2.2 DES. The baseline DES model by Spalart et al. [1] is derived from the SA RANS closure by replacing the characteristic length scale d with a hybrid length scale $\tilde{d}$, where $\tilde{d}$ is defined as the minimum of d and a characteristic grid scale, $C_{\mathrm{DES}}\Delta$:

$$\tilde{d}=\min(d,C_{\mathrm{DES}}\Delta) \tag{5}$$

Because the destruction term in the DES form of Eq. (4*a*) is proportional to the inverse of the characteristic length scale $\tilde{d}$, smaller values of $\tilde{d}$ lead to increased destruction resulting in a smaller diffusivity, $\tilde{\nu}$, and hence smaller ν_T. Thus more of the turbulence is resolved and less is subgrid. In the limit of infinitely fine resolution, $C_{\mathrm{DES}}\Delta\sim d$, $\nu_t\to0$ recovering direct numerical simulation (DNS). In the coarse grid limit, $C_{\mathrm{DES}}\Delta\sim d$, the DES length scale reverts to $\tilde{d}=d$ or to RANS modeling.

3.2.3 ZDES. The DES model discriminates RANS regions from the LES ones, solely on the relative length scale ratio, $C_{\mathrm{DES}}\Delta/d$. When $C_{\mathrm{DES}}\Delta\ll d$, the DES model is allowed to transition to LES, even within the attached boundary layers where

RANS modeling is desired; thus, the original DES formulation requires a very stringent grid generation process to avoid transition in attached boundary layers. Slimon [6] introduced ZDES to allow the model to discriminate attached boundary layers within a solution and prevent transition to LES within them. ZDES defines a discriminator function ψ, where

$$\psi = \min\left(\frac{1}{2}d\frac{C_\mu \Omega}{a_1 k^{1/2}}, \frac{d^2\Omega}{500\nu}\right) \tag{6a}$$

$\psi \leq 1$ identifies the boundary layers. The model constants, a_1 and C_μ, are

$$a_1 = 0.31, \quad C_\mu = 0.09 \tag{6b}$$

Access to the turbulent kinetic energy (TKE), k, is required to compute ψ for Eq. (6*c*). However, k is not a variable directly available from the Spalarat–Allmaras model. Slimon [6] deduced k from the strain rate and eddy diffusivity:

$$k \approx \max\left(\frac{\nu_T}{a_1}\tilde{S}^r, k_0\right) \tag{6c}$$

where k_0 is a freestream value and $\tilde{S}^r \equiv (2\tilde{S}^r_{ij}\tilde{S}^r_{ij})^{1/2}$. Note that Eq. (6*c*) corrects a typographical error in Ref. [6]. Slimon [6] also reported that numerical experiments showed that best results were obtained when $f_{v1}=f_w=1$ and $f_{v2}=0$, values also adopted here.

ZDES redefines $\tilde{d}$, such that

$$\tilde{d} = \begin{cases} d & \text{for} \quad \psi \leq 1 \\ \min(d, C_{\text{DES}}\Delta) & \text{for} \quad \psi > 1 \end{cases} \tag{7}$$

The method sharply delineates RANS and LES regions but ensures a continuous smooth solution across the ZDES interface.

3.2.4 DDES. DDES was introduced by Spalart et al. [4] also as a means to protect attached boundary layers from transition to LES. DDES replaces the length scale d in the SA model with a modified length scale $\tilde{d}$ using a discriminator function, f_d, to distinguish the RANS and LES regions:

$$\tilde{d} \equiv d - f_d \max(0, d - C_{\text{DES}}\Delta) \tag{8}$$

where

$$f_d \equiv 1 - \tanh([8r_d]^3) \tag{9}$$

The new parameter r_d replaces the parameter r in the original SA RANS formulation,

$$r_d \equiv \frac{\nu_t + \nu}{\sqrt{U_{i,j}U_{i,j}}\kappa^2 d^2} \tag{10}$$

Through the deformation tensor magnitude in the denominator, r_d is sensitive to both strain and rotation.

4 Numerical Method and Computational Grid

4.1 Numerical Method. The commercial flow solver, ACUSOLVE[4] from ACUSIM, Inc. (Mountainview, CA), was used to perform the calculations in this study. ACUSOLVE is a finite-element flow solver that is reported to be second-order accurate in space and time, a claim that will be verified in the current work. The code imports a number of grid formats. FLUENT case files provided the primary interchange between the grid generation code, GRIDGEN, from Pointwise, Inc. (Fortworth, TX), and ACUSOLVE. The code implements a broad range of boundary conditions and is richly instrumented with data monitoring and data extraction tools. Our experience with the code confirms that it is robust and accurate for the single phase, incompressible, RANS and DES cases investigated.

[4]http://www.acusim.com/.

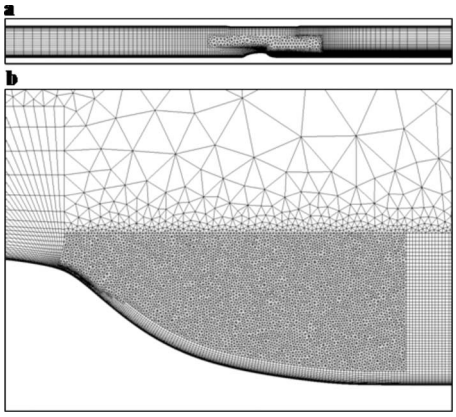

Fig. 2 Full (above) and close-up views (below) of the computational grid

4.2 Computational Grid and Boundary Conditions. Our computational grid resolution was chosen based on the mesh resolution/time-step sensitivity study of Krishnan et al. [9] for the Glauert–Goldschmied flow-control configuration studied here. They define minimum grid spacings and time-step size to resolve the physics of this flow adequately. We use their results to guide the generation of our resolved mesh, allowing our results to have nominally the same mesh resolution as the results of Krishnan et al. [9]thus facilitating intercomparisons.

Our mesh is an unstructured grid comprising hex and wedge elements. To construct our mesh, we first build a 2D mesh of triangles and quadrangles that resolve the relevant details of the flow and geometry (see Fig. 2). High grid resolution is placed in the recirculation zone on the lee side of the hump where turbulence is to be resolved (Fig. 2(*b*)). To capture the separation point, grid density is increased near $x/c=0.65$ where separation is expected. The 3D mesh is generated from the 2D mesh by extrusion in the spanwise direction.

The grid cells in the turbulence-resolving recirculation region are isotropic. The grid spacing is $\Delta x/c=\Delta y/c=\Delta z/c=3.025\times10^{-3}$, or $\Delta x^+=\Delta y^+=\Delta z^+=131.4$ in wall coordinates based on the friction velocity upstream of the hump, similar to the guidelines of Krishnan et al. [9]. The minimum distance to the wall in wall units is $y^+\sim1.25$ making the solution sublayer resolved. The 3D mesh extends 40 cells in the spanwise direction yielding a mesh depth of $z/c=0.121$, which is slightly under 10% of the width of the geometry. The inlet is placed upstream of the hump at $x/c=-6.8$ where slug flow conditions are applied. This location is chosen because it yields a developing boundary layer that matches experimental data at $x/c=-2.1$, as seen in Fig. 3, for RANS, DES,

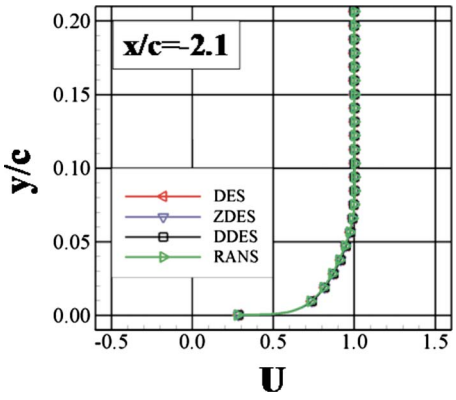

Fig. 3 Mean-velocity profiles near inflow ($x/c=-2.1$) for RANS, DES, ZDES, and DDES

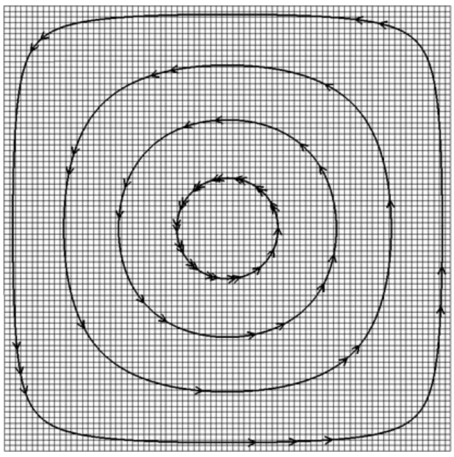

Fig. 4 Streamlines and mesh for the Taylor–Green vortex

ZDES, and DDES. A time-step size of $\Delta t = 0.0032c/U$ is used, a value found by Krishnan et al. [9] to resolve the low to midfrequencies of turbulence spectra. The downstream outlet is at $x/c = 6.0$. The upper and lower walls are no-slip surfaces. Periodic conditions are enforced in the spanwise direction.

5 Results and Discussion

In the results that follow, we first independently confirm the order of accuracy of the flow solver, ACUSOLVE, and demonstrate its ability to support resolved turbulence using LES of turbulent channel flow. We then compare our CFD solutions of the Glauert–Goldschmied flow for the baseline (no flow control) configuration to the NASA data set and assess the strengths and weaknesses of RANS and the DES variants for modeling a nonmassively separated flow.

5.1 Order of Accuracy. ACUSIM, Inc. reports that ACUSOLVE is rigorously second-order accurate in space and time. To confirm the spatial/temporal accuracy of the code, we simulated the Taylor–Green vortex used by Kim and Moin [15] for determining the order of accuracy of their code. The Taylor–Green vortex is a decaying, 2D, laminar vortex that has a known analytic solution:

$$u(x,y,t) = -\cos x \sin y \; e^{-2t}$$
$$v(x,y,t) = \sin x \cos y \; e^{-2t} \tag{11}$$
$$p(x,y,t) = -\tfrac{1}{4}(\cos 2x + \sin 2y)e^{-4t}$$

Streamlines with velocity vectors visualizing the flow are presented in Fig. 4 at the initial time $t=0$.

We defined a computational domain from $-\pi/2$ to $\pi/2$ in x and y that encompasses one Taylor–Green vortex and apply symmetry conditions at the x and y boundaries. Because ACUSOLVE requires a 3D mesh, we extruded the 2D domain by one cell in the z direction and apply slip conditions on the z boundaries. To emulate a 2D flow with ACUSOLVE, the z direction extrusion length must be much larger than the largest cell length in the x and y directions. We use a z direction extrusion distance of 10, a value larger than π, the domain length in x and y. To assess the influence of the symmetry boundary conditions on our solutions, some calculations were also performed for a domain size of $-(3/2)\pi$ to $(3/2)\pi$ in x and y which subtends three Taylor–Green vortices in x and three in y or nine vortices total for the domain. We found negligible difference between the single cell and multiple-cell solutions.

To consider the effects of grid resolution, four computational meshes were constructed distributing 11, 21, 41, and 81 grid points per π along a side. Because the hump mesh studied in this work comprises hex and wedge elements, the order of accuracy was assessed for these element types, too. The hex mesh was constructed by forming a structured mesh for the 2D computational domain consisting of quad elements that became hex elements once extruded. To form the wedge mesh, GRIDGEN's unstructured domain solver was used to create isotropic triangles filling the domain that became wedge elements once extruded. The change in grid resolution with increasing grid refinement, therefore, for both the hex and wedge meshes was a factor of 2. Order of accuracy in time was also assessed using time-step increments differing by a factor of 2. The four time-step sizes used are 2.0×10^{-3}, 1.0×10^{-3}, 5.0×10^{-4}, and 2.5×10^{-4}.

The spatial order of accuracy calculations used three grids of successive increases in resolution with a fixed time-step size of 1.0×10^{-3}. A solution was computed for each grid by integrating forward one time step. The temporal order of accuracy calculations were computed on the 41 grid points per π mesh for three consecutive time-step sizes and were confirmed using similar calculations on the 81 grid points per π mesh. The procedure was to integrate forward one time step for the coarse time-step size, two time steps for the first refinement, and four time steps for the finest time-step size, thus aligning the final solutions to the same final integration time.

Following Kim and Moin [15], we define the difference between the analytic and computational solutions for the u velocity field as the solution error extracting the maximum value from each solution, yielding a single value error metric for the coarse, moderate, and fine resolution cases, ε_U^C, ε_U^M, and ε_U^F, respectively. We subtract ε_U^F from ε_U^C and ε_U^M to generate error differences $\Delta\varepsilon_U^C$

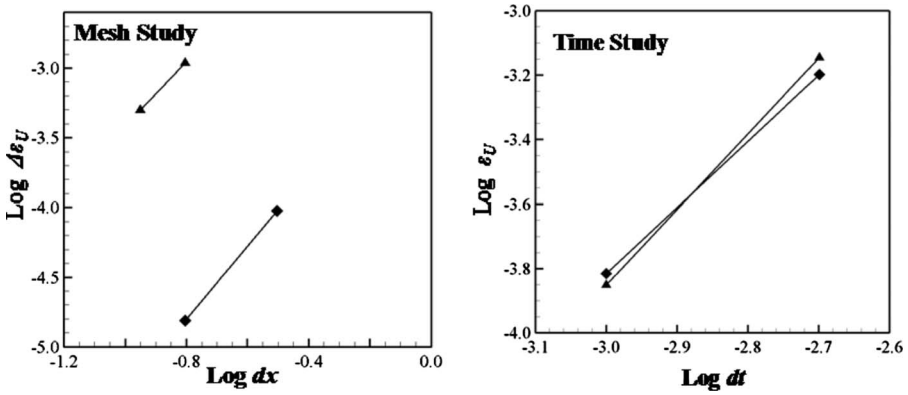

Fig. 5 Log plots of maximum error, ε_U, versus resolution for mesh study and time study for hexes (diamond) and wedges (triangle)

Table 1 Order of accuracy of ACUSOLVE in space and time for hex and wedge elements

Element type	Spatial order range	Average spatial order	Temporal order range	Average temporal order
Hexes	2.19–2.78	2.49	2.04–2.05	2.04
Wedges	1.95–2.60	2.29	2.00–2.50	2.30

and $\Delta\varepsilon_U^M$. The decay of these error differences with increasing resolution, Fig. 5, establishes the order of accuracy of the numerics, $n=\ln[\Delta\varepsilon_U^C/\Delta\varepsilon_U^M]/\ln(2)$. The results for the spatial and temporal orders of accuracy assessments are presented in Table 1. They confirm that ACUSOLVE is at least second-order accurate in space and time for hex and wedge elements. Similar results are found using the root mean square (rms) error as the order of accuracy metric.

5.2 LES of Turbulent Channel Flow. To confirm that ACUSOLVE can accurately resolve turbulence fluctuations, we performed one simulation for LES of turbulent channel flow at $\mathrm{Re}_\tau = u_\tau H/\nu = 470$, where u_τ is the friction velocity, H is the channel half height, and ν is the kinematic viscosity and compared the results to published DNS data from Ref. [16]. Table 2 presents the Reynolds number and grid parameters. Our LES subgrid parametrization implements the Smagorinsky model [17]. We used a constant mass-flux condition with periodic inflow/outflow conditions to drive the channel flow initializing turbulence fluctuations with random numbers. The flow was integrated until a statistically steady state was reached after which flow statistics were collected. The mean flow and turbulence statistics presented in Figs. 6 and 7 were averaged over approximately four large-eddy turnover times. The mean velocity profile in wall coordinates ($u^+ = U/u_\tau$ and $y^+ = u_\tau y/\nu$), Fig. 6, shows that the LES faithfully captures the near-wall behavior resolving the viscous sublayer, buffer layer, and log layer. The overshoot observed in the transition from the buffer layer to the log layer is common to LES using a Smagorinsky subgrid model. The turbulence rms statistics are presented in Fig. 7, also in wall coordinates. Near the wall, the LES data slightly overpredict u_{rms}, slightly underpredict v_{rms}, and match w_{rms}. For $y^+ > 60$, the rms profiles agree very well with Ref. [16]. The favorable comparison between our LES data and the DNS results of Moser et al. [16] establishes the ability of ACUSOLVE to support resolved turbulence and demonstrates that the solution is minimally impacted by artificial dissipation.

Table 2 Reynolds number and grid parameters for the DNS of Moser et al. [16] and the current LES of turbulent channel flow

Re_τ	L_x/H	L_z/H	$N_x \times N_y \times N_z$	Δx^+	Δz^+	Δy_c^+
			DNS data of Moser et al. [16]			
395	2π	π	$256\times193\times192$	10	6.5	6.5
590	2π	π	$384\times257\times384$	9.7	4.8	7.2
			LES data			
470	8	4	$111\times92\times129$	34.0	14.6	15.1

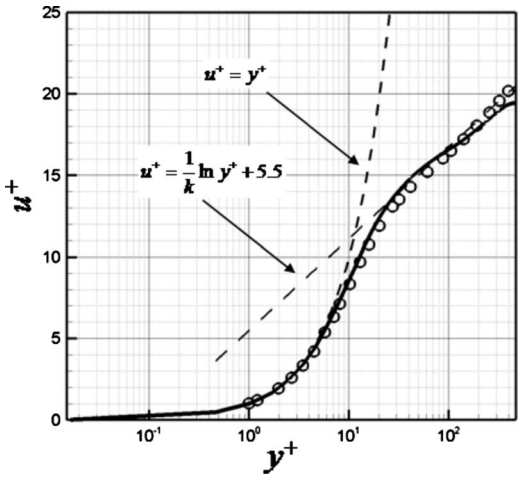

Fig. 6 LES computation $\mathrm{Re}_\tau = 470$ (solid line) compared to the DNS data of Moser et al. [16] $\mathrm{Re}_\tau = 590$ (circles) for turbulent channel flow in near-wall region in plus coordinates

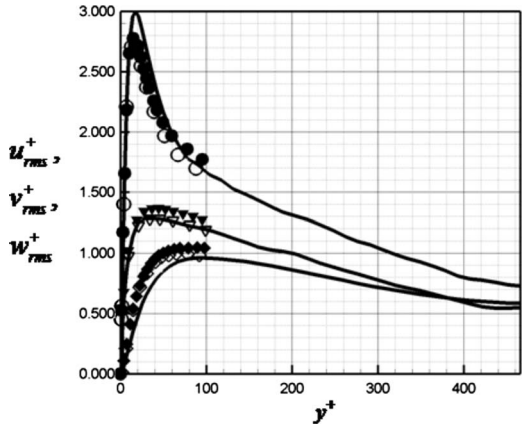

Fig. 7 ACUSOLVE LES data at $\mathrm{Re}_\tau = 470$ (solid lines) compared with the DNS data of Moser et al. [16] at $\mathrm{Re}_\tau = 590$ (filled-in symbols) and $\mathrm{Re}_\tau = 395$ (open symbols [16]. u^+_{rms} (circles), v^+_{rms} (diamonds), and w^+_{rms} (gradients).

5.3 Turbulent Flow Over the Glauert–Goldschmied Hump. Having established the order of accuracy of the flow solver and having shown that the code is able to support turbulence fluctuations with minimum artificial dissipation, we are ready to assess variants of DES for simulation of flow past the Glauert–Goldschmied hump in a turbulent boundary layer.

Because DES approaches resolve turbulence in regions modeled as LES, the separated region for the Glauert–Goldschmied flow, flow statistics must be collected over several large-eddy turn over times. We average in time and along a homogeneous direction in space. In this study, statistically stationary states are reached after about 7000 time steps. Flow statistics are then collected by averaging over 16,000 time steps (a dimensionless time of 51.2 equivalent to approximately 112 separation-bubble passage times) followed by further averaging across the homogeneous, spanwise direction.

Color contours of the mean longitudinal velocity, U, with streamlines (Fig. 8) detail the statistical separated zone for DES, ZDES, DDES, RANS, and the experiment. The ensemble-averaged RANS solution and experiment (Figs. 8(*d*) and 8(*e*)) show that the flow statistics are characterized by a dominant spanwise vortical structure on the lee side of the hump representing the statistical recirculating separated zone. Table 3 summarizes the separation and reattachment points for each of the models. In the experiment, separation occurs at $x/c = 0.665$ with reattachment occurring at $x/c = 1.11$. The DES solution differs most from the experimental data. Separation is observed at $x/c = 0.640$. Reattachment occurs at $x/c = 1.35$. The RANS, ZDES, and DDES solutions agree reasonably well with the experimental observations. Separation occurs in the RANS solution at $x/c = 0.663$ with reattachment at $x/c = 1.22$. The ZDES and DDES solutions are slightly better. Separation occurs at $x/c = 0.662$ for ZDES and $x/c = 0.661$ for DDES with reattachment at $x/c = 1.19$ for both. Premature separation in the solution, see DES Fig. 8, leads to a

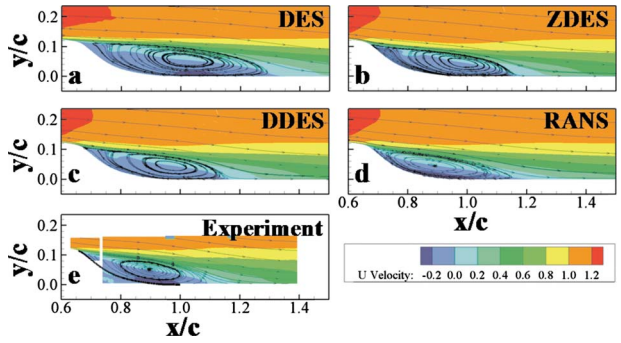

Fig. 8 Mean-velocity field: contours of longitudinal velocity (*U*) and streamlines

longer separation bubble. The ZDES, DDES, and RANS models, whose separation points are near the experimentally observed locations, show significantly shorter separation-bubble lengths, which are in better agreement with the experimental data.

The boundary layer at the top of the hump in the DES solution, $x/c=0.6$, is thicker than the boundary layers that develop in the ZDES, DDES, and RANS solutions (Fig. 9), explaining the early separation. This modeling artifact is an example of the grid-induced separation of Menter et al. [5] that results from the modeled-stress depletion of Spalart et al. [4]. Paterson and Peltier [3] noted this effect for DES of the trailing-edge flow of a 2D airfoil, a similar geometry to the aft side of the Glauert–Goldschmied hump.

The discriminator functions separating the RANS and LES regions of the DES variants are plotted in Fig. 10. One sees that the LES mode is active everywhere in the DES model (Fig. 10(*a*)) except very near the upper and lower boundaries, so without resolved turbulence scales, proper turbulence mixing cannot occur. In contrast, the ZDES model remains predominantly RANS (Fig. 10(*b*)), except within the separated zone, providing an effective shielding of the attached boundary layers from transition to LES. Similar to DES, the DDES model (Fig. 10(*c*)) allows a much broader LES regime than ZDES; thus the model may be more sensitive to modeled-stress depletion; however, like ZDES, a thicker RANS layer is maintained near walls, documenting

Table 3 Separation and reattachment points with nondimensional distance measured from the leading edge of the hump

	RANS	DES	ZDES	DDES	Expt.
Separation	0.663	0.640	0.662	0.661	0.665
Reattachment	1.22	1.35	1.19	1.19	1.11

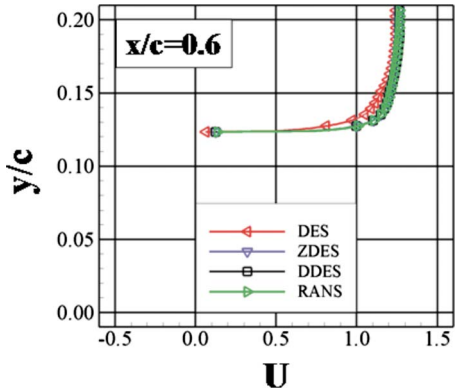

Fig. 9 Mean *U* velocity profiles prior to separation ($x/c=0.6$) for RANS, DES, ZDES, and DDES

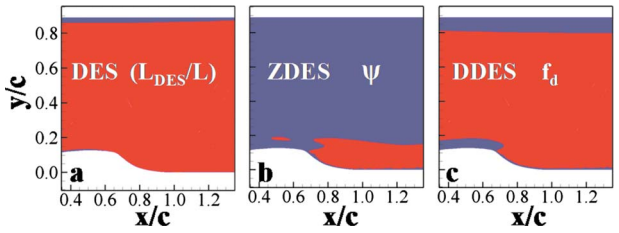

Fig. 10 Contour map of DES discriminator functions. The contour boundary separates the RANS (near boundary) and LES (separated zone) regions.

boundary-layer shielding.

Contours of the dimensionless mean eddy diffusivity are plotted in Fig. 11. Prior to separation, the ZDES, DDES, and RANS solutions are similar, showing significant modeled turbulence mixing above the top of the hump, $x/c<0.6$. This contour is absent from the DES solution, confirming modeled-stress depletion in this region and supporting the premise that modeled-stress depletion is the primary cause of premature separation. Within the separated zone, the eddy diffusivities of DES, ZDES, and DDES solutions are similarly small, relative to the RANS solution, as they need to support resolved turbulence motions.

It would be possible to maintain the fine grid upstream allowing resolved turbulence fluctuations to form. Such an approach would presumably improve the separation location of each of the DES methods, including the original DES formulation. This approach, however, does not make use of a primary strength of a hybrid method, the ability to focus grid resolution in a region of interest, so would not address the primary interest of the study—to assess DES variants for practical applications. Thus it is not beneficial to document the results of that approach in this work.

5.4 Comparisons to Experimental Data. Profiles of the *U* and *V* velocities are presented in Fig. 12 for eight stations along the flow separation ($x/c=0.65$, 0.66, 0.8, 0.9, 1.0, 1.1, 1.2, and 1.3). The computational data were extracted by interpolating onto the experimental probe measurement locations. *U* velocity profiles from the DES of Krishnan et al. [9] are also shown for stations $x/c=1.0$, 1.1, 1.2, and 1.3. Because our DES recirculation is larger than the experimentally observed one, the relative locations within the recirculating zone of the DES extraction points (as a fraction of the recirculation length) are different from the relative locations of those extraction points in the experiment. Thus, the poor observed agreement between the DES solution and the experimental data is understood. It should be noted that Krishnan et al. [9] presented very good comparisons to the Glauert–Goldschmied data for DES as is shown in Fig. 12; however, they explicitly enforced RANS to a point only slightly upstream of the

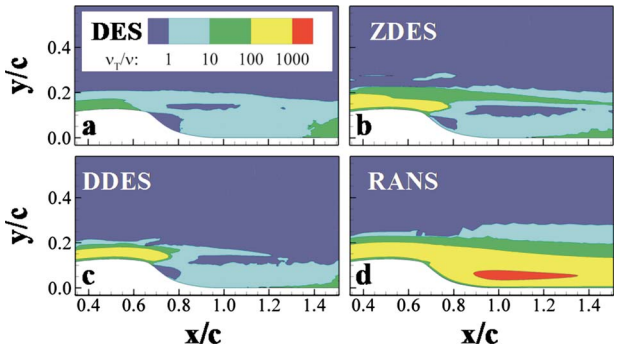

Fig. 11 Contour maps of the nondimensional, mean eddy viscosity

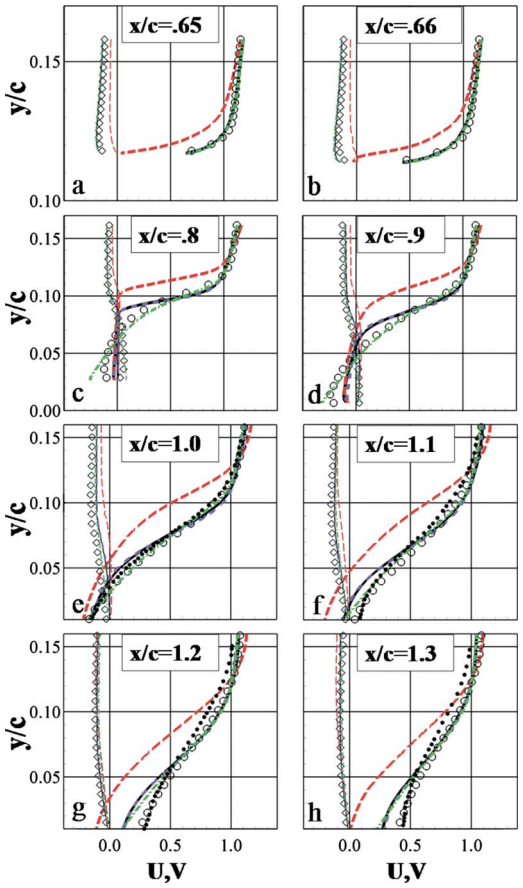

Fig. 12 Profiles of *U* (thick) and *V* (thin) for DES (long dash), ZDES (dash), DDES (solid), RANS (dash dot), and DES of Krishnan et al. [9] (squares) at *x/c* locations of interest. Other symbols are the experimental results for *U* (circle) and *V* (diamond).

known flow separation point to avoid the adverse effects of transition from RANS to LES in the upstream boundary layer, thus provided a manual boundary-layer shield.

Profiles from RANS and from the boundary-layer shielded ZDES and DDES models compare very well to the experimental results upstream and at the separation point ($x/c=0.65$ and 0.66). They also agree well near the eye of the separation bubble (at $x/c=1.0$ and 1.1). A mild discrepancy is observed near the surface close to the reattachment point (see $x/c=1.2$ and 1.3), only because the computational reattachment locations differ slightly from the experimental one. Serious differences from experiment are observed in the ZDES and DDES solutions in the region strongly affected by modeled-stress depletion, $x/c=0.8$ and 0.9. The DES solution behaves similarly. The U and V velocities are near zero at these locations where distance to the bottom wall ranges between 0.0 and 0.055, unlike the RANS prediction and the experimental measurements.

Contours of the resolved and subfilter components of the TKE are presented in Fig. 13. Both resolved turbulence and modeled subfilter turbulence contribute to the total TKE, k:

$$k = \tfrac{1}{2}\overline{u_i u_i} = \tfrac{1}{2}(\overline{u_i^r u_i^r} + \overline{u_i^s u_i^s}) \tag{12}$$

To compute Eq. (12), the resolved TKE information is extracted from the spatially averaged flow statistics and the subfilter information is diagnosed from the turbulence model, see Eq. (6*c*). Because experimental TKE fields were not available for the current case, the RANS TKE field, which models the total expected TKE for the given flow, will be used as a basis for intercomparisons of the DES variants. Velocity profiles at $x/c=0.8$ and 0.9 in Fig. 12 show that the RANS case predicts the region near separation reasonably well. TKE contours from the RANS model show significant turbulence energy within the separation and extend to the separation point. The DES variants also predict significant TKE levels in the separated zone for $x/c>0.9$; however, they do not capture the TKE levels from $x/c=0.6$ to 0.9. Because the discriminator functions of Fig. 9 show that the region from $x/c=0.6$ to 0.9 lies within the LES zone and because the RANS model results show that significant turbulence is expected, we conclude that the loss of turbulence in the DES variants is an artifact of modeled-stress depletion, however, one for which a modeling correction has yet to be identified.

Skin friction coefficient, $|C_f|$, and pressure coefficient, C_p, profiles along the bottom surface of the hump are presented in Fig. 14 where $|C_f|$ and C_p are defined as

$$C_f \equiv \frac{\tau_w}{\frac{1}{2}\rho U_r^2} \quad \text{and} \quad C_p \equiv \frac{(\tilde{p}-p_\infty)}{\frac{1}{2}\rho U_r^2} \tag{13}$$

The C_p results of Krishnan et al. [9] and Biswas' [10] C_p and C_f results are also shown. The reference pressure, p_∞, for the C_p profile is adjusted by a constant to match the first experimental data point near $x/c=-1$. Both profiles agree well with the experimental data upstream of the separation, for $x/c<0.5$, for the

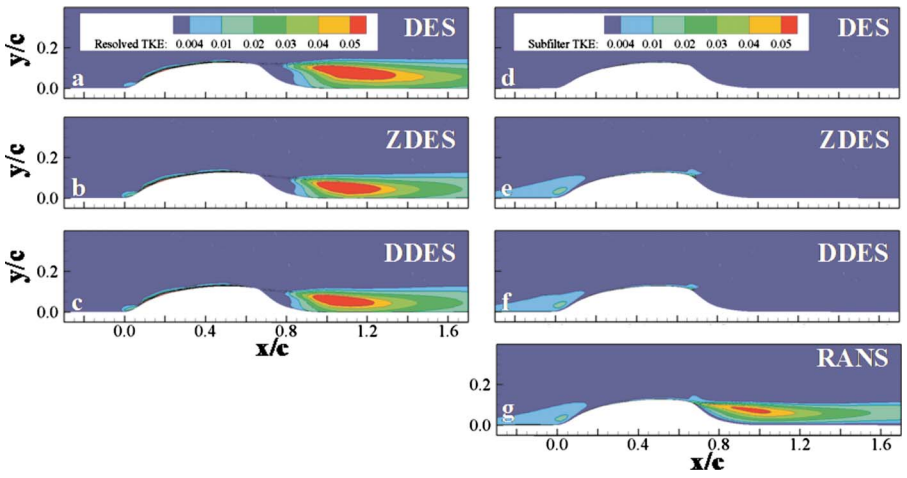

Fig. 13 Contours of resolved and subfilter turbulent kinetic energy

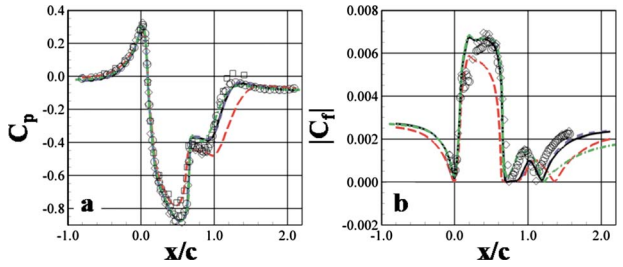

Fig. 14 Pressure and skin friction coefficient profiles for DES (long dash), ZDES (dash), DDES (solid), RANS (dash dot), experiment (circle), Biswas' [10] LES pressure and skin friction coefficients (diamond), and DES pressure coefficient (square) of Krishnan et al. [9]

ZDES, DDES, and RANS solutions. A discrepancy is observed for the DES results which overpredict C_p and underpredict $|C_f|$ in the range from $x/c \sim 0.3$ to $x/c \sim 0.7$. C_p data for the ZDES, DDES, and RANS solutions also agree well with the experiment in the pressure recovery region. Pressure recovery in the DES solution is delayed slightly because the DES recirculation zone is longer than the experimental one. The trend in the pressure recovery, however, is correct. The modeled ZDES, DDES, and RANS data are least accurate in the region from $x/c=0.6$ to 0.9, where modeled-stress depletion is significant. The amplitudes of the DES data, however, compare well in this region, a finding that may be fortuitous because the upstream DES solution differs from the experimental data.

Our C_p results fall within the spread reported by Rumsey et al. [8] summarizing contributions to the CFD validation workshop on synthetic jets and turbulent separation control (see their Fig. 22a). Our DES compare well with those presented by Krishnan et al. [9] with the exception of the delayed pressure recovery. We note that our DES solution was allowed to find its own separation point, while Krishnan et al. [9] enforced RANS until near the experimental separation point, an observation possibly accounting for the recirculation zone size differences.

ZDES and DDES are clearly more accurate for predicting skin friction (Fig. 14(*b*)). RANS performs well until the pressure recovery region where it departs from the experimental profile. Upstream of the separation point, near $x/c=0.2$, the RANS, ZDES, and DDES models overpredict skin friction. Biswas [10] was able to accurately predict the skin friction in this location using LES, so the observed overprediction may be attributed to RANS model error.

Plots of the total turbulent stress $\overline{uu}$ (resolved plus subfilter components) are shown in Fig. 15 for the DES methods and the experiment. The imprint of modeled-stress depletion is clear at $x/c=0.8$ where the modeled stress is close to zero and also has an impact at $x/c=0.9$. By $x/c=1.1$, resolved turbulence generates sufficient stress that the DDES and ZDES results begin to compare favorably with the experimental data. ZDES performs only slightly better than DDES. The upward shift in the DES profile is due to the different structures of the recirculation zone; however, the amplitude is reasonable.

6 Concluding Remarks

The boundary-layer shielding DDES and ZDES models were assessed for modeling separated flow from a flow-control hump in a turbulent boundary layer. RANS solutions and solutions using the original DES formulation provide a basis for judging model improvement. The ZDES and DDES models were shown to minimize the effects of modeled-stress depletion and grid-induced separation. Their separation point was controlled by the underlying RANS model, which performed reasonably well. Modeled-stress depletion, however, was not fully resolved as an issue for flow modeling. The major discrepancies between experimental and numerical results were shown to be the effects of modeled-stress depletion after separation and not the turbulence model performance differences within the separated zone. Turbulent stress profiles show that reasonable amplitudes are predicted by the DES variants, once sufficient resolved stresses are generated.

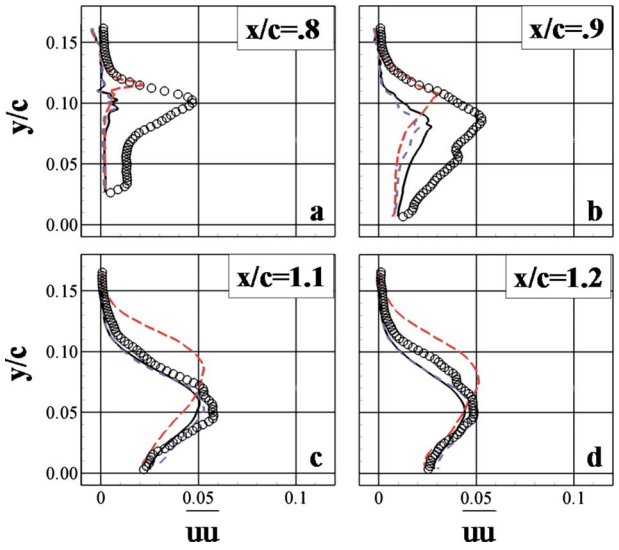

Fig. 15 Plots of turbulent stress $\overline{uu}$ for DES (long dash), ZDES (dash), DDES (solid), and experiment (open circles) at x/c =0.8, 0.9, 1.1, and 1.2

The results of this study confirm that boundary-layer shielding approaches are important for accurate prediction of separated flows using DES-based methods and that it is primarily this capability that renders the DES variants, ZDES, and DDES, as marked improvements over the original DES formulation. The results also show that modeled-stress depletion away from attached boundary layers remains a modeling issue in all DES variants for which a correction has yet to be identified.

A consideration for future research is how to avoid modeled-stress depletion in detached shear layers. One can either develop a metric to shield the flow away from boundaries from transition to LES in attached shear layers or enhance the model to allow resolved turbulence scales to form earlier. Since the current work has shown an absence of resolved turbulence scales near separation in all DES methods, development of techniques for rapidly initiating correlated turbulent motions remains a primary direction for future research.

Acknowledgment

The first author is grateful for the graduate support he received through the Exploratory and Foundational Program (E&F) of the Applied Research Laboratory at Penn State under which this research was conducted. The authors thank ACUSIM Software, Inc. for supporting this work through licensing and technical assistance. They also acknowledge the Aeronautical Systems Center and Army Research Laboratory Major Shared Resource Centers where some of the computations were performed. They are grateful to Dr. Mario Trujillo and Dr. Michael Krane for helpful discussions.

Nomenclature

c = hump chord length
Re = Reynolds number
μ = dynamic viscosity
p_∞, p, = reference and fluctuating pressures
P, $\tilde{p}$, = mean and full pressures
$\tilde{p}^r$ = resolved full pressure

ρ = density
U_r, $\tilde{u}_i$, u_i = freestream, full, and fluctuating velocities
U_i, u_i^s, u_i^r = mean, fluctuating subgrid, and fluctuating resolved velocities
u, v, w = velocity vector components
x_i = Cartesian coordinate vector
x, y, z = Cartesian coordinate vector components
u, ν, ν_w = velocity vector components
ν, $\tilde{\nu}$, ν_T = kinematic viscosity, RANS transport term, eddy viscosity
t = time
$\tilde{\tau}_{ij}$, $\tilde{\tau}_{ij}^D$ = stress tensor, deviatoric stress tensor
$\tilde{S}_{ij}^r$, S_{ij}^r = resolved strain rate tensor, resolved strain rate magnitude
c_{b1}, c_{w1}, f_w, σ, c_{b2}, c_{v1}, c_{w2}, f_{v1}, f_{v2}, f_w = Spalart–Allmaras constants
χ, g, r = Spalart–Allmaras functions
Ω_{ij}, Ω = vorticity and vorticity magnitude
d, $\tilde{d}$ = distance to the wall, DES length
κ = von Karman's constant
C_{DES} = DES constant
k = turbulent kinetic energy
ψ = ZDES black/white discriminator function
a_1, C_μ = ZDES constants
r_d, f_d, k_0 = DDES model functions
$\overline{u_i u_i}$, $\overline{u_i^r u_i^r}$ = TKE, resolved TKE
$\overline{u_i^s u_i^s}$ = subfilter TKE
τ_{wall} = wall shear stress

References

[1] Spalart, P., Jou, W.-H., and Allmaras, S., 1997, "Comments on the Feasibility of LES for Wings, and on a Hybrid RANS/LES Approach," *Advances in DNS/LES: First AFOSR International Conference on DNS/LES*, C. Liu and Z. Liu, eds., Greyden.

[2] Strelets, M., 2001, "Detached Eddy Simulation of Massively Separated Flows," 39th AIAA Aerospace Sciences Meeting and Exhibit, Reno, NV, AIAA Paper No. 2001-0879.

[3] Paterson, E. G., and Peltier, L. J., 2005, "Detached-Eddy Simulation of High-Reynolds-Number Beveled-Trailing-Edge Boundary Layers and Wakes," ASME J. Fluids Eng., **127**, pp. 897–906.

[4] Spalart, P. R., Deck, S., Shur, M. L., Squires, K. D., Strelets, M. Kh., and Travin, A., 2006, "A New Version of Detached-Eddy Simulation, Resistant to Ambiguous Grid Densities," Theor. Comput. Fluid Dyn., **20**, pp. 181–195.

[5] Menter, F. R., Kuntz, M., and Bender, R., 2003, "A Scale-Adaptive Simulation Model for Turbulent Flow Predictions," AIAA Paper No. 2003-0767.

[6] Slimon, S., 2003, "Computation Of Internal Separated Flows Using a Zonal Detached Eddy Simulation Approach, *Proceedings of the 2003 ASME International Mechanical Engineering Congress*.

[7] Seifert, L. G. P., 2002, "Active Flow Separation Control on Wall Mounted Hump at High Reynolds Number," AIAA J., **40**(7), pp. 1363–1372.

[8] Rumsey, C. L., Gatski, T. B., Sellers, W. L., Vatsa, V. N., and Viken, S. A., 2004, "Summary of the 2004 CFD Validation Workshop on Synthetic Jets and Turbulent Separation Control," AIAA Paper No. 2004-2217.

[9] Krishnan, V., Squires, K. D., and Forsythe, J. R., 2004. "Prediction of Separated Flow Characteristic Over a Hump Using RANS and DES," Second AIAA Flow Control Conference, Portland, OR.

[10] Biswas, D., 2006, "Studies on Separation Control CFD Validation Test Case Based on a Higher Order LES Model," Third AIAA Flow Control Conference, San Francisco, CA.

[11] Greenblatt, D., Paschal, K. B., Yao, C., Harris, J., Schaeffler, N. W., and Washburn, A. E., 2004. "A Separation Control CFD Validation Test Case Part 1: Baseline & Steady Suction," Second AIAA Flow Control Conference, Portland, OR.

[12] Naughton, J. W., Viken, S., and Greenblatt, D., 2004. "Wall Shear Stress Measurements on the NASA Hump Model for CFD Validation," 24th AIAA Aerodynamic Measurement Technology and Ground Testing Conference, Portland OR.

[13] Tennekes, H., and Lumley, J. L., 1972, *A First Course in Turbulence*, MIT, Cambridge, MA.

[14] Spalart, P. R., and Allmaras, S. R., 1994, "A One-Equation Turbulence Model for Aerodynamic Flows," Rech. Aerosp., **1**(5), pp. 5–21.

[15] Kim, J., and Moin, P., 1985, "An Application of Fractional Step Method to Incompressible Navier-Stokes Equations," J. Comput. Phys., **59**, pp. 308–323.

[16] Moser, R. D., Kim, J., and Mansour, N. N., 1999, "Direct Numerical Simulation of Turbulent Channel Flow Up to Re_τ=590 ," Phys. Fluids, **11**(4), pp. 943–945.

[17] Smagorinsky, J., 1963, "General Circulation Experiments With the Primitive Equations. Part I: The Basic Experiment," Mon. Weather Rev., **91**, pp. 99–164.

Creation and Maintenance of Cavities Under Horizontal Surfaces in Steady and Gust Flows

R. E. A. Arndt
W. T. Hambleton
E. Kawakami

Saint Anthony Falls Laboratory,
University of Minnesota,
Minneapolis, MN 55414

E. L. Amromin
Mechmath LLC,
Prior Lake, MN 55372-1283

An experimental study of air supply to bottom cavities stabilized within a recess under a horizontal surface has been carried out in a specially designed water tunnel. The air supply necessary for creating and maintaining an air cavity in steady and gust flows has been determined over a wide range of speed. Flux-free ventilated cavitation at low flow speeds has been observed. Stable multiwave cavity forms at subcritical values of Froude number were also observed. It was found that the cross-sectional area of the air supply ducting has a substantial effect on the air demand. Air supply scaling laws were deduced and verified with the experimental data obtained. [DOI: 10.1115/1.4000241]

1 Introduction

One of the successful technologies for friction reduction is ventilated cavitation. This technology has been already applied to ships of around 100 tons displacement, as described by Ivanov and Kalyzhny [1]. Nevertheless, there are two major unsolved scientific problems in this technology: Determination of the necessary gas supply to a ventilated cavity and locking this gas in place under various sea conditions. The methods to solve the second problem are basically understood and were recently described [2].

However, descriptions of the first problem are either absent in the literature on drag reduction by ventilated cavitation or are insufficient (as in Ref. [3]). As a result, the known successful examples of drag reduction by ventilated cavitation currently do not provide the necessary information on gas supply transferable to the other body (ship) forms and sizes. The aim of this work is to clarify the physical background of air supply to ventilated cavities with the use of relatively simple models. Nevertheless, it is also appropriate to recall the main points of the first problem. Cavitation can reduce drag because a surface under the cavity is practically free of friction. However, reduction in one drag component is usually associated with some increase in other components. For cavitating flows around bodies there is usually a drag penalty caused by cavity tail pulsation. In the case of partial cavitation, cavity pulsations can be minimized (as well as the associated drag penalty) over some range of cavity length. The example of a hydrofoil designed for friction reduction by partial cavitation with use of ideal fluid cavitation nonlinear theory was described and validated by Amromin et al. [2] and Kopriva et al. [4] This design study provides a basis for the current research. Figure 1 illustrates the drag reduction that is possible. Since one of the aims of the cited research is to provide smooth reattachment at the trailing edge of a cavity, ship bottom design for drag reduction by ventilated cavitation is a similar problem. The numerical technique used for its solution has been earlier described [5].

Omitting the mathematical details here, we would like to point out the dependence on Froude number in the solution as shown in Fig. 2. The cavitation number corresponding to the cavities shown in Fig. 2 varies from -0.2 to 0.14. Thus, for smaller values of Fr, the gas pressure necessary to maintain the cavity may exceed the unperturbed pressure in the water. Therefore, for drag reduction by cavitation within the speed range used by ships, ventilation is unavoidable. The determination of the necessary air supply is a very important aspect of ventilation design. Model tests are ordinarily employed for this determination, but there is the necessity to extrapolate the air flux Q_e for a body of length L_e moving at a speed U_e on the basis of the model test data $\{Q_m, L_m, U_m\}$ that usually correspond to the same Froude number, Fr.

Both underestimation and overestimation can reduce the expected effect, but overestimation is also associated with unnecessary demand for additional power and room for the ventilation system. This circumstance predetermines the significance of the presented study of air supply to the cavities on horizontal surfaces as the ship bottom.

2 Creation and Maintenance of Cavities in Steady Flows

The prediction of air supply for ventilated cavitation remains as a difficult problem. There is neither well-proven theory nor sufficient experimental data for verification of theory. The bulk of the available experimental data relates to ventilated supercavitation, but even these data are not sufficiently comprehensive. Possibly, the most representative set of such data was presented by Epshtein et al. [6] for disks (these data are still broadly referenced, e.g., Kuklinski et al. [7]). These data display a very sharp increase in air demand with a decrease in σ and a very significant effect of Froude number Fr. Similar trends are shown in the data collected by Wosnik et al. [8]. Unfortunately the data in Ref. [6] correspond to the same speed, $U_\infty = 30$ m/s and a greater Froude number corresponds to a smaller disk radius, d. Therefore, it is reasonable to expect a blockage effect in the enormous increase in the air supply Q in the vicinity of some critical cavitation number, $\sigma_{\min}(\mathrm{Fr})$. This issue is discussed in Ref. [8]. Inherent in the presentation of the data in normalized form is a baseless assumption on the proportionality of Q to U_∞. This is not quite correct. In fact, the air demand follows a nonlinear relation with speed terminating with zero air demand at the speed corresponding to vaporous cavitation for constant σ. Therefore, one can assume that

$$\frac{Q}{US^*} = K\left(1 - \frac{\sigma}{\sigma_V}\right) \tag{1}$$

where S^* is the area of cavity cross section, σ_V is the vapor cavitation number, and K is constant. An example of the dependency resulting from this assumption is shown in Fig. 3. It is clear that Q

Contributed by the Fluids Engineering Division of ASME for publication in the JOURNAL OF FLUIDS ENGINEERING. Manuscript received March 18, 2008; final manuscript received September 2, 2009; published online October 13, 2009. Assoc. Editor: Joseph Katz.

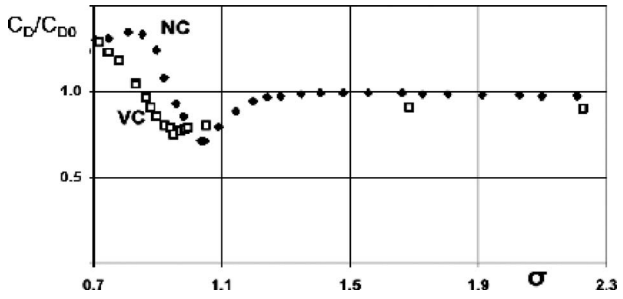

Fig. 1 Normalized drag coefficient C_D of the OK-2003 hydrofoil at 6-deg angle of attack with natural cavitation (NC) and ventilated cavitation (VC). C_{D0} is drag coefficient for cavitation-free conditions

is approximately proportional to U only at the relatively small speeds inherent in the majority of laboratory experiments.

For the reasons cited above, air demand has not been successfully calculated until recently. Some encouraging numerical results have been reported by Kinzel et al. [9]. They showed good agreement with the data of Wosnik et al. [8]. However, the Q values in the study vary strongly, depending on the selected turbulence model (and consequently, on some set of empirical parameters). In addition, the mechanism of air flux from the cavity was not explained and scale effects were not discussed, hence the understanding of air demand is still far from complete. In the case of ships with bottom cavities, the accessible information is very poor and important details are missing (e.g., [10,3]). Therefore, there is a necessity for a very basic experimental study. An experimental study of air supply to bottom cavities has been carried out in the water tunnel of the Saint Anthony Falls Laboratory (SAFL) at the University of Minnesota with a simplified model of

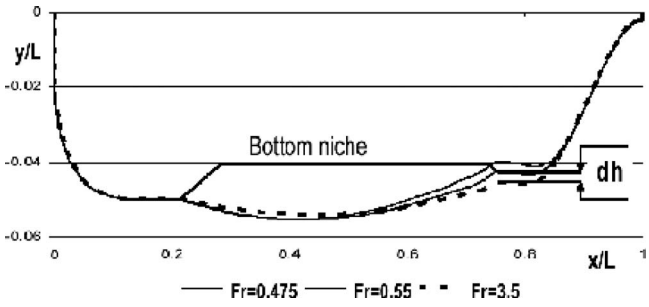

Fig. 2 Buttocks with a bottom recess, computed cavities of length L_C=0.55L and stern seals of computed shape at various Fr. All buttocks coincide upstream of the stern seals (x≈0.75). One can see that an increase in Fr leads to the increase in cavity tail thickness by dh. For ventilated cavitation, this increase in tail thickness will result in a drag penalty and an additional air demand.

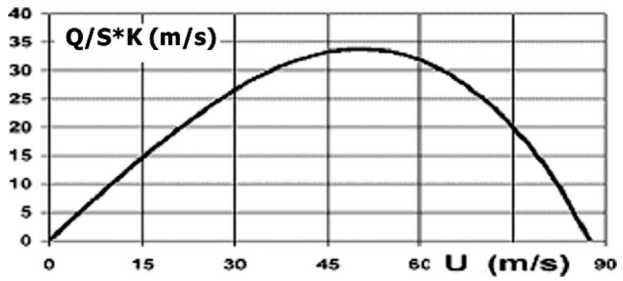

Fig. 3 Normalized air supply versus flow speed for σ=0.05 and ambient pressure of 2 atms

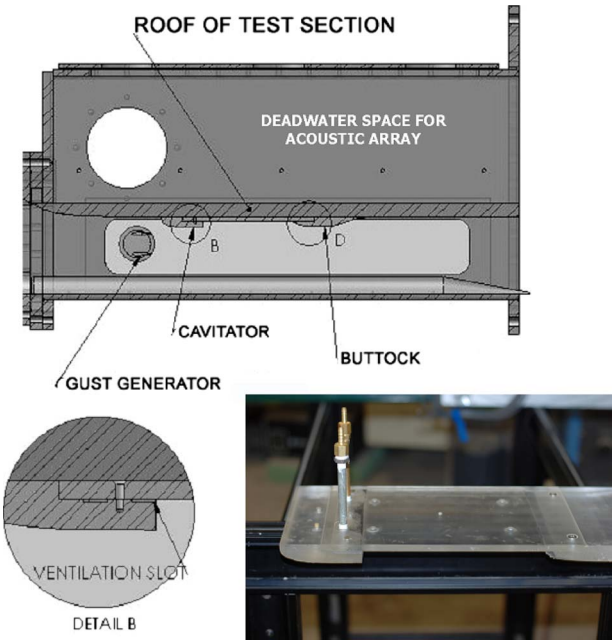

Fig. 4 Experiment setup in SAFL water tunnel. The bottom of the ship is modeled with a variable bow B and stern D that replace the water tunnel ceiling. For steady flows, the flaps are immobile.

the bottom of a ship with a 0.5 m length. This tunnel has been specially designed to handle large quantities of injected air. A description is found in Ref. [8].

The experimental setup scheme is shown in Fig. 4. As shown in the figure, a model recess is created by positioning a bow insert, B, and a stern insert, D at a given separation distance. In all there were two different bow inserts, and two stern inserts. Air is fed through a horizontal slot that spans the aft end of the bow insert (see detail B). This slot is fed by two vertical pipes that enter from the roof of the tunnel (Fig. 4(*c*)). Two different inlet diameter pipes and slot sizes were tried. Air flow was monitored with either a King rotameter with a range of 8–42 SCFM; ±2% accuracy; and 1/2% repeatability or a Gilmont rotameter with a resolution ±2.0 SLPM, depending on the flow rate to be measured. The inlet flow velocity is measured by the pressure difference across the water tunnel nozzle. The relationship between U and Δp was established with LDV measurements.

Experiments on the air demand of two bottom cavities with different shapes of the stern seal (cavity locker) are used for scaling verification here. One of two ship bottom models used in these experiments is shown in Fig. 5.

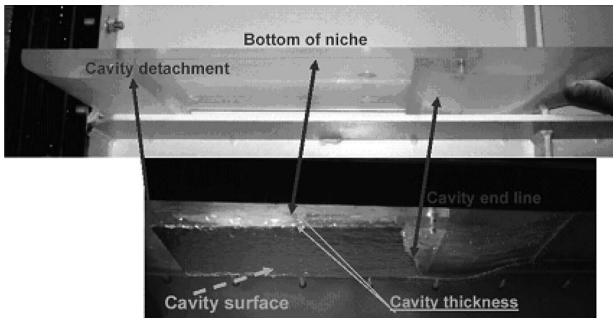

Fig. 5 Views of the model: dry (above) and wetted with a cavity in the water tunnel (bottom). The air supply is discharged at the backward step of where cavity detachment occurs

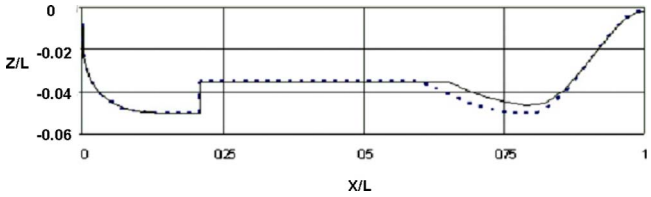

Fig. 6 Buttock comparison for the old (first) model (solid curve) and new (second) model (dashed curve). All coordinates are normalized by the body length *L*. The cutout length is 0.5*L* as shown. Note the expanded vertical scale.

The buttocks of the two models are compared in Fig. 6. One model will be named here as the old model or first model, and another as the new model or second model. Besides the air supply rate Q, the measured parameters include water tunnel speed U (varied between 0.45 m/s and 7 m/s), cavity pressure P_C, and water tunnel pressure P_∞. The accuracy of cavity pressure measurement and velocity is around 2%. For small values of U the difference $1-P_C/P_\infty$ was close to this accuracy. The calculated σ values were not accurate enough and these values are not provided here. Therefore, the obtained dependencies will be presented below mainly in dimensional physical units.

As was already noted by Ivanov [11], there is a substantial difference between the air supply rate, Q_C, necessary to create a ventilated cavity and the air supply rate, Q_M, necessary to maintain the same cavity. Therefore the phenomena of creation and maintaining a cavity should be distinguished. The determination of the air supply necessary to create a cavity is based on cavity observations assisted by video recording and photos. A general introductory explanation of the photographic observations is provided in Fig. 7. It is evident that Q_C can be defined as the sum of steady state demand and a cavity filling term, $Q_C=Q_1+Q_2+Q_3$, where Q_1 is the air flux to the cavity boundary layer through the cavity-water interface; Q_2 is the air flux through the pulsating cavity tail; and $Q_3 \approx V/dt$. It is important to point out that Q_1 and

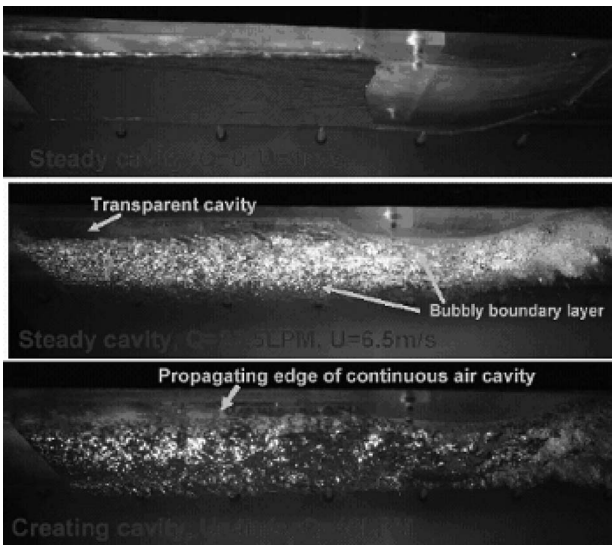

Fig. 7 View of several cavities under the first model. These and the following photos of the air cavities have been obtained through the glass wall. Flow is from left to right. The top photo shows a steady cavity at *U*=1 m/s and *Q*=0 (no air supply for cavity maintenance is necessary in this case, though its generation required some initial air supply). The middle photo shows a steady cavity at *U*=6.5 m/s and *Q*=27.5 l/min. The bottom photos shows an expanding cavity at *U*=4 m/s and *Q*=40 LPM.

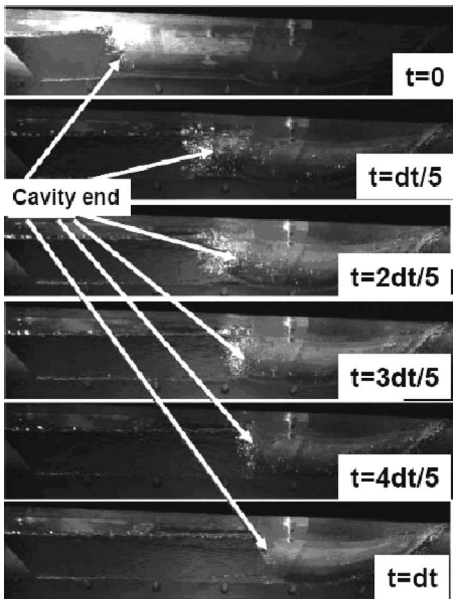

Fig. 8 Cavity creation under the first model at the water tunnel speed *U*=1.1 m/s. Air supply rate Q_C=0.5 l/min; *dt* is the cavity creation time, photos were made with the time step *dt*/5. Flow is from left to right.

Q_2 are considered as separate components of the cavity ventilation mechanism, since the relative importance of flux across the cavity surface and flux through the reattachment region will vary depending on the operating conditions. The observations have determined two different regimes of cavity creation. The *low-speed* creation regime (where Q_1 is negligible) at $U<U_{\mathrm{CRIT}}$ is illustrated by Fig. 8.

One can see the absence of bubbles (suggesting a lack of air flux across the cavity side surface) while the cavity tail is quite bubbly. The *high-speed* creation regime (at $U>U_{\mathrm{CRIT}}=1.13$ m/s for this experiment) is illustrated by Fig. 9. The transparent air cavity is surrounded by a thick bubbly layer. Unfortunately, one cannot necessarily infer Q_3 by subtracting the air supply necessary for maintaining the cavity as measured in the steady state, since Q_1 and Q_2 may also be different in the creating regime because cavity creation is a substantially unsteady phenomenon. These observations indicate that there are two different regimes for maintenance of the cavity.

The low-speed maintenance regime (at $U<U_{\mathrm{CRIT}}$) can be achieved with $Q_M=0$. Ivanov [11] already mentioned that under

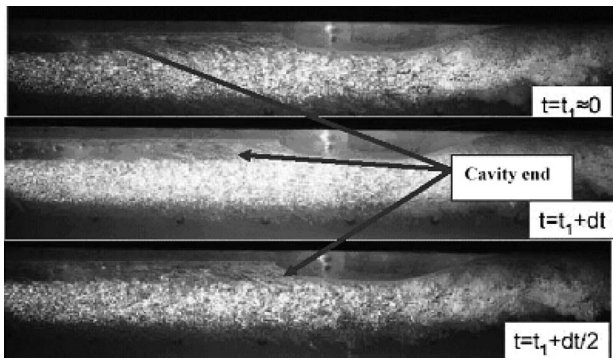

Fig. 9 Cavity creation under the first model at the water tunnel speed *U*=7 m/s with the air supply rate Q_C=57.5 l/min; *dt* is the cavity creation time and t_1 is considered as the moment of creation start. Flow is from left to right.

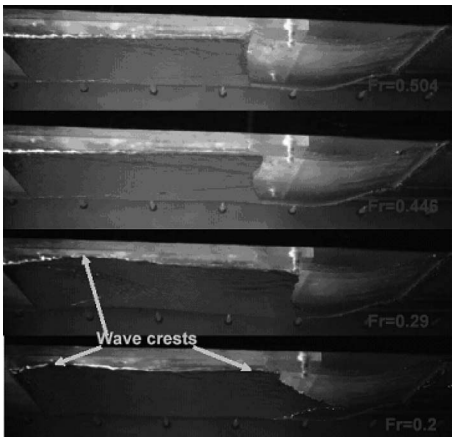

Fig. 10 Cavity steady shapes under the first model at low water tunnel speeds. Froude number is defined as $Fr=U/(gL)^{1/2}$, where L is the model length. The top photo relates to Fr =0.504, the second to Fr=0.446, the third to Fr=0.29, and the fourth to Fr=0.2.

some perturbation-free conditions, a cavity under a horizontal plane can be maintained with $Q_M=0$; however, neither description of these conditions nor photos of such cavities were provided by him. Here Fig. 10 illustrates this regime for the first model, where one can see the absence of bubbles (no evidence of air flux) over the cavity interface. This is a very favorable circumstance for observation of cavity shape in more detail.

Perfectly smooth cavity surfaces allow observation of waves over the cavities. Since all the cavity lengths, L_C, in Fig. 10 are practically equal to the recess length $L_N=L/2$ for this particular design, one can derive a relationship between cavity length and the wavelength, $\lambda=2\pi U^2/g$, of low-magnitude surface waves. The result is $\lambda/L_N=4\pi Fr^2$. Starting from the cavity at Fr=0.504, we first illustrate a cavity shorter than a half wavelength ($\lambda/L_N=3.19$). Further, one can easily identify the wave crest over the cavities at Fr=0.29 ($\lambda\approx L_N$ for this Fr) and two crests at Fr=0.2 (L_N is about 2λ for this Fr). For the second model, there is also a low-speed flux-free regime of cavity stability, as one can see in the top photo of Fig. 11.

On the other hand, there is no steady cavity of a length equal to the recess length within some intermediate range of Fr between Fr=0.29 and Fr=0.5. As is illustrated by Fig. 12 with the cavity view at Fr=0.41, cavities maintained in this range of Fr cannot cover the entire recess. Thus, there is a maximum Froude number Fr^{**} for stable cavities modulated by surface waves and a minimum (critical) Froude number Fr^* for the cavity with $L_C<\lambda/2$ (as

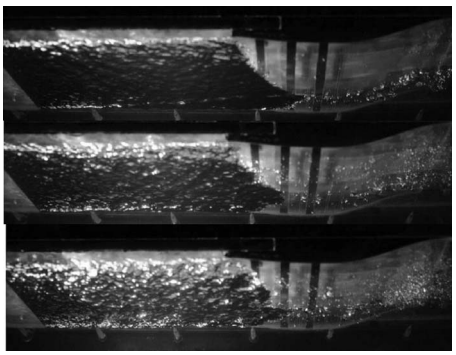

Fig. 11 Comparison of cavity surfaces under the new model in steady flow of 1 m/s speed (at subcritical speed, in the top), 1.5 m/s (in the middle), and 2 m/s (in the bottom). Bubble density on the cavity sharply increases with the speed.

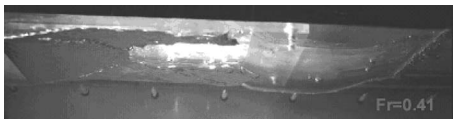

Fig. 12 Cavity shapes under the first model at an intermediate Fr=0.41. Flow is from left to right.

is clear, $Fr^{**}<Fr^*$). The existence of threshold values Fr^* and Fr^{**} was predicted by Butuzov [12] with the employment of the linear theory of cavitation in an ideal fluid. His prediction of Fr^* for cavities behind a thin wedge under a horizontal wall was in good agreement with the experimental data. However, as noted by Ivanov [11], Butuzov did not obtain a good experimental validation for his prediction of Fr^{**}.

It is also important to note that U_{CRIT} is a Fr-independent flow characteristic that depends on Re. However, the perfectly smooth cavity surfaces at speeds smaller than U_{CRIT} make it easier to observe the cavity surfaces modulated by waves at $Fr<Fr^{**}$.

The high-speed maintenance regime also allows steady cavity surfaces, but surrounded by bubbly clouds. The bubble entrainment by the water flow may be influenced by

1. Surface tension that would be insignificant at $U>U_{CRIT}$.
2. Perturbations induced by the turbulent boundary layer on the cavity surface.
3. Insufficiently smooth flow reattachment behind the cavity due to a difference of the actual Froude number and design Froude number for the cavity locker.

Water tunnel experimental data for air flux (demand) for both models in steady incoming flow are displayed in Fig. 13. Two kinds of dependency are observed. One describes the flux Q_C necessary for cavity creation. Another describes the flux Q_M necessary for stabilization of a cavity. There are also two scaling laws deduced for the air demand (flux) of cavity creation and cavity maintenance. Because these laws give a very satisfactory approximation of the measured data, a scaling relation is deduced below. Two main mechanisms of air flux have been considered here.

The first mechanism is air bubble entrainment through the boundary layer at the water cavity interface. One can suppose a proportionality of this air entrainment to the stress in the boundary layer. However, as was previously reported, this entrainment ap-

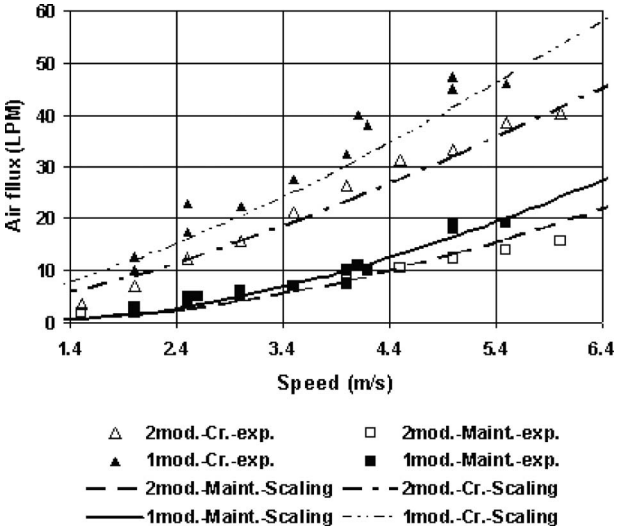

Fig. 13 Measured air flux/demand for creating and maintaining bottom cavities in steady flow together with its scaling dependencies deduced below

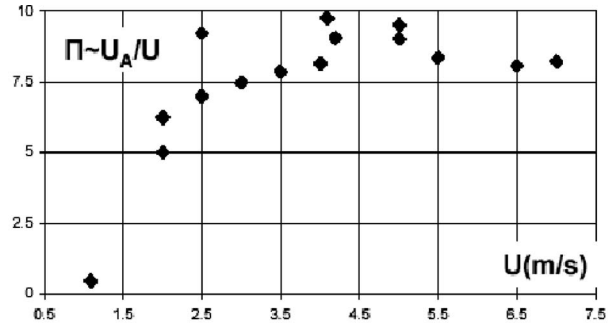

(A)

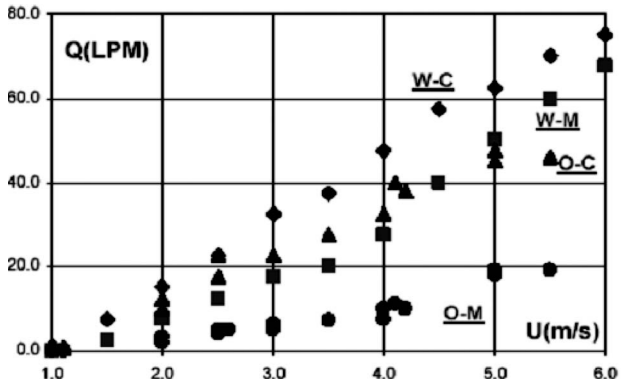

(B)

Fig. 14 (*a*) Normalized ratio of air initial velocity U_A to the water velocity U and (*b*) effect of this velocity on air demand. Data O-C and O-M relate to the old model and coincide, with given in Fig. 13; data W-C and W-M describe cavity creation and maintenance for the old model with widened holes for air supply.

pears only after exceeding a critical incoming flow speed U_{cr}. Therefore, the following scaling law can be deduced for Q_M on the basis of this hypothesis of entrainment:

$$Q_{eM} = Q_{mM}\left[\frac{U_e^{6/7}B_eL_e^{6/7}(U_e - U_{cr})}{U_m^{6/7}B_mL_m^{6/7}(U_m - U_{cr})}\right] \quad (2)$$

Here the proportionality of dimensionless stress to 1/7 power of Reynolds number is used, B is the hull beam; the subscripts m and e relate to all measured characteristics and extrapolated characteristics, respectively.

The second mechanism is the flux through the cavity tail. This mechanism is not inherent to steady cavities at the design condi-

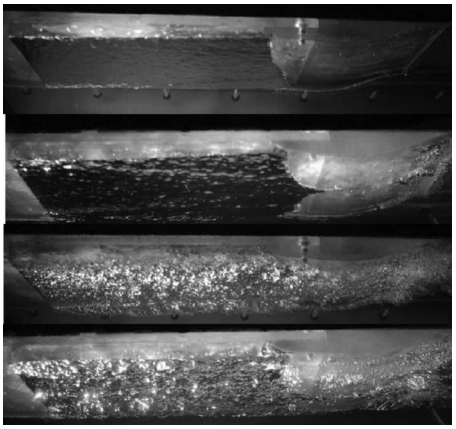

Fig. 15 Comparison of cavity shapes for the old model with initial (two upper photos) and widened ducting of the air supply (two lower photos) at U=1 m/s (first and third photos from the top) and U=4 m/s (second and fourth photos from the top)

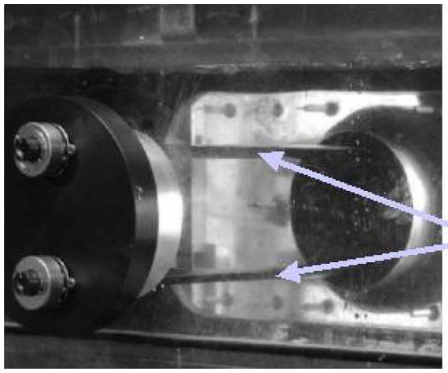

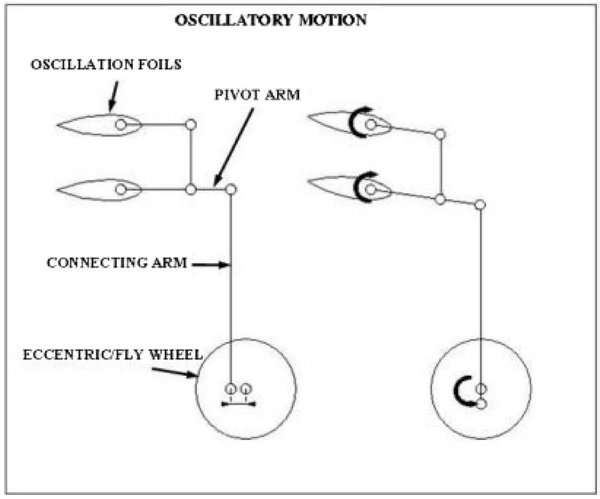

Fig. 16 View of the gust simulator installed in the tunnel (top) Flow is from left to right. A schematic of the setup is also shown (bottom).

tions, but it acts during the establishment of a cavity with ventilation and cavity maintenance at off-design conditions. According to our assumption, the air mass flux through the tail can be defined as $Q^m \sim \rho_a S^* U_a$, where ρ_a is the air density, and U_a is the gas jet velocity at the tail (supposedly proportional to U). For the air cavity, the air flux out of cavity should be proportional to P_C-P_V, where P_V is the vapor pressure and P_C is the total gas pressure in the cavity. Because the air density $\rho_a \sim (P_C\text{-}P_V)/kT$, where T is the gas temperature, one can write $Q^m = Q^{**} U S^* (P_C\text{-}P_V)/kT$. Supposing that Q^{**} is a constant coefficient, one can then obtain the following equality for two similar cavitating bodies with the similar cavity shapes:

$$T_1 Q_1^m / [U_1 S_1^* (P_{C1}\text{-}P_V)] = T_2 Q_2^m / [U_2 S_2^* (P_{C2}\text{-}P_V)] \tag{3}$$

The body sizes, freestream speeds, and air pressure can be different. According to Eq. (3) and taking into account that, according to definition of cavitation number, $\sigma\rho_{\text{water}}/2 = (P_\infty\text{-}P_{C1})/U_1^2 = (P_\infty\text{-}P_{C2})/U_2^2$, one can write

$$Q^{**} = \frac{Q_1^m T_1}{U_1 S_1^* (P_{C1} - P_{V1})} = A^* \frac{Q_2^m T_2}{U_2^3 L_2^2 (\sigma_{V2} - \sigma)} \tag{4}$$

Here A^*=const. The consequence of the above equation is

$$Q_1^m = Q_2^m \left[\frac{U_1^3 S_1^* (\sigma_{v1} - \sigma) T_2}{U_2^3 S_2^* (\sigma_{v2} - \sigma) T_1} \right] \tag{5}$$

The scaling law (5) should be applied to the difference between Q_C and Q_M. The scaling of creation air demand includes two components describing both mechanisms. For the described experiments with the constant cavity surface area, air density, and temperature, the scaling law for the measured volumetric flux is

$$Q_{eC} = Q_{eM} + (Q_{mC} - Q_{mM}) \left[\frac{U_e^3 (\sigma_{Ve} - \sigma_e)}{U_m^3 (\sigma_{Vm} - \sigma_m)} \right] \tag{6}$$

Here σ and σ_V are values of cavitation number and vapor (natural) cavitation number, and T is the air temperature. For all scaling curves in Fig. 13, U_m=5.5 m/s, whereas the varying speed U_e covers the whole range of speeds. Note that Eq. (5) gives proportionality of Q to U^3 for L=const as Eq. (1) does.

It is also useful to compare the steady state air demand for this bottom cavity with the air demand for the ventilated hydrofoil OK-2003 in the same water tunnel. The hydrofoil steady state air demand was Q_{MH}=4.3 l/min at 8 m/s, but its cavity length was six times shorter than the length of the bottom cavity in this study. Assuming air entrainment as the main air flux mechanism at design conditions, one may compare air fluxes from different cavities at their design conditions with Eq. (5). The extrapolation of the bottom cavity Q_M to conditions of this hydrofoil test gives Q_{MH}=5.6 l/min, which compares favorably with the measured values in this experiment.

One can see in Fig. 13 that measured Q_M approximately coincides for the two models at $U<4$ m/s, but the air demand is significantly higher for the first model at higher speeds. This looks reasonable because the first model was designed for a Froude number that corresponds to $U<2$ m/s, whereas the second for significantly higher Fr($U\approx 6$ m/s) and, as one can see in Fig. 2, the gap for air escape between cavity seal and water surface increases with an increase in Fr. Therefore, the creation air demand is always greater for the first model with the thinner stern seal. It is important to recall that, according to measurements in another flow with drag reduction on a horizontal surface [6], increase in air supply over some threshold value does not result in any additional drag reduction, but it may increase the drag (due to thickening of the boundary layer; an excessive oversupply can provoke

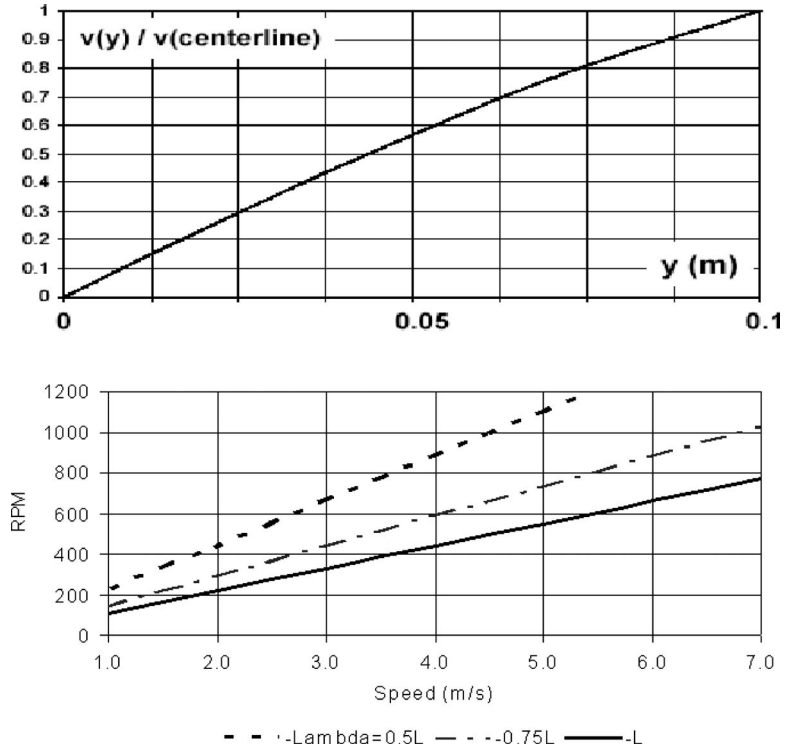

Fig. 17 Computationally estimated effect of distance from the wall Y on gust magnitude (top; the heights of the water tunnel test section ≈0.2 m) and dependency of RPM on flow speed at fixed wavelength (bottom). The model bottom is at 0.025 m from the wall.

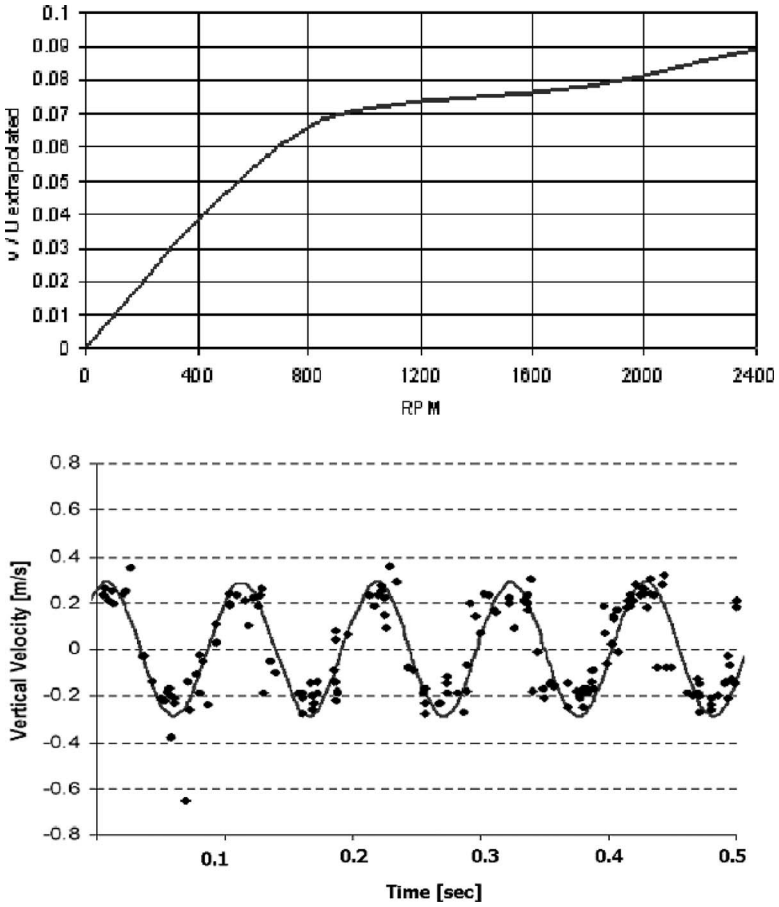

Fig. 18 Extrapolated dependency of the middle plane measured max{*v*}/*U* on flap frequency for a 6.35 cm distance from the wall (top) in comparison with measured *v* for *U*=4 m/s (bottom). This position relative to the model is 3.81 cm directly below the aft end of the bow where the cavity forms.

boundary layer separation). It was also manifested in Ref. [6] that ventilation significantly reduces drag only in the vicinity of design conditions; the difference with this study is in the main parameter predetermining the cavity shape: Here it is Fr, whereas it was σ in Ref. [6].

An additional parameter that can affect the air supply rate is its initial speed in the cavity, U_A. Because the air supply cross section is constant, U_A is proportional to Q. This ratio (or an auxiliary parameter $\Pi = Q/U$) for the old model is shown in Fig. 14(*a*). A simple way to vary U_A while holding U and other flow parameters constant is to enlarge the air supply ducting (shown in Fig. 5) This is accomplished by enlarging the supply pipes and the slot height resulting in a threefold increase in the outlet area. The effect on air demand is also shown in Fig. 14(*b*)

Comparing the photos of cavity surfaces in Fig. 15, one can certainly find more bubbles behind larger slot at the smaller speed and see their first appearance closer to cavity detachment at the greater speed. The cause for the increase in air demand is not understood at this point. One may consider the air supply as the discharge of a rectangular air jet into the low-velocity airflow within the cavity. Such a jet would have a constant expansion angle, as described by Schlichting [12], and this expansion behind a larger outlet would lead to its earlier interaction with the water surface, etc.

3 Creation and Maintenance of Cavities in Gust Flows

The water tunnel experiments with the cavitating ship bottom model in a gust flow employ a specially designed gust generator (shown in Fig. 16) developed for a previous study of a special hydrofoil [4]. That study included the meticulous measurement of velocity components in the plane of hydrofoil location. The gust angle of attack can be approximated as $\alpha_G = A_0 + A_1 \sin(\omega t)$, where A_0 and A_1 depend on rpm.

Initially this gust generator was developed to impose a gust flow on a hydrofoil mounted on the centerline of the test section, whereas the bottom ship model becomes a part of the water tunnel ceiling. There is no vertical velocity component at the roof and floor of the test section. Therefore, the variation in the vertical velocity component with distance from the walls had to be estimated using an analytical model of the velocity induced by a pair of vortex sheets. The "image" effect must be then accounted for by introducing two artificial supplementary vortex sheets behind the wall. The correction factor for dependencies measured in the middle plane is shown in Fig. 17 where $v/U = \alpha_G$.

The extrapolated maximum of velocity (in Fig. 18) appeared to be very close to the velocity maxima determined with the use of LDV (one can see that for the range of rpm from 800 to 1800, the extrapolated ratio $\max\{v\}/U$ is between 0.065 and 0.08, whereas for the LDV data, this ratio is 0.0725). It would be desirable to vary the gust flow magnitude and wavelength independently. However, the gust generator operated with the same flap oscillation magnitude of 10 deg during all the described experiments. An increase in the flap oscillation magnitude for larger waves was impossible because of the stall limit of the flaps. Therefore, considering these experimental data, one must keep in mind that the larger waves have smaller magnitudes here.

There are two main questions dealing with bottom cavities in wavy (gust) flows that can be answered experimentally:

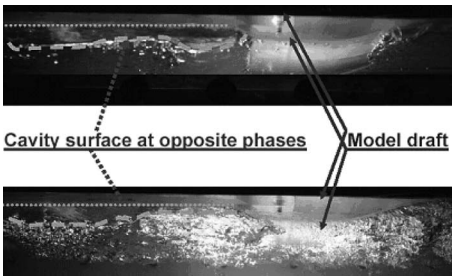

Fig. 19 Two opposite phases of cavity oscillation for Fr=2.3 and $\lambda=0.5L$ under the old model

- Will the wave break down the cavity into parts and significantly reduce the bottom dry area?
- What is the wave impact on air demand (and the possibility of its scaling)?

To answer the first question, it is necessary to check the sets of cavity photos and select two photos with opposite phases of cavity oscillation. An example of such selection for the pair $\{Fr=2.3, \lambda=L/2\}$ that is given in Fig. 19, where the cavity is so transparent that the recess upper surface is clearly seen.

The recess and stern contours in the vertical plane are clear, but the cavity surface looks rough and photo-based estimates of cavity surface ordinates will not have sufficient certainty. Although at higher incoming flow speeds the cavity surfaces are covered by bubbles, the cavity itself remains transparent. For the same wavelength, a speed increase leads to an increase in air (bubble) concentration in the cavity boundary layer, as it takes place in steady flow.

The illustration of the speed and wavelength effects on cavity evolution is given in Figs. 20 and 21. One can see in these photos that the waves do not destroy the cavity, but for the greater speed (Fr higher than the design value), the cavity oscillation opens a wider escape path for the air in the cavity tail. Further, as one can see in Fig. 20 for a greater wavelength, the cavity contour is less certain than it was for $\lambda \approx L_C$.

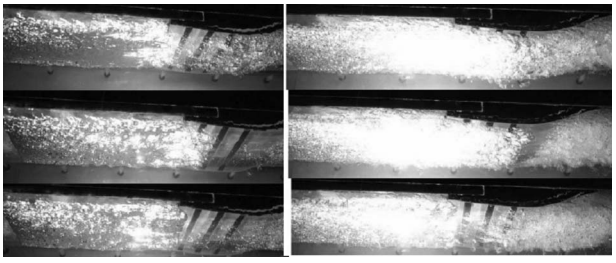

Fig. 20 Different phases of cavity oscillation under the new model for the wave of wavelength $\lambda=0.75L$ at the flow speed 3 m/s (left) and at 6 m/s (right)

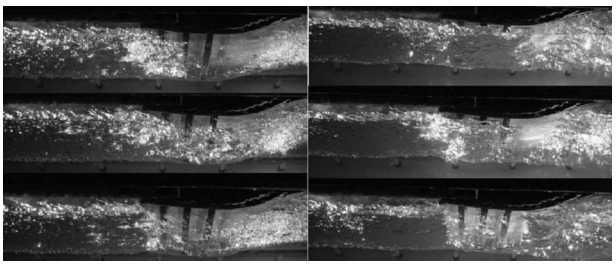

Fig. 21 Different phases of cavity oscillation under impact of the wave of wavelength $\lambda=L$ (left) and $\lambda=0.5L$ (right; this wavelength coincides with the cavity length) at the same flow speed 3 m/s.

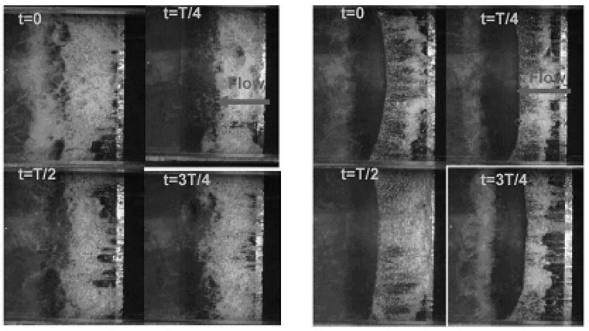

Fig. 22 Wavelength effect on shape of ventilated cavities on the hydrofoil OK-2003 at the same cavitation number and wave amplitude. *T* is the wave period. The flow is from right to left.

Incidentally, a similar "resonance" situation was observed for the OK-2003 hydrofoil [4] with drag reduction by ventilated cavitation in a gust flow (see Fig. 22 with very sharp cavity reattachment under shorter wave impact); one can also find in Ref. [4] that a greater drag corresponded to these sharper cavities.

Data for the effect of wave impact on air demand for bottom cavities are displayed in Figs. 23 and 24. The new model data for $\lambda=0.5L$ were very unstable at $U \geq 5$ m/s (with great dispersion) and, therefore, were not included. The old model air demand was either approximately the same as the new one is, or is slightly higher.

It looks reasonable to suppose that the unsteady air flux is proportional to the wave magnitude. After viewing the high-speed videos, dimensional analysis suggests the following scaling law:

$$Q^* = C^* B \omega A^2 \tag{7}$$

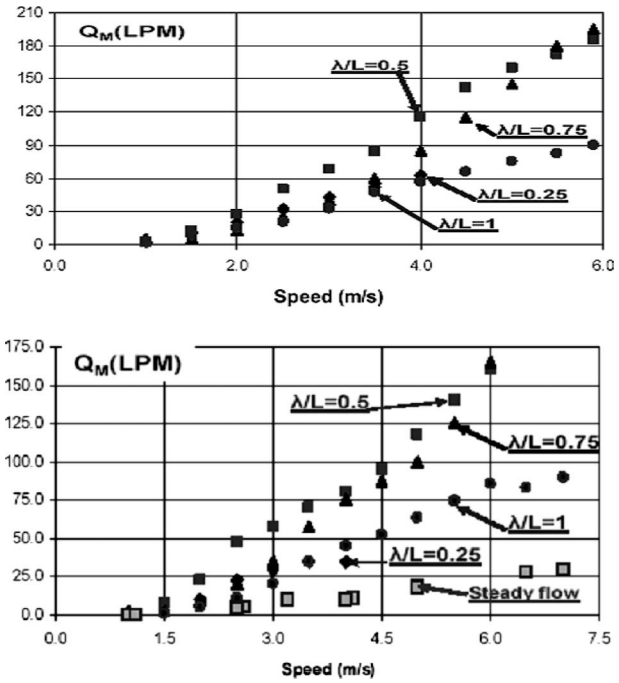

Fig. 23 Air demand for creation (top) and maintenance (bottom) of the cavity under the old model for various ratios of wavelength to the body length

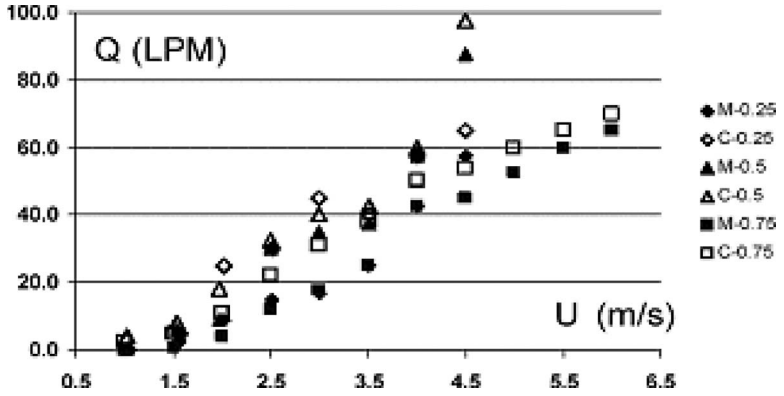

Fig. 24 Air demand for creation and maintenance of bottom cavities under wave impact for the new model versus speed at the different wavelengths. Data for cavity creation are marked by *C*, data for cavity maintenance are marked by *M*. Values of ratio of wavelength λ to the model length *L* are shown in the legend (*M*-0.25 means maintenance of cavity for wavelength λ=0.25*L*, etc.)

Here C^* is a dimensionless coefficient and B is the width of the cavity. The dimensionless ratio $Q^*/Q^*_{\max}$, for the experiments with the new model is plotted in Fig. 25 versus flow speed. As seen in Fig. 25, the function $Q^*(U)$ collapses the data reasonably well. This suggests that Eq. (7) is a reasonably accurate scaling law for the wave-induced increase in the air demand by bottom cavities. The hypothesis of proportionality of the wave-induced flux component Q^* to the wave frequency ω was experimentally verified by video observations. The use of video observations made it possible to count bubbles and their groups, estimate their volumes and compare the total air flux to its flux through the cavity tail at the certain phases of wave-cavity interaction. The video observations can be considered as preliminary since the error is in the data. Acquisition techniques is quite large, at least 30%. Video acquired with a High Speed Star 10,000 fps camera equipped with a 105 mm Nikon lens was analyzed frame by frame to determine the projected area of bubbles using IMAGE J software with a MATLAB edge detection scheme. It was then assumed that the spanwise direction was constant with respect to the bubble, which was an assumption that could have an upper bound of as high as 60% relative error. Only bubbles that appeared to have spanwise coherence were studied to minimize the error. The measured lengths were normalized with respect to a reference length. The relation between projected area and bubble volume was calculated using the assumption of spherical bubbles. The product of bubble volume and frequency of occurrence then determined the total volume flow rate as shown in Fig. 26.

One may suspect a mutual compensation of some errors in the data shown. First of all, the gas masses must be compared for flux estimation and variation in gas pressure with flow speed affects the gas density (the cavity pressure about coincides with atmosphere pressure at $U=2$ m/s becoming 5% smaller at $U=4$ m/s). Further, there is a minimal bubble size for any visualization and smaller bubbles will not counted in the estimated flux, and this could give an opposite error in the estimation. However, these errors are secondary and the presented comparison can be considered as a proof for the law expressed in Eq. (7).

4 Conclusions

A water tunnel experimental study of air supply to bottom cavities under two different models of a ship bottom has been carried out. Cavity creation, maintenance, and collapse have been observed and studied. The following conclusions were reached:

1. The air supply necessary for cavity creation and maintenance in steady and gust flows has been determined over a wide range of speeds.
2. Flux-free ventilated cavitation at the low flow speeds has been observed (below Re-dependent values U_{CRIT}).

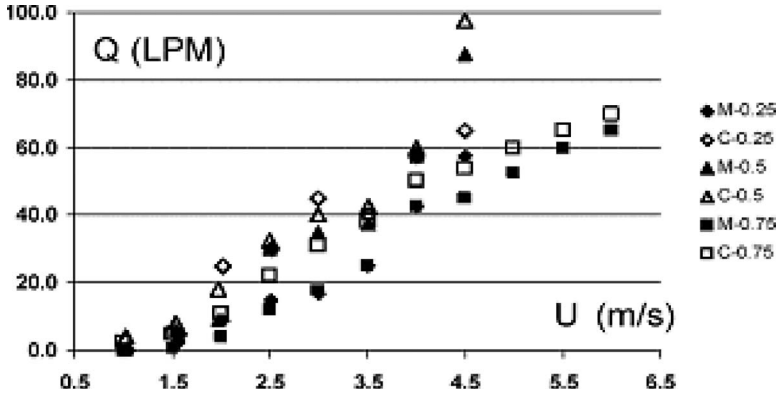

Fig. 25 Dimensionless ratio $Q^*/\max Q^*$ versus flow speed for different wavelengths. Rhombuses corresponds to λ=0.5*L*, squares to 0.75*L* and triangles to *L*.

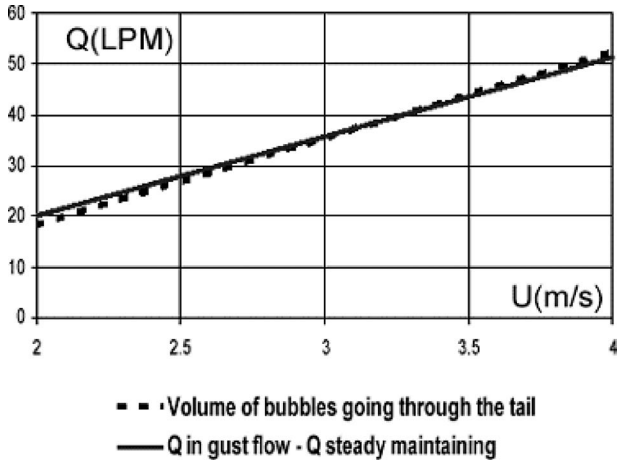

Fig. 26 Comparison of unsteady air flux with the total volume of cavity fragments moving through its tail and calculated with the use of video recording. Due to the large error in measuring the bubble volume flux, the excellent agreement shown can only be consider fortuitous until further study.

3. Stable multiwave cavity forms at subcritical values of Froude number $Fr=Fr^{**}$ were documented. For this particular model shapes, $Fr^{**}=0.29$.
4. A type of resonant interaction between waves and cavities was found.
5. A substantial effect of air speed/air nozzle diameter on the air demand by cavities was found.

The scaling laws for air supply to bottom cavities have been developed by qualitative analysis. These scaling laws were verified with data from water tunnel experiments for both steady and wavy (gust) flows. It was found that

6. The significant scaling parameters for steady flows include ship speed, cavity surface area, gas pressure, and its temperature within the cavity.
7. The significant scaling parameters for wave-induced additional air demand include the wave amplitude and frequency.

Acknowledgment

Authors are grateful to NAVSEA for the support of this study (program manager G. Karafiath). The assistance of Mr. Z. Nitzkorski, an undergraduate student, is also gratefully acknowledged.

Nomenclature

A = wave amplitude
B = cavity (recess) width
C_D = drag coefficient
C_{D0} = is drag coefficient for cavitation-free conditions
dQ = air supply drop
dt = cavity filling time
Fr = Froude number
Fr^* = critical Froude number
Fr^{**} = maximum Froude number
k = gas constant
L = body (model) length
L_C = cavity length
L_N = length of recess
P_C = cavity pressure
P_∞ = water tunnel pressure
Q = air demand
Q_C = air supply necessary for cavity creation
Q_M = air supply necessary for cavity maintenance
Q_1 = air flux to the cavity boundary layer through the cavity side surface
Q_2 = air flux through the pulsating cavity tail
Q^* = difference of Q_M in wavy and steady flows
S^* = the area of cavity cross section
U_A = speed of air exit from the nozzles
U_{CRIT} = maximum speed of zero-flux cavitation
U = freestream speed
V = cavity volume
v = vertical velocity component in the water tunnel
λ = wavelength
σ = cavitation number
σ_V = vapor cavitation number
ω = flap oscillation frequency

References

[1] Ivanov, A. N., and Kalyzhny, V. G., 1996, "The Perspectives of Applications of Ventilated Cavities on Naval Combat Ships," Int. Conf. on 300th Anniversary Russian Navy, St. Petersburg, **A2**, pp. 41–45.
[2] Amromin, E. L., Kopriva, J., Arndt, R. E. A., and Wosnik, M., 2006, "Hydrofoil Drag Reduction by Partial Cavitation," ASME J. Fluids Eng., **128**, pp. 931–936.
[3] Sverchkov, A. V., 2005, "Prospects of Artificial Cavities in Resistance Reduction for Planning Catamarans With Asymmetric Demihulls," International Conference on Fast Sea Transport FAST'2005, St. Petersburg, Russia.
[4] Kopriva, J., Arndt, R. E. A., and Amromin, E. L., 2008, "Improvement of Hydrofoil Performance by Partial Ventilated Cavitation in Steady Flow and Periodic Gusts," ASME J. Fluids Eng., **130**, p. 031301.
[5] Amromin, E. L., 2007, "Design of Bodies With Drag Reduction by Partial Cavitation as an Inverse Ill-Posed Problem for Velocity Potential," NMSH2007 Conference, Ann Arbor, MI, 3, p. 317.
[6] Epshtein, L. A., Blumin, V. I., and Starodoubzev, P. S., 1961, "Effects of Froude Number and Cavitation Number on the Sizes of Ventilated Cavity and the Air Flux," Trudy TAGI, **824**.
[7] Kuklinski, R., Henoch, C., and Castano, J., 2001 "Experimental Studies of Ventilated Cavities on Dynamic Test Model," CAV-2001 Symposium, Pasadena, CA.
[8] Wosnik, M., Schauer, T., and Arndt, R. E. A., 2003, "Experimental Study of a Ventilated Vehicle," Fifth International Symposium on Cavitation (CAV2003), Osaka, Japan, Nov. 1–4.
[9] Kinzel, M. P., Lindau, J. W., Peltier, J., Zajaczkowski, F., Arndt, R. E. A., Wosnik, M., and Mallison, T., 2007, "Computational Investigation of Air Entrainment, Hysteresis and Loading for Large-Scale, Buoyant Cavities," NMSH2007 Conference, Ann Arbor, MI, 3, p. 306.
[10] Ivanov, A. N., 1980, *Hydrodynamics of Developed Cavitation*, Sudostroenie, Leningrad.
[11] Butuzov, A. A., 1967, "Artificial Cavitation Past a Twin Wedge Under Horizontal Wall," Fluid Dyn., **2**, pp. 837–839.
[12] Schlichting, H., 1979, *Boundary Layer Theory*, McGraw-Hill, New York.

Cavitation Inception in the Wake of a Jet-Driven Body

Roger E. A. Arndt
University of Minnesota,
2 Third Avenue SE,
Minneapolis, MN 55414

Eduard L. Amromin
Mechmath LLC,
14530 Bluebird Trail,
Prior Lake, MN 55372-1283

William Hambleton
University of Minnesota,
2 Third Avenue SE,
Minneapolis, MN 55414

Although cavitation inception in jets has been studied extensively, little is known about the more complex problem of a jet flow interacting with an outer flow behind a moving body. This problem is studied experimentally by considering inception behind an axisymmetric body driven by a waterjet. Tests were carried out for various water tunnel velocities and jet speeds such that jet velocity ratio U_J/U could be varied in the range of 0–2. Distinctly different cavitation patterns were observed at zero jet velocity (when cavitation appeared in spiral vortices in such flows) and at various jet velocity ratios (when cavitation appeared around the jet in such flows). A simple superposition analysis, utilizing particle imaging velocimetry (PIV) measurements, is able to qualitatively predict the experimental result. On the basis of these observations, a numerical prediction of cavitation inception number based on viscous-inviscid interaction concept is suggested.
[DOI: 10.1115/1.4000388]

1 Introduction

Cavitation inception in jets has been studied extensively. However, previous studies mainly relate to jet discharge into immobile water. In practice, cavitation inception in the wakes of waterjet-driven ships and other bodies represents the more complex problem of a jet flow interacting with an outer flow of some complex characters.

This difference was recently clarified in an experimental study of jets discharged from coflowing nozzles by Straka et al. [1]. As observed, cavities appear between counter-rotating vortices in the mixing region of the jet and a uniform outer flow. Thus, cavitation inception in a coflowing jet is different in comparison with cavitation inception in a jet discharged into immobile water (meticulously described by Gopalan et al. [2]). Our analysis [3] of Straka's data on cavitation inception utilized a new definition of a governing velocity. As shown in Fig. 1, these data collapsed reasonably well by replacing the jet initial speed U_j by the average of the jet velocity and the velocity of the outer flow U_S in definitions of both Reynolds number Re^* and cavitation inception index σ^*.

As the next step from previous very basic studies on the analysis of real ship flows, it was decided to capture the physics of cavitation for a waterjet-driven body by utilizing a simple water tunnel model consisting of an axisymmetric body driven by a jet at the body transom, as described below. The study includes both water tunnel tests and numerical analysis for an axisymmetric Schiebe body with a blunt transom.

2 Experimental Methods

The experimental work was carried out in the Saint Anthony Falls Laboratory (SAFL) high-speed water tunnel. The test section is 190 mm $\times$ 190 mm with a length of 1250 mm and is capable of flow speed up to 30 m/s [4,5]. The experimental setup is shown in Fig. 2. The test body consists of a Schiebe nose designed for a minimum pressure coefficient of $C_{\mathrm{pm}}=-0.4$ followed by a cylindrical length of body terminated by a blunt transom. This axisymmetric body is strut mounted on a force balance. The strut has a NACA 0018 section. Interchangeable orifice plates can be mounted at the body transom. The orifice is fed by an external water supply ducted through the force balance and mounting strut. A view of the model in place in the water tunnel is shown in Fig. 3.

The 3 cm diameter Schiebe body was selected for experimental study of cavitation in jets because its shape allows cavitation-free flow upstream of the wake over the range of cavitation index envisioned in this study. The calculated pressure distribution is shown in Fig. 4. In addition, an analysis of transition utilizing the semi-empirical criterion (as described by Cebeci and Bradshaw [6]) indicates that the body boundary layer becomes turbulent upstream of the transom in the entire range of velocity used in these experiments.

The water tunnel freestream speed was varied from 5m/s to 10m/s and the jet velocity ratio U_J/U was varied from 0 to 2.0. The experimental data reported here were obtained for a 0.375 cm orifice. The nozzle diameter was 1/3 of the body diameter. Visual determination of the cavitation inception index was supplemented with PIV measurements of the flow extending approximately three diameters downstream from the body transom. In order to insure repeatable cavitation inception results, σ_i was defined by observations of desinence in strong water (as defined by Arndt and Keller [7]). The water was first degassed to a dissolved gas concentration of 4 ppm and then pressurized for 1 h. This procedure is discussed in Ref. [8] (refer to Ref. [5] for details on gas content measurement).

In order to understand the experimental results, it is useful to inspect a schematic of the flow, as shown in Fig. 5. Notice that wake development behind the body is slightly modified by the boundary layer on the body. The jet interacts and mixes with the wake within a short distance behind the transom. Further downstream the flow evolves into a fully developed wake.

Figure 6 illustrates wake development behind that body with the jet turned off ($U_j/U=0$) and with the jet turned on corresponding to $U_j/U=1.5$. Note that with or without the influence of the jet, the wake assumes a selfsimilar profile by 3 diameters downstream. Measurement of drag established that a zero-momentum wake existed at $U=5$ m/s at $U_j/U=1.95$. A tare measurement was not directly made. Instead, the strut drag was estimated for published airfoil drag data at the appropriate Reynolds number, and it was felt that this was a more precise procedure than directly measuring the strut drag with the body removed. However, in the near field, the jet substantially changes the flow topology behind the body transom. It is interesting to note that the combined jet/wake flow necks down to a minimum diameter at about $x/D=1.3$. Downstream of this near wake region the wake thickens at a

Contributed by the Fluids Engineering Division of ASME for publication in the JOURNAL OF FLUIDS ENGINEERING. Manuscript received August 19, 2008; final manuscript received September 28, 2009; published online October 27, 2009. Editor: Joseph Katz.

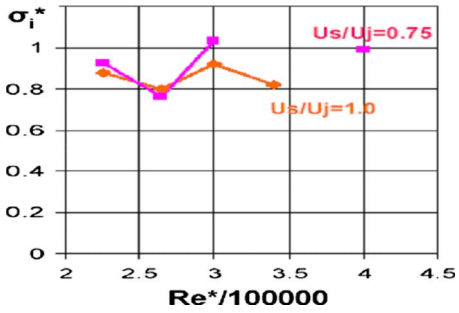

Fig. 1 Cavitation inception index for coflowing jets [1] at two ratios of coflow speed to the jet initial velocity

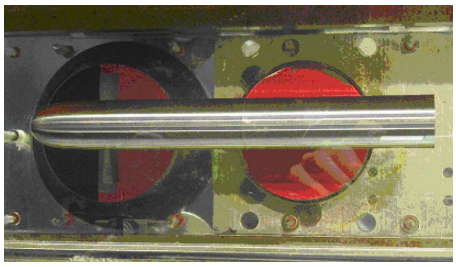

Fig. 3 Side view of test body

rate commensurate with what has been observed for other wakes. Mean flow development and cavitation patterns are qualitatively correlated, as shown in Fig. 7.

Further insight is obtained from Reynolds stress data illustrated in Fig. 8. Note that at a velocity ratio of 0, the maximum Reynolds stress occurs at the outer edge of the wake. With the jet turned on, there are two regions of the maximum stress at the outer edge of the wake and of the jet. The distinct regions of shear layer and jet cavitations should be noted for reasons that will be obvious later in the paper.

Observations indicate that for $U_j/U \ll 1$, cavitation appears in the spiral vortices shedding from the sharp edge of the body transom. For greater U_j, the cavitation inception occurs in the mixing region around the jet. The appearing cavities look like bubbles drifting along some vortices. Using photos similar to those presented in Fig. 9, we found that σ_i corresponds to bubbles sizes $l \approx 0.4$ mm.

3 Empirical Analysis

A superposition analysis originally developed for including the effects of roughness on inception in boundary layer flows [9] was adopted for this problem. Consider the difference between the minimum pressure in the liquid, p_{ml} and the upstream reference pressure, p_∞. This can be written as

$$p_{\mathrm{ml}} - p_\infty = p_w - p_\infty + p_{\mathrm{ml}} - p_w \tag{1}$$

where p_{ml} is the minimum pressure in the liquid, p_∞ is the upstream pressure, and p_w is the average pressure in the wake. This can be written in normalized form as

$$\frac{p_{\mathrm{ml}} - p_\infty}{\frac{1}{2}\rho U^2} = C_p + \frac{p_{\mathrm{ml}} - p_w}{\frac{1}{2}\rho U_J^2}\left[\frac{U_J}{U}\right]^2 \tag{2}$$

where

$$C_p = \frac{p_w - p_\infty}{\frac{1}{2}\rho U^2} \tag{3}$$

Assuming cavitation occurs when p_{ml} is equal to p_v, then

$$\sigma_i = -C_p + \sigma_{ij}\left[\frac{U_J}{U}\right]^2 \tag{4}$$

where σ_{ij} is the cavitation index for a jet exhausting into undisturbed water. This equation corresponds to the case of high jet velocity ratio, where the maximum Reynolds stress is at the edge of the jet. At low jet velocity ratio, cavitation would occur within the wake and the experimental data described in Ref. [9] suggest

$$\sigma_i = -C_p + CC_f \tag{5}$$

where $C_f = (2\langle u'v'\rangle_{\max})/U^2$ is based on the maximum Reynolds stress in the wake and the coefficient $C = 16$.

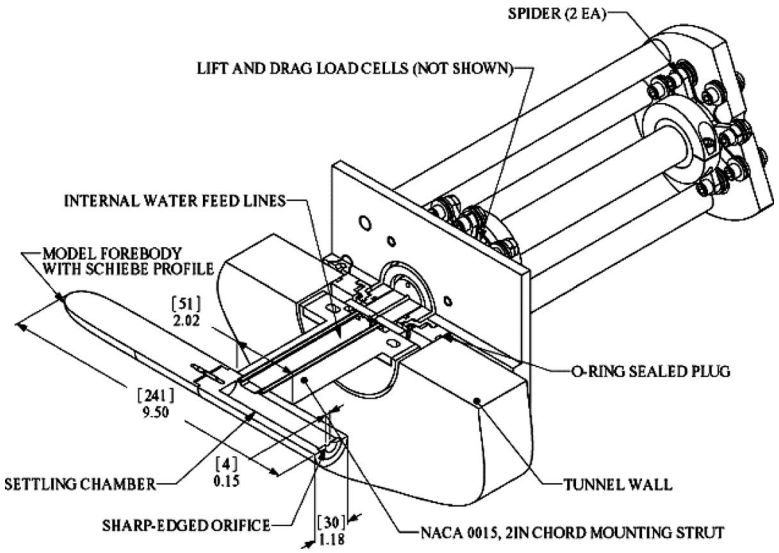

Fig. 2 Experimental setup including the test body, mounting strut, and force balance

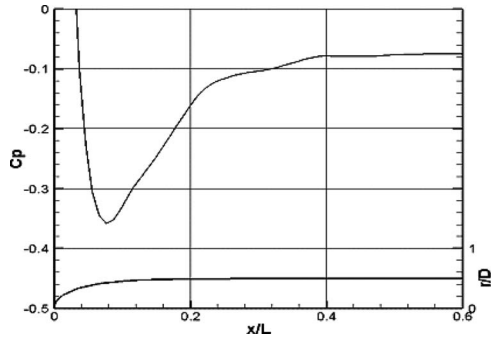

Fig. 4 Pressure distribution around the nose of the Schiebe body

Cavitation inception data are shown in Fig. 10. At high values of velocity ratio the data trend toward the square of the velocity ratio, as predicted by Eq. (4). At smaller ratios of the jet velocity to the incoming flow velocity, Eq. (5) is a reasonable approximation. At intermediate values of the velocity ratio, the inception is lower, suggesting a change in Reynolds stress due to interaction between the jet and the wake. Measurements of Reynolds stress confirm this hypothesis. This is schematically illustrated in Fig. 11.

4 Numerical Analysis of Cavitation Inception

Our observations indicated that the cavitation appears in the jet-wake mixing zone directly behind the body in the form of bubbles. In the analysis that follows consideration is given to define inception as the onset of visible cavities. Therefore, the cavitation inception index can be defined as

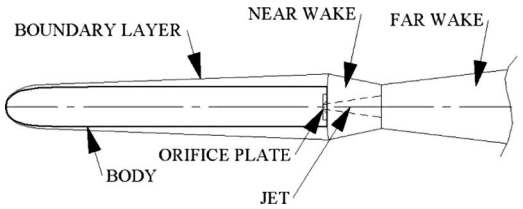

Fig. 5 Schematic of flow pattern. The boundary between jet and wake behind the transom is shown by a dashed line.

$$\sigma_i = C_P - 4D/(\mathrm{We}l) \tag{6}$$

where the cavity scale l equals the bubble diameter. Thus, the second term in the right-hand part of Eq. (6) describes the capillarity effect on cavitation inception.

Computation of C_P requires determination of both the wake time-average characteristics and vortex characteristics. The circumferential velocity in the vortex core $w(\xi)$ can be defined [10] as

$$w(\xi) = \frac{\Gamma}{2\pi}\left(\frac{\xi}{R_C^2}\right) + \frac{\langle u'v'\rangle \xi}{2\nu}\log\frac{\xi}{R_C} \tag{7}$$

where the coordinate ξ is aligned along the vortex radius. This velocity profile is the exact analytical solution of the Reynolds equation for an unbounded area with a practically constant value of the Reynolds stress component $\langle u'v'\rangle$. This solution also allows the determination of the viscous core radius as $R_C = \sqrt{-\Gamma\nu/(\pi\langle u'v'\rangle)}$. Therefore, the corresponding velocity profile in the core is $w(\xi)=(V\xi/R_C)(1-\log(\xi/R_C))$ and the pressure

$$P(\varsigma) = P(1) + \rho V^2\left[\frac{\varsigma^2(2.5+\log^2\varsigma - 3\log\varsigma)}{2} - \frac{1}{4}\right] \tag{8}$$

is substantially different from the laminar case, having a constant angular velocity. Here $V=\Gamma/(2\pi R_C)$ and $\varsigma=\xi/R_C$. The comparison of different theoretical velocity profiles and velocity measurements in vortex cores is given in Fig. 12. One can see that the profile described by Eq. (7) better corresponds to the experimental data than the laminar viscous core does.

By substituting V and R_C into Eq. (8), one can see that the second term in the right-hand side of Eq. (8) is proportional to $\langle u'v'\rangle$, where it takes place in Eq. (5), as well. The capillarity effect on inception is clarified by Fig. 13 that is based on our experimental conditions. Equation (8) was employed for the pressure computation at various r. Further, assuming that this value of r equals to the cavity radius $R_{\mathrm{bubble}}=l/2$, we substituted the corresponding l into Eq. (6), one can see that cavitation number goes down with a bubble radius decrease below 0.2mm (there is an assumption that the appearance of a small cavity does not perturb the pressure in the vortex core). Thus, cavitation inception occurs with bubbles whose size is not negligibly small.

As is clear from Eqs. (6) and (8), computation of σ_i requires the determination of the wake pressure $P(1)$, the vortex intensity Γ,

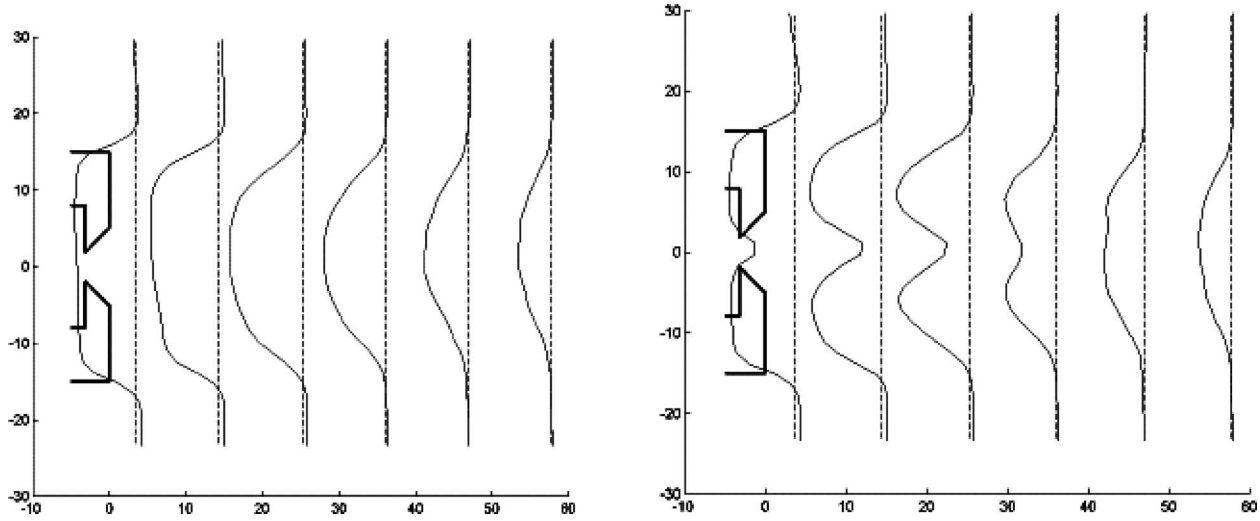

Fig. 6 Mean velocity measurements illustrating wake development at $U_j/U=0$ (left) and $U_j/U=1.5$ (right). The distances shown are in mm.

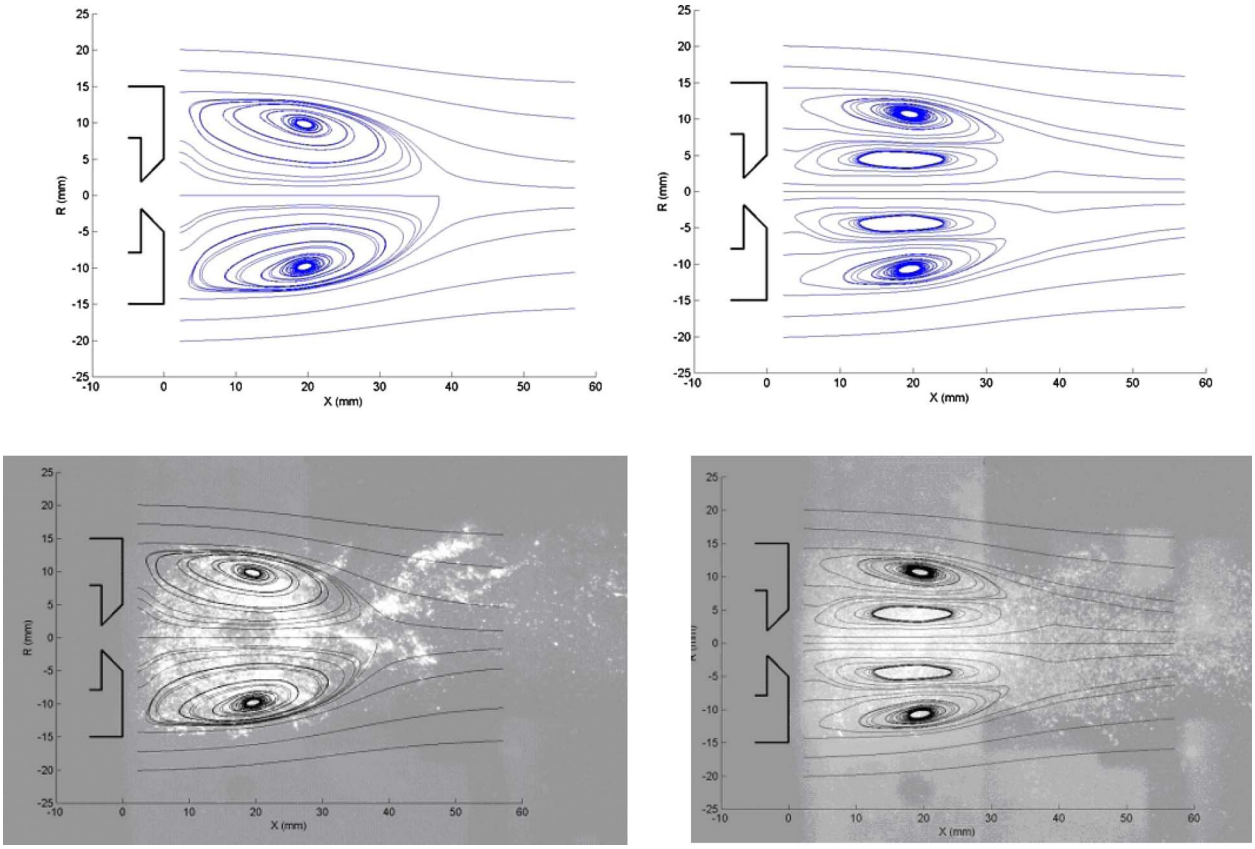

Fig. 7 Mean streamlines and photos of cavitation for velocity ratios of 0 (left) and 1.5 (right). The distances shown are in mm.

and its core radius R_C. There are two general possibilities for the determination of these parameters: direct measurements and semi-empirical computation.

For computation of the time-average wake characteristic $P(1)$, the viscous-inviscid interaction concept is used here. According to this concept, there is a viscous flow and surrounding inviscid flow. The pressure can be found by solving the boundary value problem for the velocity potential in an inviscid fluid, but the shape of the boundary between the inviscid flow and the boundary layer (or wake) depends on both the body shape and the Reynolds number because the thickness of the viscous flow is Re-dependent. On the other hand, this thickness depends also on the pressure distribu-

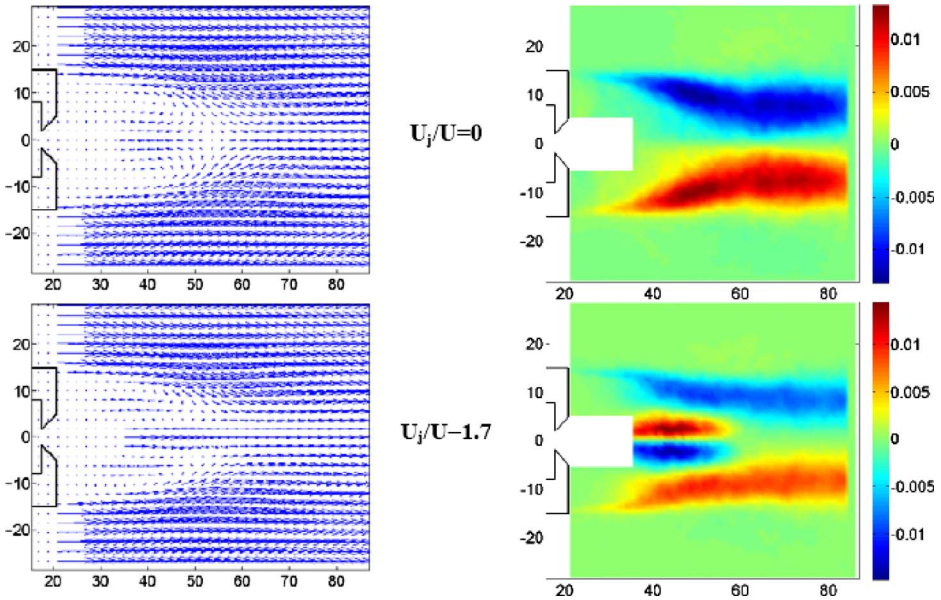

Fig. 8 PIV data. Mean velocity is shown on the left and turbulent stress $\langle u' v' \rangle$ (m^2/s^2) is shown on the right. The distances shown are in mm.

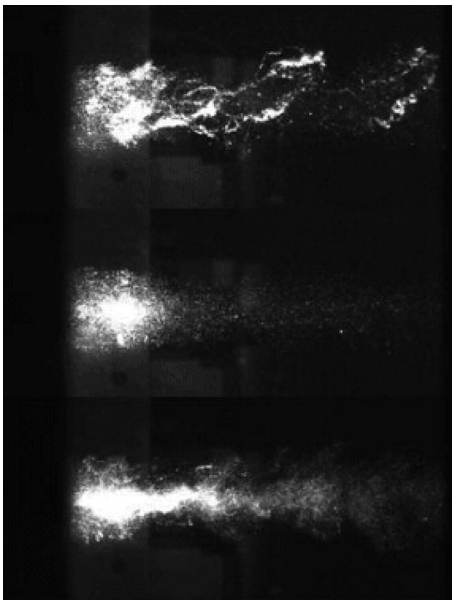

Fig. 9 Cavitation patterns for different U_j at the same U and water tunnel pressure. Top photo corresponds to $U_j/U=0$, center photo corresponds to $U_j/U=1$, and bottom photo corresponds to $U_j/U=2$.

tion. Because of such a mutual influence, computation of flow with a viscous-inviscid interaction concept is an iterative procedure with the solution in turn of potential problems and viscous layer problems (the corresponding flow scheme was given in Fig. 5).

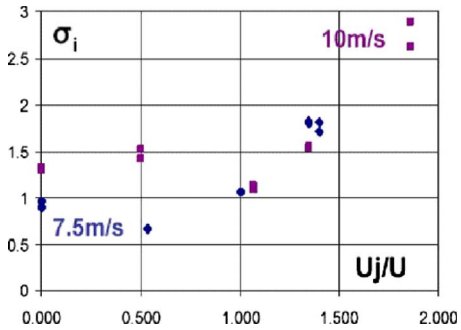

Fig. 10 Cavitation inception data

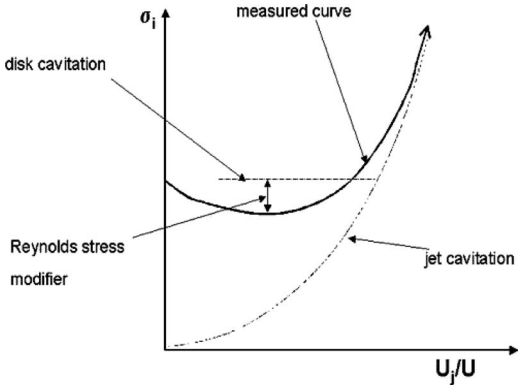

Fig. 11 Schematic of cavitation inception as influenced by the interaction of the jet and the surrounding wake

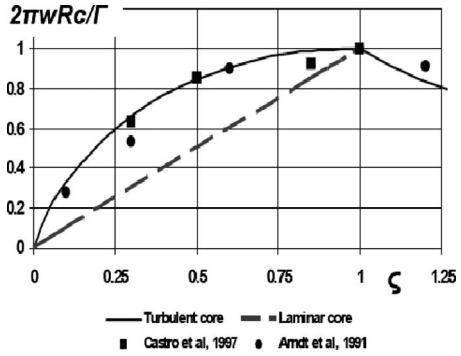

Fig. 12 Comparison of theoretical and measured dimensionless circumferential velocity $2\pi w\, R_C/\Gamma$ in the vortex core. The solid line corresponds to Eq. (7), and the dashed line corresponds to a laminar viscous core with linear dependency of the velocity w on the dimensionless radius ς. Experimental data are shown by symbols.

The description of the numerical technique utilized in this study is emphasized on the zone of viscous separation behind the transom, where jet-wake mixing starts and cavitation appears. This zone is named here as the near wake. However, an analysis of the following part of wake is necessary for determination of the thrust-drag balance (see Ref. [11], for example). Our wake analysis is based on employment of integral relations. For the near wake, the momentum conservation law (von Karman equation) has the following form:

$$\frac{\partial \theta^{**}}{\partial \delta_j}\frac{d\delta_j}{dx} = -\frac{(2\theta^{**}+\theta^{*})}{U_\delta}\frac{dU_\delta}{dx} - \frac{\partial \theta^{**}}{\partial U_0}\frac{dU_0}{dx} - \frac{\partial \theta^{**}}{\partial U_1}\frac{dU_1}{dx} \tag{9}$$

The velocity profile used (according to definitions in the nomenclature) in calculation of θ^{*} and θ^{**} is $u(x,r)=A(x)+B(x)[M+1-M\eta]\eta^{M}$. The auxiliary radial coordinate η is counted from $r=0$ for the inner part of the wake ($r<\delta_j$) and normalized by δ_j there. For its outer part ($r>\delta_j$), η is counted from $r=\delta_j$ and normalized by $\delta-\delta_j$. Correspondingly, $A=U_0$ and $A=U_1$ for these parts. Values of the parameter M can be also different; here $M=3$ in the inner part and $M=2$ in the outer part. The initial value of θ^{**} for integration of Eq. (9) from $x=0$ (from the body transom) is computed by taking into account the momentum thicknesses of jet and body boundary layer at the transom, as well as of the base pressure contribution to the body drag. The derivatives of U_0 and U_1 can be calculated with the following form of the Prandtl equa-

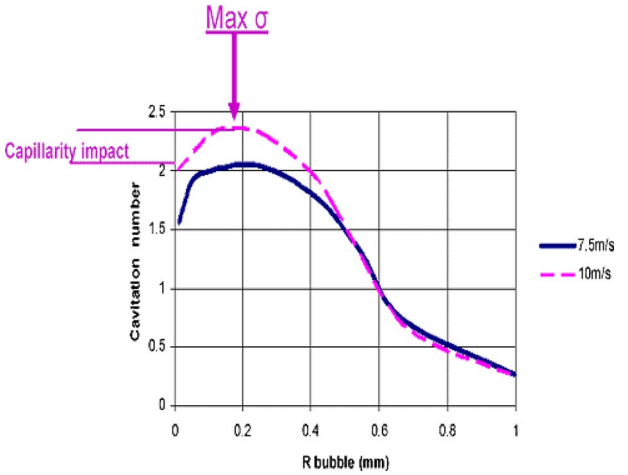

Fig. 13 Computed dependency of cavitation number on bubble radius

tion for the zero-friction lines (wake axis and boundary between jet and surrounding wake)

$$\frac{\partial U_0}{\partial x} = a^* \frac{(U_1/2 + U_\delta/2 - U_0)^2}{U_0(\delta_j + \delta)} - \frac{1}{\rho U_0} \left. \frac{\partial p}{\partial x} \right|_{x-0} \tag{10}$$

$$\frac{\partial U_1}{\partial x} = \frac{a^*}{U_1} \frac{(U_1 - U_\delta)^2}{(\delta - \delta_j)} + \frac{U_\delta}{U_1} \frac{\partial U_\delta}{\partial x} \tag{11}$$

Equations (10) and (11) are similar to that used by Semenov et al. [12] for wakes behind cavitating cascades; here, the Clauser constant a^* is selected as 0.03.

The distributions of U_δ and δ must be found known from the solution of viscous-inviscid interaction problem for the separation zone. Let us get an initial approach $r_S(x)$ to δ. By assuming that the pressure is constant in this zone and using quasilinearization, one can compute δ as

$$\delta(x) = r_S(x) + \frac{1}{2U_\delta(x)} \int_L^x q(\xi) d\xi \tag{12}$$

Integration in Eq. (12) starts from the beginning of the separation zone (from the transom). The source density q is solution of the following equation:

$$\frac{\partial \varphi}{\partial T}(q,x) = U_\delta(x) - U^*(x, r_s) \tag{13}$$

where U^* is the initial distribution of U_δ computed at $r = r_S(x)$.

The function $U_\delta(x)$ along the separation zone is composed from a constant part (for $x < L^* - dL$) and a part of decreasing U_δ (for $L^* - dL < x < L^*$). Such a distribution of U_δ (or pressure) is typical for all separation zones. There is a lot of experimental data that supports this conjecture, starting with the classical report of Tani et al. [13]. Thus, U_δ can be described with two parameters $U_\delta(0)$ and $U_\delta(L^*)$ that will be determined from the semi-empirical "reattachment" condition

$$U_\delta(L^*) \left[1 + 0.03 \frac{dL}{\delta(L^*)} \right] = U_\delta(0) \tag{14}$$

and from the restriction on $d\delta/dx$ (the mathematics of quasilinearization is described in more detail by Amromin [14]

$$\int_0^{L^*} \left[\frac{U_\delta(\xi) - U^*(\xi, r_s)}{\sqrt{\xi(L^* - \xi)}} \right] d\xi = 0 \tag{15}$$

An equation for determination of L^* is generally necessary in this problem on viscous separation. However, for cavitating flows, the effect of σ on L^* may be more important. Actually, we simply got $L^* = D$ on the basis of velocity profile measurements (for $U_j/U \geq 1.0$ representing jets behind selfdriven bodies).

For the far wake, Eqs. (10) and (11) must be also used, but δ will be determined together with δ_j from the mass conservation law

$$\frac{\partial \theta^*}{\partial \delta_j} \frac{d\delta_j}{dx} + \left(\frac{\partial \theta^*}{\partial \delta} - \delta \right) \frac{d\delta}{dx} = -\frac{\delta K_{\mathrm{MIX}}}{U_\delta} + \frac{(0.5\delta^2 - \theta^*)}{U_\delta} \frac{dU_\delta}{dx} - \frac{\partial \theta^*}{\partial U_0} \frac{dU_0}{dx} - \frac{\partial \theta^*}{\partial U_1} \frac{dU_1}{dx} \tag{16}$$

Verification of the above-described numerical technique with experimental data gave satisfactory results. For instance, the momentum-free jet ratio U_j/U was computed to be 1.9 for $U = 5$ m/s (its measured value was 1.95). Incidentally the effect of the jet on the separation zone is quite similar to the known effect of a separating plate in the wake of a blunt body. Examples of computed velocity profiles across the wake are shown in Fig. 14.

As noted, an experimental determination of Γ and R_C may be replaced by their semi-empirical numerical determination. For definition of vortex intensity, one can use the definition $\Gamma = \kappa U' l^*$, where $U' = (U_1 + U_0)/2$ and κ is the empirical coefficient. The distance l^* between vortices of the opposite intensity depends on the frequency f of the vortex shedding and speed U^{**} of their drift ($l^* = 0.5/f \times U^{**}$). Following Cantwell [15], one can suppose that U^{**} is approximately 0.8 of some principal speed that governs the local flow. Here we use the following definition $l^* = 0.8D(U_j + U_\delta)/(U_1 + U_0)$.

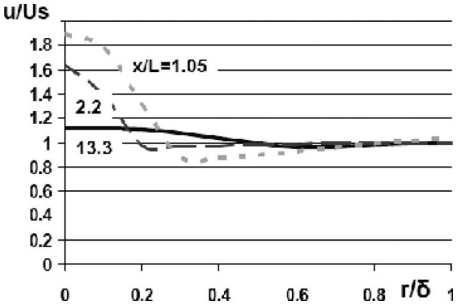

Fig. 14 Computed velocity profiles in the wake at $U=5$ m/s. The velocity profiles $u(r/\delta)$ have minima at $x=1.05L$ and $x=2.2L$. Such minima are inherent neither to jets discharged in immobile water nor to wakes behind towed bodies.

There are no relevant computations of $\langle u'v' \rangle$ behind waterjet-driven bodies. There is only a very limited set of our experiment data on $\langle u'v' \rangle$ (as shown in Fig. 8). However, a qualitative dependency on Re can be found with the experimental data of Bourgoyne et al. [16] for near turbulent wakes behind a foil. As shown in Fig. 15, the maximum of $|\langle u'v' \rangle|$ can be represented as $\langle u'v' \rangle = -B\,\mathrm{Re}^{-0.5}$, where B is a constant. Such approximation gives the value $\max\{-\langle u'v' \rangle\} = 0.012$ for the mixing zone behind a Schiebe body at $\{U = 7.5$ m/s, $U_j/U = 1.5\}$. This value agrees well with our measurements presented in Fig. 16.

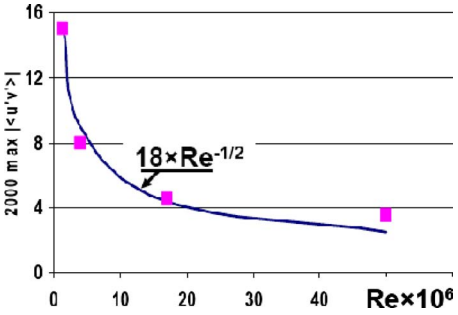

Fig. 15 Measured dependency $\langle u'v' \rangle$ on Re for a wake

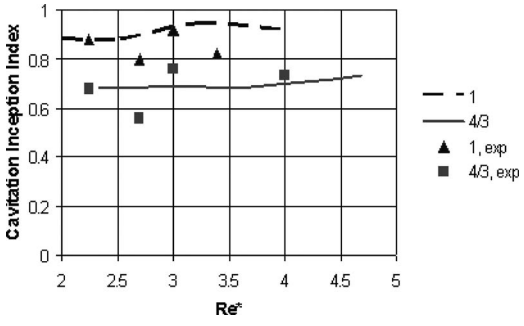

Fig. 16 Comparison of computed (lines) and measured (symbols) [1] cavitation inception indexes versus Reynolds number (calculated using the average of the jet and coflow speeds as a characteristic velocity). The comparison is made for $U_j/U=4/3$ and 1.

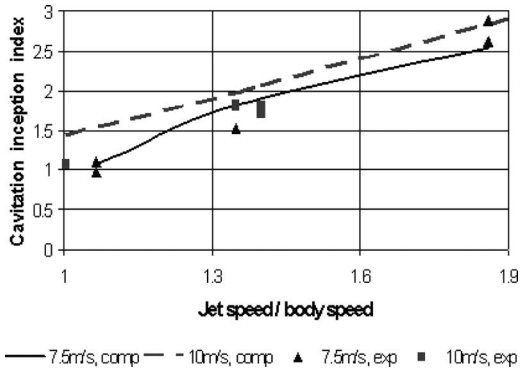

Fig. 17 Comparison of computed (lines) and measured (symbols) values of cavitation inception index versus jet speed for Schiebe body at two freestream speeds

Selection of the above empirical coefficients was verified with both our experimental data for the Schiebe body and the data of Straka et al. [1] for the blunt nozzle. It was found that a 20% variation in B has less influence on the computed values of σ_i than a 10% variation in κ has. It was also found that the observable minimum of cavity size has a very significant impact on σ_i. The results of the method of intermediate validation with data on the blunt nozzles are presented in Fig. 16. The computational results for the Schiebe body in Fig. 17 are obtained with the constant l. This is in agreement with the experimental technique of determination of cavitation inception by observation of bubble appearance. One can see in Fig. 17 that the effect of U_j on σ_i is captured in our computations.

The overall agreement of the computations with the experimental data is very satisfactory (especially in view of the state-of-the-art in prediction of vortex cavitation) (see Ref. [8] for more detail). The cavity length corresponding to cavitation inception is a given parameter in this numerical technique.

5 Conclusions

Water tunnel tests of a body with a jet discharging from its transom stern gave an overall visualization of the topology of cavitation inception behind waterjet-driven bodies for the first time. Turbulence in the jet-wake mixing region was measured with a PIV system. This information allowed us to relate the range of variation in cavitation inception index with the flow physics. It was found that for selfpropellant bodies, cavitation would appear between vortices around the jet. Impact of jet speed on cavitation inception was studied and zero-momentum wake in the water tunnel was observed.

A simple superposition analysis appears to capture the essential physics of the problem. This provided insight for a more complex computational analysis of cavitation inception that determined that the suggested model of a cavitating vortex pair in a turbulent flow can give a satisfactory prediction of cavitation inception. The employed viscous-inviscid interaction concept was flexible enough to apply to complex cavitating flows. Therefore, the developed numerical tools show promise for extension to more complex flow (body) geometry and flow perturbations.

Acknowledgment

Authors are grateful to ONR for support of this study (program manager Dr. W. Keith). Mr. Ellison Kawakami, an undergraduate research assistant, was very helpful in carrying out the experiments.

Nomenclature

C_D = drag coefficient

$C_P = 2(p_\infty - p)/\rho U^2$ = pressure coefficient

D = body diameter

K_{MIX} = empirical mixing coefficient

L = body/cavity length

l = bubble size

L^* = length of the separation zone behind the transom

l^* = distance between counter-rotating vortices

p = pressure in water

p_∞ = unperturbed pressure in water

p_C = pressure in cavity

p_v = vapor pressure

p_{ml} = minimum pressure in the liquid

R_C = viscous core radius

Re = Reynolds number

T = tangent to the wake boundary

u = water velocity

U = body speed

$\langle u'v' \rangle$ = Reynolds tress

U_0 = velocity on the wake axis

U_1 = velocity on the line between jet and surrounding wake

U_j = jet speed

U_s = coflow speed

U_δ = velocity of inviscid flow around the wake

w = circumferential velocity in the vortex core

We = Weber number, $D\rho U^2/2\chi$

(x,r) = cylindrical coordinates

Γ = vortex strength

δ = thickness of wake

δ_j = thickness of jet

φ = auxiliary velocity potential

ρ = density of water

$\sigma = 2(p_\infty - p_C)/\rho U^2$ = cavitation index

σ_i = cavitation inception index

$\theta^* = \int_0^\delta r[1 - u(r)/U_\delta]dr$ = displacement area

$\theta^{**} = \int_0^\delta ru(r)/U_\delta[1 - u(r)/U_\delta]dr$ = momentum area

χ = surface tension coefficient

References

[1] Straka, W. A., Mayer, R. S., Fontaine, A. F., and Welz, J. P., 2006, "Experimental Study of Cavitation Inception in Quiescent and Co-Flow Nozzle Jets," Cav-2006 Symposium, Wageningen.

[2] Gopalan, S., Katz, J., and Kino, O., 1999, "The Flow Structure in the Near Field of Jets and Its Effect on Cavitation Inception," J. Fluid Mech., **398**, pp. 1–43.

[3] Amromin, E. L., Arndt, R. E. A., Hambleton, W., and Kovinskaya, S. I., 2007, "Cavitation Inception Behind a Jet-Driven Body," ASME Paper No. FEDSM2007-37026.

[4] Arndt, R. E. A., Arakeri, V. H., and Higuchi, H., 1991, "Some Observations of Tip-Vortex Cavitation," J. Fluid Mech., **229**, pp. 269–289.

[5] Arndt, R. E. A., Wosnik, M., and Kawakami, D., 2007, "Measurements in Cavitating Flows," *Handbook of Experimental Fluid Mechanics*, C. Tropea, A. L. Yarin, and J. F. Foss, eds., Springer, New York, Chap. 15.1, p. 972.

[6] Cebeci, T., and Bradshaw, P., 1984, *Physical and Computational Aspects of Convective Head Transfer*, Springer-Verlag, Berlin.

[7] Arndt, R. E. A., and Keller, A., 1992, "Water Quality Effects on Cavitation Inception in a Trailing Vortex," ASME J. Fluids Eng., **114**, pp. 430–438.

[8] Arndt, R. E. A., 2002, "Cavitation in Vortical Flow," Annu. Rev. Fluid Mech., **34**, pp. 143–176.

[9] Arndt, R. E. A., 1981, "Cavitation in Fluid Machinery and Hydraulic Structures," Annu. Rev. Fluid Mech., **13**, pp. 273–328.

[10] Amromin, E. L., 2007, "Analysis of Vortex Core in Steady Turbulent Flow," Phys. Fluids, **19**, p. 118108.

[11] Naudasher, E., 1965, "Flow in the Wake of Self-Propelled Bodies and Related Sources of Turbulence," J. Fluid Mech., **22**(4), pp. 625–656.

[12] Semenov, Y. A., Fujii, A., and Tsujimoto, Y., 2004, "Rotating Choke in Cavitating Turbopump Inducer," ASME J. Fluids Eng., **126**, pp. 87–93.

[13] Tani, I., Iuchi, M., and Komoda, H., 1961, "Experimental Investigation of Flow Separation Associated With a Step or a Groove," Aeronautical Research Institute, University of Tokyo, Report No. 364.
[14] Amromin, E. L., 2002, "Scale Effect of Cavitation Inception on a 2D Eppler Hydrofoil," ASME J. Fluids Eng., **124**, pp. 186–193.
[15] Cantwell, B. J., 1981, "Organized Motion in Turbulent Flow," Annu. Rev. Fluid Mech., **13**, pp. 457–515.
[16] Bourgoyne, D. A., Ceccio, S. L., and Dowling, D. R., 2005, "Vortex Shedding From a Hydrofoil at High Reynolds Number," J. Fluid Mech., **531**, pp. 293–324.

Mirka Deza
Department of Mechanical Engineering,
Virginia Polytechnic Institute and State University,
Blacksburg, VA 24061

Nathan P. Franka

Theodore J. Heindel

Department of Mechanical Engineering,
Iowa State University,
Ames, IA 50011

Francine Battaglia[1]
Department of Mechanical Engineering,
Virginia Polytechnic Institute and State University,
Blacksburg, VA 24061
e-mail: fbattaglia@vt.edu

CFD Modeling and X-Ray Imaging of Biomass in a Fluidized Bed

Computational modeling of fluidized beds can be used to predict the operation of biomass gasifiers after extensive validation with experimental data. The present work focused on validating computational simulations of a fluidized bed using a multifluid Eulerian–Eulerian model to represent the gas and solid phases as interpenetrating continua. Simulations of a cold-flow glass bead fluidized bed, using two different drag models, were compared with experimental results for model validation. The validated numerical model was then used to complete a parametric study for the coefficient of restitution and particle sphericity, which are unknown properties of biomass. Biomass is not well characterized, and so this study attempts to demonstrate how particle properties affect the hydrodynamics of a fluidized bed. Hydrodynamic results from the simulations were compared with X-ray flow visualization computed tomography studies of a similar bed. It was found that the Gidaspow (blending) model can accurately predict the hydrodynamics of a biomass fluidized bed. The coefficient of restitution of biomass did not affect the hydrodynamics of the bed for the conditions of this study; however, the bed hydrodynamics were more sensitive to particle sphericity variation. [DOI: 10.1115/1.4000257]

1 Introduction

Biomass hydrodynamics in a fluidized bed are extremely important to industries that are using biomass material in the gasification processes to yield high quality producer gas. Producer gas can be considered as a biorenewable alternative energy resource that can potentially replace natural gas and provide low cost power production and process heating needs. Since biomass particles are typically difficult to fluidize due to their peculiar shape, a second inert material, such as sand, alumina, or calcite, is typically added to the bed [1]. However, the large differences in size and density between the biomass and inert particles lead to nonuniform distribution of the biomass within the fluidized bed, and particle interactions and mixing become major issues.

Given the nature of biomass particles (shape, moisture content, and pliability), their fluidization characteristics are of critical importance because of known problems such as particle agglomeration, defluidization, elutriation, and segregation [2–7]. Ideally, experiments can provide information on the fluidization characteristics of biomass, but the opacity of the bed material impedes visualization techniques. Since fluidization is a dynamic process, invasive monitoring methods can influence the internal flow, thereby reducing the reliability of the measurements [8]. As stated by Heindel et al. [9], noninvasive monitoring techniques for multiphase flows include electrical capacitance tomography, ultrasonic computed tomography, gamma densitometry tomography, X-ray fluoroscopy (radiography/stereography), and X-ray computed tomography. Franka et al. [10] used X-ray computed tomography (CT) and radiography to analyze differences in materials for fluidized beds operating under three gas flow rates. The CT images showed that glass beads fluidized much more uniformly compared with melamine, walnut, and corncob beds, and that walnut shell fluidized more uniformly as the gas flow rate increased.

Most of the research on biomass gasification modeling has focused on the combustion process, predicting the composition of the resulting gas and studying effects, such as temperature, composition, and moisture content of the biomass, for the combustion efficiency of the reactor. Some other aspects of biomass fluidization, such as terminal settling velocities, minimum fluidization and fluidizability, and residence time of biomass particles, have been studied, and a summary can be found in Ref. [1]. To date, there is little published information on fluidized bed hydrodynamics when biomass is injected into a reactor. Zhang and Brandani [11] proposed a modified particle bed model in bubbling fluidized beds; their computational fluid dynamics (CFD) simulations for a circulating fluidized bed showed that pressure fluctuations and bubble size and number increased with the inlet gas velocity.

Several drag models have been reported in the literature to account for the gas-solid hydrodynamics of fluidized beds. Taghipour et al. [12] compared the Syamlal–O'Brien, Gidaspow, and Wen–Yu models with experimental data and found that for relatively large Geldart B particles, the models predicted the hydrodynamics of the bed reasonably well. Du et al. [13] studied five drag models in a spouted fluidized bed and found that for dense phase simulations, the models produced noticeable differences. Among the five drag models [13] tested, namely, the Richardson–Zaky, Arastoopour, Gidaspow (blending), Di Felice, and Syamlal–O'Brien, the Arastoopour and Syamlal–O'Brien models gave good predictions of the flow, but the Gidaspow drag model gave the best agreement with the experimental data. Another extensive model comparison in fluidized beds was made by Mahinpey et al. [14] for bed expansion and pressure drop with different inlet gas velocities in a fluidized bed using the Di Felice, Gibilaro, Koch, Syamlal–O'Brien, Arastoopur, Syamlal–O'Brien (adjusted), Di Felice (adjusted), Gidaspow, Zhang–Reese, and Wen–Yu drag models. All of the models gave acceptable qualitative agreement with experimental data; however, results for the adjusted models of Syamlal–O'Brien and Di Felice showed an improvement in quantitative predictions of the bed hydrodynamics.

Finding an appropriate drag model for biomass fluidized beds is of particular interest to the research herein. The underlying issue is that the drag models cited previously, which gave better predictions, require information about the bed hydrodynamics that is not always known for biomass particles or can be easily measured experimentally. For example, the adjusted models of Di Felice or Syamlal–O'Brien require minimum fluidization velocity to tune

[1]Corresponding author.

Contributed by the Fluids Engineering Division of ASME for publication in the JOURNAL OF FLUIDS ENGINEERING. Manuscript received January 29, 2009; final manuscript received August 25, 2009; published online October 29, 2009. Editor: Joseph Katz.

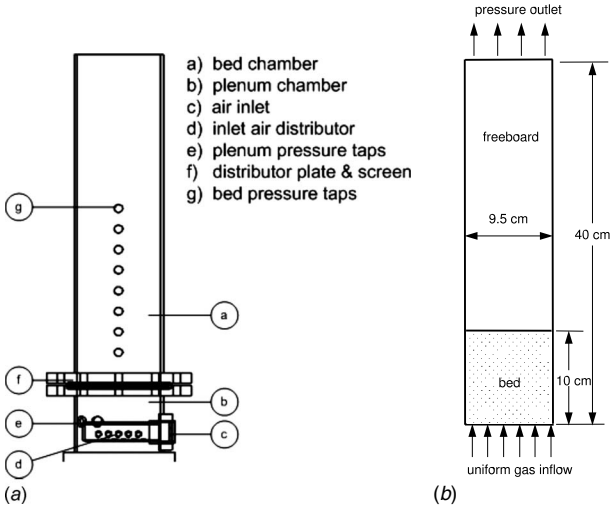

Fig. 1 Schematic of the (*a*) experimental setup for a 9.5 cm ID fluidized bed and (*b*) the 2D plane representing the simulated bed chamber of the cylindrical reactor

the drag correlations. In addition, the Syamlal–O'Brien model requires void fraction of the packed bed and particle density. Furthermore, the aforementioned drag model studies used glass beads as the solid particle in the fluidized beds; however, none of the drag models have been tested to validate the hydrodynamics of a fluidized bed using biomass particles. Two models, the adjusted Syamlal–O'Brien model and the Gidaspow model with a blending function, will be compared in this study to assess the hydrodynamics of a biomass fluidized bed. Our choice of models to test is based on results and recommendations of the previous studies [12–14].

Hence, the goal of this research is to computationally model a cold-flow fluidized bed and to compare and validate the model with experiments. In practice, biomass is not well characterized, and so this study is an attempt to demonstrate how particle properties affect the hydrodynamics of a fluidized bed. The experiments will be accomplished using X-ray computed tomography and X-ray radiography. Glass beads will be used to model the bed for purposes of validation between the experiments and computational models because the material is well characterized. Initial work is then pursued to study single component biomass gasification using ground walnut shell. Both glass beads and ground walnut shell particles correspond to Geldart's type B classification, which according to Abdullah et al. [15], satisfactorily fluidize. In this work, the simulations of the fluidized beds will be employed using the open source software Multiphase Flow with Interphase eXchanges (MFIX). The simulations will consider factors such as particle sphericity, coefficient of restitution, and drag model. Results from the simulations will be compared with the particle distribution, bed height, and pressure drop obtained from the experiments.

2 Experimental Setup

2.1 Fluidized Bed Reactor. The fluidized bed reactor used in the experiments consisted of a 9.5 cm internal diameter (ID) 40 cm tall acrylic tube (a), illustrated in Fig. 1(*a*). Air entered the acrylic plenum chamber (b) through a 1.0 cm air inlet fitting (c) and passed through a pipe (d) drilled with 16 0.6-cm diameter holes. This drilled pipe served to gradually expand gas into the plenum chamber and avoid jetting phenomena. The plenum contained two 1.0 cm pressure taps (e) used for measuring pressure drop across the bed. Air left the plenum through a distributor plate drilled with 100 0.1-cm diameter holes; each hole was spaced 0.4 cm apart on a square grid. To eliminate coarse bed particles from becoming lodged inside the distributor plate holes, a 45 mesh screen with openings of 0.04 cm was attached to the plate. The top of the vessel was open to the atmosphere. The bed chamber included several tapped holes (g) for pressure measurements; however, these were not employed in the present study. Inlet air flow rate was controlled by a 0–3300 cm^3/s flow meter and pressure regulator. The accuracy of the flow meter was $\pm 2\%$ of the full scale reading (± 67 cm^3/s).

2.2 Material Selection and Minimum Fluidization. The fluidization behavior of two materials was investigated in this study. Glass beads were studied as a benchmark since the fluidization of glass is well characterized and because glass has similar properties to inert sand used in gasification. Additionally, modeling glass bead fluidization is ideal due to its high sphericity, uniform density, narrow particle size distribution, and resistance to breaking. Ground walnut shell was studied as an alternative bed material. Ground walnut shell particles have lower density than glass beads and aspect ratios near unity. Both materials fell within Geldart's type B classification in order to maintain similar fluidization hydrodynamics between the beds. Particle diameter ranges for glass beads and ground walnut shell were 500–600 μm and 500–700 μm, respectively, and the static bed height was 10 cm for both materials ($H/D=1.05$).

The minimum fluidization velocity U_{mf} for each bed was experimentally measured using well-established procedures [16]. Initially, the beds were fluidized with air at a superficial gas velocity $U_g=28$ cm/s, and pressure was measured using a 0–3.7 kPa pressure gauge connected to a pressure tap in the plenum. Gas flow was decreased in increments of 1.2 cm/s, and the total pressure across the bed and distributor plate was measured. By measuring pressures as the gas flow decreased, bed packing effects were removed. This was necessary because packing effects create a hysteresis loop in the pressure data when the flow rate is increased. The procedure was repeated for an empty reactor in order to find the pressure drop across the distributor plate. By subtracting the empty reactor data from the total pressure drop data, the pressure drop across the bed was calculated. On the resulting plot the pressure drop across the bed appears to linearly increase with increasing superficial velocity until it reaches a point at which the pressure drop becomes constant. This point is defined as the minimum fluidization velocity. For the materials and bed conditions of this study, $U_{mf}=19.9$ cm/s for glass beads and 18.7 cm/s for ground walnut shell. For each material, flow conditions of $1.1U_{mf}$, $1.3U_{mf}$, and $1.5U_{mf}$ were tested; for this study, the numerical model will be validated with the inflow velocity of $1.3U_{mf}$.

2.3 X-Ray System. Iowa State University's XFloViz facility was used to image the fluidized bed and has been described in detail in the literature [9]. Consequently, only a brief outline will be presented here. Two LORAD LPX200 portable X-ray tubes provide the X-ray energy. Current and voltage can be adjusted from 0.1 mA to 10.0 mA and from 10 kV to 200 kV, respectively, with a maximum power of 900 W. Low energy radiation is suppressed by 1 mm thick copper and aluminum filters. Located opposite each X-ray source is an X-ray detector/charged-coupled device (CCD) camera pair. The CCD camera with image intensifier has a temporal resolution ranging from 10 frames per second (fps) to 60 fps, depending on binning options and is primarily used for radiographic imaging. The image intensifier is a 40.6 cm diameter Precise Optics PS164X screen detector with a 35.0 mm output image diameter. A DVC-1412 monochrome digital camera captures the image from the intensifier. Generally, 2×2 binning (640×512 active pixels) at 20 fps is used for radiographic movies in order to maximize picture quality while maintaining adequate temporal resolution. A second detector/camera pair is primarily used for CT imaging because of its high spatial resolution. This camera is located opposite the second source and is connected to a square 44×44 cm^2 cesium-iodide scintillator screen, which transforms radiation into visible light. A 50 mm Nikon lens cap-

tures images, which are digitized by an Apogee Alta U9 system. This system has 3072×2048 pixels and is thermoelectrically cooled to allow long exposure times. Usually, an exposure time of 1 s with 4×4 binning is chosen to minimize acquisition time while maintaining the signal strength. Both cameras and sources are located on a 1.0 m ID rotation ring that can rotate 360 deg around the fluidized bed. CT and radiographic data are acquired using software developed by Iowa State University's Center for Nondestructive Evaluation (CNDE) and a personal computer with 4 GB of RAM. The software allows for control of both camera/detector pairs, as well as motion control for the rotation ring. Volumetric reconstruction of the CT images is performed using CNDE's 64-node LINUX cluster.

2.4 CT Images. In X-ray computed tomography with a conical X-ray beam, a series of two-dimensional (2D) projections are captured at various angles and reconstructed into a three-dimensional (3D) volumetric image. Since multiple images must be acquired for one CT, the resulting 3D image is necessarily time-averaged. This image is a map of CT intensity values, which are proportional to X-ray attenuation, which, in turn, is proportional to density. In this study, CT images of the glass bead fluidized bed were taken at 135 kV 1.6 mA for every 1 deg around a 360 deg rotation. Ground walnut shell images were taken at 130 kV and 4.2 mA to improve contrast. For all tests, the exposure time was 1 s at 4×4 binning per degree, and each test took approximately 45 min. A total of 260 vertical slices were captured for glass bead beds, and 300 vertical slices were captured for ground walnut shell beds. The height was adjusted because the bed height expansion of ground walnut shell was larger than for glass beds; however, the difference in height did not affect the CT data.

To minimize image acquisition noise, the CCD camera was cooled to $0\,^{\circ}\mathrm{C}$ using the thermoelectric cooler. Two calibrations were applied to the CT data to remove image artifacts [9]. To account for pixel nonuniformity, linear normalization was employed. This calibration employed a linear interpolation routine to adjust pixels to respond identically to incident X-ray energy. The second calibration was only applied to the glass bead CTs and accounted for beam hardening. This artifact is often present in high density materials and occurs due to the preferential attenuation of polyenergetic X-rays. The result is that the center of an object appears less dense than the surroundings. To correct for beam hardening, an "effective λ" calibration was applied to the raw CT files before reconstruction. After calibration, the 2D projections were reconstructed into 3D images using the CNDE software.

2.5 Gas Holdup. In order to quantify the CT data, time-averaged local gas holdup (void fraction) was calculated for each flow condition. The local gas holdup, ϵ_g, can be determined by knowing the local X-ray attenuation for the flow (λ), the particle (λ_p), and the gas (λ_g). Since the attenuation is proportional to the CT intensity (*CTI*), the local gas holdup can be calculated by knowing CT intensity data for the flow, the particle (CTI_p), and the gas (CTI_g). Therefore, the local gas holdup is defined as

$$\epsilon_g = \frac{\lambda - \lambda_p}{\lambda_g - \lambda_p} = \frac{CTI - CTI_p}{CTI_g - CTI_p} \tag{1}$$

It is difficult to determine the CT intensity for a single particle due to its small size; however, the CT intensity for a static (bulk) bed of particles (CTI_b) can be used. From Eq. (1), the void fraction for the bulk material can be calculated using local CT intensities for the bed, where

$$\epsilon_{g,b} = \frac{CTI_b - CTI_p}{CTI_g - CTI_p} \tag{2}$$

For a granular material, the void fraction of the bulk material ($\epsilon_{g,b}$) is defined as

$$\epsilon_{g,b} = 1 - \frac{\rho_b}{\rho_p} = \text{constant} \tag{3}$$

The bed material bulk density (ρ_b) and particle density (ρ_p) can be found experimentally and in property tables, respectively. Substituting CTI_p from Eq. (2) into Eq. (1) and rearranging yields an equation to find local gas holdup based on CTs for the flow condition, the gas, and the bulk material

$$\epsilon_g(i,j,k) = \frac{CTI(i,j,k) - CTI_b(i,j,k) + [CTI_g(i,j,k) - CTI(i,j,k)]\epsilon_{g,b}}{CTI_g(i,j,k) - CTI_b(i,j,k)} \tag{4}$$

and i, j, and k represent the locations of individual voxels in the three-dimensional volume, where a voxel is a 3D pixel. For each material in this study, CT data were acquired for a bed of static bulk material, and the empty reactor (air only) at identical power settings used to capture fluidization (flow) CT data. Using Eq. (4), each flow file was converted to show local gas holdup, and a smoothing method was employed to reduce noise. The resulting time-averaged gas holdup values are determined on a 3D grid with an approximate voxel size of $0.6 \times 0.6 \times 0.6$ mm^3. Estimated absolute uncertainly in the local gas holdup is ± 0.04, which is a worst-case estimate with most data falling within an absolute gas holdup error of ± 0.02.

Three-dimensional images were viewed using an internally developed visualization software, which allowed viewing of the volumetric images at any location within the imaging volume and adjusted color mapping schemes. Since volume files contain information outside the cylindrical region of interest, a clipping feature was also used to isolate the fluidized bed. Once isolated, the spatial range was modified to show the vertical y-z plane (x-slice) and the vertical x-z plane (y-slice) through the column center, as well as horizontal x-y planes (z-slices) at heights of 4 cm and 8 cm from the distributor plate.

2.6 Radiographs. In radiography, a two-dimensional projection of the 3D attenuation is generated, which is related to the density profile. Because of the high temporal resolution, multiple radiographic images may be acquired and compiled into a video to show dynamic features of an object. In this study, a 30 s movie at 20 fps, and 2×2 binning (640×512 pixels) was captured for each flow and material condition. The radiographic images were acquired at 82 kV 1.6 mA for the glass bead bed, and 82 kV 1.0 mA for the ground walnut shell bed. The use of the image intensifier system resulted in a warping artifact in the resultant images, which appears as a distortion in an image's coordinate system; some regions appear to be rotated and squeezed relative to the horizontal and vertical axes [9]. To overcome this artifact, a second-order polynomial correction algorithm was applied to each warped image. Unwarped images were subsequently compiled and compressed into ".avi" movie files. Image unwarping and movie generation were performed with a script written in MATLAB to automate the process. Radiographic images in this paper are selected still frames from the resulting movies.

3 Two-Fluid Model

3.1 Governing Equations. The FORTRAN code, MFIX, is used for all simulations in this work. A multifluid Eulerian–Eulerian model is employed in MFIX [17] and assumes that each phase behaves as interpenetrating continua with its own physical properties. The instantaneous variables are averaged over a region that is larger than the particle spacing but smaller than the flow domain. Volume fractions are introduced to track the fraction each phase occupies in the averaging volume, where ϵ_g is the gas phase volume fraction (also referred to as the void fraction) and ϵ_s is the solid phase volume fraction for the mth solid phase. The volume fractions must satisfy the relation

$$\epsilon_g + \sum_{m=1}^{M} \epsilon_{sm} = 1 \tag{5}$$

For a mixture of particles, each distinct particle type to be modeled is represented as a solid phase m for a total of M phases. Each solid phase is described with an effective particle diameter d_p and characteristic material properties, and a conservation equation is solved for each solid phase. For this study, only one solid phase is modeled, therefore $M=1$; the remaining discussion will present equations accordingly.

The continuity equations for the gas phase and the solids phases, respectively, are

$$\frac{\partial}{\partial t}(\epsilon_g \rho_g) + \nabla \cdot (\epsilon_g \rho_g \mathbf{u}_g) = 0 \tag{6}$$

$$\frac{\partial}{\partial t}(\epsilon_s \rho_s) + \nabla \cdot (\epsilon_s \rho_s \mathbf{u}_s) = 0 \tag{7}$$

The subscripts g and s indicate the gas and solid phases. Other variables include the density (ρ) and velocity vector ($\mathbf{u}$). Note that there is no mass transfer, and therefore the right-hand sides of the equations are set to zero. It is further assumed that the gas density can be modeled using the ideal gas law.

The momentum equations for the gas and solid phases have the form

$$\frac{\partial}{\partial t}(\epsilon_g \rho_g \mathbf{u}_g) + \nabla \cdot (\epsilon_g \rho_g \mathbf{u}_g \mathbf{u}_g) = -\epsilon_g \nabla P_g + \nabla \cdot \bar{\bar{\sigma}}_g + \mathbf{I}_g + \epsilon_g \rho_g \mathbf{g} \tag{8}$$

$$\frac{\partial}{\partial t}(\epsilon_s \rho_s \mathbf{u}_s) + \nabla \cdot (\epsilon_s \rho_s \mathbf{u}_s \mathbf{u}_s) = -\epsilon_s \nabla P_g + \nabla \cdot \bar{\bar{\sigma}}_s - \mathbf{I}_g + \epsilon_s \rho_s \mathbf{g} \tag{9}$$

The expressions on the left side are the net rate of momentum increase and the net rate of momentum transfer by convection. The right side includes contributions for buoyancy caused by the fluid pressure gradient, the stress tensors ($\bar{\bar{\sigma}}$), gravity ($\mathbf{g}$), and the interaction forces ($\mathbf{I}$) accounting for the momentum transfer between the gas and solid phases; this will be discussed in detail later in this section. The constitutive equations for the gas phase tensor can be found in Ref. [17].

The granular temperature θ for the solid phase can be related to the granular energy, defined as the specific kinetic energy of the random fluctuating component of the particle velocity. The resulting transport equation for the granular temperature [18] is

$$\frac{3}{2}\left[\frac{\partial}{\partial t}(\epsilon_s \rho_s \theta) + \nabla \cdot (\epsilon_s \rho_s \theta)\mathbf{u}_s\right] = \bar{\bar{\sigma}}_s : \nabla \mathbf{u}_s - \nabla \cdot \mathbf{q}_\theta - \gamma_\theta + \phi_g \tag{10}$$

where $\mathbf{q}_\theta$ is the diffusive flux of granular energy, γ_θ is the rate of granular energy dissipation due to inelastic collisions [19], and ϕ_g is the transfer of granular energy between the gas phase and solid phase. Since the numerical simulations will model a cold-flow fluidized bed, the energy equation will not be employed in MFIX and therefore is not presented here.

3.2 Drag Models. The interaction force ($\mathbf{I}_g$) in the momentum Eqs. (8) and (9) accounts for the gas-solid momentum transfer

$$\mathbf{I}_g = F_g(\mathbf{u}_s - \mathbf{u}_g) \tag{11}$$

which is the product of the coefficient for the interphase force between the gas and solid phases (F_g) and the slip velocity between the two phases ($\mathbf{u}_s - \mathbf{u}_g$). The coefficient for the interphase force is different for each drag model.

It should be noted that for cases where the particle diameter is not perfectly spherical, the particle diameter used in the correlations is modified. The sphericity is the particle property that indicates how spherical a particle is, where a sphericity of unity signifies that the particle is a perfect sphere. Therefore, the modified particle diameter is

$$d_p = \psi \bar{d}_p \tag{12}$$

where $\bar{d}_p$ is the mean diameter and ψ is the estimated sphericity of the actual particles. Two drag models are analyzed to determine how well they predict biomass fluidization. The first model, the adjusted Syamlal–O'Brien model, requires knowledge of U_{mf} to tune the drag coefficients, which can only be obtained from experiments. The second model, the Gidaspow model, is based on semi-empirical correlations. Both models are discussed next.

3.2.1 Adjusted Syamlal–O'Brien model. Syamlal et al. [17] derived a correlation for the coefficient for the interphase drag force that converts the terminal velocity correlations to drag correlations

$$F_g = \frac{3\epsilon_s \epsilon_g \rho_g}{4 V_r^2 d_p} C_{Ds}\left(\frac{\mathrm{Re}}{V_r}\right)|\mathbf{u_s} - \mathbf{u_g}| \tag{13}$$

where the single sphere drag function [20] has the form

$$C_{Ds}\left(\frac{\mathrm{Re}}{V_r}\right) = \left(0.63 + \frac{4.8}{\sqrt{\mathrm{Re}/V_r}}\right)^2 \tag{14}$$

The terminal velocity correlation (V_r) and the Reynolds number (Re) of the particle are represented as follows

$$V_r = 0.5(A - 0.06\ \mathrm{Re} + \sqrt{(0.06\ \mathrm{Re})^2 + 0.12\ \mathrm{Re}(2B - A) + A^2}) \tag{15}$$

$$\mathrm{Re} = \frac{d_p |\mathbf{u}_s - \mathbf{u}_g| \rho_g}{\mu_g} \tag{16}$$

The Syamlal–O'Brien drag model can be adjusted using experimental parameters to match the minimum fluidization velocity U_{mf} [21]. The functions A and B in Eq. (15) are

$$A = \epsilon_g^{4.14} \tag{17}$$

$$B = \begin{cases} c\epsilon_g^{1.28} & \text{for } \epsilon_g \le 0.85 \\ \epsilon_g^{d} & \text{for } \epsilon_g > 0.85 \end{cases} \tag{18}$$

The coefficients c and d are part of the adjustments that can be made to the model and must satisfy the relation

$$c 0.85^{1.28} = 0.85^d \tag{19}$$

3.2.2 Gidaspow model with blending function. The Gidaspow model [22] calculates the interphase drag force coefficient using two correlations depending on the local void fraction value and blending function. For void fractions less than 0.8, the Ergun equation is used to calculate the interphase force coefficient, and for void fractions greater than or equal to 0.8 the Wen–Yu equation is used. To avoid a discontinuity between the models, the blending function φ_{gs} introduced by [23] is

$$\varphi_{gs} = \frac{\arctan[150 \times 1.75(0.2 - \epsilon_s)]}{\pi} + 0.5 \tag{20}$$

The interphase drag force for the Gidaspow model has been implemented into MFIX using the form [24]

$$F_g = (1 - \varphi_{gs}) F_{g(\mathrm{Ergun})} + \varphi_{gs} F_{g(\mathrm{Wen–Yu})} \tag{21}$$

where F_g for the dense phase uses the Ergun equation when $\epsilon_g < 0.8$

Table 1 Particle properties and flow conditions

	Glass beads	Walnut shells
$\bar{d}_p$ (cm)	0.055	0.062
ρ_p (g/cm^3)	2.60	1.30
ρ_b (g/cm^3)	1.63	0.62
ψ	0.9	0.5, 0.6, 0.7
e	0.95	0.75, 0.85, 0.95
U_{mf} (cm/s)	19.9	18.7
ϵ_g^*	0.373	0.522
U_g (cm/s)	25.8	24.3

Table 2 Grid resolution cases

No. of cells	Δx (cm)	Δz (cm)
19×40	0.50	1.00
38×80	0.25	0.50
76×160	0.13	0.25
19×80	0.50	0.50
38×160	0.25	0.25
76×380	0.13	0.13

$$F_{g(\text{Ergun})} = 150\frac{\epsilon_s^2\mu_g}{\epsilon_g d_p^2} + 1.75\frac{\rho_g\epsilon_s}{d_p}|\mathbf{u}_s - \mathbf{u}_g| \quad (22)$$

and F_g for the dilute phase uses the Wen–Yu equation when $\epsilon_g \geq 0.8$

$$F_{g(\text{Wen–Yu})} = \frac{3}{4}C_D\frac{\rho_g\epsilon_g\epsilon_s}{d_p}|\mathbf{u}_s - \mathbf{u}_g|\epsilon_g^{-2.65} \quad (23)$$

where

$$C_D = \begin{cases} 24[1 + 0.15(\epsilon_g\ \text{Re})^{0.687}]/(\epsilon_g\ \text{Re}) & \text{for Re} < 1000 \\ 0.43 & \text{for Re} \geq 1000 \end{cases} \quad (24)$$

using the same definition of Reynolds number shown in Eq. (16).

3.3 Numerical Methodology. To discretize the governing equations in MFIX, a finite volume approach for a staggered grid is used to reduce numerical instabilities [25]. Velocities are stored at the cell surfaces and scalars, such as void fraction and pressure, are stored at the center of the cell. Discretization of time derivatives are first-order, and discretization of spatial derivatives are second-order. An important feature is the use of a higher-order discretization scheme for the convective terms, known as the Superbee method [26], which improves convergence and accuracy of the solution. A modification of the semi-implicit method for pressure-linked equations (SIMPLE) algorithm is used to solve the governing equations [25]. The first modification uses an equation for the solid volumes fraction that includes the effect of the solids pressure to help facilitate convergence for both loosely and densely packed regions. The second modification uses a variable time-stepping scheme to improve convergence and execution speeds.

3.4 Domain Specification. The cylindrical reactor for the cold-flow experiments is modeled as a 2D plane representing the centerplane of the cylinder with a 9.52 cm diameter and 40 cm height, as shown in Fig. 1(*b*). A Cartesian coordinate system is used to capture the random bubble dynamics characteristic of fluidized beds, and Xie et al. [27] validated the accuracy of a 2D approach. A uniform inlet velocity is specified at the bottom equal to the superficial gas velocity, and atmospheric pressure is specified at the exit. The no-slip condition is used to model the gas-wall interactions and a partial-slip condition [31] for the particle-wall interactions.

The packed bed height for all cases is 10 cm. Two solid materials are simulated to predict the fluidization experiments and to evaluate the current computational modeling efforts. Glass beads will be used to initially validate the simulations with the experiments because the properties of glass beads are well characterized. Of particular concern is the coefficient of restitution (e) and sphericity (ψ) of the materials, especially for biomass. Glass beads have a high value of e and ψ; however, biomass properties are not always known. The material used to represent biomass is ground walnut shell because (i) it tends to fluidize uniformly [10], (ii) it falls within the Geldart type B classification, (iii) it has a density similar to saw dust but is less heterogeneous, and (iv) it is readily available (Opta Minerals, Inc., Waterdown, ON, Canada). Table 1 summarizes the particle properties and flow conditions in this study.

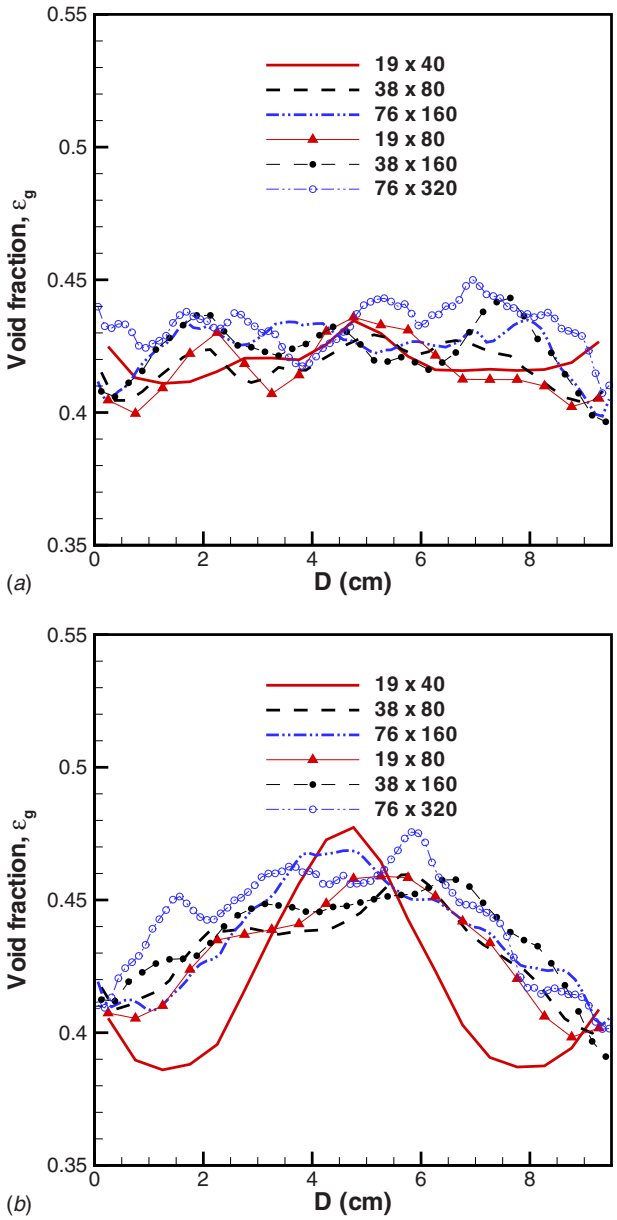

Fig. 2 Time-averaged void fraction profiles of the glass bead bed simulations comparing six grid resolutions at (*a*) *z*=4 cm and (*b*) *z*=8 cm

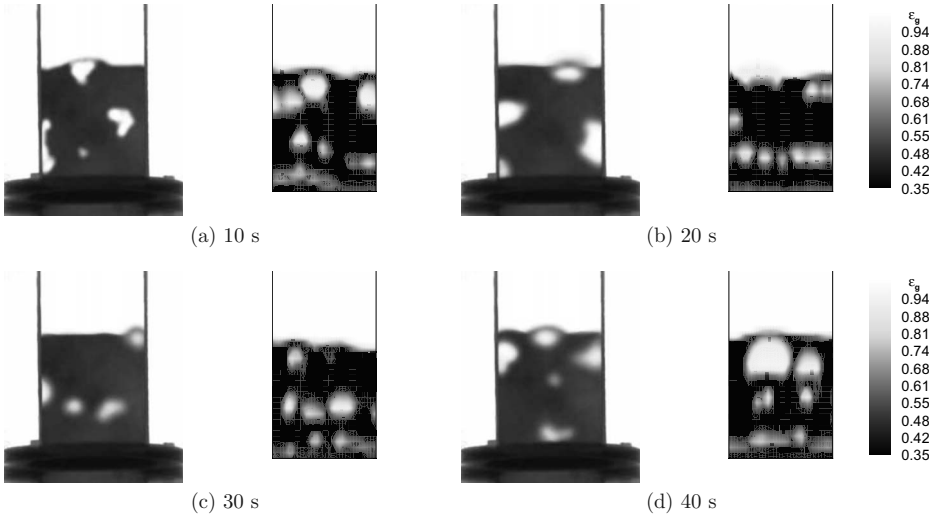

Fig. 3 Instantaneous gas-solid distributions of the glass bead fluidized bed. For each pair of images, the left side is the X-ray radiograph, and the right side is the void fraction contour from the simulation using the medium grid size at (*a*) 10 s, (*b*) 20 s, (*c*) 30 s, and (*d*) 40 s. Note: the gray scale legends are only applicable to the simulations.

4 Cases and Results

4.1 Grid Resolution Study. A fluidized bed consisting of glass beads as the bed material is used to validate the numerical modeling and will also be used to determine appropriate grid resolution. Six grid resolution cases are used to discretize the flow domain into rectangular cells with aspect ratios of 1:1 or 1:2, as shown in Table 2. All numerical data are time-averaged from 5 s to 40 s using equally spaced time intervals of 0.01 s with 3500 time realizations. Time-averaged void fraction profiles for all six grid resolutions are shown in Fig. 2 for the bed heights of $z=4$ and 8 cm. Upon examining the profiles for increasing grid resolution, there is no discernable trend, and all six profiles fall within similar ranges for each bed height. The largest discrepancy in the profiles is for the coarsest resolution of 19×40, as seen in Fig. 2(*b*). Based on Richardson's extrapolation, the largest relative error is less than 1% for the coarsest grid. For the remainder of the grid study discussion, results will be presented for the worst-case grid resolution scenarios with a cell aspect ratio of 1:2.

The gas-solid distributions at approximately 10 s intervals are shown in Fig. 3. Each subfigure shows two images: radiographs from the experiments on the left and numerical simulations on the right. The experimental images are obtained using X-ray radiography. The comparisons between experiments and simulations are not at the exact same time but rather in a time frame of ±1 s. The gray scale legend corresponds to the CFD predictions of void fraction and is shown to compare with the X-ray images. The X-ray images have been enhanced to more clearly show gas bubbles but the X-ray projections do not represent void fraction. The enhanced X-ray images show qualitative bubble locations in the fluidized bed because they are actually projections of the entire 3D volume; hence, the images do not show the three-dimensionality of the flow nor the solid particles in front of or behind the bubbles in the viewing direction and, thus, these results are qualitative. It can be observed that small bubbles develop near the bottom and coalesce forming larger bubbles toward the top of the bed. The qualitative correspondence between the experiment and simulation is very good.

Time-averaged void fraction (ϵ_g) contours for the entire domain for each grid size and two perpendicular planes of the CT scan images are shown in Fig. 4. It is obvious that the coarse grid (Fig. 4(*a*)) predicts a nonhomogeneous flow with dense "pockets" of glass beads near the top of the bed. The medium and fine grids (Figs. 4(*b*) and 4(*c*)) predict a more even distribution of bubbles throughout the bed. Comparisons of the average void fraction indicate that the medium and fine grid predictions compare better with the experiments (Figs. 4(*d*) and 4(*e*)).

The void fraction profiles at two bed heights of $z=4$ and 8 cm are shown in Fig. 5 comparing the simulations with the experiments. The error bars in Fig. 5 represent an absolute gas holdup error of ±0.02, which is typical of most data. A single error bar is provided for each set of experimental data in each figure to avoid confusion, but the error magnitude should be applied to all experimental data. The variations in the experimental data are attributed to the nonuniform inlet conditions that result from the 100 discrete air inlet holes. At the lower bed height, the void fraction distribu-

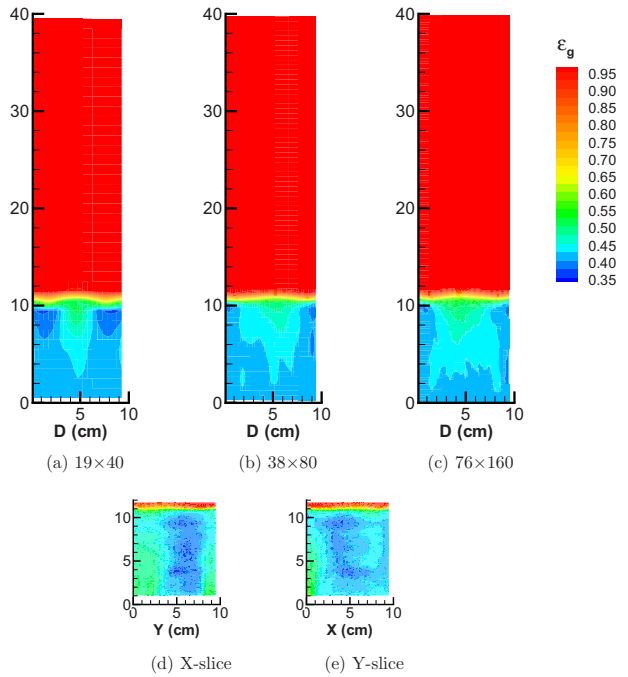

Fig. 4 Time-averaged void fraction contours of the glass bead fluidized bed comparing the simulations using grid resolutions of (*a*) 19×40, (*b*) 38×80, and (*c*) 76×160 with the CT images for an (*d*) *X*-slice and (*e*) *Y*-slice

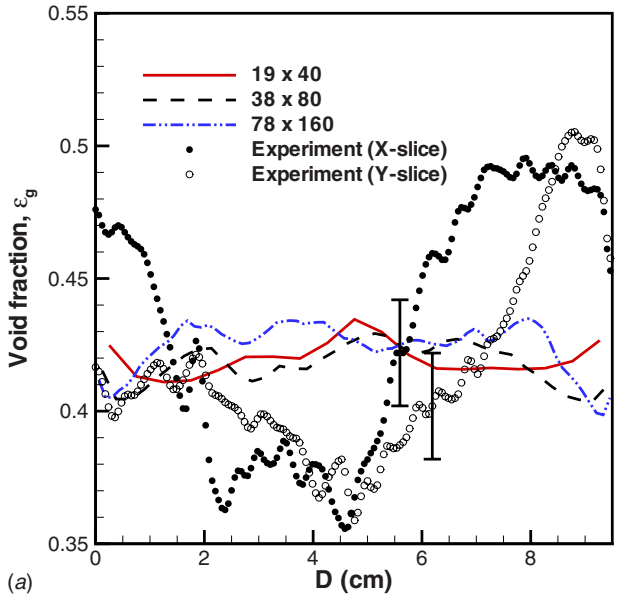

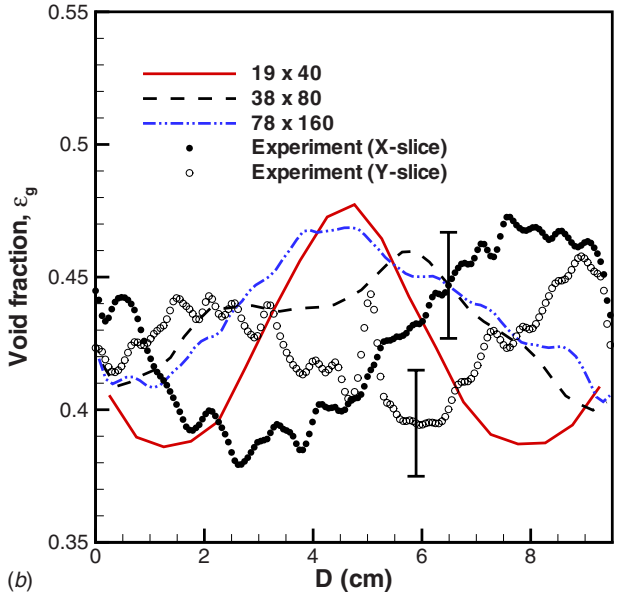

Fig. 5 Time-averaged void fraction profiles of the glass bead fluidized bed comparing the simulations using different grid resolutions with the experiments at (*a*) *z*=4 cm and (*b*) *z* =8 cm

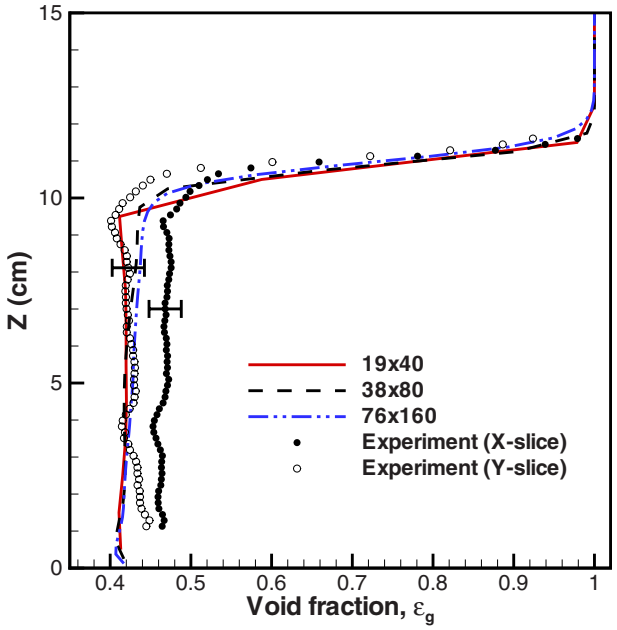

Fig. 6 Time-averaged void fraction profiles of the glass bead fluidized bed comparing the simulations using different grid resolutions with the experiments for data spatially averaged across the bed width versus axial direction

tion is similar for all three grid resolutions. It can be seen that there are qualitative differences in the profiles for the coarse grid as compared with the medium and fine grids at the higher bed height. The lower two minima in the coarse grid profile correspond to the presence of more bead material near the region where the bed expands. Therefore, simulations are assumed independent of the grid size at a resolution of 38×80.

The time-averaged local void fractions shown in Fig. 5 modestly compare between the simulations and 3D experiments, with the results on the same order of magnitude. Similar discrepancies have been shown by others [12,13,28,29]. Two possible reasons may cause this discrepancy. First, the orientation of the experimental *x*- and *y*-slice locations, which are mutually perpendicular, is arbitrary. The 3D volume could be rotated about the central axis for slightly different *x*- and *y*-slice experimental data. Second, as stated by Taghipour et al. [12], the hydrodynamics near the base of the bed can be significantly affected by the distributor design, which was not modeled in the CFD simulations because of the computational expense (each aeration hole would have to be resolved in the computational grid). The influence of the distributor design on the bed hydrodynamics was also identified by Patel et al. [30]. We believe the distributor has a significant influence on the time-averaged local void fraction, and this is not captured in the simulations that use a uniform velocity profile inlet condition. Clearly, the data shown closer to the distributor (Fig. 5(*a*)) show much greater variations.

Although the time-averaged local void fraction across the bed width accentuates the local hydrodynamic influences of the experiments, averaging these values across a horizontal line dampens local variations and provides a better comparison. For example, the void fraction averaged across the bed width versus the domain height for each grid size is compared with the experiments in Fig. 6. Again, the error bars represent typical experimental error in the measured data. The bed height expands to approximately 11.3 cm, which compares well with the expansion height of 11.2 cm measured in the experiments.

The similarity in instantaneous gas-solid distributions between the experiments and simulations and quantitative comparisons of void fraction distribution throughout the bed provide confidence in the computational modeling. Based on the validation study of the glass bead bed, it is concluded that a medium grid resolution will be sufficient for use in the following studies.

4.2 Drag Model Study. The drag models of Syamlal–O'Brien and Gidaspow (with the blending function) are compared with experimental data for glass beads. Figure 7 represents the pressure drop in the glass bead bed versus superficial gas velocity for the simulations with the two drag models and the experiments. Once the bed fluidizes at a superficial gas velocity of 25 cm/s, both drag models have a pressure drop of 1550 Pa, which agrees very well with the theoretical value and is reasonably close to 1470 Pa obtained in the experiments. It should be noted that the Syamlal–O'Brien drag model predictions may not compare well with the measured pressure drop for $U_g < U_{mf}$ because the models were developed for drag forces in a state of fluidization.

Figure 8 compares the average void fraction in the fluidized bed for both drag models with the results obtained from the CT images. The predictions using the different drag models (Figs. 8(*a*)

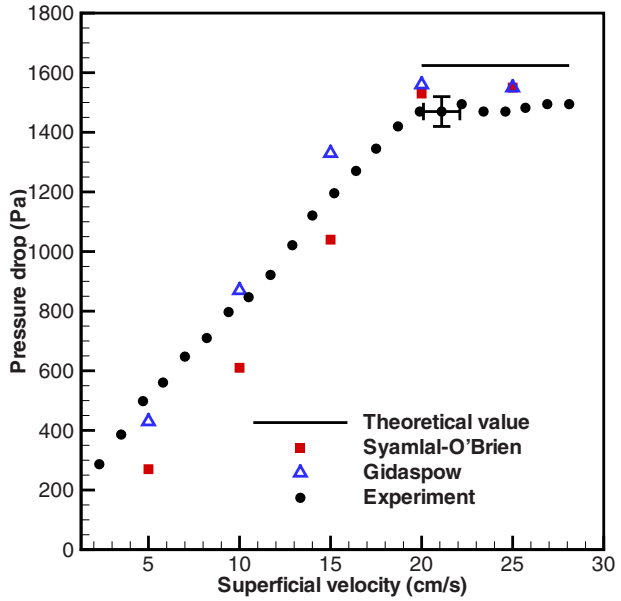

Fig. 7 Pressure drop versus superficial gas velocity through the glass bead bed comparing the simulations using different drag models with the experiments

and 8(*b*)) are similar to the experiments (Figs. 8(*c*) and 8(*d*)); however, the Gidaspow model predicts a more uniform distribution across the bed. The void fraction at two bed heights of z=4 and 8 cm are shown in Fig. 9; in both cases, the average void fraction is greater for the Gidaspow model. A comparison of the simulations and experiments is also shown in Fig. 10, which represents the void fraction averaged across the bed width versus the domain height. The average height of the expanded bed from the experiment is 11.2 cm, while numerical simulations yield an average bed height of 11.1 cm and 11.3 cm for Syamlal–O'Brien and

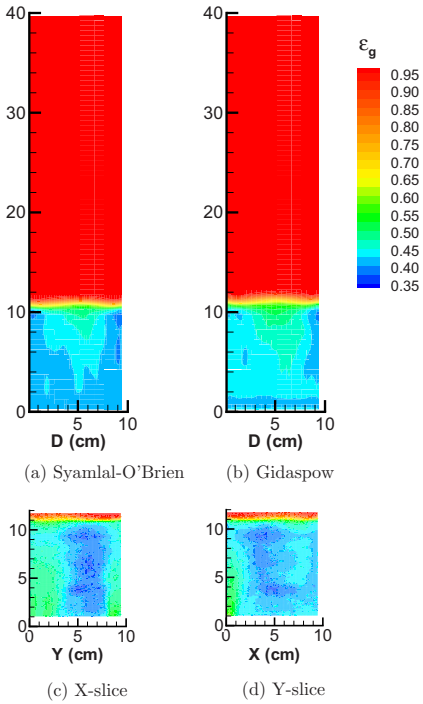

Fig. 8 Time-averaged void fraction contours of the glass bead fluidized bed comparing the simulations using the (*a*) Syamlal–O'Brien drag model and (*b*) the Gidaspow drag model with the CT images for an (*c*) *X*-slice and (*d*) *Y*-slice

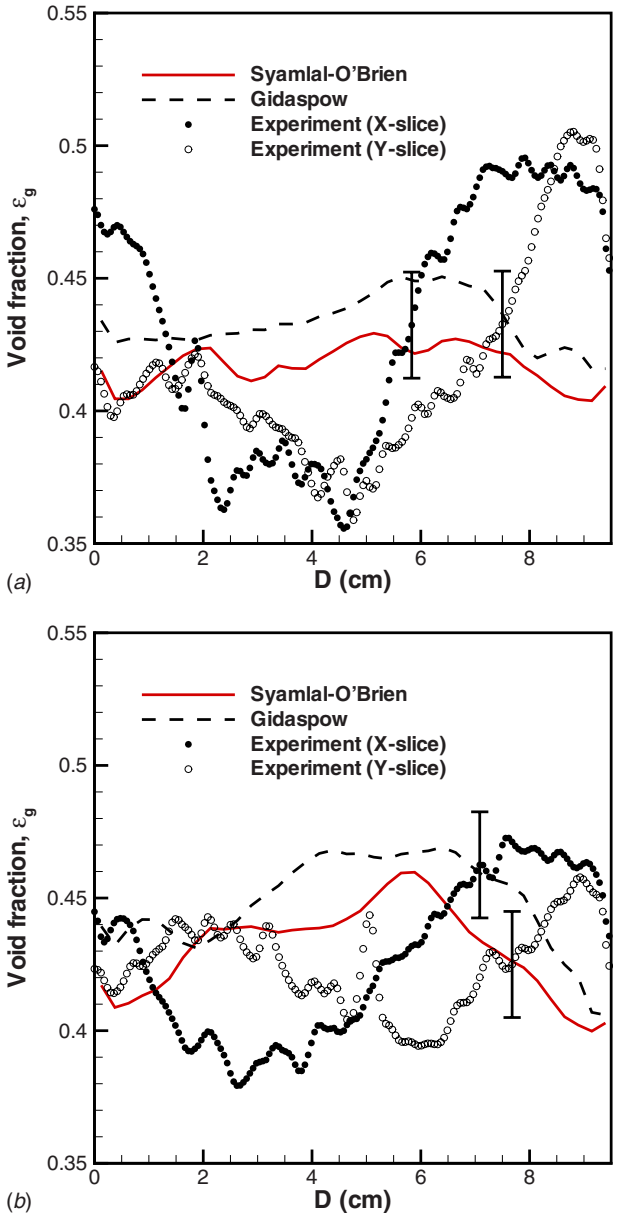

Fig. 9 Time-averaged void fraction profiles of the glass bead fluidized bed comparing the simulations using different drag models with the experiments at (*a*) *z*=4 cm and (*b*) *z*=8 cm

Gidaspow drag models, respectively.

Of particular interest to this study is the use of a drag model that does not completely require à priori information from experiments, e.g., the minimum fluidization velocity. Biomass materials are not well characterized and therefore make computational modeling challenging. The quantitative comparisons just presented indicate that the Gidaspow model is suitable for modeling fluidized beds and will be used in the parametric study to determine the coefficient of restitution and particle sphericity for biomass. The advantage of the Gidaspow model is that it only requires basic particle properties such as mean diameter and sphericity. However, irrespective of the drag model, the coefficient of restitution is needed for the solid-solid interactions. Thus, Sec. 4.3 explores properties such as sphericity and the coefficient of restitution on biomass fluidization.

4.3 Biomass Modeling Validation. Ground walnut shell particles are used as a case study for a biomass fluidized bed. Particle properties and flow conditions are found in Table 1. As a starting

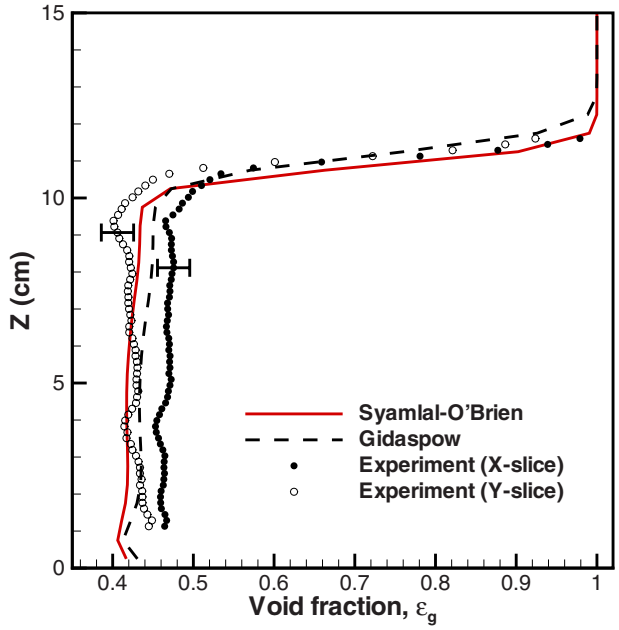

Fig. 10 Time-averaged void fraction profiles of the glass bead fluidized bed comparing the simulations using different drag models with the experiments for data spatially averaged across the bed width versus axial direction

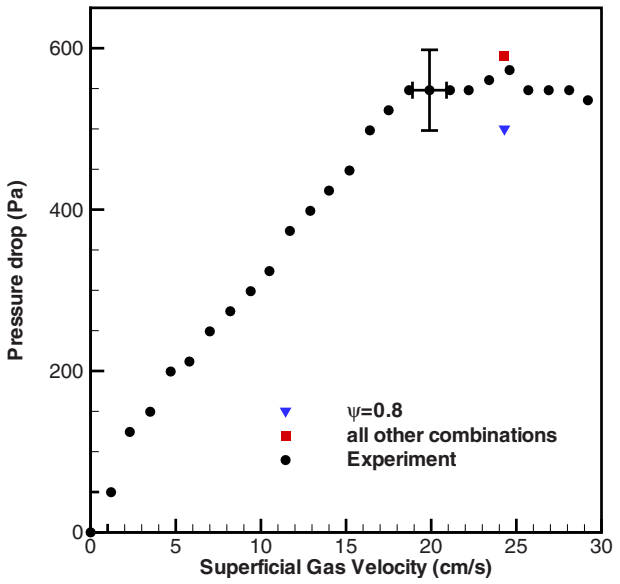

Fig. 12 Pressure drop versus superficial gas velocity through the ground walnut shell bed comparing the experiments with the simulations using the Gidaspow drag model at $U_g=1.3U_{mf}$ =24.3 cm/s

point, a qualitative comparison is made between the experiments and simulations. The gas-solid distributions at approximately 10 s intervals are shown in Fig. 11. Each subfigure shows images of the radiographs on the left and numerical simulations (using e =0.85 and ψ=0.6) on the right. The comparisons between experiments and simulations are not at the exact same time but rather in a time frame of ±1 s. As with the glass bead bed, there is good qualitative agreement with the formation and coalescence of bubbles. The similarities in instantaneous gas-solid distributions between the experiments and simulations provide initial confidence with using the Gidaspow model to predict biomass fluidization.

Pressure drop across the ground walnut shell bed was calculated for a superficial gas velocity of $1.3U_{mf}$=24.3 cm/s for a combination of coefficients of restitution (e=0.75, 0.85, and 0.95) and particle sphericity (ψ=0.5, 0.6, 0.7, and 0.8) using the Gidaspow drag model. Results from the computational simulations, shown in Fig. 12, indicate that with a particle sphericity of 0.8, irrespective of the coefficient of restitution, the pressure drop is 500 Pa, compared with 590 Pa for all of the other ψ-e combinations and the experimentally measured value of 570 Pa. The reason that the simulations using a particle sphericity of 0.8 do not compare well is because the bed has not fluidized. As presented in Eq. (12), the sphericity reduces the mean particle diameter; thus, sphericity values smaller than 0.8 represent smaller, more irregular particles that can easily fluidize.

The hydrodynamics of the bed are first analyzed to study the

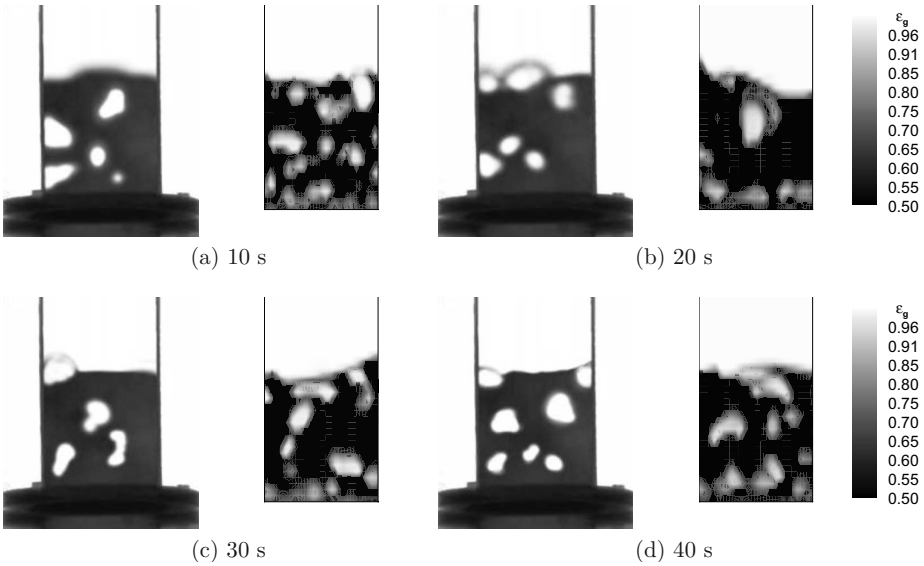

Fig. 11 Instantaneous gas-solid distributions of the ground walnut shell fluidized bed. For each pair of images, the left side is the X-ray radiograph and the right side is the void fraction contour from the simulation using the Gidaspow drag model at (*a*) 10 s, (*b*) 20 s, (*c*) 30 s, and (*d*) 40 s. Note: the gray scale legends are only applicable to the simulations.

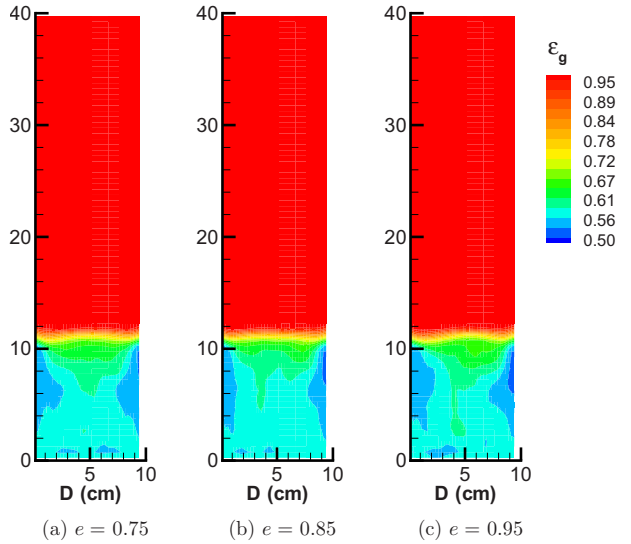

(a) $e = 0.75$ (b) $e = 0.85$ (c) $e = 0.95$

Fig. 13 Time-averaged void fraction contours of the ground walnut shell fluidized bed comparing the simulations using (*a*) *e*=0.75, (*b*) *e*=0.85, and (*c*) *e*=0.95

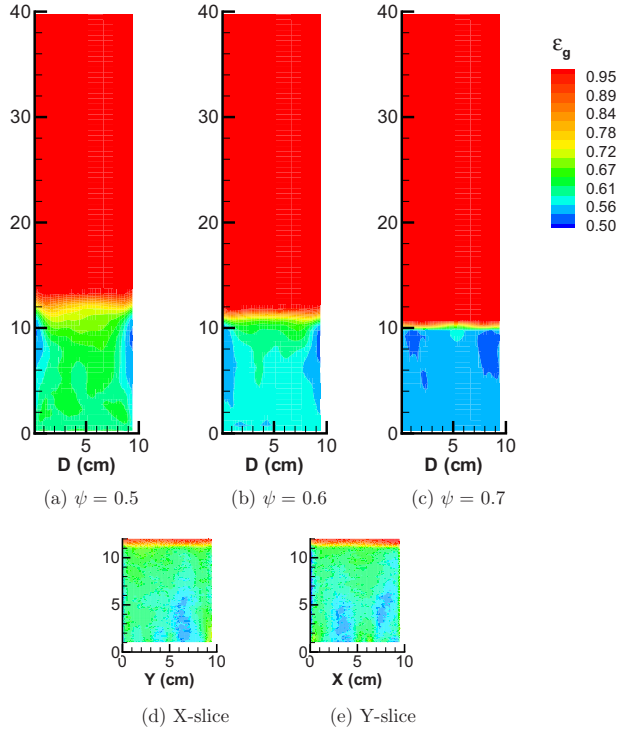

(a) $\psi = 0.5$ (b) $\psi = 0.6$ (c) $\psi = 0.7$

(d) X-slice (e) Y-slice

Fig. 14 Time-averaged void fraction contours of the ground walnut shell fluidized bed comparing the simulations using (*a*) ψ=0.5, (*b*) ψ=0.6, and (*c*) ψ=0.7 with the CT images for an (*d*) *X*-slice and (*e*) *Y*-slice

effects of coefficient of restitution with sphericity fixed at 0.6. The coefficient of restitution cannot be easily determined experimentally for the irregular shaped ground walnut shell particles; one way to find a value that best represents the actual coefficient is through a parametric study. The results should provide how sensitive the hydrodynamics are to the coefficient of restitution and how it affects the overall performance of the fluidized bed. Time-averaged void fraction contours from 5 s to 40 s for the numerical simulations are shown in Figs. 13(*a*)–13(*c*) for different coefficients of restitution. No considerable differences are observed between these three results. The parametric study for coefficient of restitution indicates that this variable does not have a significant influence on the bed hydrodynamics for these flow conditions, perhaps due to the lower superficial inlet gas velocity of $1.3U_{mf}$.

Another parameter tested is the biomass particle sphericity. The coefficient of restitution is fixed at 0.85, and the superficial gas velocity is $1.3U_{mf}$. Time-averaged void fraction contours from 5 s to 40 s for the simulations, and two perpendicular planes of the CT scan images are shown in Fig. 14. It can be seen that the particles with sphericity of 0.5 and 0.6 tend to have noticeable areas of higher concentration along the walls near z=8 and 6 cm, respectively. The distribution of particles with sphericity of 0.7 is mostly constant throughout the bed. As the sphericity increases, the effective mean particle diameter increases, the particle distribution is more uniform in the bed and the overall bed height decreases. A comparison of the simulations with the experiments is shown in Fig. 15, which presents the void fraction averaged across the bed width versus the domain height. The sphericity parametric study indicates that sphericity does change the bed hydrodynamics and is a sensitive value in modeling biomass. Based on the results shown in Fig. 15, the numerical simulations compare well with the experiments when ψ=0.6. The average height of the expanded bed from the experiment is 11.3 cm, while numerical simulations for particle sphericities of 0.5, 0.6, and 0.7 yielded an average bed height of 12.3 cm, 11.4 cm, and 10.3 cm, respectively.

5 Conclusions

Glass beads were used to establish the validity of the multifluid Eulerian–Eulerian model to numerically simulate and predict the hydrodynamics of a fluidized bed. Glass beads were also used to determine an adequate grid resolution and then to validate the Syamlal–O'Brien and Gidaspow drag models. Numerical simulations of the bubbling regime for an inflow gas velocity of $1.3U_{mf}$ were compared with CT and X-ray radiograph images for the gas-solid distribution to demonstrate the qualitative agreement in bubble formation and bed fluidization. The pressure drop, void fraction, and mean bed height expansion were in quantitative agreement between the experiments and simulations using both drag models. It was encouraging that the Gidaspow model predictions were in close agreement because the model does not require

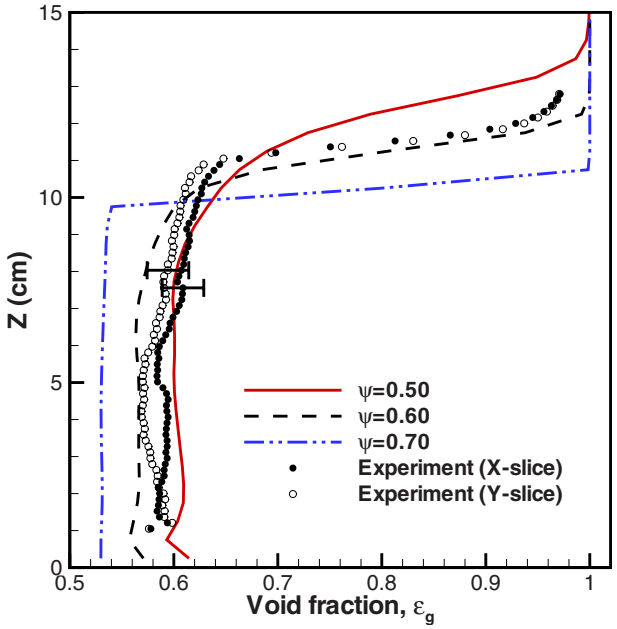

Fig. 15 Time-averaged void fraction profiles of the ground walnut shell fluidized bed comparing the simulations using different particle sphericity with the experiments for data spatially averaged across the bed width versus axial direction

knowing the minimum fluidization as an input, which is an issue when biomass is the bed material because, in practice, the minimum fluidization velocity is not typically known.

Ground walnut shells were used to represent biomass because the material fluidizes uniformly and is classified as a Geldart type B particle. Simulations of ground walnut shells were analyzed to determine parameters that cannot easily be measured experimentally. Both coefficient of restitution and sphericity were varied to determine the effects on the predictions. The coefficient of restitution study showed no significant differences in the hydrodynamics of the fluidized bed for values between 0.75 and 0.95. However, the particle sphericity study showed that sphericity does affect the behavior of the fluidized bed. It was shown that with decreasing sphericity, the bed more readily fluidized because the effective mean particle diameter decreased. Thus, higher sphericity values either underpredicted the bed expansion or the bed did not fluidize, whereas lower sphericities overpredicted the bed expansion.

This research showed qualitative and quantitative comparisons between numerical and experimental data. Although this study is specific to the bed medium, it does demonstrate that biomass can be modeled using the Gidaspow correlations. Furthermore, the parametric study for ground walnut shell indicated that the material can be characterized with a medium sphericity ($\approx$0.6) and a relatively large coefficient of restitution ($\approx$0.85).

Nomenclature

C_D = drag coefficient
CTI = intensity of the CT scan image
d = diameter
$\bar{d}$ = mean diameter
e = coefficient of restitution
F = coefficient of the interphase momentum transfer
$\mathbf{g}$ = gravitational acceleration
$\mathbf{I}$ = interphase momentum transfer
P = pressure
$\mathbf{q}$ = diffusive flux of granular energy
Re = Reynolds number
t = time
$\mathbf{u}$ = velocity vector
U = fluidization velocity
V_r = terminal velocity correlation

Greek Letters

ϵ = volume fraction
ϕ = transfer of granular energy
φ = blending function
γ = rate of granular energy dissipation due to inelastic collisions
λ = local X-ray attenuation
μ = dynamic viscosity
θ = granular temperature
ρ = density of gas or solid
$\bar{\bar{\sigma}}$ = viscous stress tensor
ψ = particle sphericity

Superscripts/Subscripts

b = bulk
g = gas phase
mf = minimum fluidization
p = particle
s = solid phase

References

[1] Cui, H., and Grace, J. R., 2007, "Fluidization of Biomass Particles: A Review of Experimental Multiphase Flow Aspects," Chem. Eng. Sci., **62**(1–2), pp. 45–55.
[2] Ohman, M., Pommer, L., and Nordin, A., 2005, "Bed Agglomeration Characteristics and Mechanisms During Gasification and Combustion of Biomass Fuels," Energy Fuels, **19**(4), pp. 1742–1748.
[3] Scala, F., Chirone, R., and Salatino, P., 2006, "Combustion and Attrition of Biomass Chars in a Fluidized Bed," Energy Fuels, **20**(1), pp. 91–102.
[4] Chirone, R., Miccio, F., and Scala, F., 2006, "Mechanism and Prediction of Bed Agglomeration During Fluidized Bed Combustion of Biomass Fuel: Effect of the Reactor Scale," Chem. Eng. J., **123**(3), pp. 71–80.
[5] Huilin, L., Yunhua, Z., Ding, J., Gidaspow, D., and Wei, L., 2007, "Investigation of Mixing/Segregation of Mixture Particles in Gas-Solid Fluidized Beds," Chem. Eng. Sci., **62**(1–2), pp. 301–317.
[6] Nijenhuis, J., Korbee, R., Lensselink, J., Kiel, J. H. A., and van Ommen, J. R., 2007, "A Method for Agglomeration Detection and Control in Full-Scale Biomass Fired Fluidized Beds," Chem. Eng. Sci., **62**(1–2), pp. 644–654.
[7] Bartels, M., Lin, W., Nijenhuis, J., Kapteijn, F., and van Ommen, J. R., 2008, "Agglomeration in Fluidized Beds at High Temperatures: Mechanisms, Detection and Prevention," Prog. Energy Combust. Sci., **34**(5), pp. 633–666.
[8] Heindel, T. J., Hubers, J. L., Jensen, T. C., Gray, J. N., and Striegel, A. C., 2005, "Using X-rays for Multiphase Flow Visualization," ASME Paper No. FEDSM2005-77359.
[9] Heindel, T. J., Gray, J. N., and Jensen, T. C., 2008, "An X-ray System for Visualizing Fluid Flows," Flow Meas. Instrum., **19**(2), pp. 67–78.
[10] Franka, N. P., Heindel, T. J., and Battaglia, F., 2008, "Visualizing Cold-Flow Fluidized Beds With X-rays," ASME Paper No. IMECE2007-43073.
[11] Zhang, K., and Brandani, S., 2005, "CFD Simulation in a Circulating Fluidized-Bed Biomass Gasifier—A Modified Particle Bed Model in Bubbling Fluidized Beds," Ranliao Huaxue Xuebao/Journal of Fuel Chemistry and Technology, **33**(1), pp. 1–5.
[12] Taghipour, F., Ellis, N., and Wong, C., 2005, "Experimental and Computational Study of Gas-Solid Fluidized Bed Hydrodynamics," Chem. Eng. Sci., **60**(24), pp. 6857–6867.
[13] Du, W., Bao, X., Xu, J., and Wei, W., 2006, "Computational Fluid Dynamics (CFD) Modeling of Spouted Bed: Assessment of Drag Coefficient Correlations," Chem. Eng. Sci., **61**(5), pp. 1401–1420.
[14] Mahinpey, N., Vejahati, F., and Ellis, N., 2007, "CFD Simulation of Gas-Solid Bubbling Fluidized Bed: An Extensive Assessment of Drag Models," 4th International Conference on Computational and Experimental Methods in Multiphase and Complex Flow 2007, Bologna, Italy, June 12–14, Vol. 56, pp. 51–60.
[15] Abdullah, M. Z., Husain, Z., and Yin Pong, S. L., 2003, "Analysis of Cold Flow Fluidization Test Results for Various Biomass Fuels," Biomass Bioenergy, **24**(6), pp. 487–494.
[16] Richardson, J. F., 1971, "Incipient Fluidization and Particulate Systems," *Fluidization*, J. Davidson and D. Harrison, eds., American Press, London, pp. 27–29.
[17] Syamlal, M., Rogers, W., and O'Brien, T., 1993, "MFIX Documentation: Theory Guide," National Energy Technology Laboratory, Department of Energy, Technical Note DOE/METC-95/1013 and NTIS/DE95000031.
[18] Agrawal, K., Loezos, P. N., Syamlal, M., and Sundaresan, S., 2001, "The Role of Meso-Scale Structures in Rapid Gas-Solid Flows," J. Fluid Mech., **445**, pp. 151–185.
[19] Lun, C. K., Savage, S. B., Jeffrey, D. J., and Chepurniy, N., 1984, "Kinetic Theories for Granular Flow: Inelastic Particles in Couette Flow and Slightly Inelastic Particles in a General Flowfield," J. Fluid Mech., **140**, pp. 223–256.
[20] Dalla Valle, J. M., 1948, *Micromeritics, The Technology of Fine Particles*, Pitman, New York.
[21] Syamlal, M., and O'Brien, T., 2003, "Fluid Dynamic Simulation of O_3 Decomposition in a Bubbling Fluidized Bed," AIChE J., **49**(11), pp. 2793–2801.
[22] Gidaspow, D., 1994, *Multiphase Flow and Fluidization: Continuum and Kinetic Theory Descriptions*, Academy, Boston, MA.
[23] Huilin, L., and Gidaspow, D., 2003, "Hydrodynamics of Binary Fluidization in a Riser: CFD Simulation Using Two Granular Temperatures," Chem. Eng. Sci., **58**(16), pp. 3777–3792.
[24] Lathouwers, D., and Bellan, J., 2000, "Modeling and Simulation of Bubbling Fluidized Beds Containing Particle Mixtures," Proc. Combust. Inst., **28**, pp. 2291–2304.
[25] Syamlal, M., 1998, "MFIX Documentation: Numerical Technique," National Energy Technology Laboratory, Department of Energy, Technical Note DOE/MC31346–5824 and NTIS/DE98002029.
[26] Syamlal, M., 1998, "High Order Discretization Methods for the Numerical Simulation of Fluidized Beds," Department of Energy, Technical Note DOE/FETC/C-98/7305 and CONF-971113.
[27] Xie, N., Battaglia, F., and Pannala, S., 2008, "Effects of Using Two-Versus Three-Dimensional Computational Modeling of Fluidized Beds: Part I, Hydrodynamics," Powder Technol., **182**(1), pp. 1–13.
[28] Cao, J., Cheng, Z., Fang, Y., Jing, H., Huang, J., and Wang, Y., 2008, "Simulation and Experimental Studies on Fluidization Properties in a Pressurized Jetting Fluidized Bed," Powder Technol., **183**(1), pp. 127–132.
[29] Ahuja, G. N., and Patwardhan, A. W., 2008, "CFD and Experimental Studies of Solids Hold-Up Distribution and Circulation Patterns in Gas-Solid Fluidized Beds," Chem. Eng. J., **143**(1–3), pp. 147–160.
[30] Patel, A. K., Waje, S. S., Thorat, B. N., and Mujumdar, A. S., 2008, "Tomographic Diagnosis of Gas Maldistribution in Gas-Solid Fluidized Beds," Powder Technol., **185**(3), pp. 239–250.
[31] Johnson, P. C., and Jackson, R., 1987, "Frictional-Collision Constitutive Relations for Granular Materials With Application to Plane Shearing," J. Fluid Mech., **176**, pp. 67–93.

Application of MI Simulation Using a Turbulent Model for Unsteady Orifice Flow

Mitsuhiro Nakao
e-mail: nakao.m.aa@m.titech.ac.jp

Kenji Kawashima

Toshiharu Kagawa

Precision and Intelligence Laboratory,
Tokyo Institute of Technology,
Yokohama 2268503, Japan

Measurement-integrated (MI) simulation is a numerical simulation in which experimental results are fed back to the simulation. The calculated values become closer to the experimental values. In the present paper, MI simulation using a turbulent model is proposed and applied to steady and unsteady oscillatory airflows passing an orifice plate in a pipeline. Velocity and pressure feedbacks are conducted and both feedback methods showed good agreement with the experimental results. Moreover, the calculation times between the MI simulation and ordinary simulation were compared in steady and unsteady conditions. The calculation time was demonstrated to be significantly reduced compared with ordinary simulation. [DOI: 10.1115/1.4000259]

Keywords: unsteady flow, flow measurement, measurement-integrated simulation, turbulence model

1 Introduction

Visualizing the state of plant or engine pipelines is very important in order to ensure safe operation and to diagnose faults. The methods used to investigate the flow conditions can be classified into two approaches: one is experimental measurement, and the other is numerical simulation by solving several equations [1]. Experimental measurement methods include the use of velocity and pressure sensors and visualization techniques such as particle image velocimetry and particle tracking velocimetry. Flow conditions can be accurately obtained at measured points by using sensors. However, sensors are not suitable for obtaining velocity profiles or pressure distributions. By contrast, visualization techniques are able to obtain these distributions. However, the available flow field is limited because particle behavior is tracked using a laser and a camera [2].

In contrast, simulation can easily obtain a flow field. However, a long calculation time is needed to obtain good results, especially under turbulent conditions. As a result, both measurement and simulation have a disadvantage in obtaining the flow field.

Therefore, measurement-integrated (MI) simulation is proposed [3]. This method is a numerical simulation in which experimental results are fed back to the simulation, and the method can obtain results that are closer to the real flow. In another respect, even if a rough grid is used, the calculation results have sufficient accuracy. MI simulation was performed for the Karman vortex street behind a square cylinder [4] and complex blood flows [5].

We have applied MI simulation to unsteady orifice flow and confirmed that the calculation results approach those of the experiments [6]. However, a laminar model was used for the calculation. As a result, the accuracy was insufficient.

In the present paper, a turbulent k-ε model is used for MI simulation in order to improve the calculation accuracy. Two feedback methods, namely, velocity feedback and pressure feedback, are applied and compared experimentally under the steady and unsteady conditions using an unsteady flow generator. The calculation time and accuracy of the proposed simulation are investigated when the feedback values are either the flow velocities or pressures.

2 MI Simulation

2.1 Numerical Simulation. Figure 1 shows the concept of MI simulation. Some output signals are defined for the real flow measurement and for the numerical simulation in order to evaluate the difference between the both the results. Numerical simulation is carried out with the additional body force as the feedback signal that is derived from the difference between the both output signals. If the feedback law is designed properly, the computational result closes to the real flow.

Air is treated as an incompressible viscous fluid and is considered to remain in an isothermal condition. Two-dimensional cylindrical coordinates are considered. The governing equations for the flow in the pipeline considered in this simulation are the nondimensional Navier–Stokes equations including the feedback term and the equation of continuity, which are given as follows:

$$\frac{\partial u}{\partial t}+u\frac{\partial u}{\partial x}+v\frac{\partial u}{\partial r}=-\frac{\partial}{\partial x}\left(p+\frac{2}{3}k\right)+\frac{1}{\mathrm{Re}_{\mathrm{eff}}}\left\{\frac{\partial^2 u}{\partial x^2}+\frac{1}{r}\frac{\partial}{\partial r}\left(r\frac{\partial u}{\partial r}+r\frac{\partial v}{\partial x}\right)+\frac{\partial^2 u}{\partial x^2}\right\}+f \tag{1}$$

$$\frac{\partial v}{\partial t}+u\frac{\partial v}{\partial x}+v\frac{\partial v}{\partial r}=-\frac{\partial}{\partial r}\left(p+\frac{2}{3}k\right)+\frac{1}{\mathrm{Re}_{\mathrm{eff}}}\left\{\frac{\partial^2 v}{\partial x^2}+\frac{1}{r}\frac{\partial}{\partial r}\left(r\frac{\partial v}{\partial r}\right)+\frac{\partial}{\partial x}\left(\frac{\partial u}{\partial r}\right)+\frac{1}{r}\frac{\partial}{\partial r}\left(r\frac{\partial v}{\partial r}\right)-2\frac{v}{r^2}\right\} \tag{2}$$

$$\frac{\partial u}{\partial x}+\frac{1}{r}\frac{\partial (rv)}{\partial r}=0 \tag{3}$$

$$\mathrm{Re}=\frac{\rho U_0 R_0}{\mu},\quad \frac{1}{\mathrm{Re}_{\mathrm{eff}}}=\frac{1}{\mathrm{Re}}+\nu_t$$

In Eq. (1), the last term f represents the feedback value. As a turbulent model, we employ the standard k-ε model. Therefore, the transport equations of k and ε are given as

$$\frac{\partial k}{\partial t}+u\frac{\partial k}{\partial x}+v\frac{\partial k}{\partial r}=\frac{1}{\mathrm{Re}\,k}\left\{\frac{\partial}{\partial x}\left(\frac{\partial k}{\partial x}\right)+\frac{1}{r}\frac{\partial}{\partial r}\left(r\frac{\partial k}{\partial r}\right)\right\}+G-\varepsilon \tag{4}$$

Contributed by the Fluids Engineering Division of ASME for publication in the JOURNAL OF FLUIDS ENGINEERING. Manuscript received August 26, 2008; final manuscript received: August 6, 2009; published online October 30, 2009. Editor: Joseph Katz.

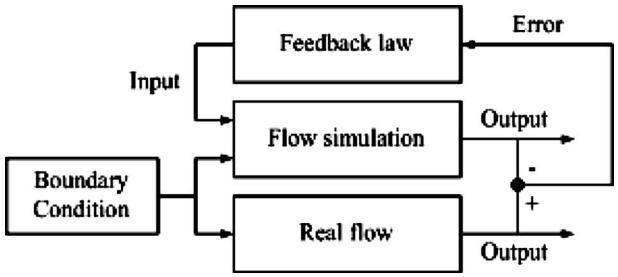

Fig. 1 MI simulation

$$\frac{\partial \varepsilon}{\partial t} + u\frac{\partial \varepsilon}{\partial x} + v\frac{\partial \varepsilon}{\partial r} = \frac{1}{\mathrm{Re}\,\varepsilon}\left\{\frac{\partial}{\partial x}\left(\frac{\partial \varepsilon}{\partial x}\right) + \frac{1}{r}\frac{\partial}{\partial r}\left(r\frac{\partial \varepsilon}{\partial r}\right)\right\} + C_1 G\frac{\varepsilon}{k} - C_2\frac{\varepsilon^2}{k}$$

$$G = \nu_t\left\{2\left(\frac{\partial u}{\partial x}\right)^2 + 2\left(\frac{\partial v}{\partial r}\right)^2 + \left(\frac{\partial u}{\partial r} + \frac{\partial v}{\partial x}\right)^2 + 2\left(\frac{v}{r}\right)^2\right\} \tag{5}$$

$$\frac{1}{\mathrm{Re}\,k} = \frac{1}{\mathrm{Re}} + \frac{\nu_t}{\sigma_k}, \quad \frac{1}{\mathrm{Re}\,\varepsilon} = \frac{1}{\mathrm{Re}} + \frac{\nu_t}{\sigma_\varepsilon}$$

$$C_1 = 1.44, \quad C_2 = 1.92, \quad C\mu = 0.09, \quad \sigma_k = 1.0, \quad \sigma_\varepsilon = 1.3$$

The governing equations are discretized using the finite volume method on a staggered grid system and are solved using the SIMPLE algorithm [7].

The calculation time of MI simulation was compared with that of standard k-ε model using fine mesh. The number of calculation grids is about 30,000. Time interval was determined to satisfy the Courant number as 1. The calculation was performed using the commercially available software package called SCRYU/TETRA manufactured by Software Cradle Co., Ltd.

2.2 Integration Method of Measurement and Simulation Feedback Law. Standard k-ε model has a problem in the expression of the separation flow. Therefore, we apply the MI simulation to the k-ε model. The velocities and pressures, as shown in Fig. 3, are measured for the simulation. Measurement points of pressure are same as standard orifice flow meters. In this paper, we selected the points considering practical use for a first step.

A flow chart of calculation using the SIMPLE algorithm is shown in Fig. 2. In the first step of calculation, the initial conditions and boundary conditions are determined, and the estimated pressure field p^* is obtained in the next step. The result of the previous calculation for pressure is used for p^*, except for the calculation of the first time step, in which the atmospheric pressure is used.

In the third step, velocity fields u^* and v^* are calculated based on the estimated pressure field p^*. The feedback signal of the velocity feedback or the pressure feedback f_p is added to the calculation of u^*.

The velocity feedback signal is added to the right-hand side of Eq. (1) in the velocity calculation of the measurement point and also to the entire cross section of the point. This signal is described as follows:

$$f_u = K \times \bar{u} \times (u_{\mathrm{exp}} - u_{\mathrm{sim}}) \tag{6}$$

In pressure feedback, two equations are used. The feedback signal f_p is added to the velocity calculation in the velocity calculation of the grid.

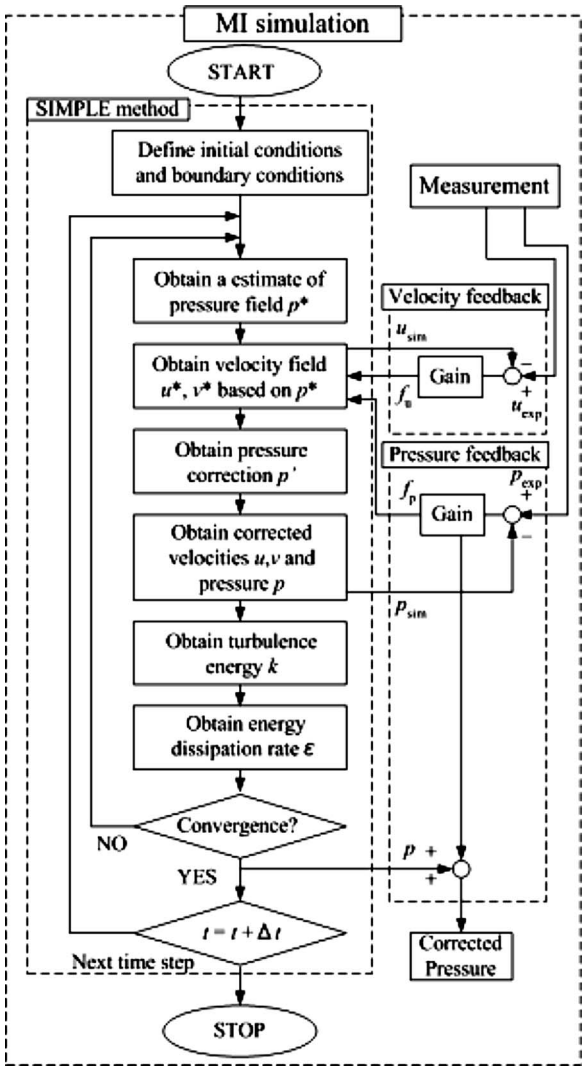

Fig. 2 Calculation algorithm

$$f_p = K_p \times (\Delta p_{\mathrm{exp}} - \Delta p_{\mathrm{sim}}) \tag{7}$$

Both feedback and pressure terms in Eq. (1) are treated as body force. The feedback term causes pressure calculation error. Therefore, pressure correction is needed.

In the fourth step, pressure correction p' is obtained and velocity fields u^* and v^* and estimated pressure p^* are corrected. In the SIMPLE method, the pressures are calculated from the equation of continuity and Navier–Stokes equations. Since adding the feedback to the equation of continuity will destroy the conservation

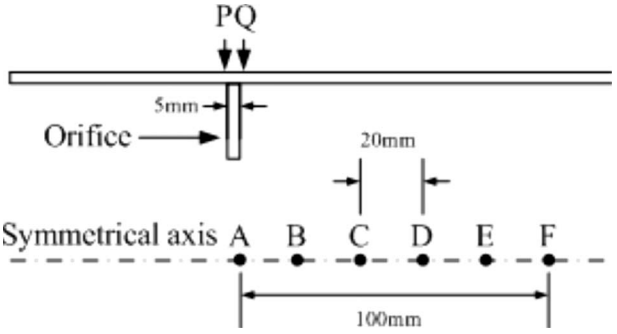

Fig. 3 Measurement points

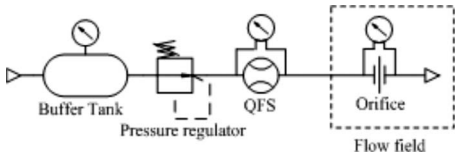

Fig. 4 Experimental apparatus for steady flow

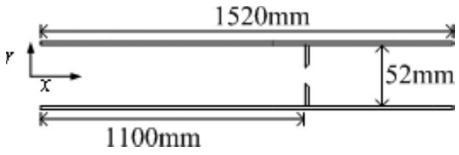

Fig. 5 Flow field

law, the feedback term is added for pressure correction after calculation is converged, as shown in Fig. 2. Pressures on upstream of feedback cross section are calculated as follows:

$$p = p_{\text{sim}} + f_p \Delta x \Delta r \tag{8}$$

All measured velocities at points A through F or measured differential wall pressures between point P and Q were fed back to the calculation in the velocity feedback or pressure feedback. However, in the first calculation loop on the first time step, the feedback signal is fed back after no feedback calculation converges because calculated values are much different in the first calculation time step.

3 Steady Flow

3.1 Apparatus. We first confirmed the effectiveness of MI simulation using steady flow. Figure 4 shows the experimental apparatus for steady flow. Air is supplied by an air compressor, and a buffer tank is used to reduce the pressure fluctuation. The flow rates are controlled by operating a pressure regulator. A quick flow sensor (QFS) is used for the flow measurement [8]. The target flow field is installed downstream of the QFS. Velocities were measured by hot wire anemometers, and pressures at point P and Q were measured by diaphragm differential pressure sensors (Nagano Keiki, Co. Ltd., KL-17).

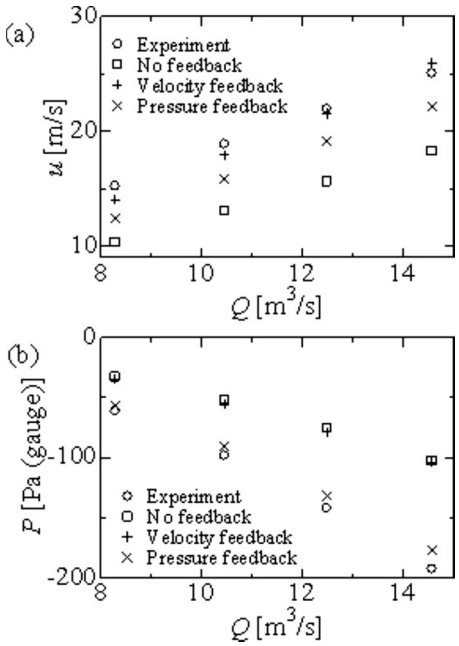

Fig. 6 Comparisons of several methods: (*a*) axial velocity at point F and (*b*) pressure at point R

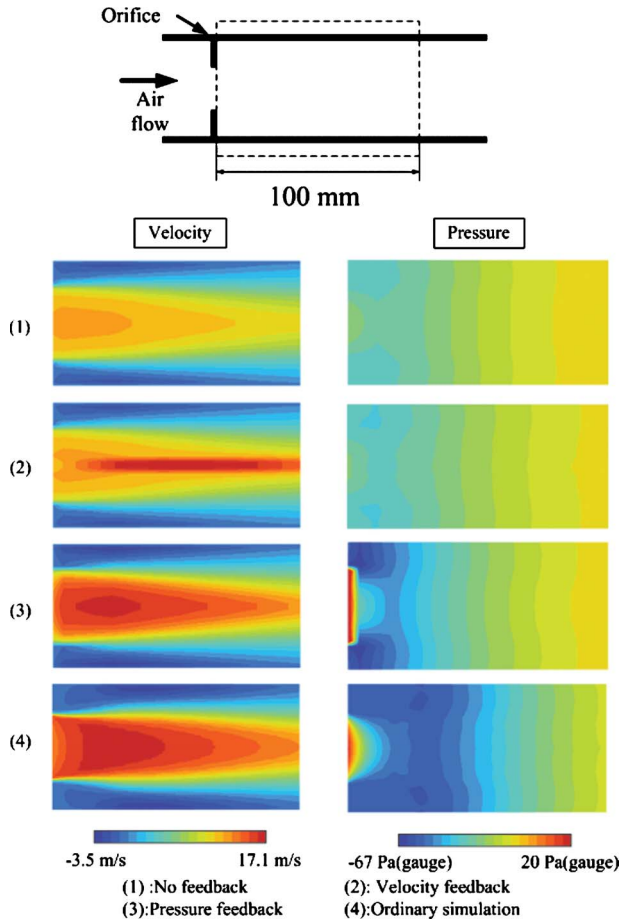

Fig. 7 Comparison of velocity (left) and pressure (right) distribution downstream of the orifice

The MI simulation was applied to a pipeline with an orifice plate. Figure 5 shows the experimental setup of the tested pipeline with the orifice plate. The pipeline used in the experiment had a length of 1520 mm and a diameter of 52 mm. The orifice with a critical ratio of 0.6 is installed 1100 mm from the inlet of the pipeline. The air flow is discharged to the atmosphere 420 mm downstream of the orifice plate.

Two methods—the velocity feedback and pressure feedback—were applied and compared. The grid sizes $h_{\text{axial}} \times h_{\text{radial}}$ were 5.0×0.5 mm^2 in the upstream region of the orifice, 0.5×0.5 mm^2 in the orifice region, and 2.0×0.5 mm^2 in the downstream region of the orifice. Grid points $N_{\text{axial}} \times N_{\text{radial}}$ are 48×10. The feedback gains K and K_p are 4.0 and 1.0, respectively.

3.2 Calculation Results. The velocity at point F and the pressure at point R were compared among four methods, as follows: experiment, no feedback, MI simulation with velocity feedback, and pressure feedback.

The calculations were executed for four different flow rates. The results are shown in Fig. 5. The lateral axis shows the flow rate. The upper figure shows the flow velocities in the x-direction, and the lower figure shows the pressures.

Figure 6 indicates that good agreement is obtained by MI simulation with velocity feedback for the axial velocities and improvement is seen in pressures. MI simulation with pressure feedback shows good agreement with the experimental results, both velocities and pressures.

Figure 7 compares the distribution of the axial velocity downstream of the orifice between the experiment and simulations with

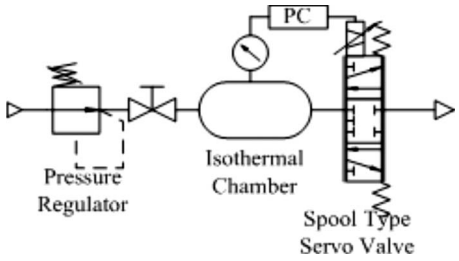

Fig. 8 Apparatus of the unsteady flow generator

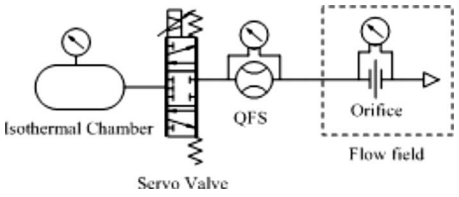

Fig. 9 Experimental apparatus for unsteady flow

a flow rate of 8.5×10^{-3} m^3/s. The graph numbers (1), (2), (3) and (4) figures show the results of no feedback, MI simulations with velocity feedback, MI simulation with pressure feedback, and ordinary simulation with fine grid by SCRYU/TETRA, respectively. In ordinary simulation, about 3×10^4 calculation meshes were used.

The results of MI simulation with velocity feedback show that the feedback effects in velocity distribution around the central axis are better than those obtained without feedback. However, the shape of the pressure distribution is insufficient compared with ordinary simulation.

As the measured pressures are fed back to the entire cross section in the pipeline with the pressure feedback, some different can be seen in the velocity distribution compared with ordinary simulation. This disagreement of velocity distribution is assumed to primary factor of disagreement of axial velocities shown in Fig. 6. However, the entire trend of velocity distribution and the pressure distribution around the orifice becomes closer to that obtained by ordinary simulation.

4 Unsteady Flow

4.1 Unsteady Flow Generator. The simulations are calculated for unsteady oscillatory flows. The unsteady mass flow is generated using an isothermal chamber and a servo valve, as shown in Fig. 8 [9]. The state equation for compressible fluids in a chamber can be written as

$$pV = WR\bar{\theta} \tag{9}$$

The following equation can be derived by differentiating Eq. (9), if the chamber volume is constant:

$$V\frac{dp}{dt} = Q_m R\bar{\theta} + WR\frac{d\bar{\theta}}{dt} \tag{10}$$

The controlled mass flow rate G, which is the generated flow, is discharged through the servo valve installed downstream of the isothermal chamber. The generated flow G is given by the following equation by transforming Eq. (10):

$$Q_m = \frac{V}{R\theta_a}\frac{dp}{dt} + \frac{W}{\bar{\theta}}\frac{d\bar{\theta}}{dt} \tag{11}$$

If the state of the air in the chamber during discharge remains isothermal, the generated mass flow rate can be obtained from Eq. (11) as

$$Q_m = \frac{V}{R\theta_a}\frac{dp}{dt} \tag{12}$$

Since the condition remains isothermal, the average temperature in the chamber is equal to room temperature $\bar{\theta}$. Equation (4) indicates that if the volume of the chamber V and the room temperature $\bar{\theta}$ are known, then the generated mass flow rate can be controlled by the pressure difference in the isothermal chamber. The pressure change in the isothermal chamber is controlled by the servo valve.

4.2 Apparatus. Figure 9 shows the experimental apparatus for the unsteady flow experiments. The inlet flow rate was given as a sinusoidal oscillatory flow having an average flow rate of 8.5×10^{-3} m^3/s, an amplitude of 1.6×10^{-3} m^3/s, and a frequency of 0.5 Hz. The results of unsteady flow generation at a frequency of 0.5 Hz are shown in Fig. 10. A low-pass filter was used to process the measured data. The cutoff frequency of the filter was set at 10 Hz.

Filtered data were used for the feedback. The grid size, grid points, and feedback gains are the same as for the steady conditions. The increment time Δt was selected as 2 ms. The feedback data rate is synchronized to Δt.

4.3 Calculation Result. The velocities at points C and F were compared between the experiment and simulations. The results are shown in Fig. 11. Since the Reynolds number is approximately 13,000, the flow is turbulent. However, little turbulence was observed in the velocities at point C, which is a region of accelerating flow because of the jet flow. At this point, MI simulation with velocity feedback shows good agreement with that of the experiment. The feedback effect can also be seen in MI simulation with pressure feedback, and the effect is smaller compared with the velocity feedback.

The flow fluctuation is large at the measured point F. Not all simulated velocities can recapture the velocity fluctuations caused by the flow turbulence. This is because the k-ε model was used. However, the average velocities calculated by MI simulation with velocity feedback and pressure feedback show good agreement with the experimentally obtained results.

The pressures at points P and Q were compared between the experiment and simulations. The results are shown in Fig. 12. The pressures calculated by MI simulation with pressure feedback can represent the measured pressure at both points P and Q. Since point P is upstream of feedback point, the pressures at point P calculated by MI simulation with velocity feedback have large error compared with that of experiment. However, the pressures at point Q are close to that of experiment.

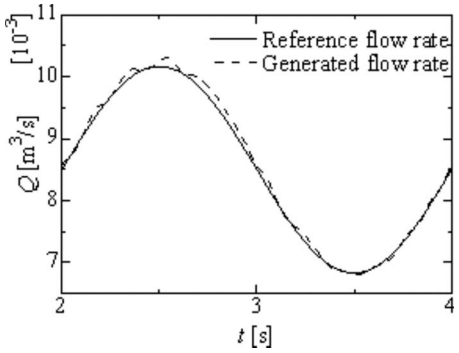

Fig. 10 Flow generation results with an average flow rate of 8.5×10^{-3} m^3/s, an amplitude of 1.6×10^{-3} m^3/s, and a frequency of 0.5 Hz

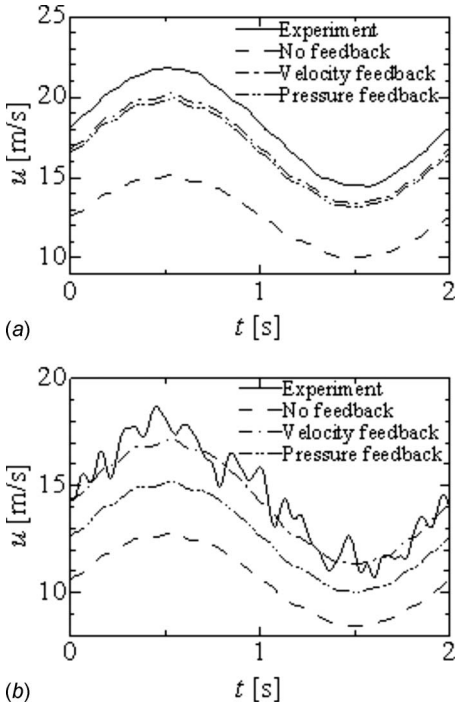

Fig. 11 Comparisons of *x*-direction velocities obtained by several methods: (*a*) at point C and (*b*) at point F

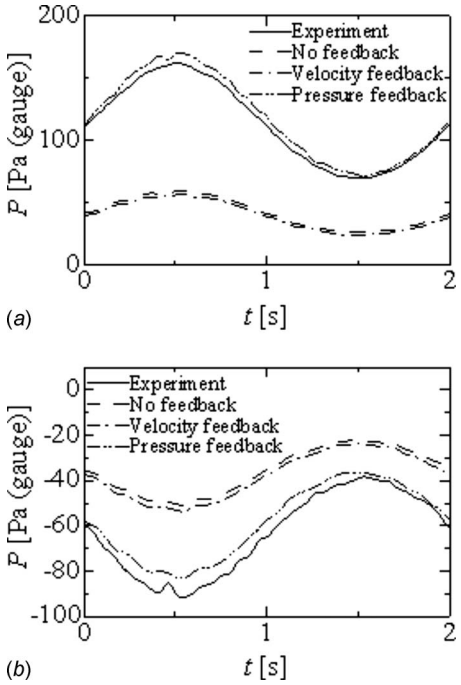

Fig. 12 Comparisons of pressures between several methods: (*a*) at point O and (*b*) at point P

5 Effect of Increment Time

5.1 Calculation Accuracy. The computer used in the simulations had a 2.4 GHz CPU with 2048 Mbytes memory. In steady flow calculation, the flow rate is given as 8.5×10^{-3} m^3/s. In unsteady flow calculation, the oscillatory flow rate is given as $8.5\times10^{-3}+1.6\times10^{-3}\sin(22\pi ft)$ (m^3/s) and one cycle of sinusoidal flow rate was used for the calculations. The increment times were set to three different ways; 2 ms, 256 ms, and 512 ms. The feedback data rate is synchronized to the increment time. The feedback gains K and K_p are 4.0 and 1.0, respectively.

Figure 13 shows the comparisons of velocity at point F with several increment times. Since we employ SIMPLE algorithm, which is a semi-implicit method, all calculations were stable. Furthermore, same calculation results were obtained.

5.2 Calculation Time. Comparison of the calculation time between MI simulation with velocity feedback, pressure feedback, and ordinary simulation is summarized in Tables 1 and 2. In the steady condition, calculation time of MI simulation with velocity feedback is 10% less than that of MI simulation with pressure feedback. However, both methods can reduce the calculation time compared with the ordinary simulation taking about 2 h.

Under the unsteady condition, MI simulation, which has an increment time of 2 ms with velocity and pressure feedbacks, takes two times longer than the steady flow calculation. Calculation time of MI simulation, which has an increment time of 256 ms or 512 ms, is almost same as that of steady condition. Meanwhile, ordinary simulation takes approximately several days. It is clear that MI simulation can significantly reduce the calculation time.

6 Conclusion

A k-ε model generated by measurement-integrated simulation was applied to steady and unsteady oscillatory airflows passing over an orifice plate in a pipeline. The feedback values were investigated. The flow velocities or pressures were measured and fed back to the simulation.

Comparisons of the velocities and pressures and visualizations were performed between the no feedback, MI simulation with velocity feedback, and pressure feedback cases. It was confirmed that the velocity distribution becomes closer to real flow with the

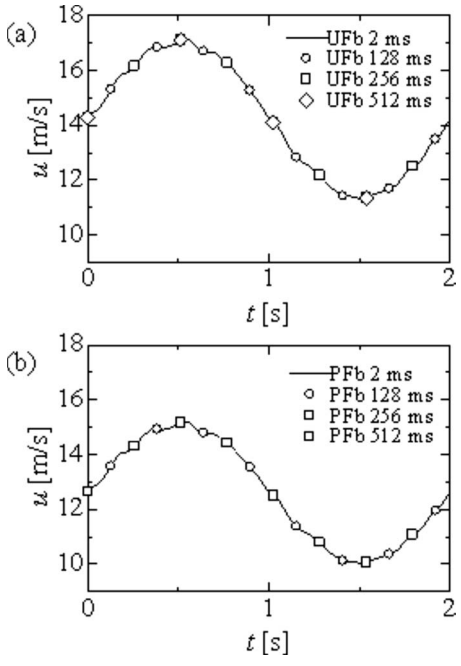

Fig. 13 Comparisons of increment time: (*a*) velocity feedback, (*b*) pressure feedback

Table 1 Comparisons of calculation time in steady condition

	Velocity feedback	Pressure feedback	Ordinary simulation
Steady	3.8 s	4.2 s	2 h

Table 2 Comparisons of calculation time in unsteady condition

	Unsteady
Velocity feedback (2 ms)	8.1 s
Velocity feedback (256 ms)	3.8 s
Velocity feedback (512 ms)	3.8 s
Pressure feedback (2 ms)	8.5 s
Pressure feedback (256 ms)	4.3 s
Pressure feedback (512 ms)	4.2 s
Ordinary simulation	Several days

velocity feed back, and the pressure feedback is superior for obtaining a global image of the flow field.

Comparisons of the calculation time were performed between MI simulation and ordinary simulation under the steady and unsteady conditions. The calculation time was demonstrated to be significantly reduced compared with ordinary simulation for both velocity and pressure feedbacks. The proposed method is useful for monitoring the state of flow and pressure in pipelines in near real time.

Nomenclature

f = feedback signal
f_u = velocity feedback signal
f_p = pressure feedback signal
k = turbulent energy
ε = dissipation of turbulent energy
Re = Reynolds number
(x,r) = cylindrical coordinate system
u = x-direction velocity
v = r-direction velocity
μ = viscosity
ν_t = turbulent kinematic viscosity
$\mathrm{Re}_{\mathrm{eff}}$ = effective Reynolds number
$C_1, C_2, C_\mu, \sigma_k, \sigma_\tau$ = model constants of standard k-ε model
G = mass flow rate
h_{axial} = grid size in the axial direction
h_{radia} = grid size in the radial direction
K = feedback gain of the velocity feedback signal ($\mathrm{m/s^2}$)
K_p = feedback gain of pressure feedback signal ($\mathrm{m/s^2}$)
p = :pressure (Pa)
Q = volume flow rate ($\mathrm{m^3/s}$)
Q_m = mass flow rate (kg/s)
R = gas constant (J/kg K))
R_0 = pipe radius (m)
U_0 = average velocity at the inlet (m/s)
V = volume of the chamber ($\mathrm{m^3}$)
W = mass of gas in the chamber (kg)
θ = temperature of gas (K)
θ_a = room temperature (K)
$\bar{\theta}$ = average temperature (K)
ρ = density ($\mathrm{kg/m^3}$)

Subscript

– = average value
exp = experimental value
sim = simulated value

References

[1] Ferziger, J. H., and Peric, M., 2003, *Computational Methods for Fluid Dynamics*, 2nd ed., Springer-Verlag, Tokyo.
[2] F. T. M. Nieuwstadt, ed., 1993, *Flow Visualization and Image Analysis*, Kluwer Academic Publishers, Dordrecht, Boston.
[3] Hayase, T., and Hayashi, S., 1997, "State Estimator of Flow as an Integrated Computational Method With the Feedback of Online Experimental Measurement," ASME J. Fluids Eng., **119**, pp. 814–822.
[4] Funamoto, K., Hayase, T., Shirai, A., Saijo, Y., and Yamabe, T., 2005, "Fundamental Study of Ultrasonic-Measurement-Integrated Simulation of Real Blood Flow in the Aorta," Ann. Biomed. Eng., **33**(4), pp. 415–428.
[5] Nisugi, K., Hayase, T., and Shirai, A., 2004, "Fundamental Study of Hybrid Wind Tunnel Integrating Numerical Simulation and Experiment in Analysis of Flow Field," JSME Int. J., Ser. B, **47**(3), pp. 593–604.
[6] Funaki, T., Kawashima, K., Inoue, S., and Kagawa, T., 2006, "Application of Measurement Integrated Simulation to Unsteady Flow Monitoring," SICE-ICASE International Joint Conference, pp. 5218–5221.
[7] Patankar, S. V., 1980, *Numerical Heat Transfer and Fluid Flow*, McGraw-Hill, New York.
[8] Funaki, T., Sengoku, K., Kawashima, K., and Kagawa, T., 2004, "Dynamic Calibration of Laminar Flow Sensor for Gases," SICE Annual Conference.
[9] Kawashima, K., and Kagawa, T., 2003, "Unsteady Flow Generator for Gases Using Isothermal Chamber," Measurement, **33**(4), pp. 333–340.